

The Pennsylvania State University

The Graduate School

Department of Mechanical and Nuclear Engineering

OECD/NRC BENCHMARK BASED ON NUPEC PWR SUBCHANNEL AND BUNDLE
TESTS (PSBT) - ANALYSIS USING SUBCHANNEL CODE CTF AND SYSTEM CODE
TRACE

A Thesis in

Nuclear Engineering

by

Adam Joseph Rubin

Submitted in Partial Fulfillment
of the Requirements
for the Degree of

Master of Science

May 2011

The thesis of Adam Joseph Rubin was reviewed and approved* by the following:

Maria Avramova
Assistant Professor of Nuclear Engineering
Thesis Advisor

Kostadin Ivanov
Distinguished Professor of Nuclear Engineering

Alexander Velazquez-Lozada
U.S. Nuclear Regulatory Commission

Arthur Motta
Professor of Nuclear Engineering and Materials Science and Engineering
Chair of Nuclear Engineering Department

*Signatures are on file in the Graduate School

ABSTRACT

The OECD/NRC Benchmark Based on NUPEC PWR Subchannel and Bundle Tests (PSBT) was designed to provide a data set with which to evaluate the abilities of existing subchannel, system, and computational fluid dynamics (CFD) thermal-hydraulics codes to predict void distribution and departure from nucleate boiling (DNB) in a pressurized water reactor (PWR) for steady-state and transient conditions. The benchmark consists of seven exercises divided into two phases, a void distribution benchmark and a DNB benchmark. A specification was created to distribute experimental information to participants. In addition, two studies were performed to determine the reliability of the experimental data.

Results from the benchmark participants were then compiled and analyzed. Based on the final results for the first phase and preliminary results for the second phase, a number of conclusions were drawn. The codes involved tended to overpredict the void fraction at the lower elevations of the test sections and underpredict it at the higher elevations. This was attributed to the x-ray densitometer measurement method used, which was sensitive to the dependence of subchannel void distribution on flow regime. It was noted that the participants' results showed a time shift in the temperature increase transients, indicating unexpected heat transfer between the test section and downcomer. Many of the codes also experienced difficulty in accurately modeling the brief flow reduction transient, generally underpredicting the void fraction early in the transient.

TRACE is a thermal-hydraulics code developed by the U.S. Nuclear Regulatory Commission for system analysis. TRACE calculations were performed for the transient bundle void distribution test cases and the results were presented with analysis. It was concluded that TRACE was able to stay within the 5% error bound for the power increase test case, but was not able to stay within this bound for the other cases. A time shift was seen in the temperature increase test case, which was likely due to heat transfer between the downcomer and test section. This indicates that the experimental section may not have actually been adiabatic.

The PSU in-house code CTF, an improved version of the advanced thermal-hydraulic subchannel code COBRA-TF, was also used for preliminary scoping calculations of selected benchmark exercises. CTF was generally able to predict the void fraction in the subchannel test cases within 10% void, but was not able to stay within the 3% error bound for these cases. The CTF results stayed within the error bound for the power increase transient, but the code was not able to maintain this accuracy for the other three test cases. As with TRACE, a time shift was seen in the temperature increase transient.

TABLE OF CONTENTS

LIST OF FIGURES	vi
LIST OF TABLES	xii
ACKNOWLEDGEMENTS	xiii
Chapter 1 Introduction	1
1.1 Introduction	1
1.2 Benchmark Objective	1
1.3 Definition of Benchmark Phases	1
1.3.1 Phase I – Void Distribution Benchmark.....	2
1.3.2 Phase II – Departure from Nucleate Boiling (DNB) Benchmark.....	2
1.4 Benchmark Team and Sponsorship	2
1.5 Test Facility.....	3
Chapter 2 Void Distribution Benchmark	5
2.1 Specification.....	5
2.1.1 Single Subchannel Test Section and Assemblies	5
2.1.2 Rod Bundle Test Section and Assemblies	7
2.1.2.1 Spacer Grid Data.....	10
2.1.2.2 Heater Rod Data.....	13
2.1.3 Measurement Techniques.....	13
2.1.4 Test Cases	17
2.1.4.1 Exercise 1 – Steady-state Single Subchannel.....	17
2.1.4.2 Exercise 2 – Steady-state Rod Bundle	17
2.1.4.3 Exercise 3 – Transient Bundle	17
2.1.4.4 Exercise 4 – Pressure Drop.....	19
2.2 Analysis.....	20
2.2.1 Studies Performed on Data.....	20
2.2.1.1 Study Performed on Calculation of Void Fraction	20
2.2.1.2 Study Performed on Calculation of Quality	21
2.2.2 Participant Results.....	24
2.2.2.1 Exercise 1 – Steady-state Single Subchannel.....	25
2.2.2.2 Exercise 2 – Steady-state Rod Bundle	25
2.2.2.3 Exercise 3 – Transient Rod Bundle.....	25
2.2.2.4 Exercise 4 – Pressure Drop.....	25
Chapter 3 Departure from Nucleate Boiling (DNB) Benchmark	26
3.1 Specification.....	26
3.1.1 Test Assemblies	26
3.1.2 Measurement Techniques.....	29
3.1.3 Test Cases	32
3.1.3.1 Exercise 1 – Fluid Temperature	32
3.1.3.2 Exercise 2 – Steady-state Rod Bundle	32
3.1.3.3 Exercise 3 – Transient Rod Bundle.....	32
3.2 Analysis.....	34
3.2.1 Participant Results.....	35
3.2.1.1 Exercise 1 – Fluid Temperature	35
3.2.1.2 Exercise 2 – Steady-state Rod Bundle	35
3.2.1.3 Exercise 3 – Transient Rod Bundle.....	35
Chapter 4 Analysis Using Subchannel Code CTF and System Code TRACE.....	36

4.1 TRACE.....	36
4.1.1 Modeling Considerations	36
4.1.2 Results	37
4.2 CTF	39
4.2.1 Modeling Considerations	39
4.2.2 Results	43
4.3 Comparison	46
Chapter 5 Conclusion.....	47
Bibliography	48
Appendix I Exercise I-1 Results	50
Appendix II Exercise I-2 Results	64
Appendix III Exercise I-3 Results.....	83
Appendix IV Exercise I-4 Results	101
Appendix V Exercise II-1 Results	103
Appendix VI Exercise II-2 Results	122
Appendix VII Exercise II-3 Results.....	128

LIST OF FIGURES

Figure 1.1 PSBT Benchmark Team	2
Figure 1.2 NUPEC Test Facility	4
Figure 2.1 Test Section for Central Subchannel Void Distribution Measurement	5
Figure 2.2 Cross-sectional View of Subchannel Test Assembly	6
Figure 2.3 Test Section for Rod Bundle Void Distribution Measurement	8
Figure 2.4 Radial Power Distribution A	9
Figure 2.5 Radial Power Distribution B	10
Figure 2.6 View of Simple Spacer Grid.....	11
Figure 2.7 View of Non-Mixing Vane Spacer Grid	12
Figure 2.8 View of Mixing Vane Spacer Grid.....	12
Figure 2.9 Cross-sectional View of Heater Rod	13
Figure 2.10 Relation Between Chordal and CT Averaged Densities (for S1).....	16
Figure 2.11 Variation of Properties for Test Case 5T (Power Increase)	18
Figure 2.12 Variation of Properties for Test Case 5T (Flow Reduction)	18
Figure 2.13 Variation of Properties for Test Case 5T (Depressurization).....	19
Figure 2.14 Variation of Properties for Test Case 5T (Temperature Increase)	19
Figure 2.15 Deviation of Measured Void Fraction from Recalculated Void Fraction	21
Figure 2.16 Deviation of Measured Quality from Recalculated Quality for Test Series 1 and 2.	22
Figure 2.17 Deviation of Measured Quality from Recalculated Quality for Test Series 5	23
Figure 2.18 Deviation of Measured Quality from Recalculated Quality for Test Series 6	23
Figure 2.19 Deviation of Measured Quality from Recalculated Quality for Test Series 7	24
Figure 2.20 Deviation of Measured Quality from Recalculated Quality for Test Series 8	24
Figure 3.1 Radial Power Distribution C	28
Figure 3.2 Radial Power Distribution D	29
Figure 3.3 Locations of Thermocouples for Test Assemblies	30
Figure 3.4 Diagram of Fluid Temperature Measurement Setup	31
Figure 3.5 Variation of Properties for Test Case 11T (Power Increase)	33
Figure 3.6 Variation of Properties for Test Case 11T (Flow Reduction)	33
Figure 3.7 Variation of Properties for Test Case 11T (Depressurization).....	34
Figure 3.8 Variation of Properties for Test Case 11T (Temperature Increase)	34
Figure 4.1 TRACE Model of Test Series 5T	36
Figure 4.2 Decomposition of Fuel Bundle Into Two-Ring Vessel	36
Figure 4.3 TRACE Results for Test Series 5T (Power Increase)	37
Figure 4.4 TRACE Results for Test Series 5T (Flow Reduction)	38
Figure 4.5 TRACE Results for Test Series 5T (Depressurization).....	38
Figure 4.6 TRACE Results for Test Series 5T (Temperature Increase)	39
Figure 4.7 CTF Predictions of Steady-state Void Fraction in a Single Subchannel.....	44
Figure 4.8 Illustration of Chordal Measurements Taken at High and Low Void Fractions	45

Figure 4.9 CTF Prediction of Transient Void Fraction in a Rod Bundle	46
Figure AI.1 Test Series 1 Density Results	50
Figure AI.2 Test Series 2 Density Results	50
Figure AI.3 Test Series 3 Density Results	51
Figure AI.4 Test Series 4 Density Results	51
Figure AI.5 Test Series 1 Void Fraction (Calculated vs. Measured) Results	52
Figure AI.6 Test Series 1 Void Fraction (Calculated vs. Recalculated) Results	52
Figure AI.7 Test Series 2 Void Fraction (Calculated vs. Measured) Results	53
Figure AI.8 Test Series 2 Void Fraction (Calculated vs. Recalculated) Results	53
Figure AI.9 Test Series 3 Void Fraction (Calculated vs. Measured) Results	54
Figure AI.10 Test Series 3 Void Fraction (Calculated vs. Recalculated) Results	54
Figure AI.11 Test Series 4 Void Fraction (Calculated vs. Measured) Results	55
Figure AI.12 Test Series 4 Void Fraction (Calculated vs. Recalculated) Results	55
Figure AI.13 Test Series 1 Thermal Equilibrium Quality (Calculated vs. Measured) Results	56
Figure AI.14 Test Series 1 Thermal Equilibrium Quality (Calculated vs. Recalculated) Results	56
Figure AI.15 Test Series 2 Thermal Equilibrium Quality (Calculated vs. Measured) Results	57
Figure AI.16 Test Series 2 Thermal Equilibrium Quality (Calculated vs. Recalculated) Results	57
Figure AI.17 Test Series 3 Thermal Equilibrium Quality (Calculated vs. Recalculated) Results	58
Figure AI.18 Test Series 4 Thermal Equilibrium Quality (Calculated vs. Recalculated) Results	58
Figure AI.19 CFD Code Results of Run 1.2211	61
Figure AI.20 CFD Code Results of Run 1.2223	61
Figure AI.21 CFD Code Results of Run 1.2237	62
Figure AI.22 CFD Code Results of Run 1.4326.....	62
Figure AI.23 CFD Code Results of Run 1.4325	63
Figure AII.1 Test Series 5 Region-Averaged Void Fraction Results – Lower Elevation.....	64
Figure AII.2 Test Series 5 Region-Averaged Void Fraction Results – Middle Elevation	64
Figure AII.3 Test Series 5 Region-Averaged Void Fraction Results – Upper Elevation	65
Figure AII.4 Test Series 6 Region-Averaged Void Fraction Results – Lower Elevation.....	65
Figure AII.5 Test Series 6 Region-Averaged Void Fraction Results – Middle Elevation	66
Figure AII.6 Test Series 6 Region-Averaged Void Fraction Results – Upper Elevation	66
Figure AII.7 Test Series 7 Region-Averaged Void Fraction Results – Lower Elevation.....	67
Figure AII.8 Test Series 7 Region-Averaged Void Fraction Results – Middle Elevation	67
Figure AII.9 Test Series 7 Region-Averaged Void Fraction Results – Upper Elevation	68
Figure AII.10 Test Series 8 Region-Averaged Void Fraction Results – Lower Elevation.....	68
Figure AII.11 Test Series 8 Region-Averaged Void Fraction Results – Middle Elevation	69
Figure AII.12 Test Series 8 Region-Averaged Void Fraction Results – Upper Elevation	69
Figure AII.13 Test Series 5 Bundle-Averaged Void Fraction Results – Lower Elevation.....	70
Figure AII.14 Test Series 5 Bundle-Averaged Void Fraction Results – Middle Elevation	70
Figure AII.15 Test Series 5 Bundle-Averaged Void Fraction – Upper Elevation.....	71
Figure AII.16 Test Series 6 Bundle-Averaged Void Fraction – Lower Elevation	71

Figure AII.17 Test Series 6 Bundle-Averaged Void Fraction – Middle Elevation	72
Figure AII.18 Test Series 6 Bundle-Averaged Void Fraction (Upper Elevation)	72
Figure AII.19 Test Series 7 Bundle-Averaged Void Fraction Results – Lower Elevation.....	73
Figure AII.20 Test Series 7 Bundle-Averaged Void Fraction Results – Middle Elevation	73
Figure AII.21 Test Series 7 Bundle-Averaged Void Fraction – Upper Elevation.....	74
Figure AII.22 Test Series 8 Bundle-Averaged Void Fraction – Lower Elevation	74
Figure AII.23 Test Series 8 Bundle-Averaged Void Fraction – Middle Elevation	75
Figure AII.24 Test Series 8 Bundle-Averaged Void Fraction – Upper Elevation.....	75
Figure AII.25 Test Series 5 Bundle-Averaged Thermal Equilibrium Quality – Lower Elevation	76
Figure AII.26 Test Series 5 Bundle-Averaged Thermal Equilibrium Quality – Middle Elevation	76
Figure AII.27 Test Series 5 Bundle-Averaged Thermal Equilibrium Quality – Upper Elevation	77
Figure AII.28 Test Series 6 Bundle-Averaged Thermal Equilibrium Quality – Lower Elevation	77
Figure AII.29 Test Series 6 Bundle-Averaged Thermal Equilibrium Quality – Middle Elevation	78
Figure AII.30 Test Series 6 Bundle-Averaged Thermal Equilibrium Quality – Upper Elevation	78
Figure AII.31 Test Series 7 Bundle-Averaged Thermal Equilibrium Quality – Lower Elevation	79
Figure AII.32 Test Series 7 Bundle-Averaged Thermal Equilibrium Quality – Middle Elevation	79
Figure AII.33 Test Series 7 Bundle-Averaged Thermal Equilibrium Quality – Upper Elevation	80
Figure AII.34 Test Series 8 Bundle-Averaged Thermal Equilibrium Quality – Lower Elevation	80
Figure AII.35 Test Series 8 Bundle-Averaged Thermal Equilibrium Quality – Middle Elevation	81
Figure AII.36 Test Series 8 Bundle-Averaged Thermal Equilibrium Quality – Upper Elevation	81
Figure AIII.1 Test Series 5T (Power Increase) – Lower Elevation Results	83
Figure AIII.2 Test Series 5T (Power Increase) – Middle Elevation Results	83
Figure AIII.3 Test Series 5T (Power Increase) – Upper Elevation Results.....	84
Figure AIII.4 Test Series 6T (Power Increase) – Lower Elevation Results	84
Figure AIII.5 Test Series 6T (Power Increase) – Middle Elevation Results	85
Figure AIII.6 Test Series 6T (Power Increase) – Upper Elevation Results.....	85
Figure AIII.7 Test Series 7T (Power Increase) – Lower Elevation Results	86
Figure AIII.8 Test Series 7T (Power Increase) – Middle Elevation Results	86
Figure AIII.9 Test Series 7T (Power Increase) – Upper Elevation Results.....	87
Figure AIII.10 Test Series 5T (Flow Reduction) – Lower Elevation Results	87
Figure AIII.11 Test Series 5T (Flow Reduction) – Middle Elevation Results	88
Figure AIII.12 Test Series 5T (Flow Reduction) – Upper Elevation Results.....	88
Figure AIII.13 Test Series 6T (Flow Reduction) – Lower Elevation Results	89
Figure AIII.14 Test Series 6T (Flow Reduction) – Middle Elevation Results	89
Figure AIII.15 Test Series 6T (Flow Reduction) – Upper Elevation Results.....	90
Figure AIII.16 Test Series 7T (Flow Reduction) – Lower Elevation Results	90

Figure AIII.17 Test Series 7T (Flow Reduction) – Middle Elevation Results	91
Figure AIII.18 Test Series 7T (Flow Reduction) – Upper Elevation Results.....	91
Figure AIII.19 Test Series 5T (Depressurization) – Lower Elevation Results.....	92
Figure AIII.20 Test Series 5T (Depressurization) – Middle Elevation Results.....	92
Figure AIII.21 Test Series 5T (Depressurization) – Upper Elevation Results	93
Figure AIII.22 Test Series 6T (Depressurization) – Lower Elevation Results.....	93
Figure AIII.23 Test Series 6T (Depressurization) – Middle Elevation Results.....	94
Figure AIII.24 Test Series 6T (Depressurization) – Upper Elevation Results	94
Figure AIII.25 Test Series 7T (Depressurization) – Lower Elevation Results.....	95
Figure AIII.26 Test Series 7T (Depressurization) – Middle Elevation Results.....	95
Figure AIII.27 Test Series 7T (Depressurization) – Upper Elevation Results	96
Figure AIII.28 Test Series 5T (Temperature Increase) – Lower Elevation Results	96
Figure AIII.29 Test Series 5T (Temperature Increase) – Middle Elevation Results	97
Figure AIII.30 Test Series 5T (Temperature Increase) – Upper Elevation Results.....	97
Figure AIII.31 Test Series 6T (Temperature Increase) – Lower Elevation Results	98
Figure AIII.32 Test Series 6T (Temperature Increase) – Middle Elevation Results	98
Figure AIII.33 Test Series 6T (Temperature Increase) – Upper Elevation Results.....	99
Figure AIII.34 Test Series 7T (Temperature Increase) – Lower Elevation Results	99
Figure AIII.35 Test Series 7T (Temperature Increase) – Middle Elevation Results	100
Figure AIII.36 Test Series 7T (Temperature Increase) – Upper Elevation Results.....	100
Figure AIV.1 Test Series 1 Pressure Drop Results.....	101
Figure AIV.2 Test Series 5 Pressure Drop Results.....	101
Figure AIV.3 Test Series 7T Pressure Drop Results	102
Figure AV.1 Test Case 01-5343 All Participants - Average Relative Error of Calculated Fluid Temperature	103
Figure AV.2 Test Case 01-5343 CATHARE 3 –Relative Error of Calculated Fluid Temperature	103
Figure AV.3 Test Case 01-5343 FLICA-OVAP – Relative Error of Calculated Fluid Temperature	104
Figure AV.4 Test Case 01-5343 THYC – Relative Error of Calculated Fluid Temperature	104
Figure AV.5 Test Case 01-5342 All Participants – Average Relative Error of Calculated Fluid Temperature	105
Figure AV.6 Test Case 01-5342 CATHARE 3 – Relative Error of Calculated Fluid Temperature	105
Figure AV.7 Test Case 01-5342 FLICA-OVAP – Relative Error of Calculated Fluid Temperature	106
Figure AV.8 Test Case 01-5342 THYC – Relative Error of Calculated Fluid Temperature	106
Figure AV.9 Test Case 01-5215 All Participants – Average Relative Error of Calculated Fluid Temperature	107

Figure AV.10 Test Case 01-5215 CATHARE 3 – Relative Error of Calculated Fluid Temperature	107
Figure AV.11 Test Case 01-5215 FLICA-OVAP – Relative Error of Calculated Fluid Temperature	108
Figure AV.12 Test Case 01-5215 THYC – Relative Error of Calculated Fluid Temperature ...	108
Figure AV.13 Test Case 01-5125 All Participants – Average Relative Error of Calculated Fluid Temperature	109
Figure AV.14 Test Case 01-5125 CATHARE 3 – Relative Error of Calculated Fluid Temperature	109
Figure AV.15 Test Case 01-5125 FLICA-OVAP – Relative Error of Calculated Fluid Temperature	110
Figure AV.16 Test Case 01-5125 THYC – Relative Error of Calculated Fluid Temperature ...	110
Figure AV.17 Test Case 01-5237 All Participants – Average Relative Error of Calculated Fluid Temperature	111
Figure AV.18 Test Case 01-5237 CATHARE 3 – Relative Error of Calculated Fluid Temperature	111
Figure AV.19 Test Case 01-5237 FLICA-OVAP – Relative Error of Calculated Fluid Temperature	112
Figure AV.20 Test Case 01-5237 FLICA-OVAP – Relative Error of Calculated Fluid Temperature	112
Figure AV.21 Test Case 01-6232 All Participants – Average Relative Error of Calculated Fluid Temperature	113
Figure AV.22 Test Case 01-6232 CATHARE 3 – Relative Error of Calculated Fluid Temperature	113
Figure AV.23 Test Case 01-6232 FLICA-OVAP – Relative Error of Calculated Fluid Temperature	114
Figure AV.24 Test Case 01-6232 THYC – Relative Error of Calculated Fluid Temperature ...	114
Figure AV.25 Test Case 01-6233 All Participants – Average Relative Error of Calculated Fluid Temperature	115
Figure AV.26 Test Case 01-6233 CATHARE 3 – Relative Error of Calculated Fluid Temperature	115
Figure AV.27 Test Case 01-6233 FLICA-OVAP – Relative Error of Calculated Fluid Temperature	116
Figure AV.28 Test Case 01-6233 THYC – Relative Error of Calculated Fluid Temperature ...	116
Figure AV.29 Test Case 01-1237 All Participants – Average Relative Error of Calculated Fluid Temperature	117
Figure AV.30 Test Case 01-1237 CATHARE 3 – Relative Error of Calculated Fluid Temperature	117
Figure AV.31 Test Case 01-1237 FLICA-OVAP – Relative Error of Calculated Fluid Temperature	118

Figure AV.32 Test Case 01-1237 THYC – Relative Error of Calculated Fluid Temperature ...	118
Figure AV.33 Test Case 01-5252 All Participants – Average Relative Error of Calculated Fluid Temperature	119
Figure AV.34 Test Case 01-5252 CATHARE 3 – Relative Error of Calculated Fluid Temperature	119
Figure AV.35 Test Case 01-5252 FLICA-OVAP – Relative Error of Calculated Fluid Temperature	120
Figure AV.36 Test Case 01-5252 THYC – Relative Error of Calculated Fluid Temperature ...	120
Figure AVI.1 Test Series 0 DNB Power Results	122
Figure AVI.2 Test Series 2 DNB Power Results	122
Figure AVI.3 Test Series 3 DNB Power Results	123
Figure AVI.4 Test Series 4 DNB Power Results	123
Figure AVI.5 Test Series 8 DNB Power Results	124
Figure AVI.6 Test Series 13 DNB Power Results	124
Figure AVI.7 Test Series 4 Elevation of First Detected DNB Results	125
Figure AVI.8 Test Series 8 Elevation of First Detected DNB Results	125
Figure AVI.9 Test Series 13 Elevation of First Detected DNB Results	126
Figure AVII.1 Exercise 3 Time of Detected DNB Results	128
Figure AVII.2 Exercise 3 DNB Power Results	128

LIST OF TABLES

Table 1.1 PSBT Benchmark	1
Table 1.2 Range of NUPEC PWR Test Facility Operating Conditions	4
Table 1.3 Transient Parameters of NUPEC PWR Test Facility	4
Table 2.1 Properties of Subchannel Heating Elements.....	6
Table 2.2 Assembly Data for Assemblies S1, S2, S3, S4.....	7
Table 2.3 Assembly Data for Assemblies B5, B6, B7	9
Table 2.4 Cosine Axial Power Distribution.....	10
Table 2.5 Grid Geometry Data.....	11
Table 2.6 Properties of Heater Rods	13
Table 2.7 Accuracy of Process Parameters in Void Distribution Measurement.....	14
Table 2.8 Sources of Error for Void Distribution Measurement	15
Table 2.9 Number of Gamma Ray Beams	16
Table 2.10 Time Required to Perform Void Fraction Measurements	16
Table 2.11 Test Series for Void Fraction Measurements	17
Table 3.1 Assembly Data for Assembly A0	26
Table 3.2 Assembly Data for Assemblies A1, A2, A3	27
Table 3.3 Assembly Data for Assemblies A4, A8, A11, A12	28
Table 3.4 Accuracy of Process Parameters in DNB Measurement	31
Table 3.5 Test Series for DNB Measurements	32
Table 4.1 CTF Modeling of the Interfacial Drag.....	42
Table 4.2 CTF Models for Turbulent Mixing and Void Drift	43
Table AI.1 Results of Recalculation of Subchannel-Averaged Void Fraction.....	59
Table AI.2 Results of Recalculation of Subchannel-Averaged Thermal Equilibrium Quality	60
Table AII.1 Results of Recalculation of Bundle-Averaged Thermal Equilibrium Quality	82
Table AV.1 Relative Error (%) by Subchannel Type	121
Table AVI.1 Radial Position of First Predicted DNB	127

ACKNOWLEDGEMENTS

The author would like to thank his readers, Dr. Kostadin Ivanov and Alexander Velazquez-Lozada, as well as Dr. Arthur Motta, for their support in the development of this thesis. He would also like to thank his advisor, Dr. Maria Avramova, for her support and guidance throughout the benchmark, Dr. Hideaki Utsuno, for his willingness to provide information about the original NUPEC experiments, and Anthony Schoedel, who was helpful early in the benchmark by transferring hard copy data into electronic form.

Chapter 1 Introduction

1.1 Introduction

Recently, the need to refine models for best-estimate calculations based on good-quality experimental data has arisen for various nuclear applications. One of the most extensive and valuable databases available was developed by the Nuclear Power Engineering Corporation (NUPEC) of Japan, consisting of both void distribution and departure from nucleate boiling (DNB) data for a representative pressurized water reactor (PWR) fuel assembly. A part of this database has been made available for the NUPEC PWR Subchannel and Bundle Tests (PSBT) benchmark. This benchmark follows the highly successful OECD/NRC NUPEC BWR Full-size Fine-mesh Bundle Tests (BFBT) benchmark.

1.2 Benchmark Objective

The objective of the benchmark is twofold. First, the benchmark aims to evaluate currently available computational approaches in an effort to understand the strengths and weaknesses of current thermal-hydraulic codes. Second, the benchmark is intended to encourage the development of the next generation of approaches that focus more on microscopic processes.

1.3 Definition of Benchmark Phases

The PSBT benchmark is divided into two separate phases, with each consisting of individual exercises. The structure of the benchmark phases, as well as a mapping showing which test series are included in each exercise, is shown in Table 1.1.

Table 1.1 PSBT Benchmark

Items of Data	Test Series
Void fraction measurements data	
- Steady-state void fraction in subchannel by CT measurement	1, 2, 3, 4
- Steady-state void distribution image in subchannel by CT measurement	1, 2
- Steady-state void fraction in rod bundle by chordal measurement	5, 6, 7, 8
- Steady-state void distribution image in rod bundle by chordal measurement	5, 6, 7, 8
- Transient void fraction in rod bundle by chordal measurement	5T, 6T, 7T
DNB measurements data	
- Steady-state DNB data in rod bundle	0, 2, 3, 4, 8, 13
- Steady-state DNB detected location in rod bundle	4, 8, 13
- Steady-state fluid temperature distribution in rod bundle	1
- Transient DNB data in rod bundle	11T, 12T

1.3.1 Phase I – Void Distribution Benchmark

Exercise 1 – Steady-state single subchannel benchmark. These test cases involve predicting void distribution in a single subchannel under steady-state conditions.

Exercise 2 – Steady-state bundle benchmark. These test cases involve predicting void distribution in a bundle under steady-state conditions.

Exercise 3 – Transient bundle benchmark. These test cases involve predicting void distribution in a bundle under transient conditions.

Exercise 4 – Pressure drop benchmark. These test cases involve predicting the axial pressure drop across a bundle.

1.3.2 Phase II – Departure from Nucleate Boiling (DNB) Benchmark

Exercise 1 – Steady-state fluid temperature benchmark. These test cases involve predicting fluid temperatures at the exit of the heated section of a bundle.

Exercise 2 – Steady-state DNB benchmark. These test cases involve predicting DNB in a bundle under steady-state conditions.

Exercise 3 – Transient DNB benchmark. These test cases involve predicting DNB in a bundle under transient conditions.

1.4 Benchmark Team and Sponsorship

The benchmark activities are being performed as an international project supported by USNRC and METI (Japan), and endorsed by OECD/NEA. The benchmark team is organized based on the collaboration between USA and Japan as shown in Figure 1.1.

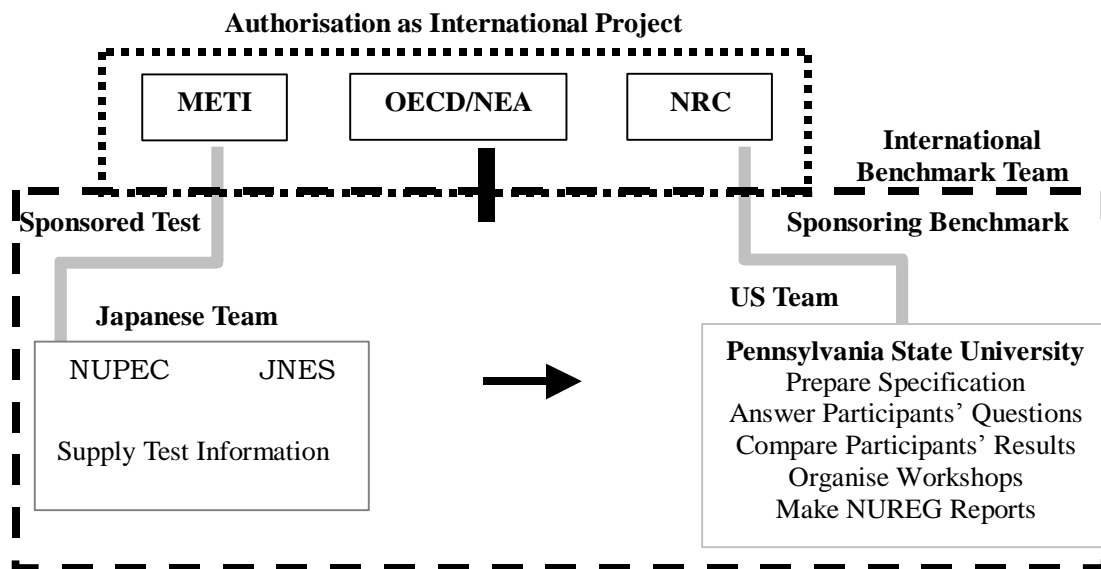


Figure 1.1 PSBT Benchmark Team

1.5 Test Facility

The void distribution and DNB measurements took place at the NUPEC test facility shown in Figure 1.2. The facility is able to simulate the conditions found in pressurized water reactors (PWR). The same test loop was used for both benchmark phases, but different test sections were constructed to simulate single subchannels and complete rod bundles. The range of operating conditions for the facility is given in Table 1.2 and the operating conditions for the four transient scenarios are given in Table 1.3.

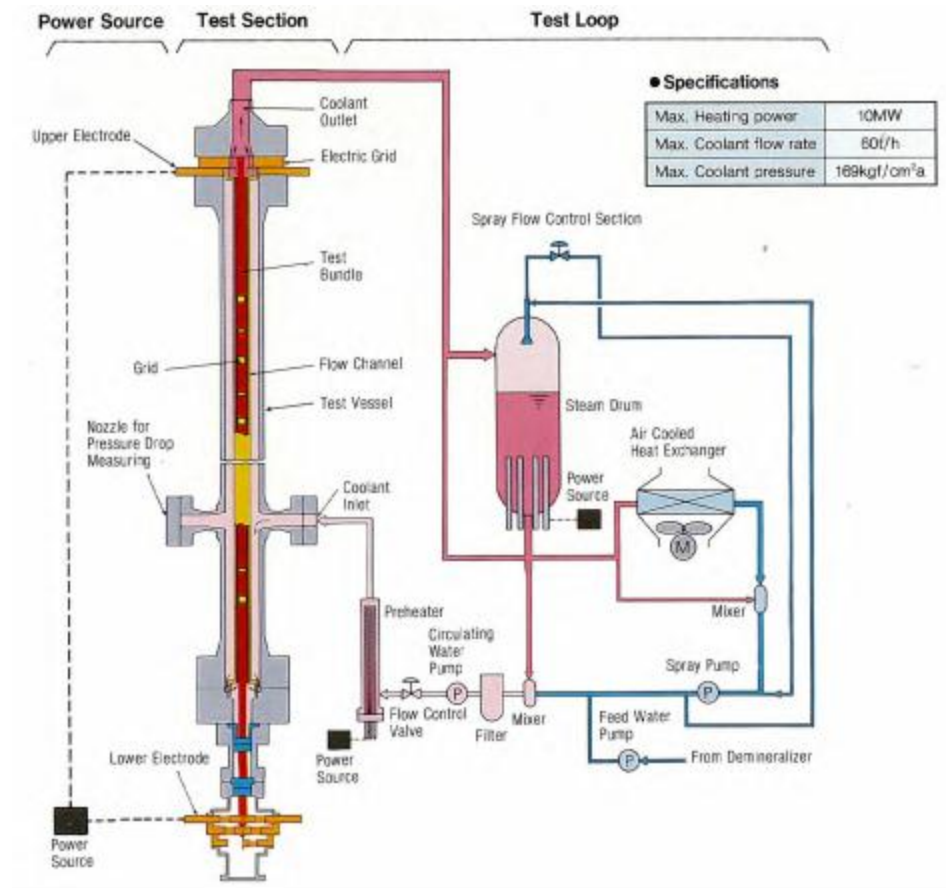


Figure 1.2 NUPEC Test Facility

Table 1.2 Range of NUPEC PWR Test Facility Operating Conditions

Quantity	Range
Pressure	4.9 – 16.6 MPa
Mass Velocity	550 – 4150 kg/m ² s
Inlet Coolant Temperature	140 – 345 °C

Table 1.3 Transient Parameters of NUPEC PWR Test Facility

Transient Scenario	Transient Change
Depressurization	-0.03 MPa/s
Temperature Increase	1 °C/s
Flow Reduction	-25 %/s
Power Increase	15 %/s

Chapter 2

Void Distribution Benchmark

2.1 Specification

The first phase of the PSBT benchmark is intended to provide data for the verification of void distribution models in participants' codes. This phase is composed of four exercises: a steady-state single subchannel benchmark, a steady-state rod bundle benchmark, a transient rod bundle benchmark, and a pressure drop benchmark.

2.1.1 Single Subchannel Test Section and Assemblies

Figure 2.1 shows the test section used for the single subchannel void distribution measurements. The heated section is 1.555m long measured from the coolant inlet, with a measuring section 1.4m above the start of the heated section. Figure 2.2 shows cross-sectional views of the four different subchannel test assemblies. The location and number of heater elements changes to represent four different types of subchannel found in a typical fuel assembly; central (typical), central (thimble), side, and corner.

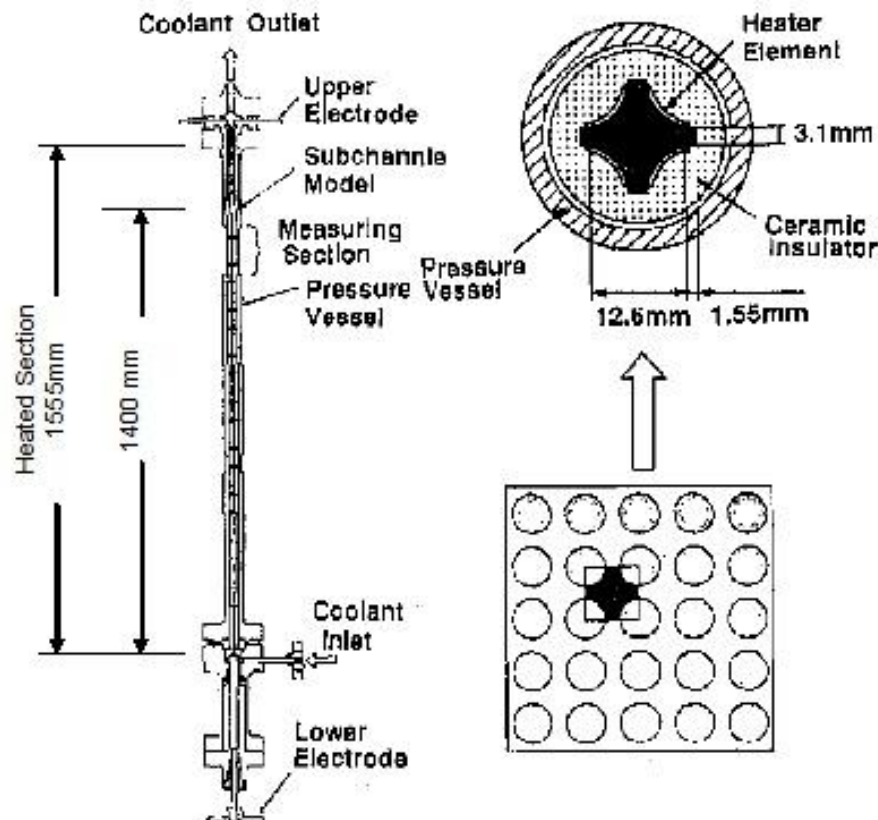


Figure 2.1 Test Section for Central Subchannel Void Distribution Measurement

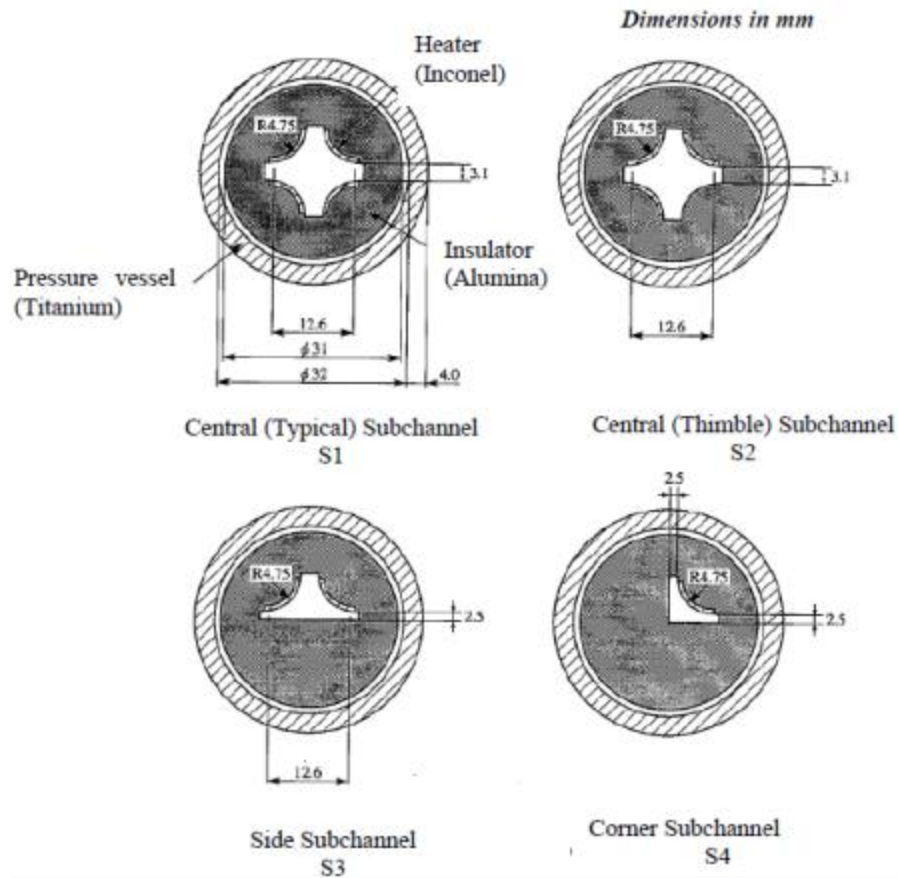


Figure 2.2 Cross-sectional View of Subchannel Test Assembly

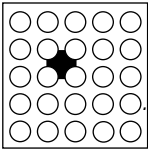
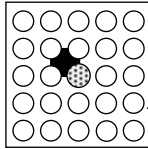
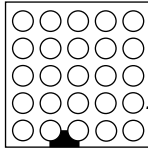
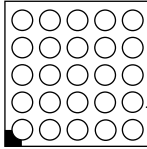
Table 2.1 summarizes the material and geometrical properties of the subchannel heating elements.

Table 2.1 Properties of Subchannel Heating Elements

Item		Data
Heater	Outer radius (mm)	4.75
	Thickness (mm)	0.85
	Material	Inconel 600
	Heating Method	Direct Heating
Insulator	Outer diameter (mm)	31
	Material	Alumina
Pressure vessel	Inner Diameter (mm)	32
	Thickness (mm)	4
	Material	Titanium

The properties of each subchannel assembly are given in Table 2.2. It should be noted that the rod bundles shown are simply for illustrative purposes, and the actual experimental test assembly took the form of those shown in Figure 2.2.

Table 2.2 Assembly Data for Assemblies S1, S2, S3, S4

Item	Data			
Assembly (Subjected subchannel)				
	S1	S2	S3	S4
Subchannel type	Center (Typical)	Center (Thimble)	Side	Corner
Number of heaters	4×1/4	3×1/4	2×1/4	1×1/4
Axial heated length (mm)	1555	1555	1555	1555
Axial power shape	Uniform	Uniform	Uniform	Uniform

■: Subjected subchannel ○Heated rod ⊗Thimble rod

2.1.2 Rod Bundle Test Section and Assemblies

Figure 2.3 shows the test section used for the bundle void distribution measurements. The heated section is 3.658m long, beginning 630mm above the bottom of the pressure vessel, with measurement locations at 2.216m, 2.669m, and 3.177m from the start of the heated section. The coolant flows horizontally into the section inlet, then down through a downcomer section before turning vertically up through the test section.

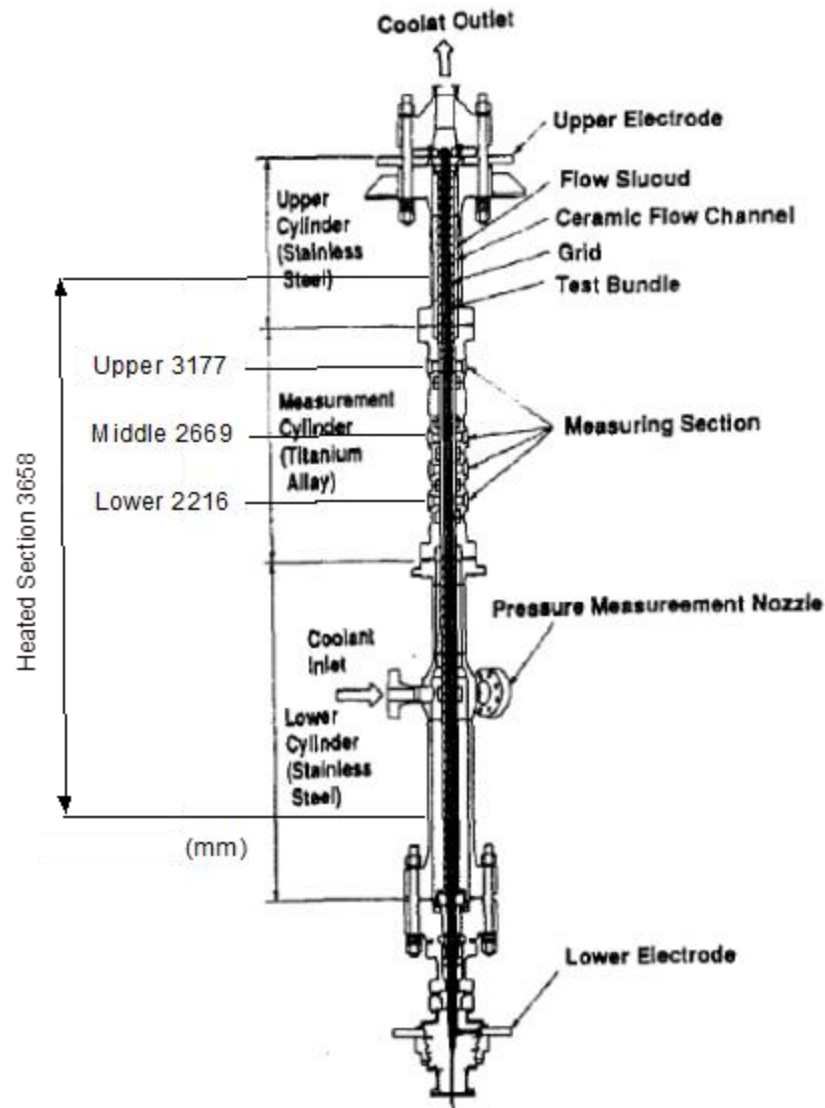
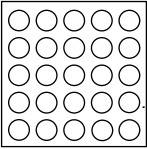
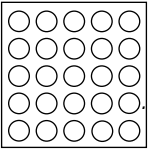
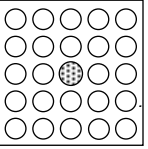


Figure 2.3 Test Section for Rod Bundle Void Distribution Measurement

According to experimental data, the area between the downcomer and test section was fully insulated so there would not be heat transfer between the two flows.

The properties of the bundle assemblies to be used are given in Table 2.3.

Table 2.3 Assembly Data for Assemblies B5, B6, B7

Item	Data		
Assembly			
	B5	B6	B7
Rods array	5×5	5×5	5×5
Number of heated rods	25	25	24
Number of thimble rods	0	0	1
Heated rod outer diameter (mm)	9.50	9.50	9.50
Thimble rod outer diameter (mm)	-	-	12.24
Heated rods pitch (mm)	12.60	12.60	12.60
Axial heated length (mm)	3658	3658	3658
Flow channel inner width (mm)	64.9	64.9	64.9
Radial power shape	A	A	B
Axial power shape	Uniform	Cosine	Cosine
Number of MV spacers	7	7	7
Number of NMV spacers	2	2	2
Number of simple spacers	8	8	8
MV spacer location (mm)	471, 925, 1378, 1832, 2285, 2739, 3247		
NMV spacer location (mm)	2.5, 3755		
Simple spacer location (mm)	237, 698, 1151, 1605, 2059, 2512, 2993, 3501		

○: Heated rod ⊗: Thimble rod MV: Mixing vane, NMV: No mixing vane

Spacer location is distance from bottom of heated length to spacer bottom face.

0.85	0.85	0.85	0.85	0.85
0.85	1.00	1.00	1.00	0.85
0.85	1.00	1.00	1.00	0.85
0.85	1.00	1.00	1.00	0.85
0.85	0.85	0.85	0.85	0.85

Figure 2.4 Radial Power Distribution A

0.85	0.85	0.85	0.85	0.85
0.85	1.00	1.00	1.00	0.85
0.85	1.00	0.00	1.00	0.85
0.85	1.00	1.00	1.00	0.85
0.85	0.85	0.85	0.85	0.85

Figure 2.5 Radial Power Distribution B

Table 2.4 Cosine Axial Power Distribution

Node	Relative Power
	<i>Cosine</i>
<i>(Bottom)</i>	
1	0.42
2	0.47
3	0.56
4	0.67
5	0.80
6	0.94
7	1.08
8	1.22
9	1.34
10	1.44
11	1.51
12	1.55
13	1.55
14	1.51
15	1.44
16	1.34
17	1.22
18	1.08
19	0.94
20	0.80
21	0.67
22	0.56
23	0.47
24	0.42
<i>(Top)</i>	

2.1.2.1 Spacer Grid Data

Data for the three types of grids used in the experiment was not made available for the benchmark. As a result, the benchmark team, with the assistance of a benchmark participant, was forced to develop a grid model based on the understanding that the grids used in the experiments were similar to grids for which data was readily available. Table 2.5 summarizes the grid data

that was available as part of the benchmark. Figure 2.6, Figure 2.7 and Figure 2.8 provide three-dimensional views of the simple spacer, non-mixing vane, and mixing vane grids. The simple spacer has dimples while the mixing vane and non-mixing vane grids have both dimples and springs. These dimples provide a 0.127mm gap around each heating rod, which prevents bowing of these rods when they linearly expand at high temperatures.

Table 2.5 Grid Geometry Data

Item		Data
Spacer width (mm)		64.5
Spacer heights (mm)	Simple spacer	12.8
	MV and NMV spacer	43.6

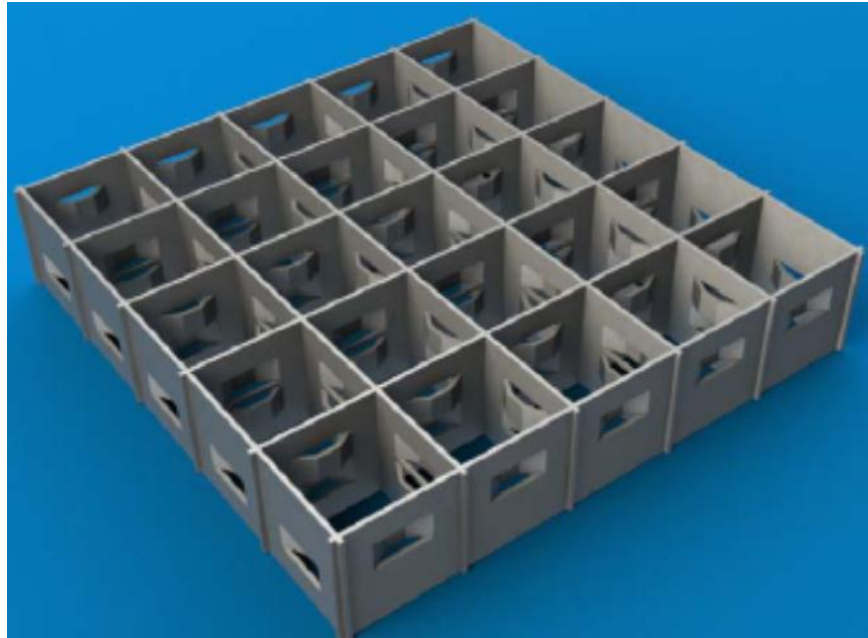


Figure 2.6 View of Simple Spacer Grid

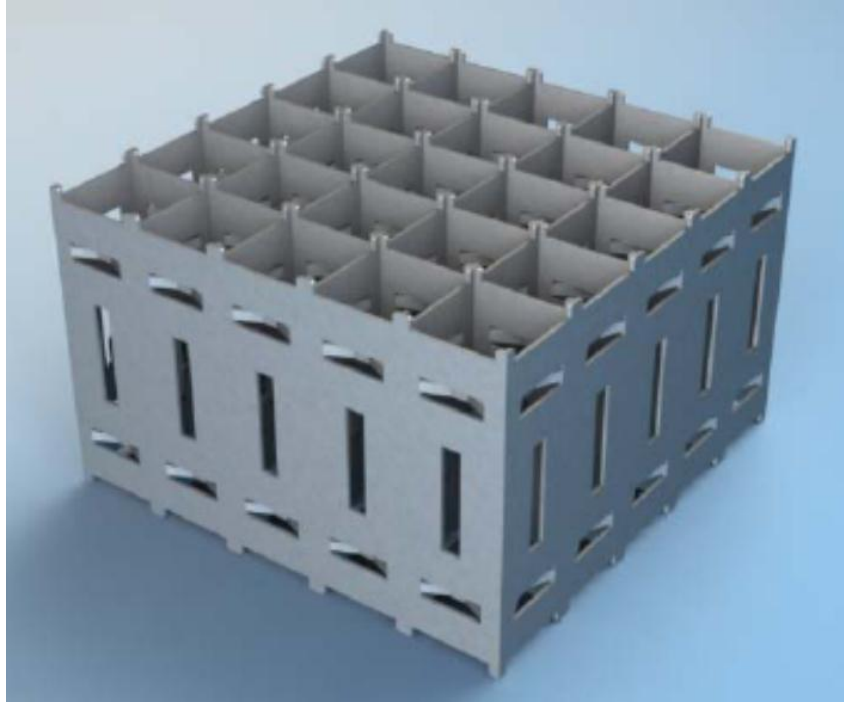


Figure 2.7 View of Non-Mixing Vane Spacer Grid

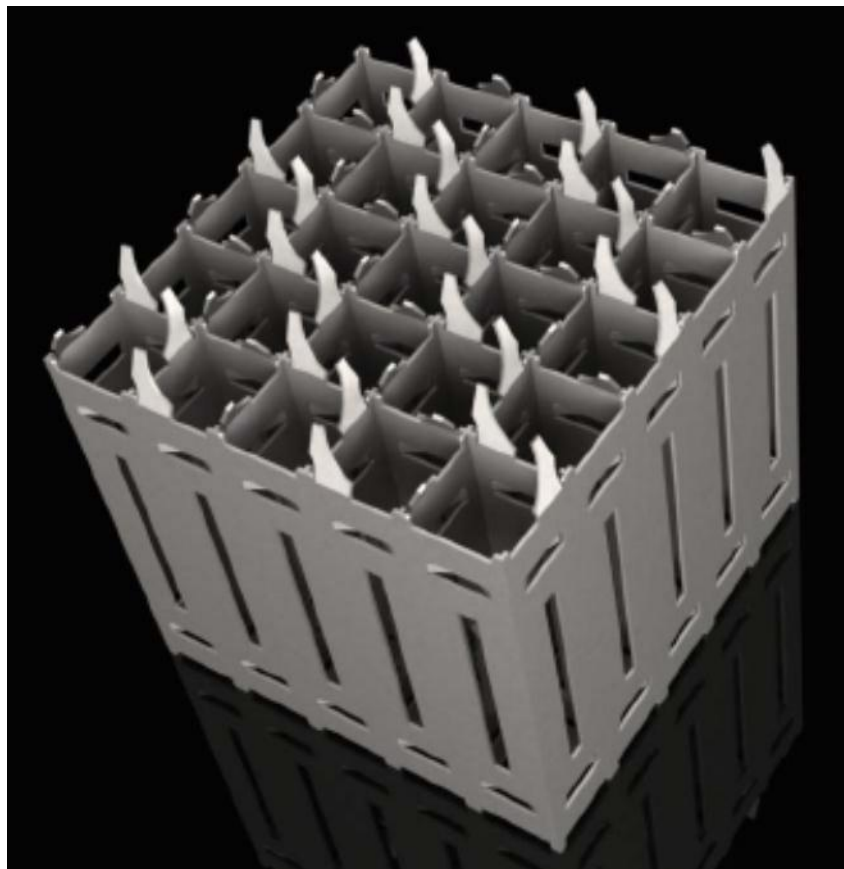


Figure 2.8 View of Mixing Vane Spacer Grid

2.1.2.2 Heater Rod Data

Table 2.6 summarizes the material and geometrical properties of the heater rods used in the rod bundle tests. Figure 2.9 provides a cross-sectional view of the heater rods and gives dimensions.

Table 2.6 Properties of Heater Rods

Item		Data
Heater	Outer diameter (mm)	9.5
	Thickness (mm)	0.65
	Material	Inconel 600
	Heating Method	Direct Heating
Insulator	Outer diameter (mm)	8.2
	Inner diameter (mm)	5.8
	Material	Alumina

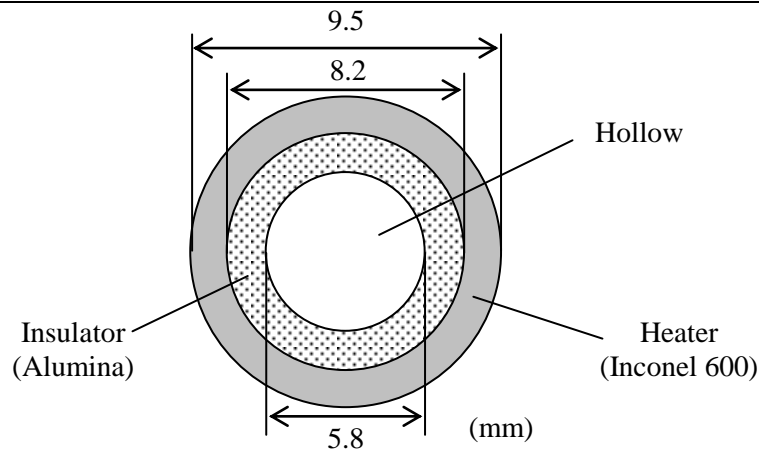


Figure 2.9 Cross-sectional View of Heater Rod

2.1.3 Measurement Techniques

The gamma ray transmission method was used to measure the density of the fluid at the measurement locations. Table 2.7 shows the accuracy of the various parameters involved in the experiment. Table 2.8 summarizes the sources of error in the experiment.

Table 2.7 Accuracy of Process Parameters in Void Distribution Measurement

Quantity	Accuracy
Process parameters	
Pressure	1 %
Flow	1.5%
Power	1 %
Fluid temperature	1 Celsius
Void fraction measurement	
CT measurement	
Gamma-ray beam width	1 mm
Subchannel averaged (steady state)	3% void
Spatial resolution of one pixel	0.5 mm
Chordal measurement	
Gamma-ray beam width (center)	3 mm
Gamma-ray beam width (side)	2 mm
Subchannel averaged (steady state)	4% void
Subchannel averaged (transient)	5% void

Table 2.8 Sources of Error for Void Distribution Measurement

Error source		Chordal Averaged		CT Averaged
		Steady-state	Transient	
γ -ray Measurement	Effect of surrounding condition (magnetic-field and temperature) on measurement system	0.1%	0.1%	0.1%
	Randomness of γ -ray source decay	0.02%	0.2%	0.1%
	Correction error due to back ground	0.0%	0.0%	0.0%
	Correction error due to counting loss	<0.5%	<0.5%	<0.1%
	Calibration error	0.1%	0.1%	0.1%
	Correction error due to attenuation by surrounding water	0.0%	0.0%	-
	Correction error due to scattering from multi γ -rays	<0.2%	<0.2%	-
	Total	<0.55%	<0.6%	<0.2%
Sub-channel Density	Transfer to density	<9 kg/m ³	<10 kg/m ³	<15 kg/m ³
	Distribution error to Sub-channel	<5 kg/m ³	<5 kg/m ³	-
Correlation error from Chordal averaged to CT averaged		<6 kg/m ³	<6 kg/m ³	-
Sub-channel Density		<20 kg/m ³	<21 kg/m ³	<15 kg/m ³
Sub-channel Void*		0.040	0.042	0.030
Uncertainty (1 σ)		4 %	5 %	3 %

* Reference averaged density is 500 kg/m³.

Figure 2.10 illustrates the relationship between chordal and CT averaged densities as a function of pressure.

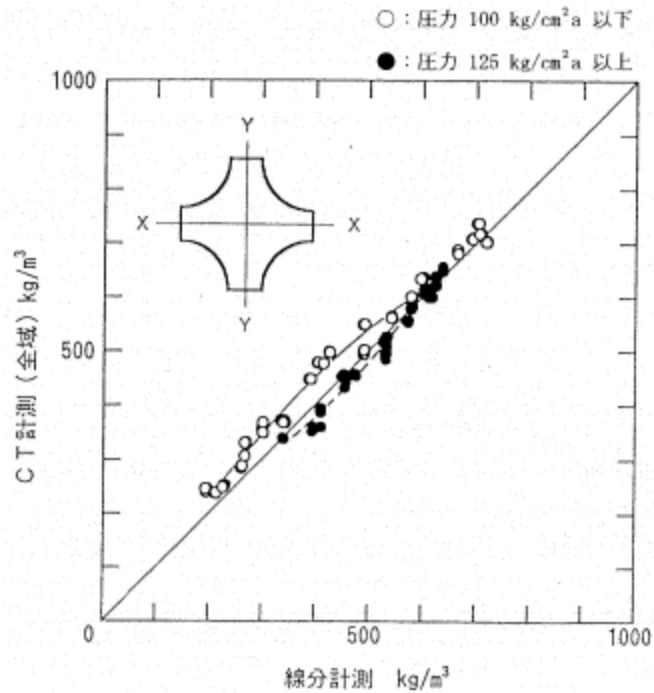


Figure 2.10 Relation Between Chordal and CT Averaged Densities (for S1)

Table 2.9 shows the number of gamma ray beams used in the fluid density measurement for both subchannel and rod bundle exercises.

Table 2.9 Number of Gamma Ray Beams

Test assembly	CT Measurement	Chordal Measurement
Subchannel	2 (X and Y direction)	2 (X and Y direction)
Rod bundle	-	6 beam \times 2 \times 3 section (total 36 beams)

Table 2.10 shows the amount of time required to perform the density measurement.

Table 2.10 Time Required to Perform Void Fraction Measurements

Item		CT Measurement	Chordal Measurement
Steady-state	Time needed	5 s/step \times ^T 33 \times ^R 17 step (it takes 2 h)	100 s sampling cycle 0.1 s
	Measurement	2 times	3 times
Transient	Time needed	-	200 s
	Measurement	-	1 time

2.1.4 Test Cases

Table 2.11 summarizes the test series used in the void fraction distribution part of the benchmark.

Table 2.11 Test Series for Void Fraction Measurements

Test series	Test section	Assembly	Test mode		Void measurement	
			Steady-state	Transient	CT	Chordal
1	Subchannel	S1	Y		Y	Y
2		S2	Y		Y	Y
3		S3	Y		Y	Y
4		S4	Y		Y	Y
5	5×5 Rod bundle	B5	Y			Y
5T				Y		Y
6		B6	Y			Y
6T				Y		Y
7		B7	Y			Y
7T				Y		Y
8		B5	Y			Y

2.1.4.1 Exercise 1 – Steady-state Single Subchannel

The available data for this exercise consisted of CT scan measurements of fluid density for four subchannel types (central typical, central thimble, side, and corner), as well as images of the subchannel void distribution for the central typical and central thimble subchannels. The measured density was used to calculate the void fraction in the subchannel.

2.1.4.2 Exercise 2 – Steady-state Rod Bundle

The available data for this exercise consisted of chordal-averaged x-ray densitometer measurements of fluid density in the rod bundle. The measured density was then used to calculate the void fraction. The given values are the average of the void fraction over the four central subchannels of the bundle. Images of the void distribution in the rod bundle were also available.

2.1.4.3 Exercise 3 – Transient Bundle

The available data for this exercise consisted of chordal-averaged x-ray densitometer measurements of fluid density in the rod bundle. The measured density was then used to calculate the void fraction. The given values are the average of the void fraction over the four central subchannels of the bundle.

Four transient scenarios (temperature increase, power increase, depressurization, and flow reduction) were used in this exercise for each test series, yielding twelve total test cases. The boundary conditions for test series 5T are shown in Figure 2.11, Figure 2.12, Figure 2.13, and

Figure 2.14. Similar boundary conditions are given in the benchmark specification for test series 6T and 7T.

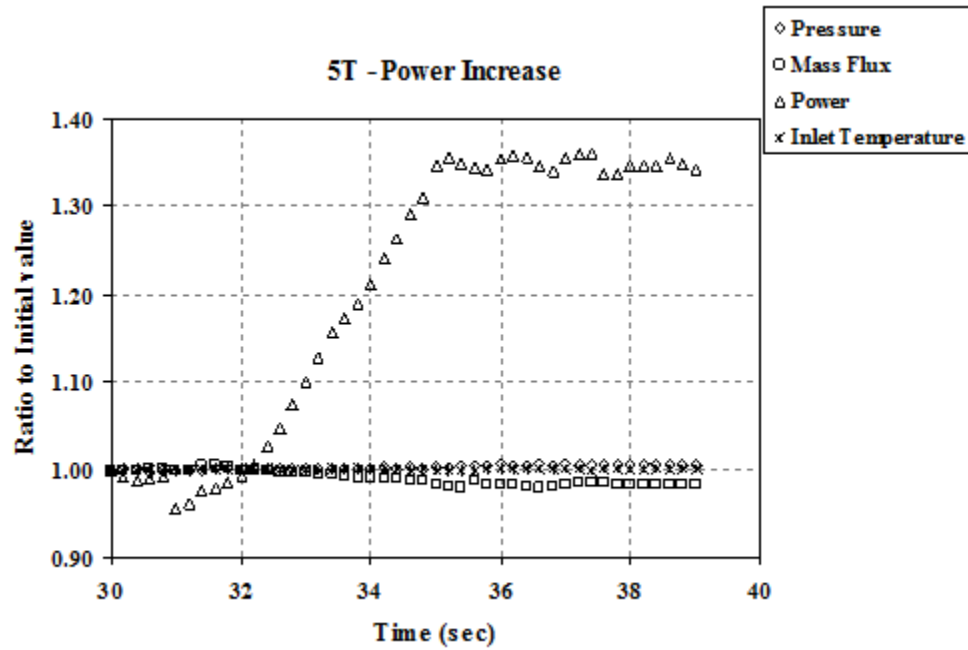


Figure 2.11 Variation of Properties for Test Case 5T (Power Increase)

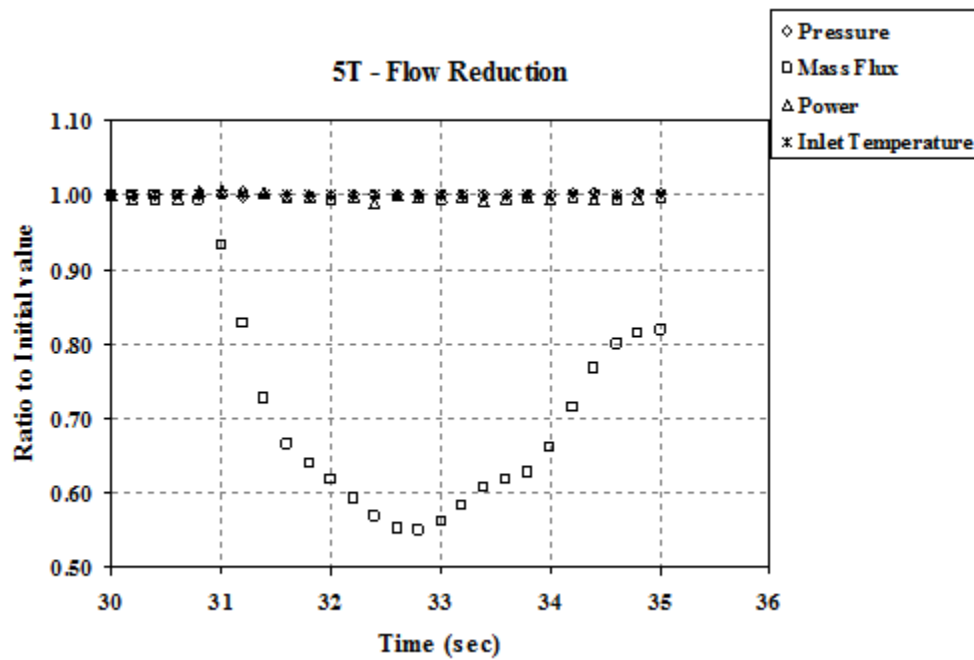


Figure 2.12 Variation of Properties for Test Case 5T (Flow Reduction)

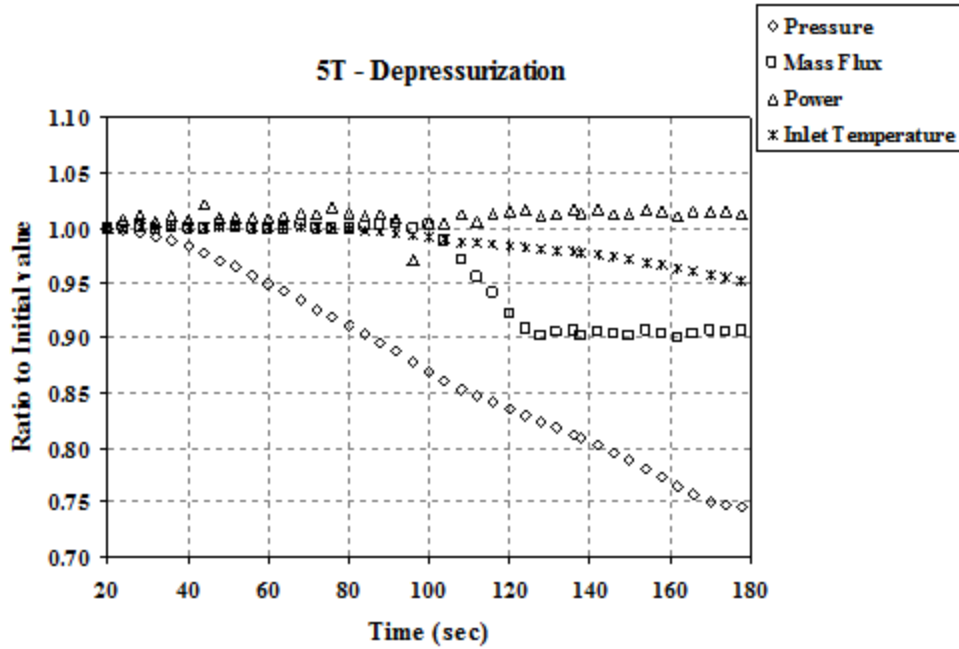


Figure 2.13 Variation of Properties for Test Case 5T (Depressurization)

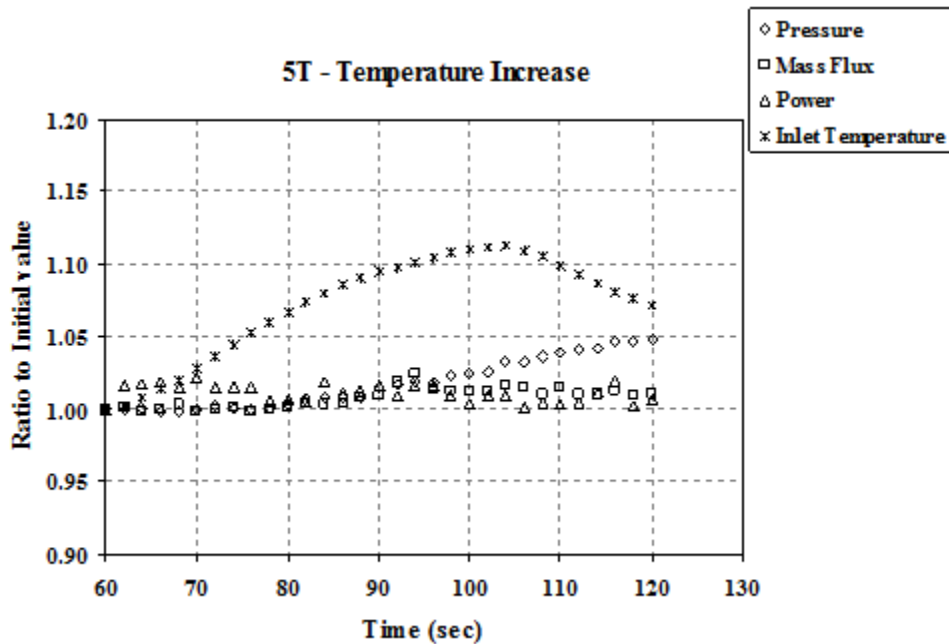


Figure 2.14 Variation of Properties for Test Case 5T (Temperature Increase)

2.1.4.4 Exercise 4 – Pressure Drop

No pressure drop information was available for the benchmark, so it was decided that code-to-code comparisons would be performed for selected test cases in Test Series 1, Test Series 5, and Test Series 7T. The only data available was the initial value of the pressure drop for the B7

bundle under the single-phase rated condition for the power increase transient in Test Series 7T (given as 1.6 kg/cm²). This value was used as the reference value for the rod bundle pressure drop calculations.

2.2 Analysis

Based on participant feedback, two studies were performed to determine the validity of the benchmark data. Additionally, participants' results are presented for preliminary analysis. At the time of the writing of this Thesis, however, the second benchmark had not yet been held. As a result, final results were only available for some of the participants.

2.2.1 Studies Performed on Data

At the first PSBT workshop, it was noted by several participants that the “measured” void fractions (which were actually calculated from measured density data) were not consistent with void fractions calculated using the measured densities. As a result, a study was performed to recalculate the void fraction and quality for each test case in the void distribution benchmark.

2.2.1.1 Study Performed on Calculation of Void Fraction

Starting with the standard representation for mixture density based on void fraction,

$$\bar{\rho} = \alpha \rho_g + (1 - \alpha) \rho_f$$

This equation can be solved for void fraction to show that

$$\alpha = \frac{\bar{\rho} - \rho_f}{\rho_g - \rho_f}$$

Where the liquid and gas densities are taken at saturation, and the mixture density is taken from the benchmark data. After the recalculation, it was noted that the measured void fraction was consistently higher than the recalculated void fraction. This recalculation was only performed for the subchannel test cases since those are the only test cases for which fluid density data was available.

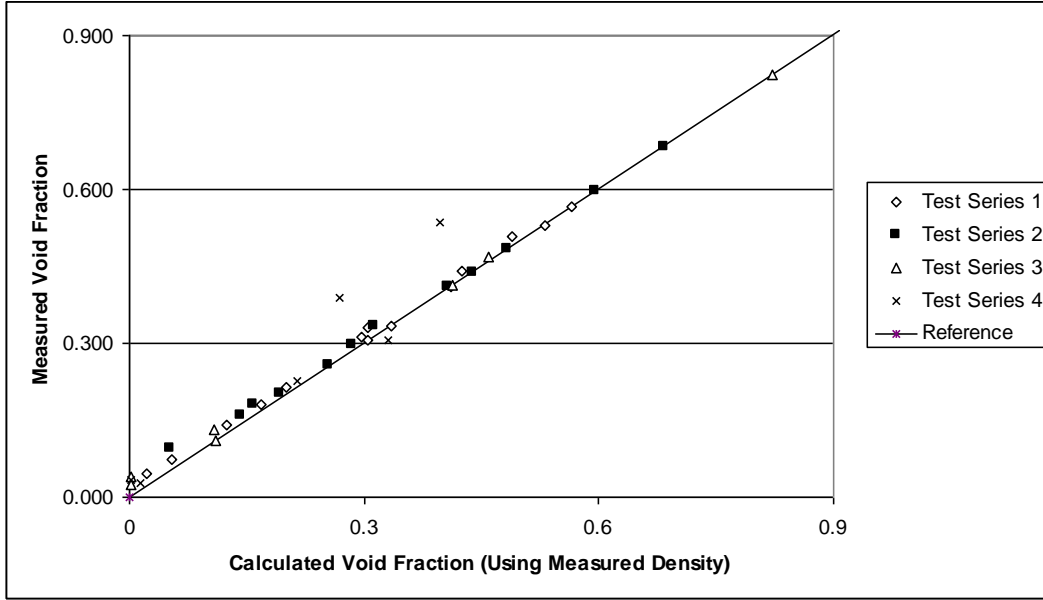


Figure 2.15 Deviation of Measured Void Fraction from Recalculated Void Fraction

2.2.1.2 Study Performed on Calculation of Quality

Upon completion of the study performed on void distribution, the benchmark team began a study of the calculation of quality based on the experimentally-determined densities.

It is recalled that quality can be expressed using mixture enthalpy. The equation is given as

$$x = \frac{h_{mix} - h_f}{h_g - h_f}$$

Where h_f and h_g are the liquid and vapor enthalpies, respectively. A number of different expressions were derived to determine the mixture enthalpy in the test sections assuming conservation of energy. After verifying that the axial power distribution was normalized for both the uniform and cosine power shapes, the following equations were obtained.

Subchannel Assembly

All four subchannel test sections utilized a uniform axial power distribution. Thus, for all subchannel assemblies, the mixture enthalpy at the measurement section can be given by

$$h_{mix} = h_{in} + \frac{1400mm}{1555mm} Q[kW] \times \frac{3600 \left[\frac{S}{h} \right]}{A[m^2]G \left[\frac{kg}{m^2h} \right]}$$

Figure 2.16 shows the resulting deviation of the experimental quality from the recalculated quality.

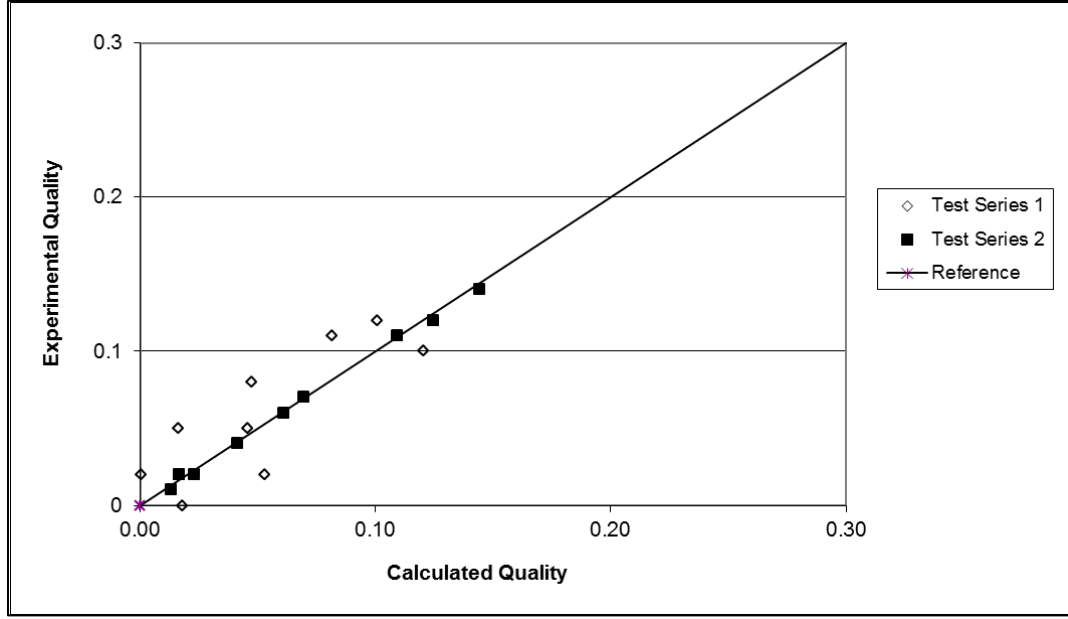


Figure 2.16 Deviation of Measured Quality from Recalculated Quality for Test Series 1 and 2

Bundle Assembly

Assembly B5 utilized a uniform axial power distribution, so the mixture enthalpies at the three measurement locations can be given as

$$h_{mix} = h_{in} + \frac{2216mm}{3658mm} Q[kW] \times \frac{3600 \left[\frac{s}{h} \right]}{A[m^2] G \left[\frac{kg}{m^2 h} \right]} \quad \text{Lower Elevation}$$

$$h_{mix} = h_{in} + \frac{2669mm}{3658mm} Q[kW] \times \frac{3600 \left[\frac{s}{h} \right]}{A[m^2] G \left[\frac{kg}{m^2 h} \right]} \quad \text{Middle Elevation}$$

$$h_{mix} = h_{in} + \frac{3177mm}{3658mm} Q[kW] \times \frac{3600 \left[\frac{s}{h} \right]}{A[m^2] G \left[\frac{kg}{m^2 h} \right]} \quad \text{Upper Elevation}$$

Assemblies B6 and B7 utilized a cosine axial power shape. Recalling that the power shape is normalized, it is possible to determine what fraction of the total power has been imparted to the fluid between the flow inlet and the measurement sections. The mixture enthalpies for these two assemblies can be given as

$$h_{mix} = h_{in} + 0.6598 Q[kW] \times \frac{3600 \left[\frac{s}{h} \right]}{A[m^2] G \left[\frac{kg}{m^2 h} \right]} \quad \text{Lower Elevation}$$

$$h_{mix} = h_{in} + 0.8172 Q[kW] \times \frac{3600 \left[\frac{s}{h} \right]}{A[m^2] G \left[\frac{kg}{m^2 h} \right]} \quad \text{Middle Elevation}$$

$$h_{mix} = h_{in} + 0.9353 Q[kW] \times \frac{3600 \left[\frac{s}{h} \right]}{A[m^2] G \left[\frac{kg}{m^2 h} \right]} \quad \text{Upper Elevation}$$

After applying these equations and calculating the qualities for each case, the following results were obtained. Figure 2.17, Figure 2.18, Figure 2.19, and Figure 2.20 show the deviation of experimental quality from recalculated quality for Test Series 5, 6, 7, and 8 (respectively).

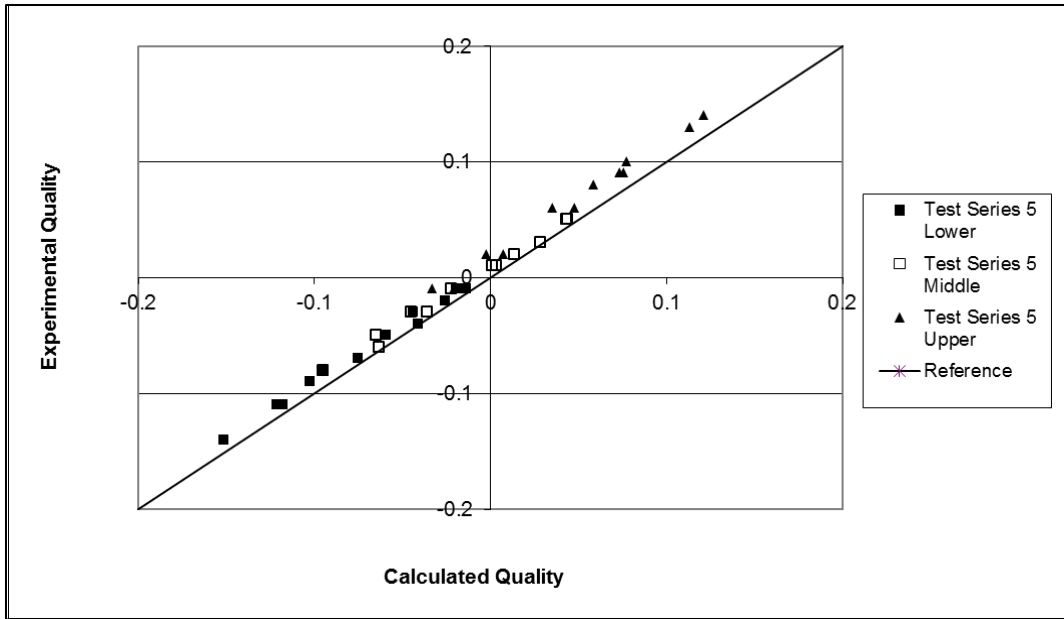


Figure 2.17 Deviation of Measured Quality from Recalculated Quality for Test Series 5

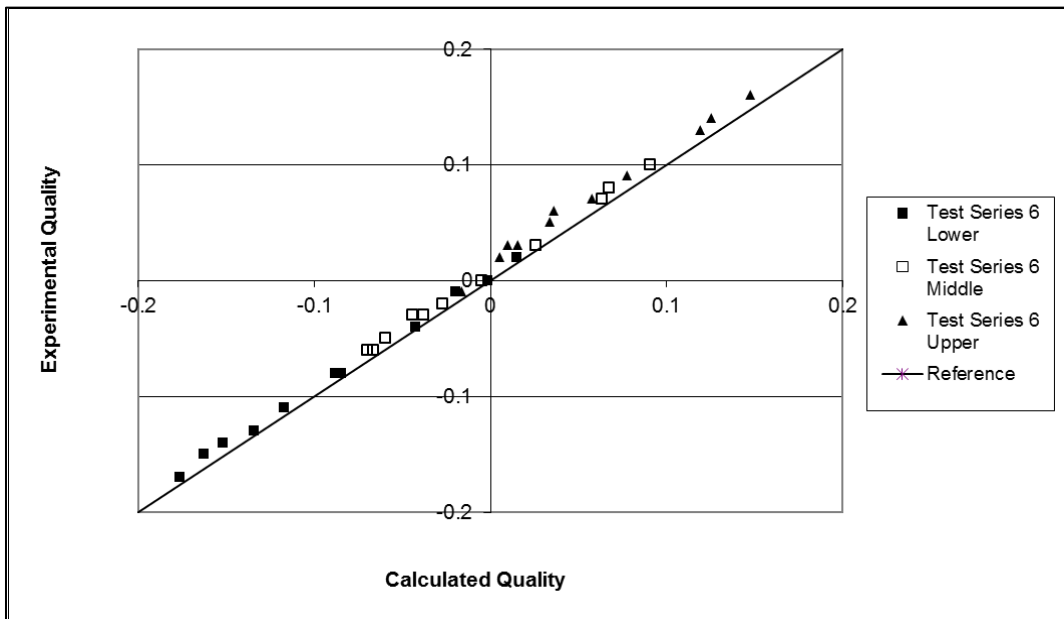


Figure 2.18 Deviation of Measured Quality from Recalculated Quality for Test Series 6

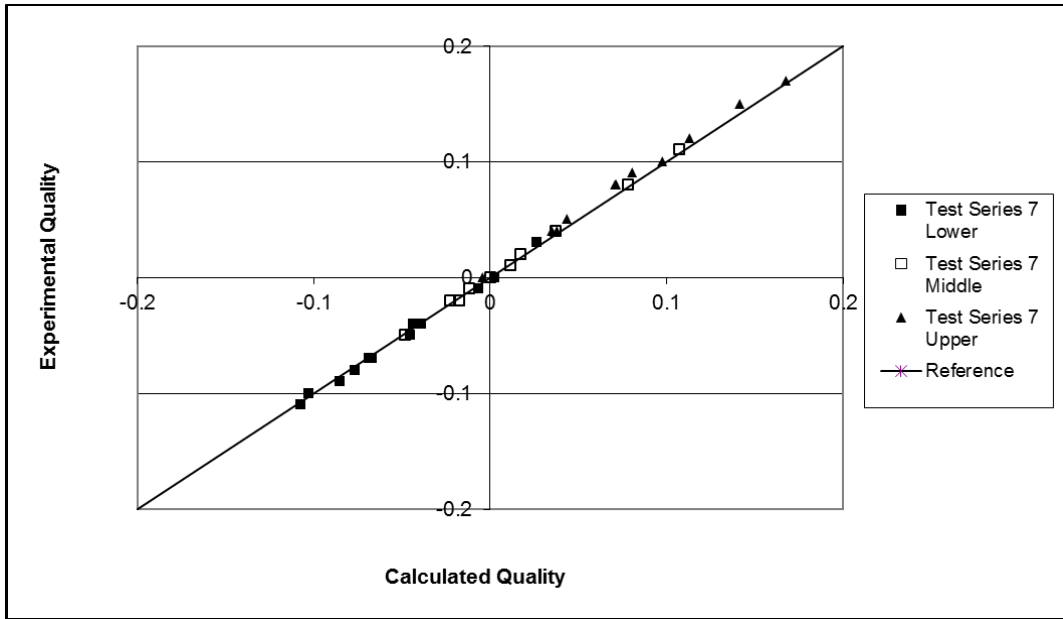


Figure 2.19 Deviation of Measured Quality from Recalculated Quality for Test Series 7

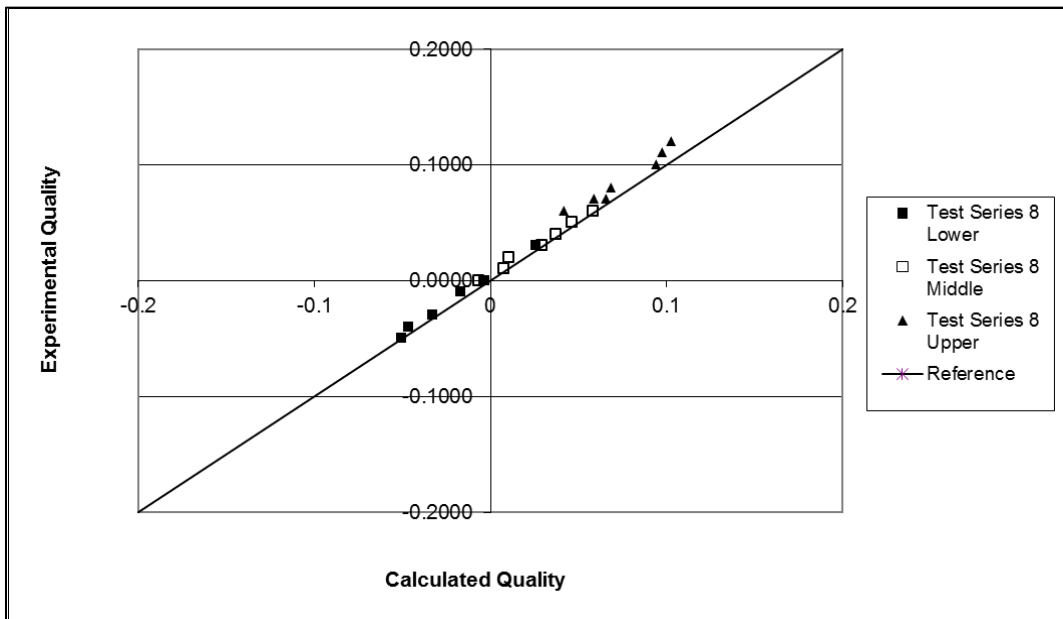


Figure 2.20 Deviation of Measured Quality from Recalculated Quality for Test Series 8

The results of these studies can be applied by participants to their data in an effort to correct for the experimental values.

2.2.2 Participant Results

The complete set of available results from participants can be found in Appendix I, Appendix II, Appendix III, and Appendix IV.

2.2.2.1 Exercise 1 – Steady-state Single Subchannel

There was no clear bias in the calculation of void fraction for any of the four subchannels. Although some of the codes consistently predicted the correct thermal equilibrium quality, there was a tendency to overpredict it at the low elevation and underpredict it at the high elevation.

2.2.2.2 Exercise 2 – Steady-state Rod Bundle

It was noted that the codes consistently overpredicted the void fraction at the lower elevation in the bundle. However, the results were generally improved at higher elevations. The majority of the codes also consistently predicted the correct thermal equilibrium quality at the lower elevations, with the only exception being KTH's TRACE, which overpredicted the quality. All of the codes tended to underpredict the quality at the upper bundle elevations.

2.2.2.3 Exercise 3 – Transient Rod Bundle

A slight time shift can be seen in the void fraction results when they are compared to the experimental data for the temperature increase cases. It has been suggested that the structure between the downcomer and test section was not truly adiabatic and, as a result, there was some heat transfer between these regions that was responsible for this shift. Aside from that observation, the codes generally performed well in predicting the void fraction throughout the different transients, yielding better results at the highest elevation in the bundle and worse results at the lowest elevation. Some codes (such as KTH's version of TRACE) consistently underestimated the void fraction, especially at higher elevations. There was also consistent underprediction of void fraction at higher elevations for the depressurization cases.

2.2.2.4 Exercise 4 – Pressure Drop

It was observed that there were major differences between codes in the reported values for the pressure drop in subchannel S1. Since there were not experimental values given for pressure drop for these cases, or for the cases using bundle B5, it is not possible to determine which codes are correctly predicting the pressure drop. It was noted, however, that the codes yielded results for the bundle pressure drop cases that were more similar to each other. For the only case with an experimental data point, the codes generally performed well, with a maximum deviation of 0.6 kg/cm² (or a 37.5% deviation from the measured value of 1.6 kg/cm²).

Chapter 3

Departure from Nucleate Boiling (DNB) Benchmark

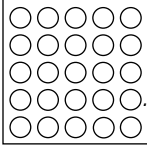
3.1 Specification

The second phase of the PSBT Benchmark is intended to provide data for the verification of departure from nucleate boiling (DNB) prediction in existing thermal-hydraulics codes and provide direction in the development of future methods. This phase is composed of three exercises: a fluid temperature benchmark, a steady-state rod bundle benchmark, and a transient rod bundle benchmark.

3.1.1 Test Assemblies

Table 3.1, Table 3.2, and Table 3.3 provide information about the assemblies used in the DNB portion of the benchmark. The spacer grids and heater rods used in these assemblies are the same as those used in the assemblies for the void distribution benchmark (see Figure 2.6, Figure 2.7, Figure 2.8, Figure 2.9).

Table 3.1 Assembly Data for Assembly A0

Item	Data
Assembly	 A0
Rods array	5×5
Number of heated rods	25
Number of thimble rods	0
Heated rod outer diameter (mm)	9.50
Thimble rod outer diameter (mm)	-
Heated rods pitch (mm)	12.60
Axial heated length (mm)	3658
Flow channel inner width (mm)	64.9
Radial power shape	A
Axial power shape	Uniform
Number of MV spacers	5
Number of NMV spacers	2
Number of simple spacers	6
MV spacer location (mm)	610, 1219, 1829, 2438, 3048
NMV spacer location (mm)	0, 3658
Simple spacer location (mm)	305, 914, 1524, 2134, 2743, 3353

○: Heated rod ⊗: Thimble rod MV: Mixing vane, NMV: No mixing vane
 Spacer location is distance from bottom of heated length to spacer bottom face.

Table 3.2 Assembly Data for Assemblies A1, A2, A3

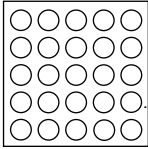
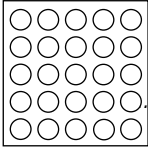
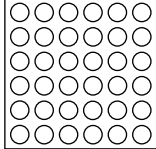
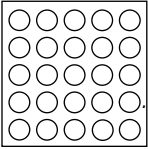
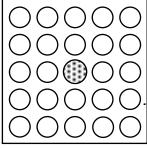
Item	Data		
Assembly			
	A1	A2	A3
Rods array	5×5	5×5	6×6
Number of heated rods	25	25	36
Number of thimble rods	0	0	0
Heated rod outer diameter (mm)	9.50	9.50	9.50
Thimble rod outer diameter (mm)	-	-	-
Heated rods pitch (mm)	12.60	12.60	12.60
Axial heated length (mm)	3658	3658	3658
Flow channel inner width (mm)	64.9	64.9	77.5
Radial power shape	C	A	D
Axial power shape	Uniform	Uniform	Uniform
Number of MV spacers	7	7	7
Number of NMV spacer	2	2	2
Number of simple spacers	8	8	8
MV spacer location (mm)	457, 914, 1372, 1829, 2286, 2743, 3200		
NMV spacer location (mm)	0, 3658		
Simple spacer location (mm)	229, 686, 1143, 1600, 2057, 2515, 2972, 3429		

Table 3.3 Assembly Data for Assemblies A4, A8, A11, A12

Item	Data	
Assembly	 A4, A11	 A8, A12
Rods array	5×5	5×5
Number of heated rods	25	24
Number of thimble rods	0	1
Heated rod outer diameter (mm)	9.50	9.50
Thimble rod outer diameter (mm)	-	12.24
Heated rods pitch (mm)	12.60	12.60
Axial heated length (mm)	3658	3658
Flow channel inner width (mm)	64.9	64.9
Radial power shape	A	B
Axial power shape	Cosine	Cosine
Number of MV spacers	7	7
Number of NMV spacer	2	2
Number of simple spacers	8	8
MV spacer location (mm)	471, 925, 1378, 1832, 2285, 2739, 3247	
NMV spacer location (mm)	2.5, 3755	
Simple spacer location (mm)	237, 698, 1151, 1605, 2059, 2512, 2993, 3501	

1.00	1.00	0.25	0.25	0.25
1.00	1.00	1.00	0.25	0.25
1.00	1.00	0.25	0.25	0.25
1.00	1.00	1.00	0.25	0.25
1.00	1.00	0.25	0.25	0.25

Figure 3.1 Radial Power Distribution C

0.85	0.85	0.85	0.85	0.85	0.85
0.85	1.00	1.00	1.00	1.00	0.85
0.85	1.00	1.00	1.00	1.00	0.85
0.85	1.00	1.00	1.00	1.00	0.85
0.85	1.00	1.00	1.00	1.00	0.85
0.85	0.85	0.85	0.85	0.85	0.85

Figure 3.2 Radial Power Distribution D

3.1.2 Measurement Techniques

The bundle power was gradually increased in fine steps to the expected vicinity of DNB, which was based on previous analysis operator experience. The onset of DNB is confirmed by a rod temperature rise greater than 11°C (20°F) as measured by the thermocouples seen in Figure 3.3. The DNB power is defined as the power corresponding to the step immediately preceding the step in which this temperature rise is seen. The accuracy of the process parameters involved in this process is seen in Table 3.4. The exit fluid temperatures were measured by the thermocouples shown in Figure 3.4.

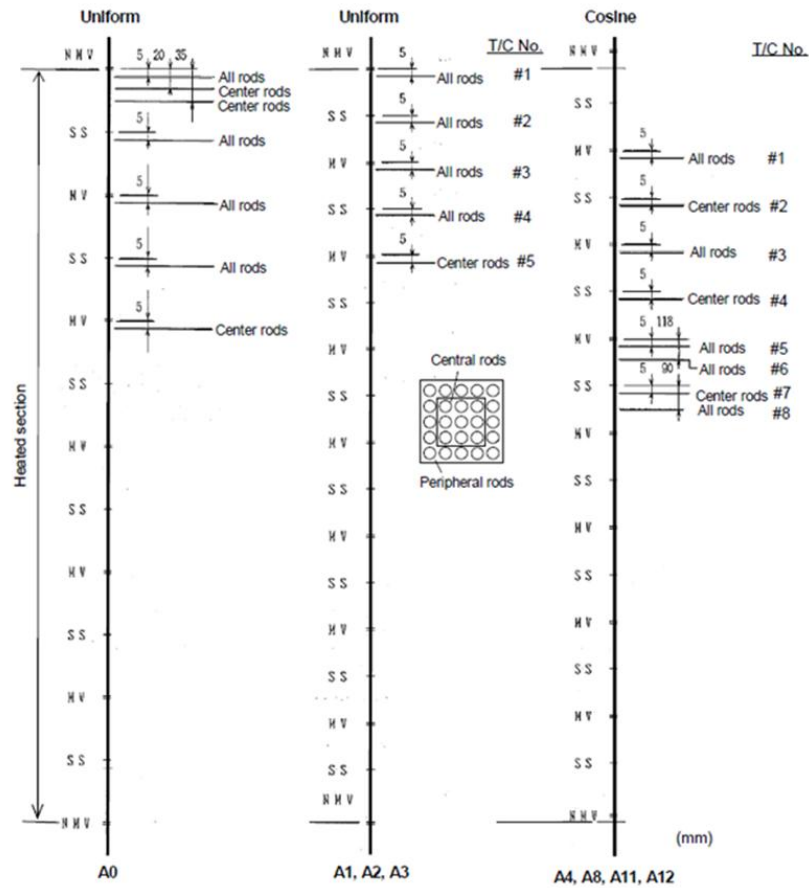


Figure 3.3 Locations of Thermocouples for Test Assemblies

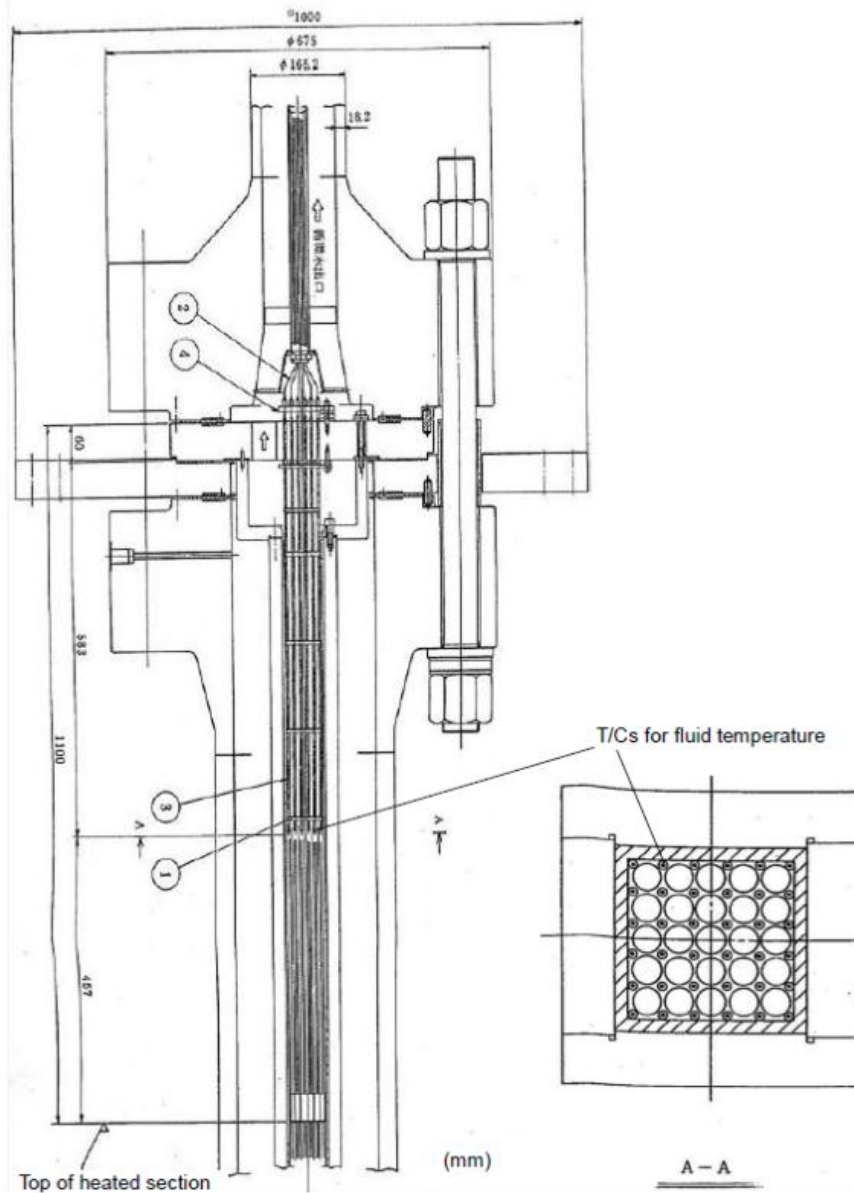


Figure 3.4 Diagram of Fluid Temperature Measurement Setup

Table 3.4 Accuracy of Process Parameters in DNB Measurement

Quantity	Accuracy
Process parameters	
Pressure	1 %
Flow	1.5%
Power	1 %
Fluid temperature	1 Celsius

3.1.3 Test Cases

Table 3.5 summarizes the test series used in the DNB portion of the benchmark.

Table 3.5 Test Series for DNB Measurements

Test series	Test section	Assembly	Test mode		Measurement	
			Steady-State	Transient	DNB	Fluid temperature
0	5×5	A0	Y		Y	
1		A1	Y			Y
2		A2	Y		Y	
3	6×6	A3	Y		Y	
4	5×5	A4	Y		Y	
8		A8	Y		Y	
11T		A11		Y	Y	
12T		A12		Y	Y	
13		A4	Y		Y	

3.1.3.1 Exercise 1 – Fluid Temperature

The available data for this exercise consisted of fluid temperature measurements taken at the exit of the test section using the thermocouples shown in Figure 3.4. These temperatures were taken for each subchannel in the bundle assembly.

3.1.3.2 Exercise 2 – Steady-state Rod Bundle

The available data for this exercise consisted of the powers at which DNB could be confirmed. It was also requested that participants submit the axial and radial locations of DNB in the bundle for code-to-code comparisons.

3.1.3.3 Exercise 3 – Transient Rod Bundle

The available data for this exercise consisted of the transient time at which DNB was first detected in the rod bundle. It was also requested that participants submit the power at which DNB was confirmed for code-to-code comparisons.

Four transient scenarios (temperature increase, power increase, depressurization, and flow reduction) were used in this exercise for each test series, yielding eight total test cases. The boundary conditions for test series 11T are shown in Figure 3.5, Figure 3.6, Figure 3.7, and Figure 3.8. Similar boundary conditions are given for test series 12T in the benchmark specification.

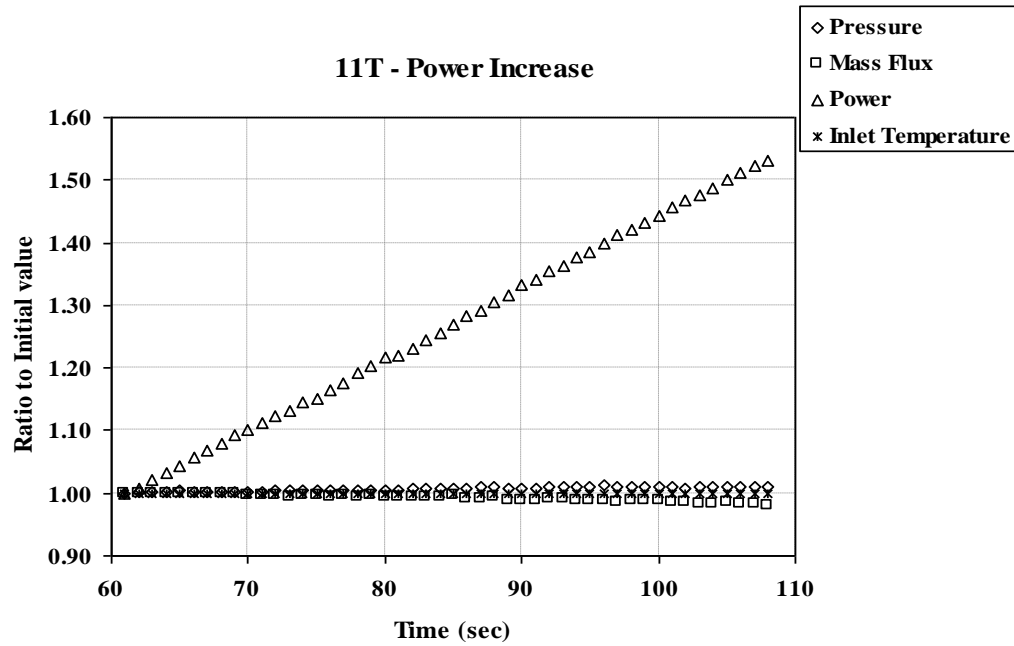


Figure 3.5 Variation of Properties for Test Case 11T (Power Increase)

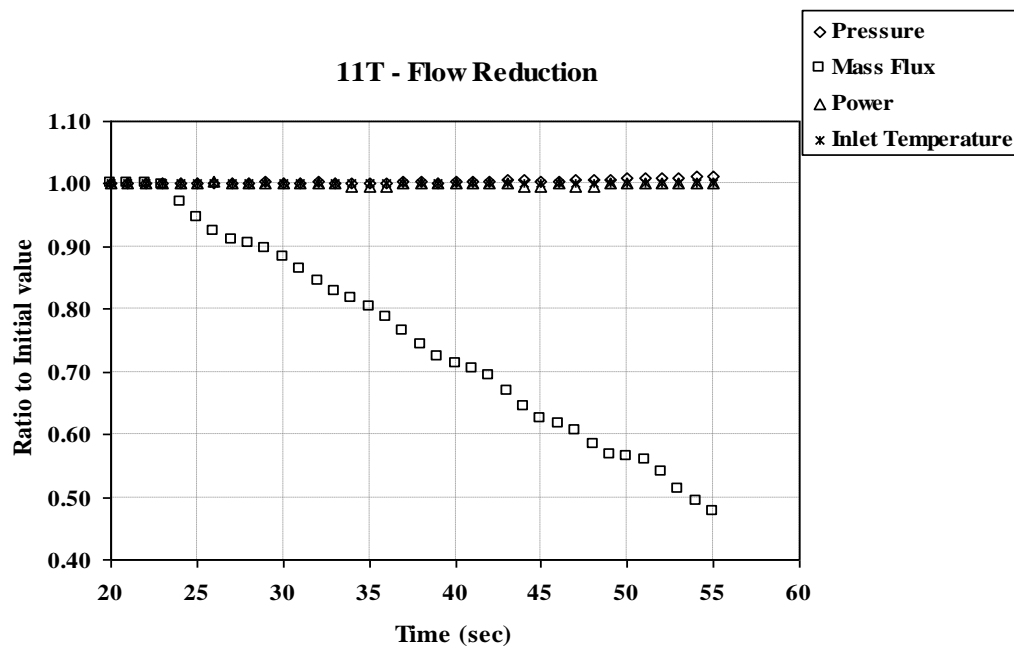


Figure 3.6 Variation of Properties for Test Case 11T (Flow Reduction)

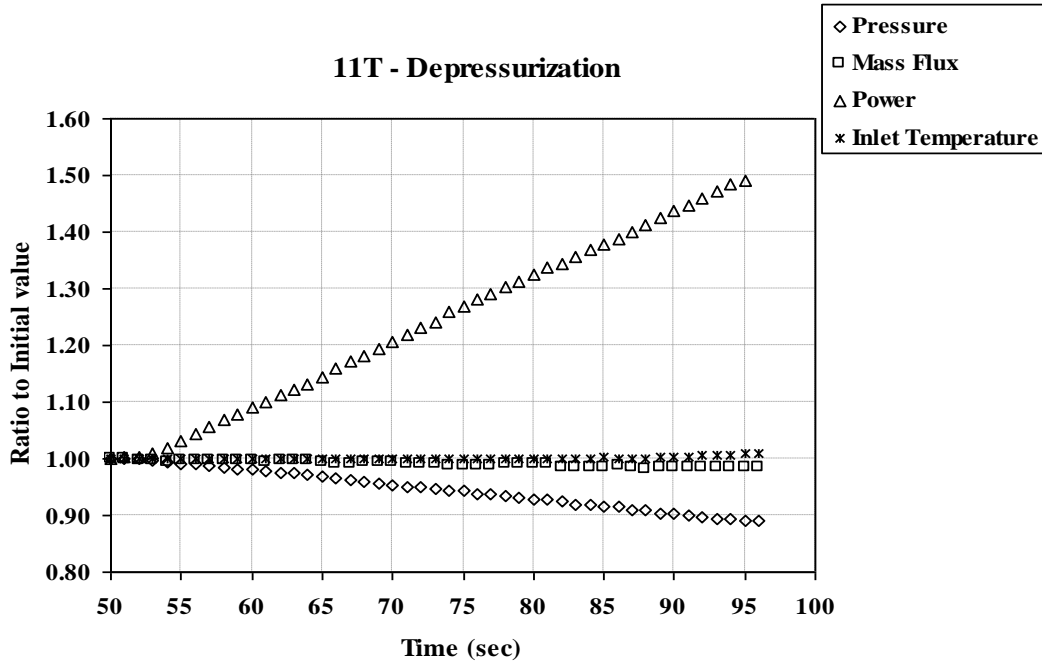


Figure 3.7 Variation of Properties for Test Case 11T (Depressurization)

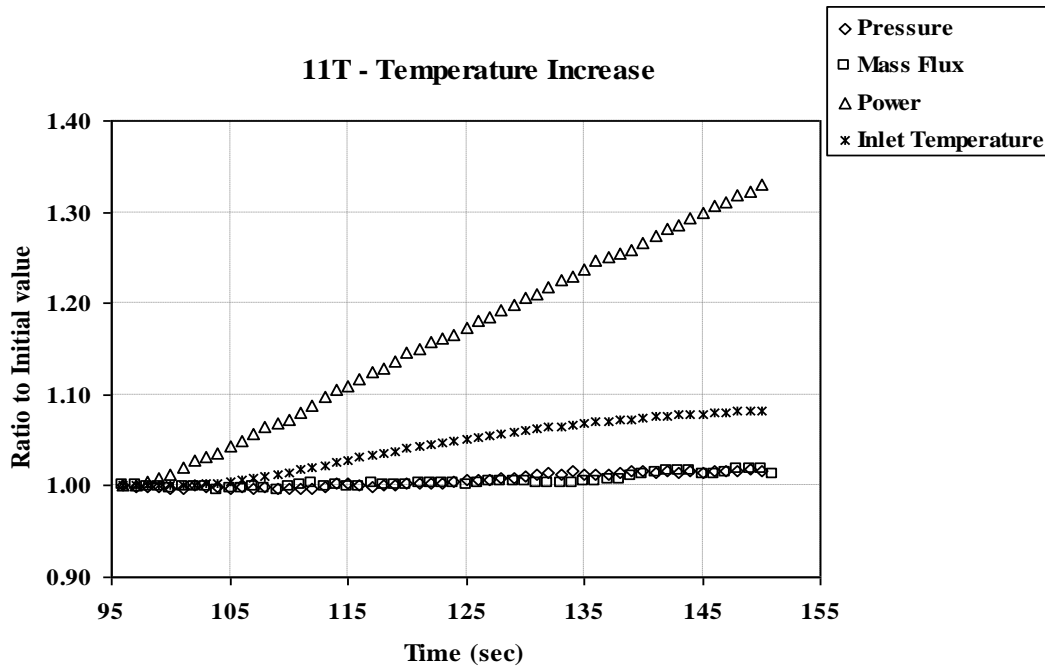


Figure 3.8 Variation of Properties for Test Case 11T (Temperature Increase)

3.2 Analysis

Participants' results are presented here for preliminary analysis. As mentioned earlier, at the time of the writing of this Thesis, the second benchmark had not yet been held. As a result, final results were only available for some of the participants, while preliminary results were available

for others. All available results are presented here regardless of whether they are considered “final” or “preliminary”.

3.2.1 Participant Results

The complete set of available results from participants can be found in Appendix V, Appendix VI, and Appendix VII.

3.2.1.1 Exercise 1 – Fluid Temperature

In several cases, the codes were unable to accurately model the fluid temperature at the right side of the bundle, either overpredicting or underpredicting significantly. These cases generally involved a high pressure, high inlet temperature, high mass flow, and moderate-to-high power or a very low pressure, high mass flow, low inlet temperature, and high power. These conditions, coupled with the strong power gradient (seen in Figure 3.1) across the bundle, create an environment that is difficult for the codes to model accurately. While CATHARE 3 and FLICA-OVAP were generally able to stay within 5% relative error of the experimental value, THYC had difficulty with cases that featured a high mass flow. For example, Test Case 01-1237 is a case that has a very low pressure (4.922 MPa), high mass flow (4722 kg/m²s), low inlet temperature (359K), and high power (3.44 MW). In cases like this, THYC tended to overpredict the fluid temperature on the right side of the bundle by 30-40%. Conversely, in cases like Test Case 01-5125, which had a high pressure (14.74MPa), high inlet temperature (562K), high mass flow (3039 kg/m²s), and moderate power (1.5MW), THYC tended to underpredict the fluid temperature by about 30%.

3.2.1.2 Exercise 2 – Steady-state Rod Bundle

The codes were generally able to calculate the DNB power satisfactorily, and there was no observable bias across test series. The DNB power was consistently overpredicted in Test Series 0, while it was underpredicted in Test Series 2, 3, 4, and 13. There was also considerable variation in the predictions of axial elevation of first detected DNB. It should be noted that the measured data represents the first thermocouple at which DNB was detected. Therefore, it is the latest (axially speaking) that the onset of DNB would have occurred, and is not an exact value, as DNB could have occurred lower on the bundle.

3.2.1.3 Exercise 3 – Transient Rod Bundle

It is difficult to draw any useful conclusions from the submitted data for this exercise since the data set is so small (and the data that is available is only preliminary). The available data does suggest, however, that codes are able to predict the time of DNB reasonably well in the studied transients.

Chapter 4

Analysis Using Subchannel Code CTF and System Code TRACE

4.1 TRACE

TRACE is a thermal-hydraulic system code developed by the USNRC in an effort to provide independent analysis of nuclear reactor thermal-hydraulic systems. It was decided that TRACE would be used to model bundles in Exercises 2 and 3 of Phase 1 and all three exercises of phase 2.

4.1.1 Modeling Considerations

For exercises 2 and 3, the same basic model was used, with only slight modifications required to account for changes in the fuel bundle or initial/boundary conditions. The model consisted of a VESSEL component (acting as the test section), four PIPE components, and two BREAK and two FILL components as seen in Figure 4.1. In addition to these hydraulic components, two HTSTR (heat structure) components and two POWER components were used to simulate the heating elements.

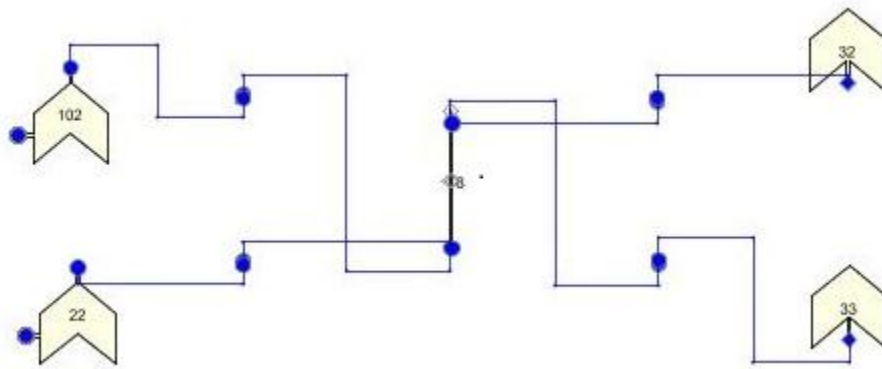


Figure 4.1 TRACE Model of Test Series 5T

To simulate the rod bundle as a vessel, the bundle was broken into two concentric rings, while maintaining total flow area and power. Figure 4.2 shows this model.

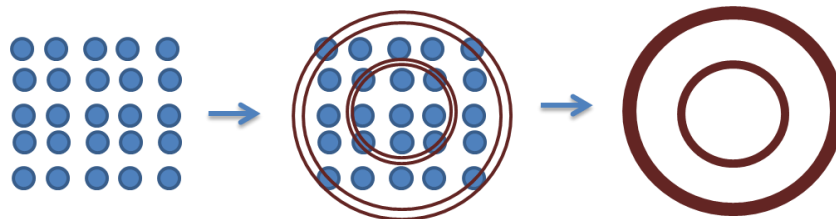


Figure 4.2 Decomposition of Fuel Bundle Into Two-Ring Vessel

The two heat structure components used zero flux boundary conditions at the inner surfaces, and the outer surfaces were attached to the rings (HTSTR1 was attached to the inner wall of the first ring and HTSTR2 was attached to the inner wall of the second ring). The power components were then applied to these heat structures to simulate heating from the rods. Due to the use of the vessel structure seen above, the power needed to be distributed between the two power

structures. The powers for each ring were determined based on the total number of rods represented per ring as well as the relative power of each of these rods. Using assembly B5 as an example, we see that the “inner” and “outer” powers (P_1 and P_2 , respectively) are given as

$$P_1 = \frac{9}{9 + 16 * 0.85} = 0.39823 \quad P_2 = 1 - P_1 = 1 - 0.39823 = 0.60177$$

By multiplying the total power in each case by these fractions, it was possible to assign the appropriate power to each heat structure.

Generalized state tables were used to input the model properties such as pressure, temperature, and flow rate.

4.1.2 Results

The TRACE results for test series 5T are shown in Figure 4.3, Figure 4.4, Figure 4.5, Figure 4.6.

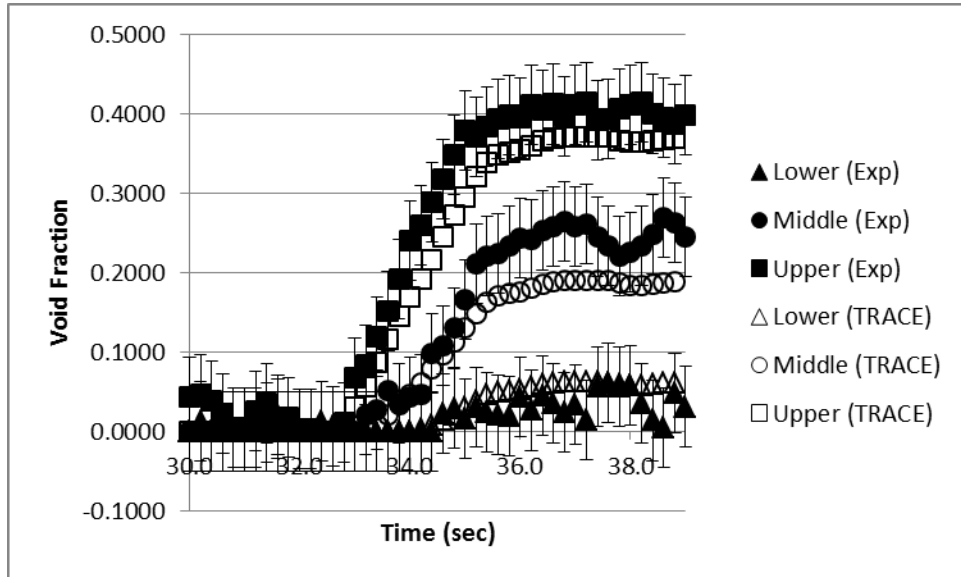


Figure 4.3 TRACE Results for Test Series 5T (Power Increase)

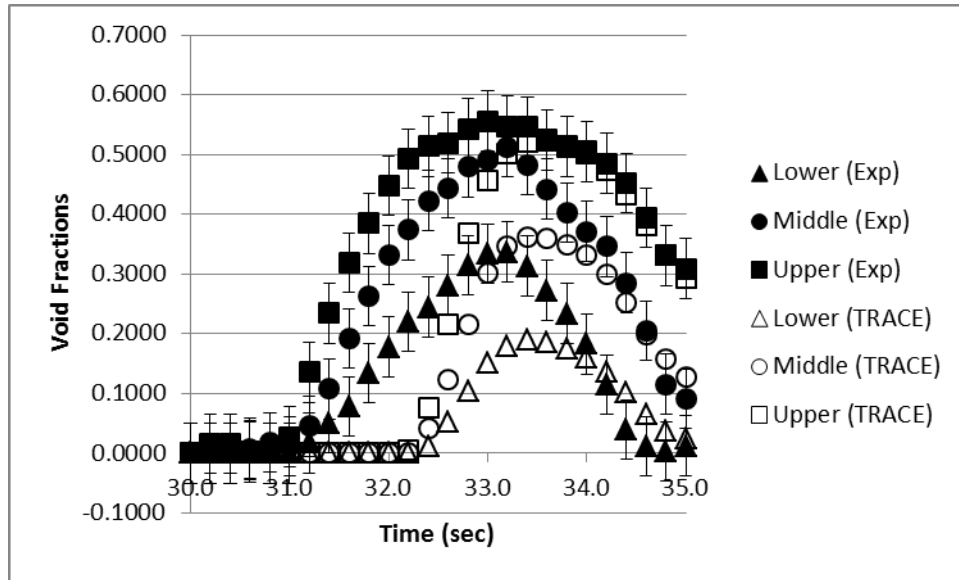


Figure 4.4 TRACE Results for Test Series 5T (Flow Reduction)

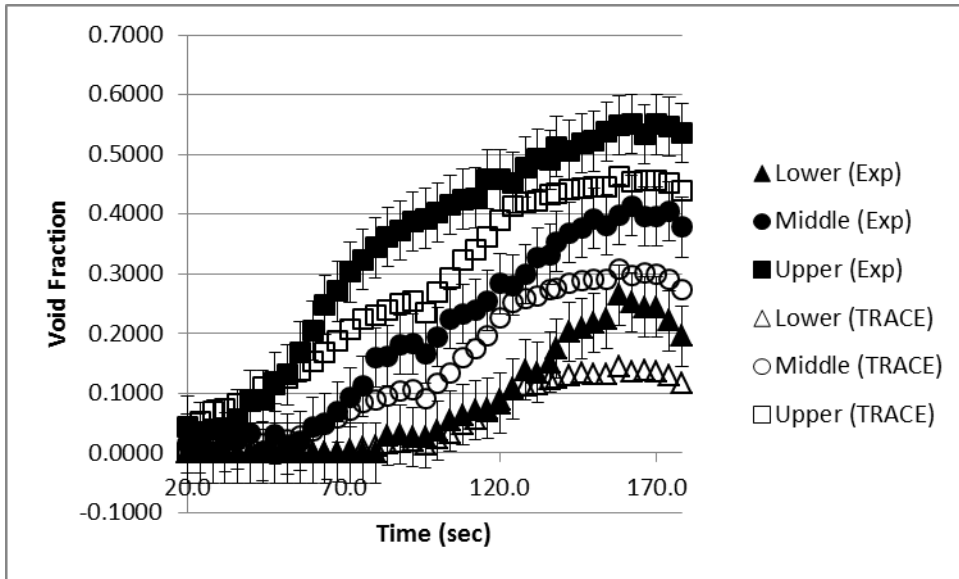


Figure 4.5 TRACE Results for Test Series 5T (Depressurization)

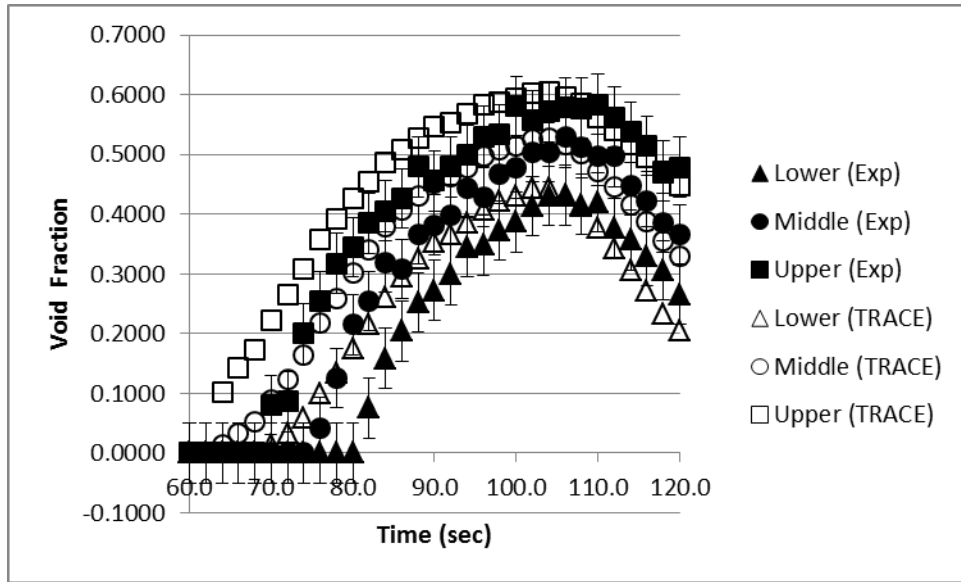


Figure 4.6 TRACE Results for Test Series 5T (Temperature Increase)

4.2 CTF

CTF is a version of the well-known and widely used COBRA-TF code whose models have been continuously improved and validated at the Reactor Dynamics and Fuel Management Group (RDFMG) at PSU over the last years [9]. The original version of COBRA-TF was developed at the Pacific Northwest Laboratory as a part of the COBRA/TRAC thermal-hydraulic code [10]. Since then, various academic and industrial organizations have adapted, developed and modified the code in many directions. The code is used worldwide for academic and general research purposes as well. The code version used at PSU originates from a version modified during the FLECHT SEASET program [7]. Besides using the code to teach and train students in the area of nuclear reactor thermal-hydraulic safety analyses, the theoretical models and numerics of COBRA-TF were substantially improved at PSU during the last few years [6][11][12]. The code was subjected to an extensive verification and validation program and was applied to variety of LWR steady state and transient simulations. Recently, a 3D neutron kinetics module was implemented into COBRA-TF by a serial integration coupling to the PSU Nodal Expansion Method (NEM) code. The new PSU coupled code system was named CTF/NEM.

4.2.1 Modeling Considerations

CTF is a transient code based on a separated flow representation of the two-phase flow. The two-fluid formulation, generally used in thermal-hydraulic codes, separates the conservation equations of mass, energy, and momentum to vapor and liquid. CTF extends this treatment to three fields: vapor, continuous liquid and entrained liquid droplets, which results in a set of nine time-averaged conservation equations. The conservation equations for each of the three fields and for heat transfer from and within the solid structure in contact with the fluid are solved using a semi-implicit, finite-difference numerical technique on an Eulerian mesh, where time intervals are assumed to be long enough to smooth out the random fluctuations in the multiphase flow, but short enough to preserve any gross flow unsteadiness. The code is able to handle both hot wall

and normal flow regimes maps and it is capable of calculating reverse flow, counter flow, and crossflow situations. The code is developed for use with either 3D Cartesian or subchannel coordinates and, therefore, features extremely flexible noding for both the thermal-hydraulic and heat-transfer solutions. This flexibility allows a full 3D treatment in geometries amenable to description in a Cartesian coordinate system.

The three-field formulation of the two-phase flow used in CTF is a straightforward extension of the general two-fluid model. Dividing the liquid phase into a continuous liquid field and an entrained liquid drop field allows both fields to have different velocities. The generalized phasic momentum equation is then given as:

$$\frac{\partial}{\partial t}(\alpha_k \rho_k \underline{U}_k) + \nabla \cdot (\alpha_k \rho_k \underline{U}_k \underline{U}_k) = \alpha_k \rho_k \underline{g} - \alpha_k \nabla P + \nabla \cdot (\alpha_k \underline{\tau}_k) + \underline{M}_k^\Gamma + \underline{M}_k^d + \underline{M}_k^T,$$

where α_k is the average k-phase void fraction; ρ_k is the average k-phase density; \underline{U}_k is the average k-phase velocity vector; \underline{g} is the acceleration of gravity vector; $\underline{\tau}_k$ is the average k-phase viscous stress tensor; \underline{M}_k^Γ is the average supply of momentum to phase k due to mass transfer to phase k; \underline{M}_k^d is the average drag force on phase k by the other phases; and \underline{M}_k^T is the average supply of momentum to phase k due to turbulent mixing and void drift.

The generalized phasic momentum equations assume that gravity is the only body force and pressure is the same in all phases.

In the generalized phasic momentum equation the terms representing the momentum exchange at the interface (interfacial momentum terms) are expressed as

$$\begin{aligned} \underline{M}_{\text{vap}}^d &= -\underline{\tau}_{i,\text{vap_liq}}''' - \underline{\tau}_{i,\text{vap_ent}}''' && \text{for the vapor phase,} \\ \underline{M}_{\text{liq}}^d &= \underline{\tau}_{i,\text{vap_liq}}''' && \text{for the continuous liquid phase,} \\ \underline{M}_{\text{ent}}^d &= \underline{\tau}_{i,\text{vap_ent}}''' && \text{for the entrained liquid phase,} \end{aligned}$$

where $\underline{\tau}_{i,\text{vap_liq}}'''$ is the average drag force per unit volume by the vapor on the continuous liquid and $\underline{\tau}_{i,\text{vap_ent}}'''$ is the average drag force per unit volume by the vapor on the entrained liquid.

The momentum exchange due to mass transfer between the three fields can be written as

$$\begin{aligned} \underline{M}_{\text{vap}}^\Gamma &= (\Gamma''' \underline{U}) && \text{for the vapor phase,} \\ \underline{M}_{\text{liq}}^\Gamma &= -(\Gamma_{\text{liq}}''' \underline{U}) - (S''' \underline{U}) && \text{for the continuous liquid phase,} \\ \underline{M}_{\text{ent}}^\Gamma &= -(\Gamma_{\text{ent}}''' \underline{U}) + (S''' \underline{U}) && \text{for the entrained liquid phase,} \end{aligned}$$

where the Γ''' is the average rate of vapor generation per unit volume and S''' is the average net rate of entrainment per unit volume. Since both liquid fields contribute to the vapor generation, then $\Gamma''' = \Gamma_{\text{liq}}''' + \Gamma_{\text{ent}}'''$.

If η denotes the fraction of the total vapor generation coming from the entrained liquid field, then

$$\Gamma_{\text{vap}}''' = \Gamma''',$$

$$\Gamma_{\text{ent}}''' = \eta \Gamma''' = -\Gamma_{\text{ent}}''' + S''' = -\eta \Gamma''' + S''',$$

and

$$\Gamma_{\text{liq}}''' = (1 - \eta) \Gamma''' = -\Gamma_{\text{liq}}''' - S''' = -(1 - \eta) \Gamma''' - S'''.$$

The following assumptions are used to obtain the CTF three-field momentum equations:

- 1) The momentum exchange due to turbulent mixing and void drift is neglected in the entrained liquid field in the annular flow regime: $M_{\text{ent}}^T = 0$ if $\alpha_{\text{vap}} \geq 0.8$;
- 2) The viscous stresses can be partitioned into a wall shear and a fluid-fluid shear; the fluid-fluid shear is neglected: $\nabla \cdot (\alpha_k \underline{\tau}_k) = \underline{\tau}_{\text{wall},k}$.

The model for interfacial mass transfer is obtained from the energy jump condition by neglecting the mechanical terms and averaging:

$$\Gamma''' = \frac{-q_{I\ell}''' - q_{IV}'''}{h_{fg}}$$

The interfacial heat transfer, q_I''' , for phase k is given by

$$q_{I_k}''' = h A_I''' (T_s - T_k),$$

where A_I''' is the average interfacial area per unit volume and h is a surface heat transfer coefficient. The vapor generation is divided into four components; two for each phase, depending on whether the phase is superheated or subcooled, and the total vapor generation rate is given by the sum of these components.

The interfacial area per unit volume, A_I''' , is based on the flow regime, as are the heat transfer coefficients, h . Correlations for the various heat transfer coefficients are given in [7].

The interfacial drag force per unit volume between any two fields is assumed to be a function of the relative velocity between both fields. The interfacial friction coefficients are flow regime dependent and, therefore, neither void correlation nor two-phase pressure drop correlation has to be applied. Interfacial drag forces are modeled between continuous liquid and disperse vapor in the bubbly flows and between continuous liquid film and vapor core and entrained droplets and vapor core in the annular flow. The treatment of the interfacial drag is described in Table 4.1.

Turbulent mixing and void drift phenomena are modeled in CTF by the Lahey and Moody approach [13], where the net two-phase mixing (including void drift) is assumed to be proportional to the non-equilibrium void fraction gradient. The void drift is only assumed to occur in bubbly, slug, and churn flow, where liquid is the continuous phase and vapor is the dispersed phase. The single phase mixing coefficient might be either specified as an input value or calculated using an empirical correlation derived by Rogers and Rosehart [14]. The Beus'

model for two-phase turbulent mixing is utilized [15]. In the 1980s, both approaches were representing the state-of-art in turbulent mixing and void drift modeling and are still used in most of the subchannel codes. A detailed description of the current CTF turbulent mixing and void drift models is given in Table 4.2.

Table 4.1 CTF Modeling of the Interfacial Drag

Interfacial Drag Forces, [N/m³]	<p>Between continuous liquid and vapor: $\tau_{I,vap_liq} = K_{I,vap_liq} U_{vap_liq}$</p> <p>Between entrained liquid and vapor: $\tau_{I,vap_ent} = K_{I,vap_ent} U_{vap_ent}$</p>
Interfacial Drag Coefficients, [kg/m³s]	<p>Bubbly Flows</p> <p>For small bubbles:</p> $K_{I,vap_liq} = 0.375 \frac{C_{D_{bub}}}{r_{bub}} \alpha_{vap} \rho_{liq} U_{vap} - U_{liq} ; \quad C_{D_{bub}} = \frac{24}{Re_{bub}} (1 + 0.1 Re_{bub}^{0.75})$ <p>For large bubbles:</p> $K_{I,vap_liq} = 0.375 \frac{C_{D_{Lbub}}}{r_{bub}} \alpha_{vap} \rho_{liq} U_{vap} - U_{liq} ; \quad C_{D_{Lbub}} = \max \left(\frac{24}{Re_{Lbub}} (1 + 0.1 Re_{Lbub}^{0.75}) \alpha_{liq}^2, 0.45 \alpha_{liq}^2 \right)$ <p>Annular Flow</p> <p>Between continuous liquid film and vapor core:</p> $K_{I,vap_liq} = 2 \frac{f_I}{D_{hyd}} \sqrt{\alpha_{vap} + \alpha_{ent}} \rho_{vap} U_{vap} - U_{liq} ; \text{ interfacial friction factor } f_I \text{ by Henstoch}$ <p>and Hanratty</p> <p>Between entrained liquid film and vapor core:</p> $K_{I,vap_drop} = 0.375 \frac{C_{D_{drop}}}{r_{drop}} \alpha_{ent} \rho_{vap} U_{vap} - U_{ent} ; \quad C_{D_{drop}} = \frac{24}{Re_{drop}} (1 + 0.1 Re_{drop}^{0.75})$

Table 4.2 CTF Models for Turbulent Mixing and Void Drift

Turbulent Mixing	<p>Mass exchange of the phase k: $\dot{m}_k^{TM} = -\beta_{TP} \frac{\bar{G}}{\bar{\rho}} (\alpha_{k,j} \rho_{k,j} - \alpha_{k,i} \rho_{k,i})$</p> <p>Momentum exchange of the phase k: $\dot{I}_k^{TM} = -\beta_{TP} \frac{\bar{G}}{\bar{\rho}} \Delta G_k A$</p> <p>Energy exchange of the phase k: $\dot{Q}_k^{TM} = -\beta_{TP} \frac{\bar{G}}{\bar{\rho}} \Delta(\alpha_k \rho_k h_k) A$</p>
Single-Phase Turbulent Mixing Coefficient	<p>User specified single value based on experimental data or Internally calculated using the correlation by Rogers & Rozehart:</p> $\beta_{SP} = \frac{1}{2} 0.0058 \left(\frac{D_{gap}}{D_{rod}} \right)^{-1.46} Re^{-0.1} \left[1 + \left(\frac{D_{hyd,j}}{D_{hyd,i}} \right)^{1.5} \right] \frac{D_{hyd,i}}{D_{rod}}$
Two-Phase Turbulent Mixing Coefficient	<p>Two-phase multiplier by Beus: $\beta_{TP} = \Theta_{TP} \beta_{SP}$;</p> $\Theta_{TP} = 1 + (\Theta_{max} - 1) \frac{x}{x_{max}} \quad \text{if } x \leq x_{max}$ $\Theta_{TP} = 1 + (\Theta_{max} - 1) \frac{x_{max} - x_0}{x - x_0} \quad \text{with } \frac{x_0}{x_{max}} = 0.57 Re^{0.0417} \quad \text{if } x > x_{max}$ <p>with $\Theta_{max} = 5$ and $x_{max} = \frac{0.4 \sqrt{g \rho_{liq} (\rho_{liq} - \rho_{vap}) d_{hyd}}}{G_{tot}} + 0.6 \sqrt{\frac{\rho_{liq}}{\rho_{vap}}} + 0.6$</p>
Void Drift	<p>Mass exchange of the phase k: $\dot{m}_k^{VD} = \beta \frac{\bar{G}}{\bar{\rho}} (\alpha_{k,j,EQ} \rho_{k,j,EQ} - \alpha_{k,i,EQ} \rho_{k,i,EQ}) A$;</p> <p>Momentum exchange of the phase k: $\dot{I}_k^{VD} = \beta \frac{\bar{G}}{\bar{\rho}} (G_{k,j,EQ} - G_{k,i,EQ}) A$</p> <p>Energy exchange of the phase k:</p> $\dot{Q}_k^{VD} = \beta \frac{\bar{G}}{\bar{\rho}} (\alpha_{k,j,EQ} \rho_{k,j,EQ} h_{k,j,EQ} - \alpha_{k,i,EQ} \rho_{k,i,EQ} h_{k,i,EQ}) A$ $(\alpha_{k,j,EQ} \rho_{k,j,EQ} - \alpha_{k,i,EQ} \rho_{k,i,EQ}) = \pm \frac{\overline{\alpha_{vap} \rho_k}}{\bar{G}_{tot}} (G_{tot,j,EQ} - G_{tot,i,EQ})$

4.2.2 Results

The Exercise I-1 test cases were calculated for all four subchannel types – S1, S2, S3, and S4. Only the heated length of the subchannel was modeled in an axial discretization of forty equidistant nodes. Code-to-data comparisons are given in Figure 4.7. It can be seen that the CTF predictions stay within the error bound of 10% void. The experimental uncertainties for the steady state void fraction CT scanner measurements indicated in the plots were specified as 3% void [1].

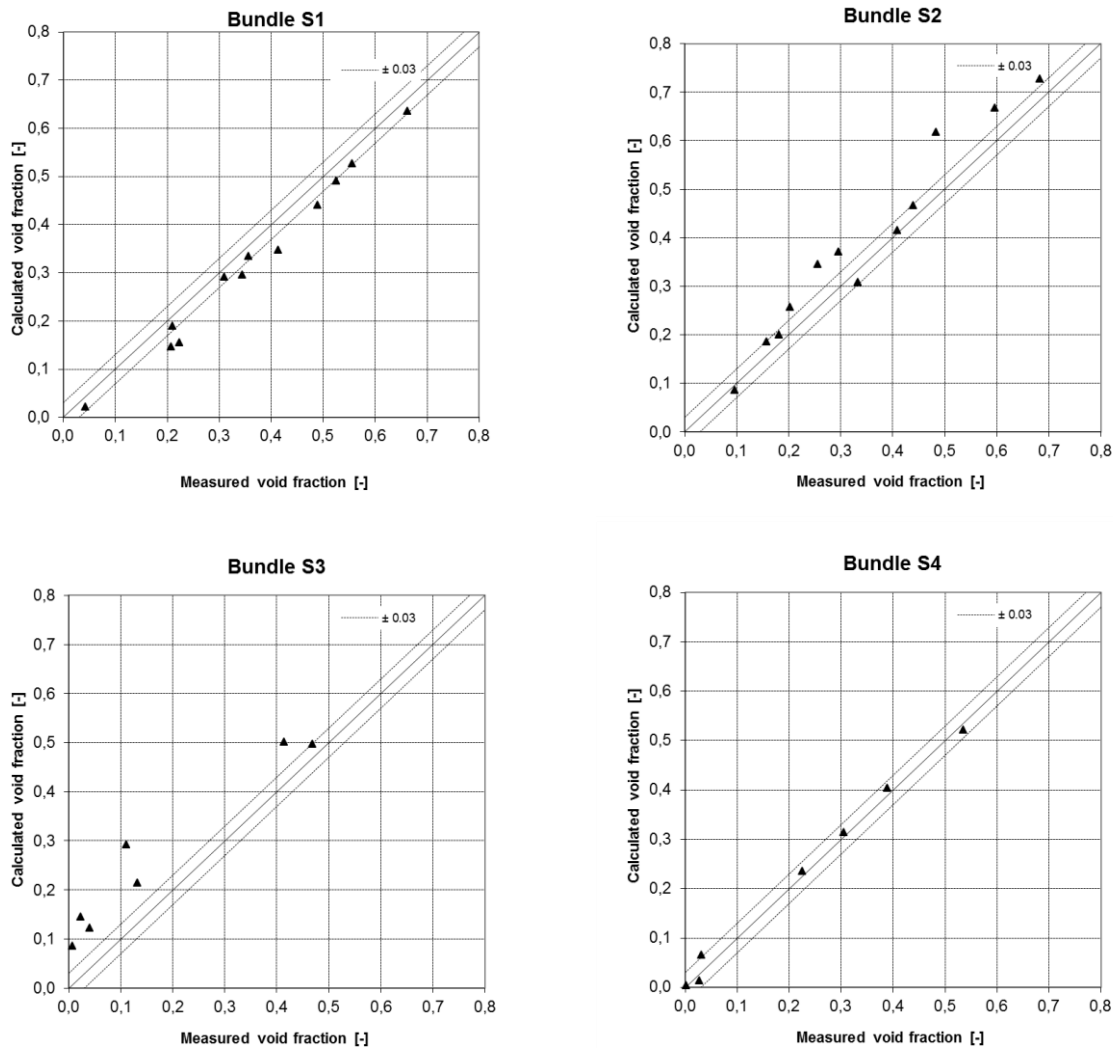


Figure 4.7 CTF Predictions of Steady-state Void Fraction in a Single Subchannel

As previously discussed, four anticipated transients (power increase, flow reduction, depressurization, and temperature increase) were simulated by NUPEC and selected as benchmark exercise cases. The space-averaged instantaneous axial void fraction profiles during the transients were supplied for code-to-data comparisons. CTF was applied to all four transient scenarios. The entire B5 (test series T5) bundle was modeled in a subchannel-by-subchannel basis - no symmetry was used. The heated length was divided axially into seventy equidistant nodes. The pressure losses due to spacer grids were calculated as velocity head losses with a loss coefficient of 1.0. The total cross-flow between two adjacent subchannels was simulated as a sum of the diversion cross-flow due to lateral pressure gradients and the lateral flow due to turbulent mixing and void drift. The measurements have been taken at three intermediate elevations along the heated length. The X-ray densitometers were located at 2216 mm, 2669 mm, and 3177 mm along the heated length. The X-ray densitometer measurements were taken by a beam passing through the subchannels' centerlines. Since, under boiling conditions, the vapor

volume fraction is higher at high velocity regions, the subchannel void fractions measured with the X-ray densitometers will be overestimated at churn-turbulent and annular film flow regimes. As a result, in these high-void conditions, the voids will be drawn to the location with the highest flow velocity (namely, the center of the subchannel), and a higher local void fraction will be seen. Under subcooled boiling conditions, the tendency will be opposite since the bubbles are concentrated mostly near heated surfaces. These tendencies are illustrated in Figure 4.8.

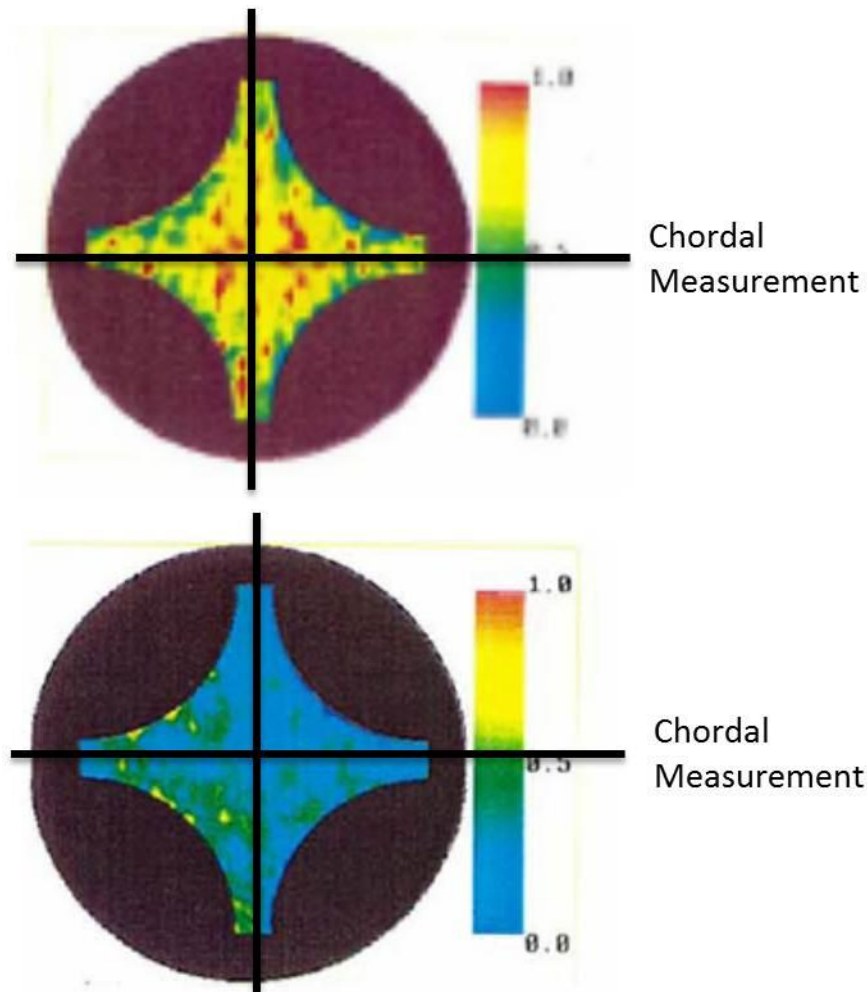


Figure 4.8 Illustration of Chordal Measurements Taken at High and Low Void Fractions

As a result, code-to-densitometer measurement comparisons should focus mostly on the qualitative aspects. Regarding the CTF predictions, it can be seen that the code is capable of reproducing the transient behavior of the bundle average void fraction. The large discrepancies at the first second of the transient are explained with the above discussed inaccuracy in the X-ray densitometer measurements at low void fraction. The agreement is very good at higher void fraction regions, where the code predictions generally stay within the error bound of 5% void.

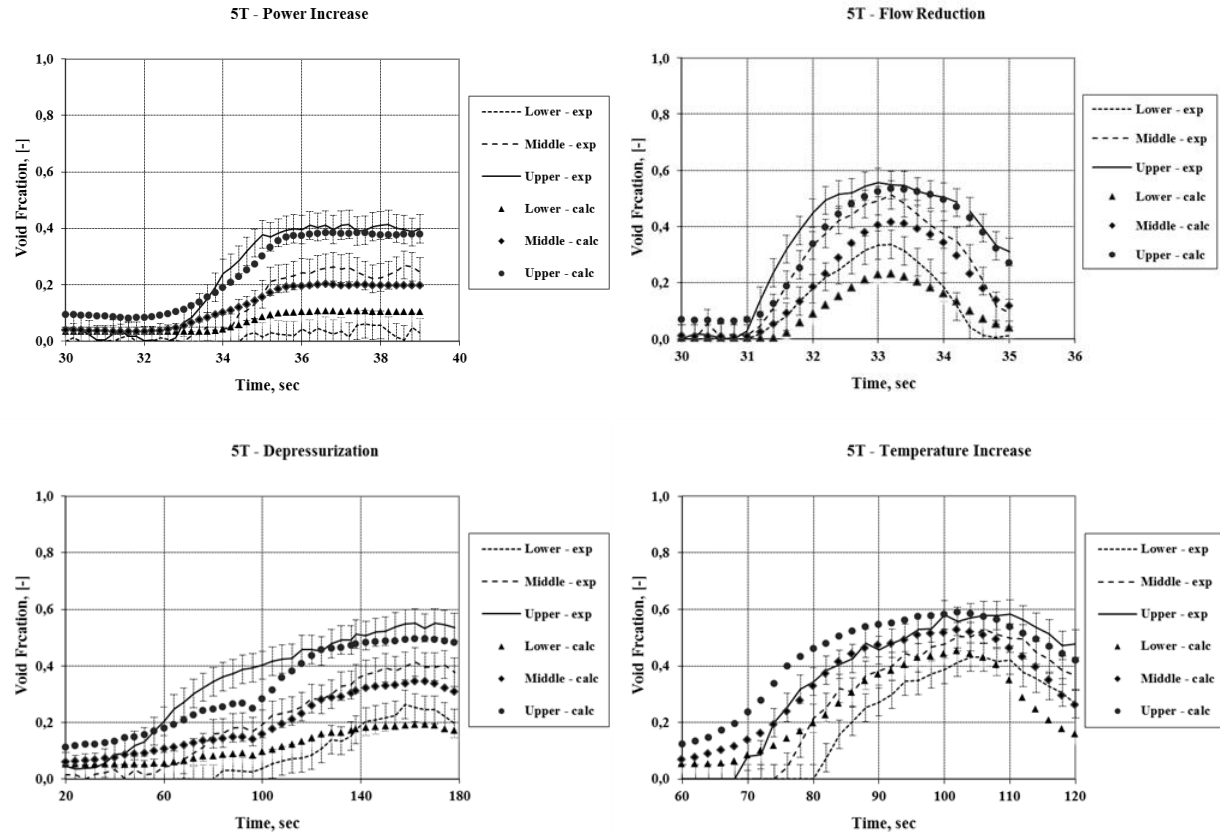


Figure 4.9 CTF Prediction of Transient Void Fraction in a Rod Bundle

4.3 Comparison

Both CTF and TRACE were used to model the four transient scenarios involving bundle B5 (test series 5T). Both codes performed well in the power increase transient, generally staying within the 5% void error bounds for the duration of the transient. For the flow reduction case, CTF performed better than TRACE, which experienced a time shift in the onset of void generation. This was attributed to the short time span involved in the transient, but CTF did not experience this difficulty. TRACE and CTF both underpredicted the void fraction but were able to follow the general transient shape in the depressurization case, and actually produced very similar results for this transient case. Finally, both experienced a time shift in the temperature increase transient, overpredicting the void fraction early in the transient. This again indicates that there was likely some heat transfer between the downcomer and test section region, leading to later void generation in the experimental data. It should be noted that this phenomenon was not important for the steady-state cases because the system had reached thermal equilibrium, and thus there was no heat transfer across the interface.

Chapter 5

Conclusion

The OEC/NRC PSBT Benchmark was designed to provide a set of data for the development and validation of the next generation of thermal-hydraulic codes. It consisted of two phases: a void fraction benchmark and a departure from nucleate boiling benchmark. Data regarding the test sections and conditions was provided to participants for use in calculations. The code results from all participants were then compiled and analyzed.

In the development of the benchmark specification, a number of support studies were performed. The experimental void fraction and quality were recalculated using the experimentally-determined fluid density for each of the benchmark test cases, and a deviation between these recalculated values and the measured values was observed.

The benchmark is ongoing and final results were only available for the first phase. The results presented for the second phase are considered preliminary, and final results for both phases will be presented in a final report at the completion of the benchmark.

The participants' results for each benchmark exercise were analyzed and conclusions were drawn. In the results for the first phase, it was observed that the codes tended to overpredict the thermal equilibrium quality at lower elevations and underpredict it at higher elevations. There was also a tendency to overpredict void fraction at lower elevations and underpredict it at high elevations for the bundle test cases. The overprediction of void fraction at low elevations is likely caused by the x-ray densitometer measurement method used. Under subcooled boiling conditions, the voids accumulate at heated surfaces (and are therefore not seen in the center of the subchannel, where the measurements are being taken), so the experimentally-determined void fractions will be lower than the actual void fraction. A time shift was noted in the void fraction results for the temperature increase transient cases, indicating that the test apparatus may have experienced unexpected heat transfer between the downcomer and test section. This heat transfer is only expected to be of significance in the transient test cases, as the steady-state cases allow the system to reach thermal equilibrium.

The subchannel code CTF and system code TRACE were used by the benchmark team to perform calculations based on the data provided in the benchmark specification. TRACE performed reasonably well in the power increase and depressurization transient test cases, but worse in the flow reduction and temperature increase transients. The problems in the flow reduction transient are attributed to the brevity of the transient while the problems in the temperature increase transient are attributed to the heat transfer between the downcomer and test section. CTF performed well for both subchannel and bundle test cases, but did not perform well predicting the correct void fraction at lower elevations due to the previously-discussed phenomena regarding x-ray densitometer measurement techniques. At higher void fractions, the CTF calculations were generally within the 5% void error bound for the bundle test cases. However, like TRACE, the CTF results showed a time shift in the temperature increase transient, again indicating heat transfer between the downcomer and test section.

Bibliography

- 1) A. Rubin, A. Schoedel, M. Avramova, H. Utsuno, S. Bajorek, and A. Velazquez-Lozada "OECD/NEA/NRC Benchmark Based on NUPEC PWR Subchannel and Bundle Tests (PSBT), Volume I: Experimental Database and Final Problem Specifications", OECD-NEA/NRC Report NEA/NSC/DOC(2010)1, Dec. 2009
- 2) "OECD/NEA Benchmark Based on NUPEC PWR Subchannel and Bundle Tests (PSBT)." Japan Nuclear Energy Safety Organization, JNES/SAE-TH08-0019, Apr. 2009. Web. <<http://www.oecd-nea.org/science/egrs/tb/PSBT/NUPEC%20PSBT%20Volume%20I%20%20%28JNES%209.pdf>>.
- 3) "Proving Test on the Reliability for Nuclear Fuel Assemblies." *Summary Report of Proving Tests on the Reliability for Nuclear Power Plant - 1989*. Nuclear Power Engineering Test Center, 1989. Web. <<http://www.oecd-nea.org/science/egrs/tb/PSBT/Ref.%281%29%20Proving%20Test%20on%20the%20Reliability%20for%20Nuclear%20Fuel%20Assemblies%20%281989%29.pdf>>.
- 4) Hori, K. et al., "In-Bundle Void Fraction Measurement of PWR Fuel Assembly", ICONE-2, Vol.1, pp.69-76, San Francisco, California, 21-24 Mar. 1993
- 5) "Pamphlet of Takasago Engineering Laboratory." Nuclear Power Engineering Center (NUPEC). Web. <<http://www.oecd-nea.org/science/egrs/tb/PSBT/Ref.%285%29%20Pamphlet%20of%20Takasago%20Engineering%20Lab.%20%28NUPEC%29.pdf>>.
- 6) M. Avramova, et al., "Improvements and Applications of COBRA-TF for Stand-Alone and Coupled LWR Safety Analyses", *Proceedings: PHYSOR-2006*, Vancouver, Canada, Sept. 2006
- 7) C. Y. Payk et al., "Analysis of FLECHT SEASET 163-Rod Blocked Bundle Data using COBRA-TF", NUREG/CR-4166, 1985
- 8) A. Rubin, M. Avramova, and H. Utsuno, "OECD/NRC Benchmark Based on NUPEC PWR Subchannel and Bundle Tests (PSBT)", *Proceedings: PHYSOR-2010*, Pittsburgh, PA, USA, May 2010
- 9) Reactor Dynamics and Fuel Management Group, Nuclear Engineering Program, "CTF – A Thermal-Hydraulic Subchannel Code for LWRs Transient Analyses, Users' Manual", University Park, PA, 2009.
- 10) M.J. Thurgood, et al., "COBRA/TRAC – A Thermal-Hydraulic Code for Transient Analysis of Nuclear Reactor Vessel and Primary Coolant Systems", NUREG/CR-3046 (1983)
- 11) M. Avramova, "COBRA-TF Development, Qualification, and Application to LWR Analysis", MS Thesis in Nuclear Engineering, The Pennsylvania State University (2003)

- 12) Cuervo, D., M. Avramova, K. Ivanov, and R. Miro. "Evaluation and Enhancement of COBRA-TF Efficiency for LWR Calculations." *Annals of Nuclear Energy* 33.9 (2006): 837-47. Print.
- 13) Lahey, Richard T., and F. J. Moody. *The Thermal-hydraulics of a Boiling Water Nuclear Reactor*. La Grange Park, Ill., USA: American Nuclear Society, 1993. Print.
- 14) J. T. Rogers and R. G. Rosehart, *Mixing by Turbulent Interchange in Fuel Bundles. Correlations and Inferences*, ASME, 72-HT-53,(1972)
- 15) S. G. Beus, *A two-phase turbulent mixing model for flow in rod bundles*. Bettis Atomic Power Laboratory, WAPD-T-2438, (1970)

Appendix I Exercise I-1 Results

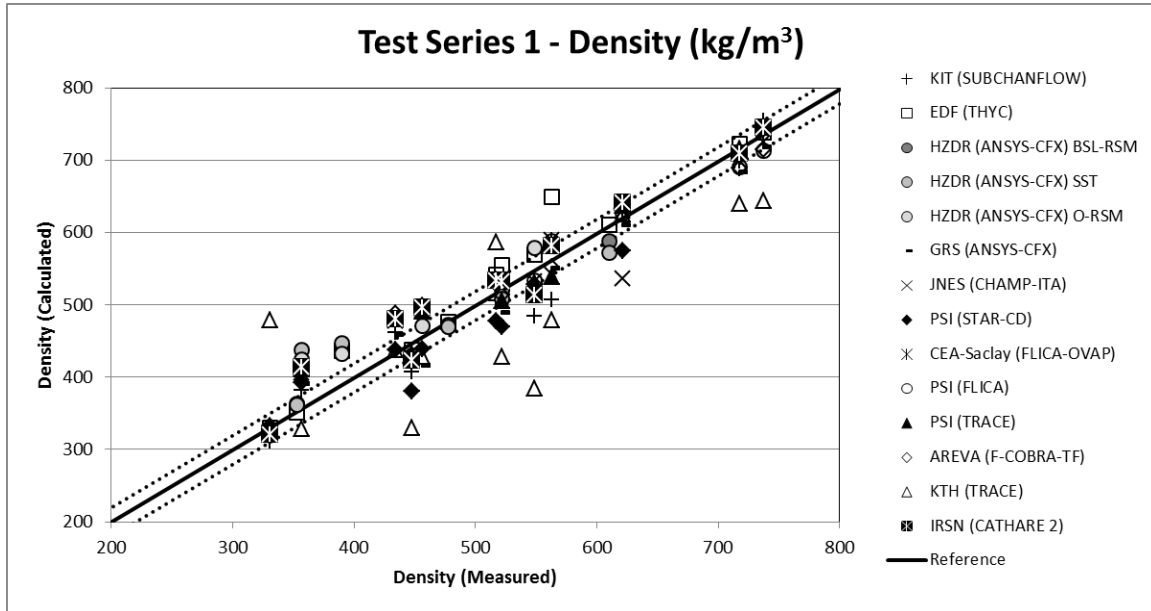


Figure AI.1 Test Series 1 Density Results

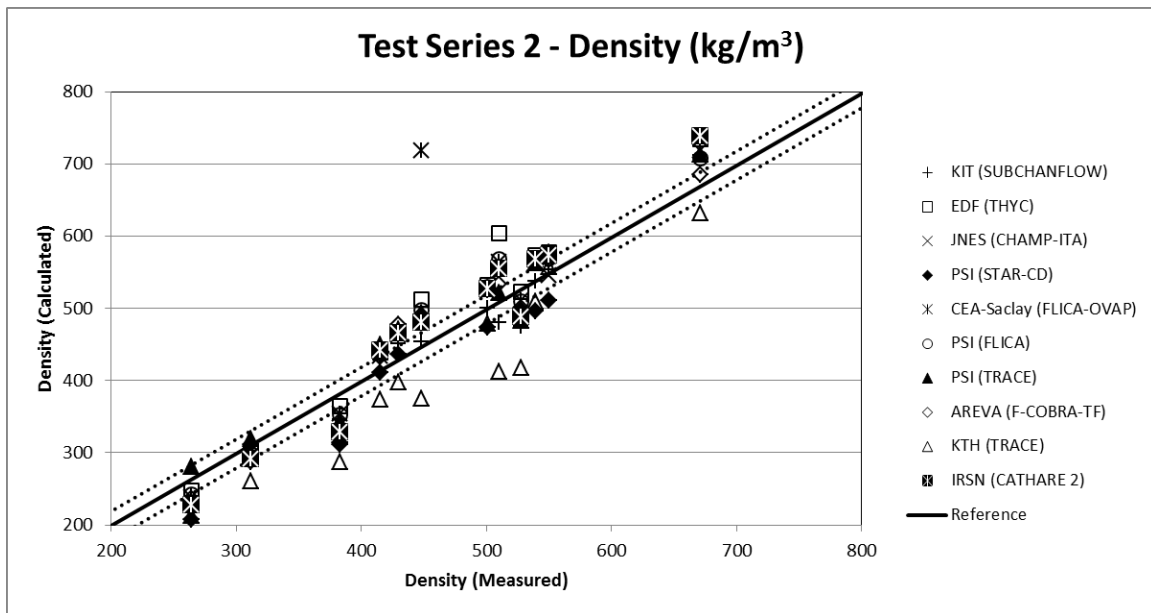


Figure AI.2 Test Series 2 Density Results

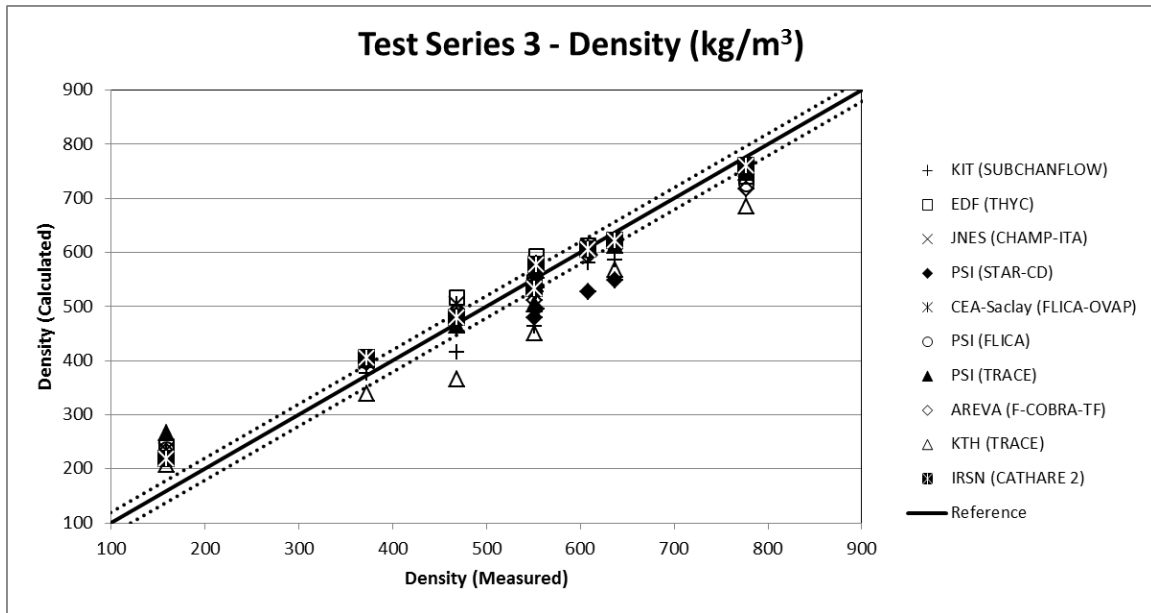


Figure AI.3 Test Series 3 Density Results

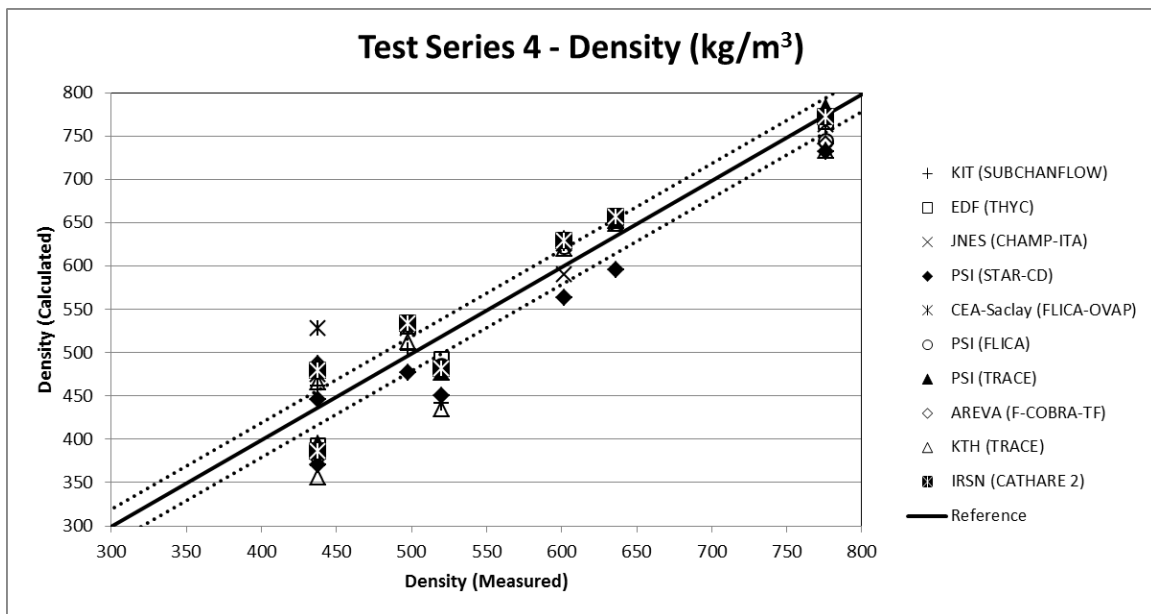


Figure AI.4 Test Series 4 Density Results

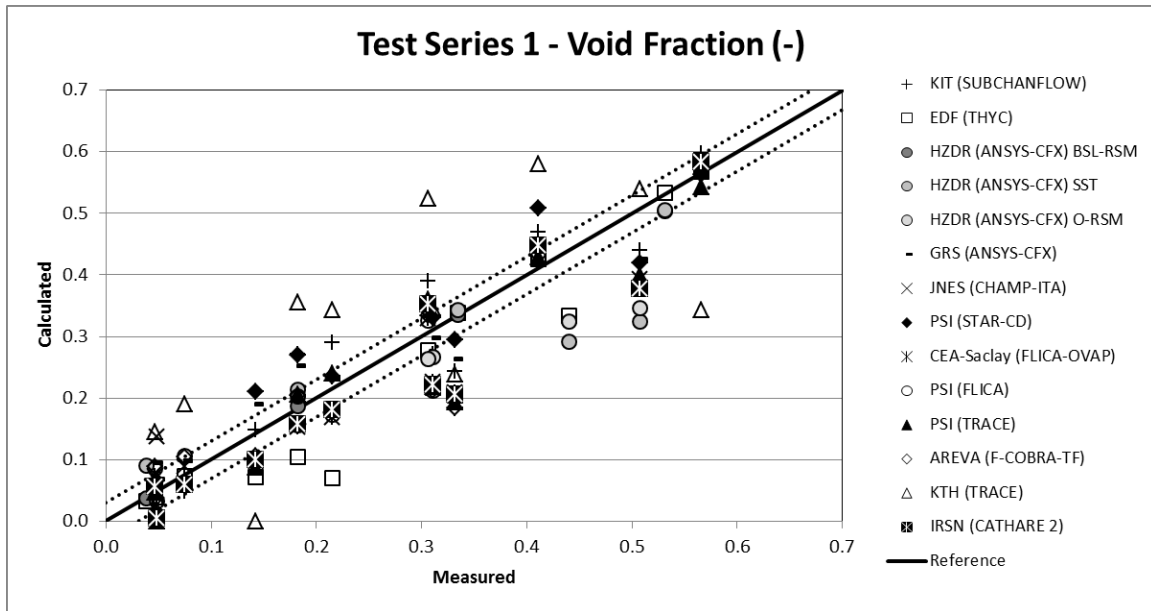


Figure AI.5 Test Series 1 Void Fraction (Calculated vs. Measured) Results

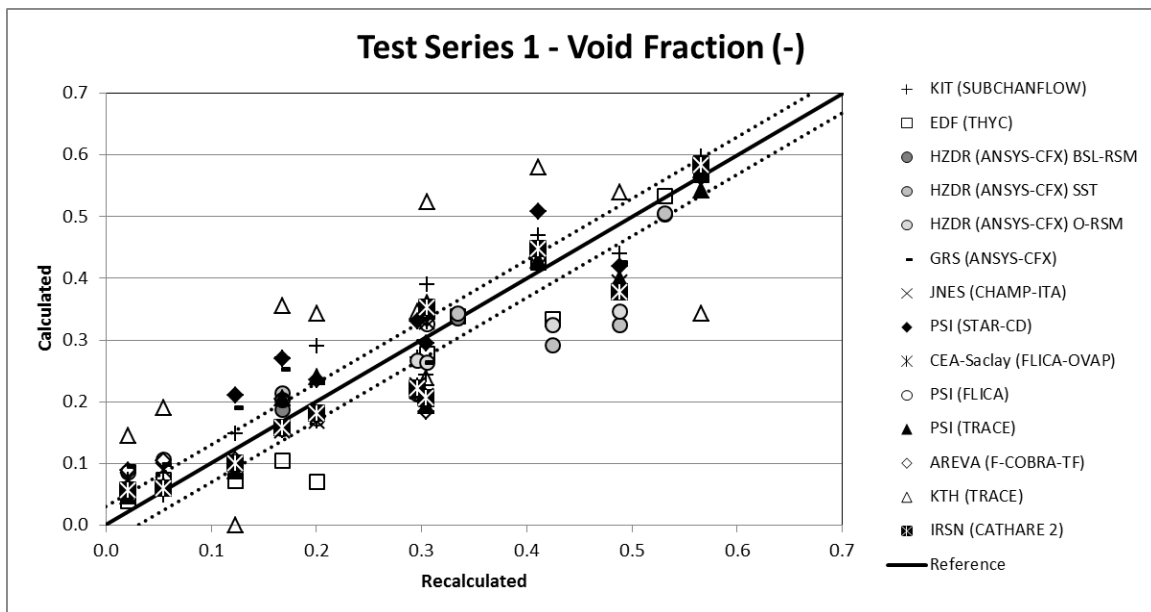


Figure AI.6 Test Series 1 Void Fraction (Calculated vs. Recalculated) Results

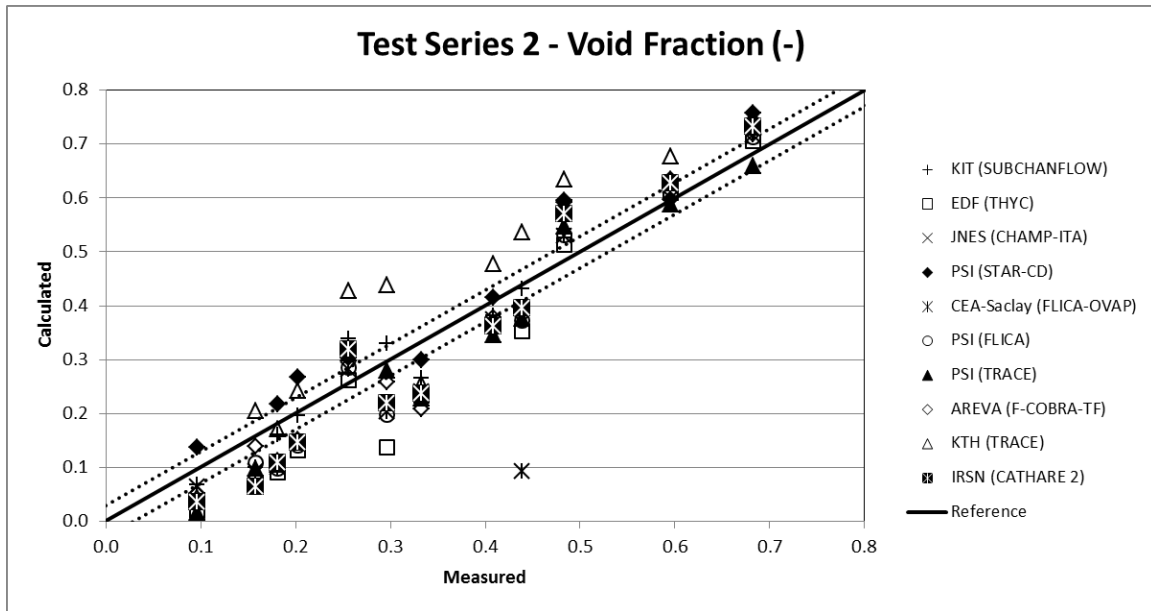


Figure AI.7 Test Series 2 Void Fraction (Calculated vs. Measured) Results

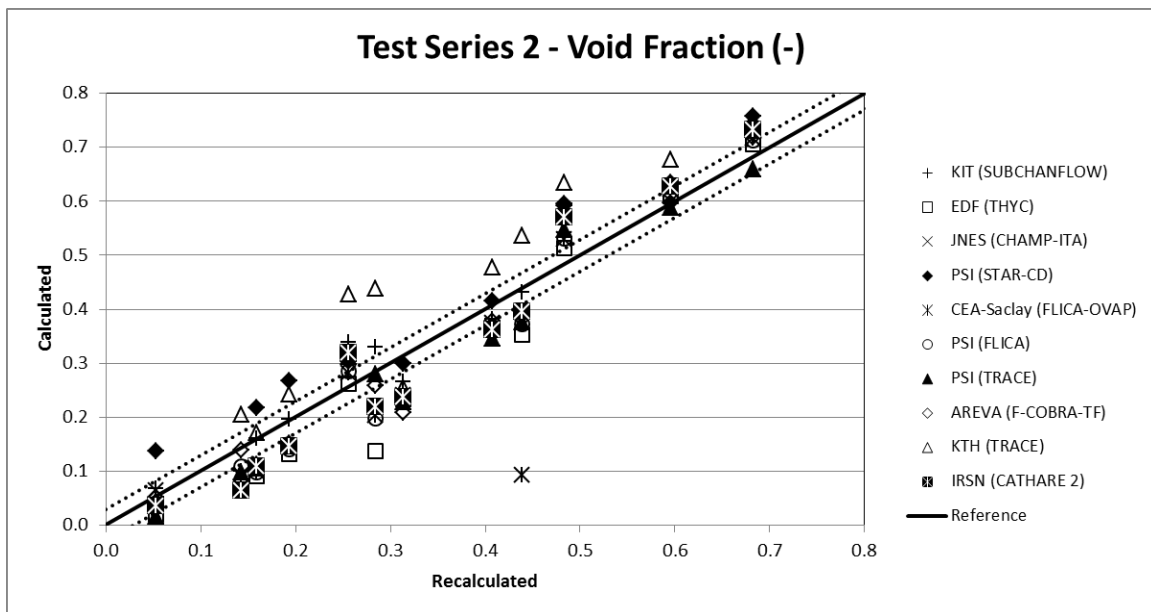


Figure AI.8 Test Series 2 Void Fraction (Calculated vs. Recalculated) Results

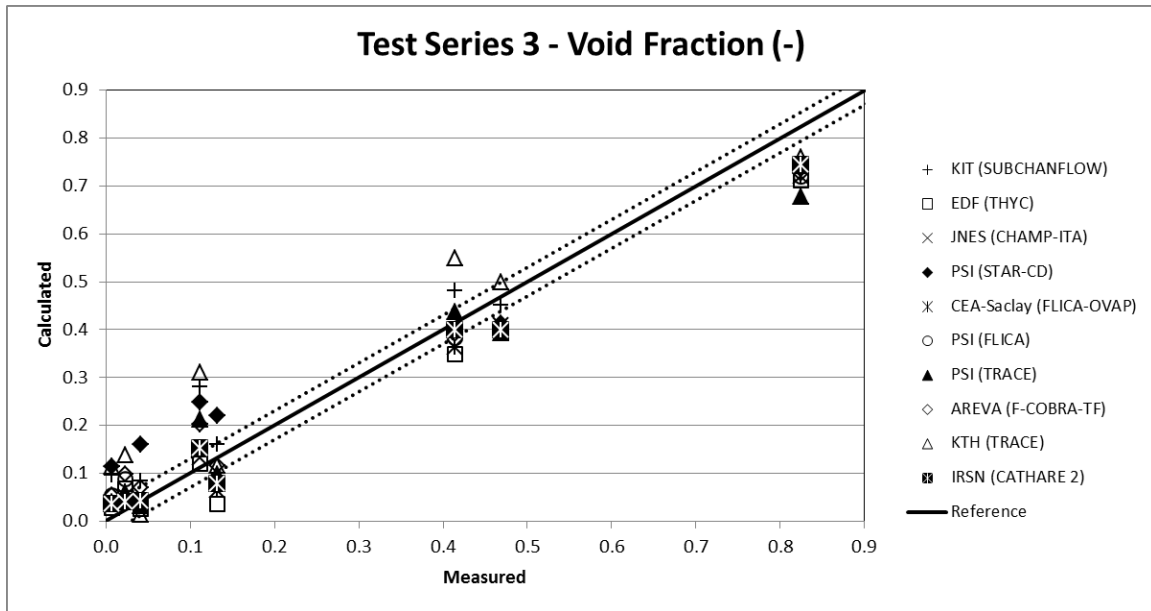


Figure AI.9 Test Series 3 Void Fraction (Calculated vs. Measured) Results

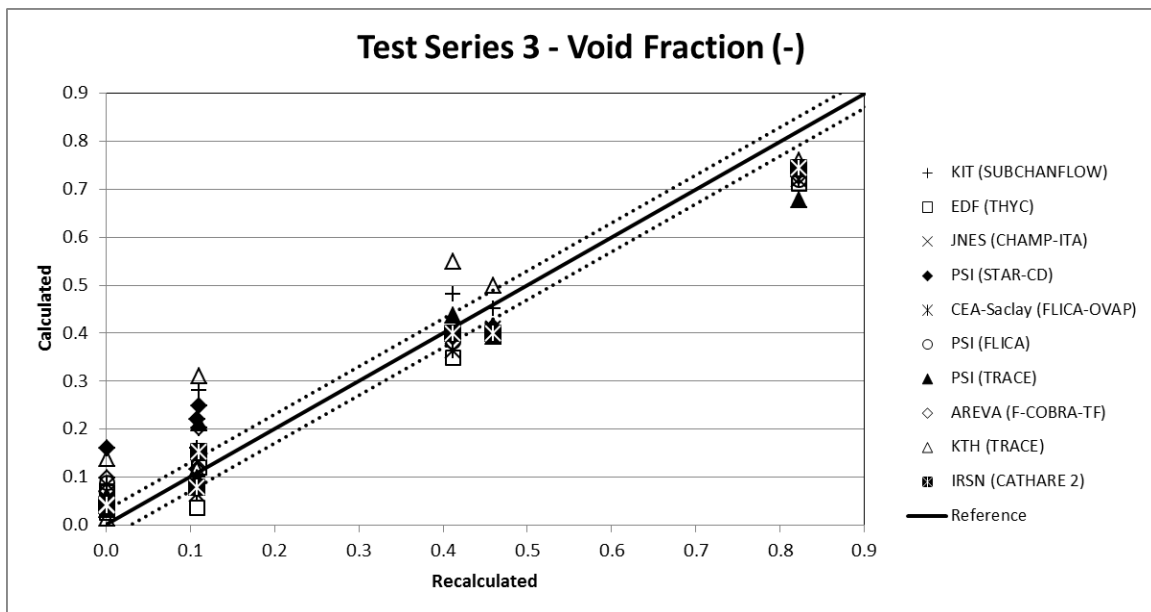


Figure AI.10 Test Series 3 Void Fraction (Calculated vs. Recalculated) Results

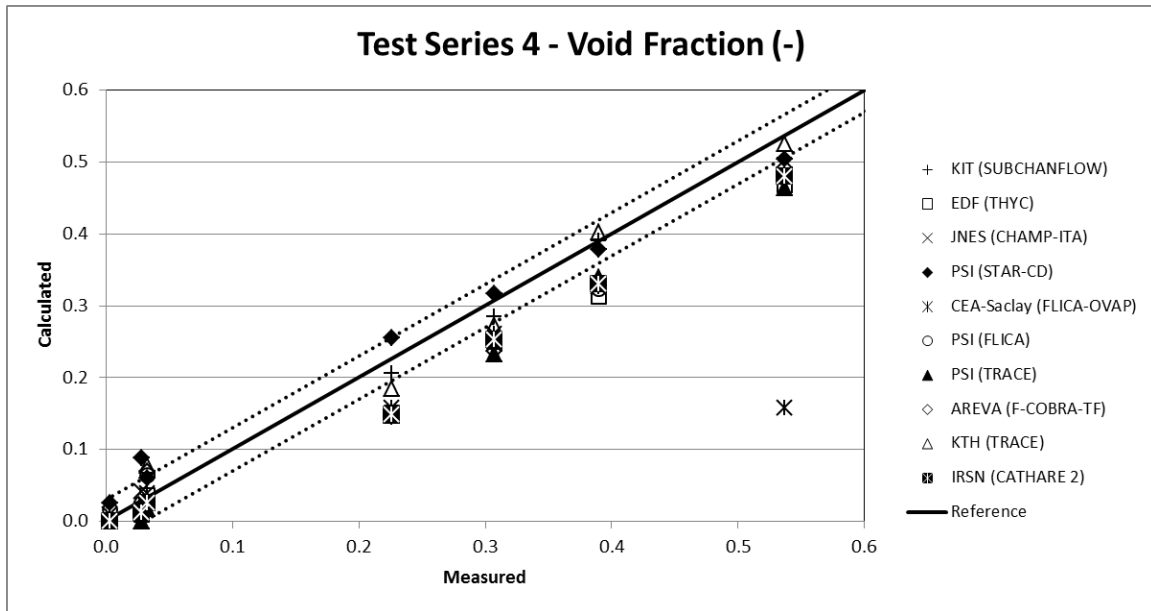


Figure AI.11 Test Series 4 Void Fraction (Calculated vs. Measured) Results

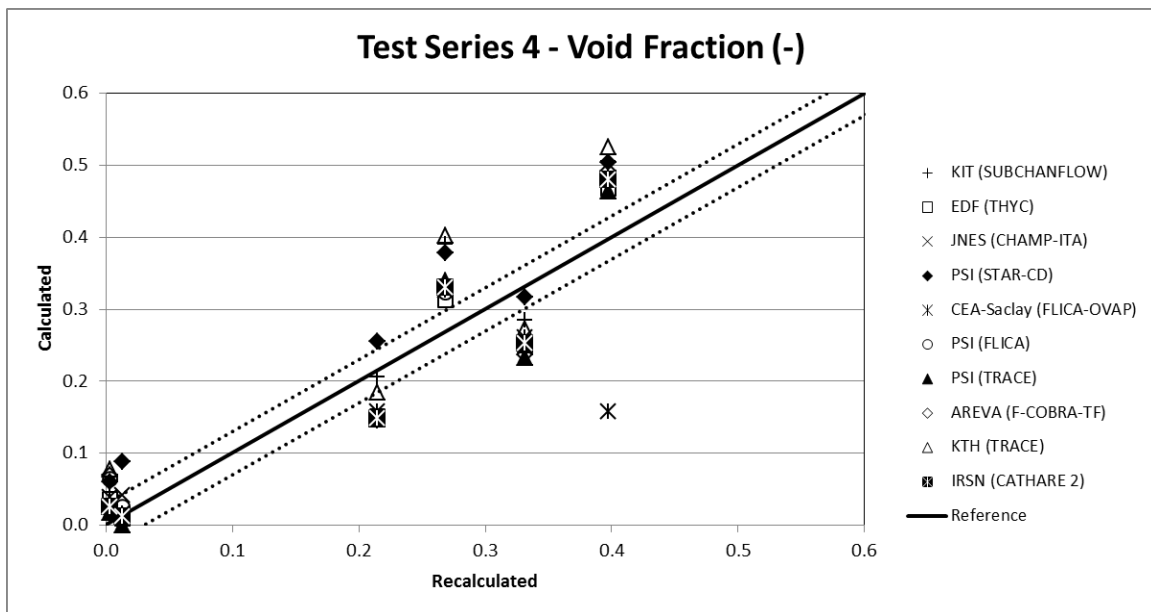


Figure AI.12 Test Series 4 Void Fraction (Calculated vs. Recalculated) Results

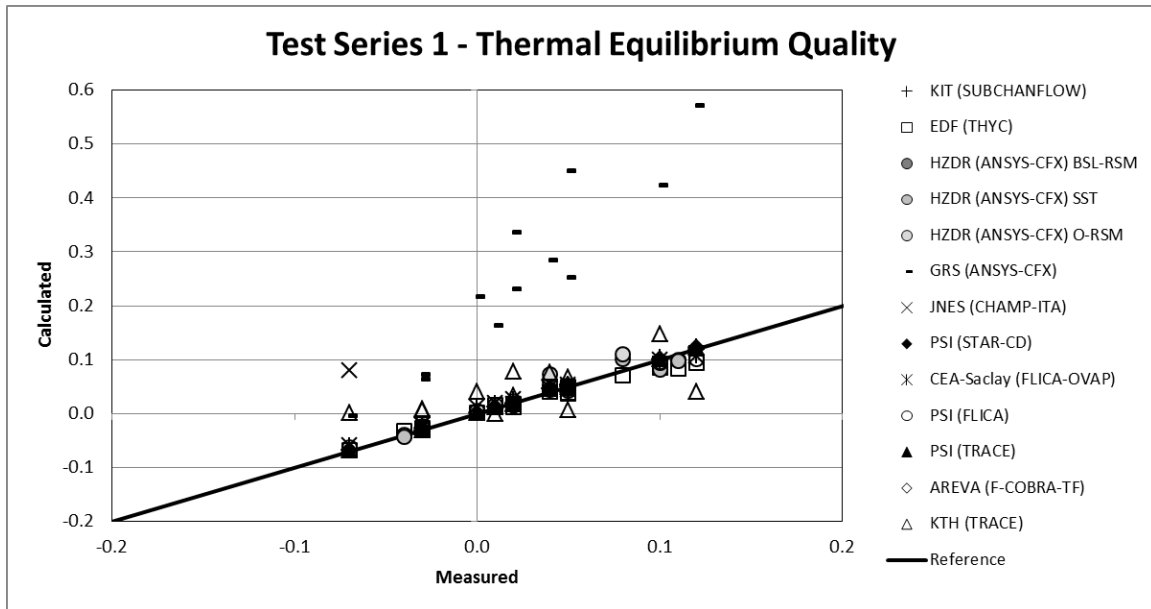


Figure AI.13 Test Series 1 Thermal Equilibrium Quality (Calculated vs. Measured) Results

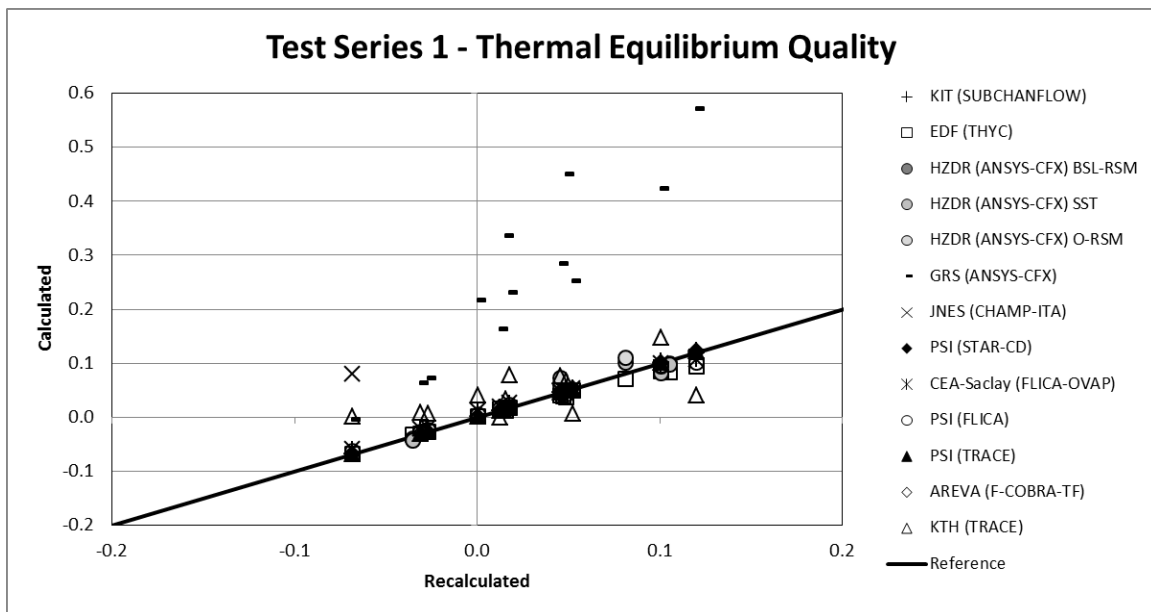


Figure AI.14 Test Series 1 Thermal Equilibrium Quality (Calculated vs. Recalculated) Results

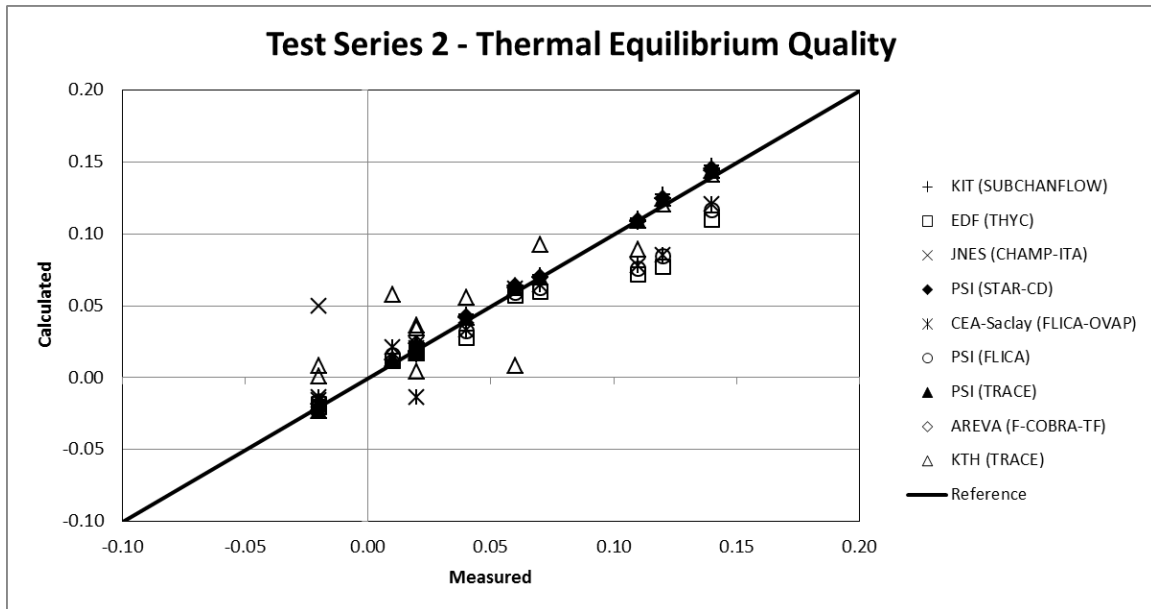


Figure AI.15 Test Series 2 Thermal Equilibrium Quality (Calculated vs. Measured) Results

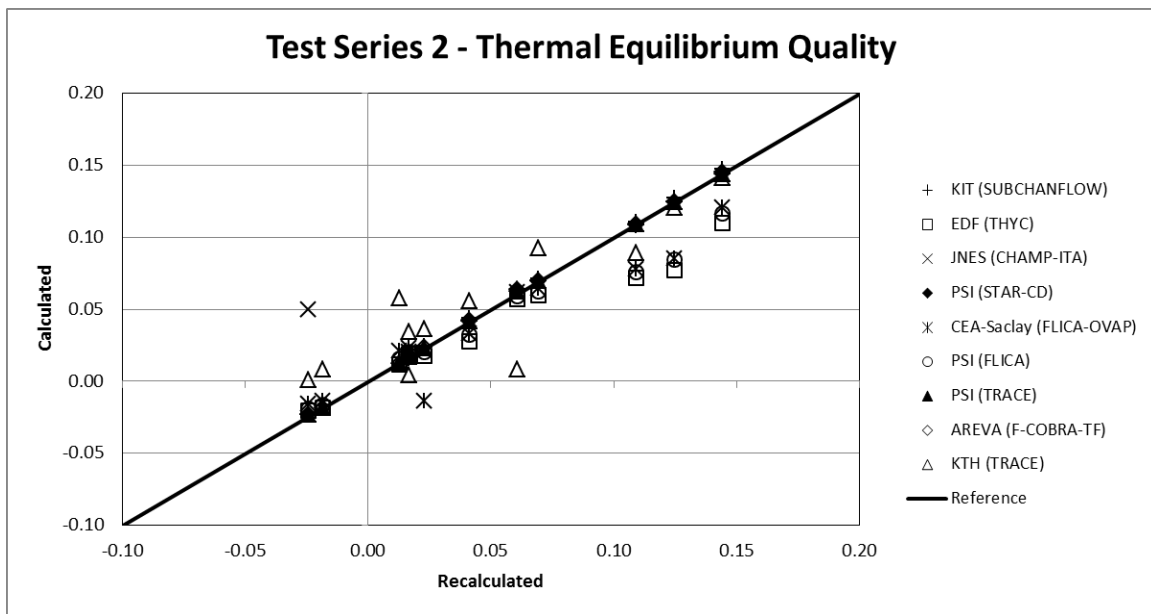


Figure AI.16 Test Series 2 Thermal Equilibrium Quality (Calculated vs. Recalculated) Results

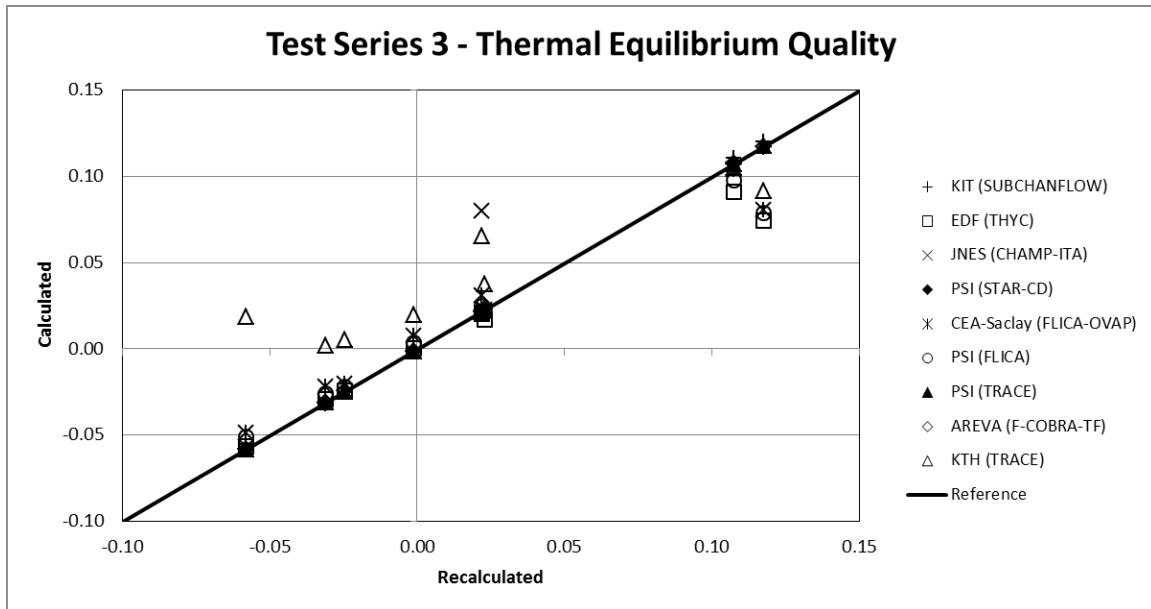


Figure AI.17 Test Series 3 Thermal Equilibrium Quality (Calculated vs. Recalculated) Results

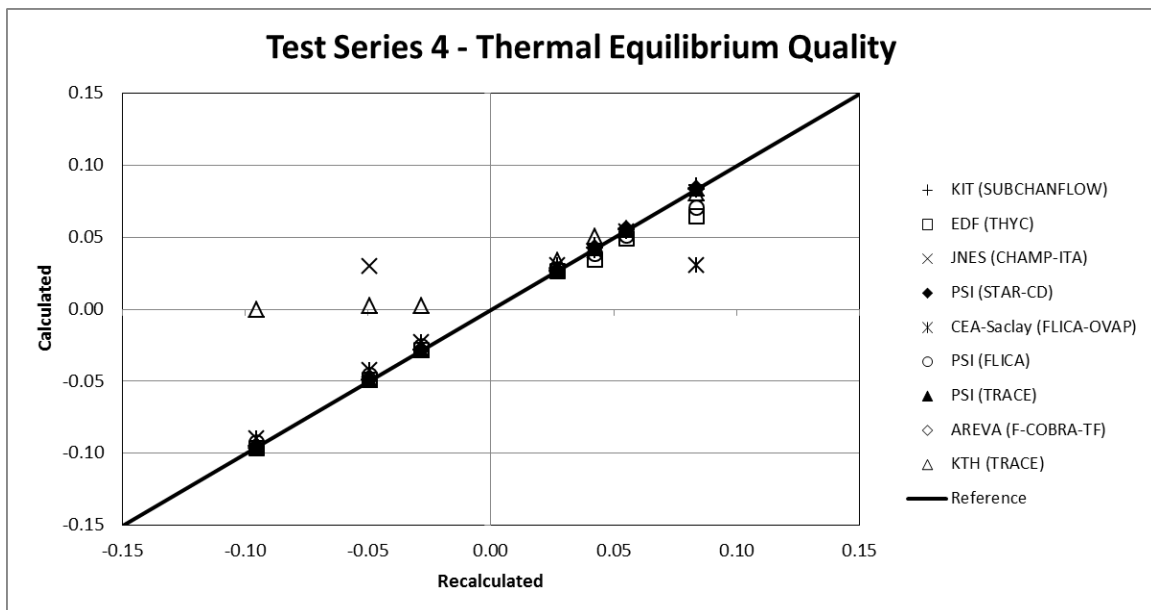


Figure AI.18 Test Series 4 Thermal Equilibrium Quality (Calculated vs. Recalculated) Results

Table AI.1 Results of Recalculation of Subchannel-Averaged Void Fraction

Subchannel Averaged Void Fraction		
Test Case	Recalculated	Measured
1.1222	0.123	0.142
1.1223	0.304	0.332
1.2211	-0.003	0.038
1.2221	-0.024	0.048
1.2223	0.296	0.311
1.2237	0.424	0.440
1.2422	0.168	0.182
1.2423	0.489	0.508
1.4311	0.201	0.215
1.4312	0.566	0.566
1.4325	0.335	0.335
1.4326	0.531	0.531
1.5221	0.021	0.047
1.5222	0.411	0.411
1.6221	0.055	0.075
1.6222	0.305	0.306
2.1231	0.052	0.096
2.1232	0.159	0.181
2.1233	0.313	0.333
2.3232	0.193	0.202
2.3233	0.408	0.409
2.4421	0.284	0.296
2.4422	0.595	0.596
2.4551	0.255	0.256
2.4552	0.484	0.483
2.6431	0.142	0.158
2.6432	0.438	0.439
2.6433	0.683	0.683
3.2231	0.002	0.041
3.2232	0.109	0.132
3.2451	-0.056	0.007
3.2452	0.111	0.111
3.2453	0.459	0.469
3.6431	0.412	0.414
3.6432	0.822	0.825
3.6461	0.002	0.023
4.2251	-0.053	0.003
4.2253	0.013	0.028
4.2256	0.215	0.226
4.2257	0.332	0.307
4.4455	0.268	0.390
4.4456	0.397	0.537
4.6461	0.003	0.033

Table AI.2 Results of Recalculation of Subchannel-Averaged Thermal Equilibrium Quality

Subchannel Averaged Thermal Equilibrium Quality		
Test Case	Recalculated	Measured
1.1222	0.012	0.010
1.1223	0.053	0.050
1.2211	-0.035	-0.040
1.2221	-0.068	-0.070
1.2223	0.046	0.040
1.2237	0.081	0.080
1.2422	0.018	0.020
1.2423	0.101	0.100
1.4311	0.000	0.000
1.4312	0.120	0.120
1.4325	0.047	0.050
1.4326	0.105	0.110
1.5221	-0.031	-0.030
1.5222	0.049	0.050
1.6221	-0.027	-0.030
1.6222	0.016	0.020
2.1231	-0.024	-0.020
2.1232	0.017	0.020
2.1233	0.061	0.060
2.3232	0.017	0.020
2.3233	0.069	0.070
2.4421	0.013	0.010
2.4422	0.144	0.140
2.4551	0.041	0.040
2.4552	0.125	0.120
2.6431	-0.019	-0.020
2.6432	0.023	0.020
2.6433	0.109	0.110
3.2231	-0.031	
3.2232	-0.001	
3.2451	-0.058	
3.2452	0.022	
3.2453	0.107	
3.6431	0.023	
3.6432	0.118	
3.6461	-0.025	
4.2251	-0.095	
4.2253	-0.049	
4.2256	0.027	
4.2257	0.055	
4.4455	0.043	
4.4456	0.084	
4.6461	-0.028	

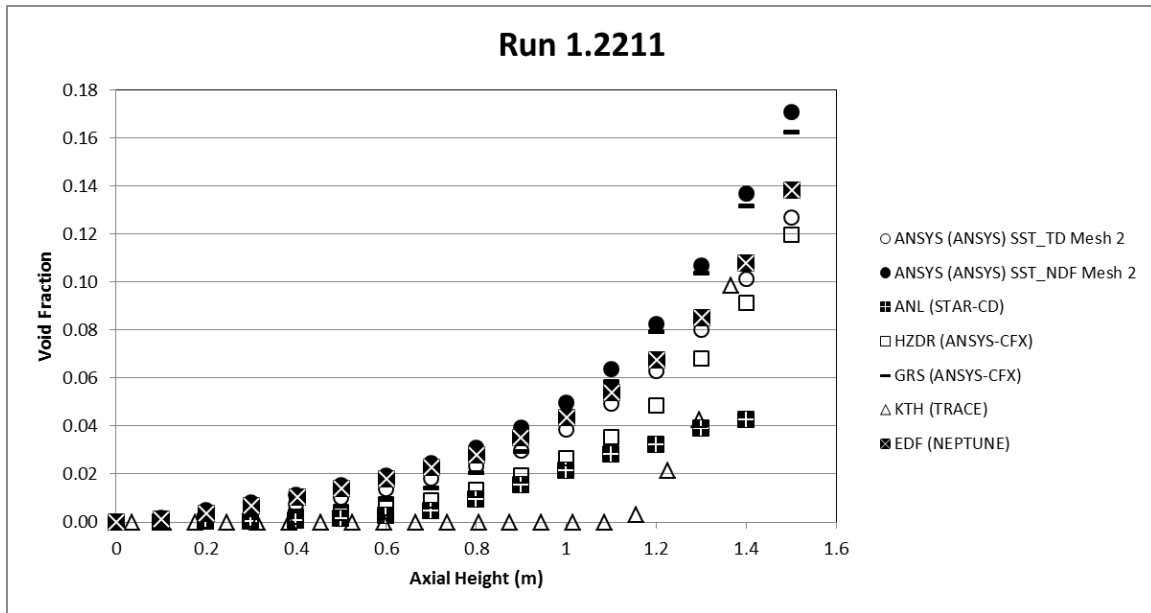


Figure AI.19 CFD Code Results of Run 1.2211

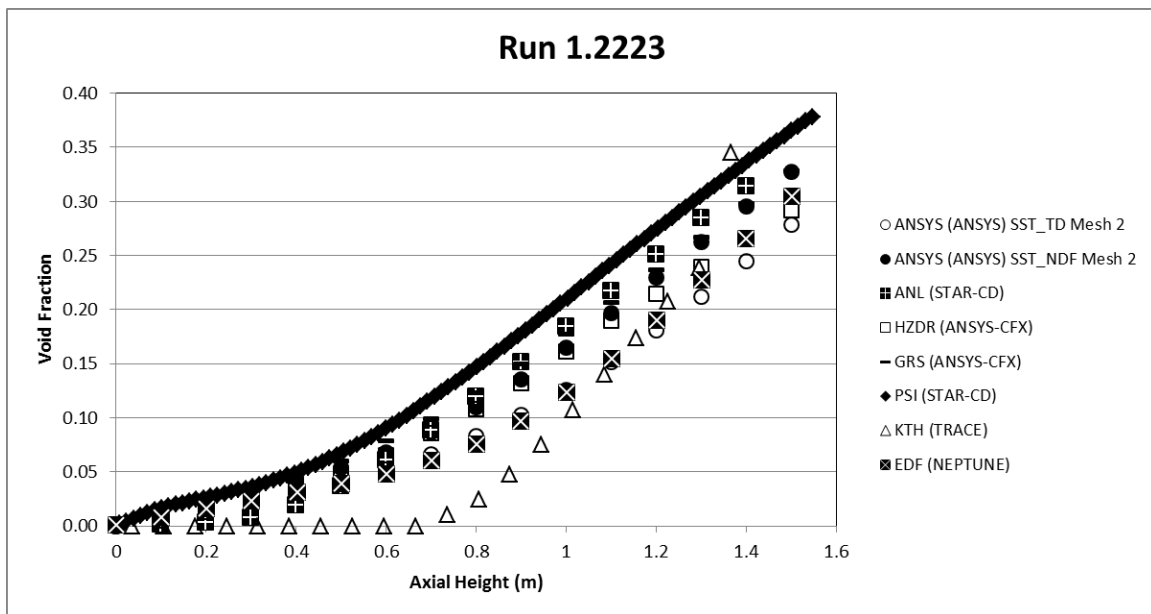


Figure AI.20 CFD Code Results of Run 1.2223

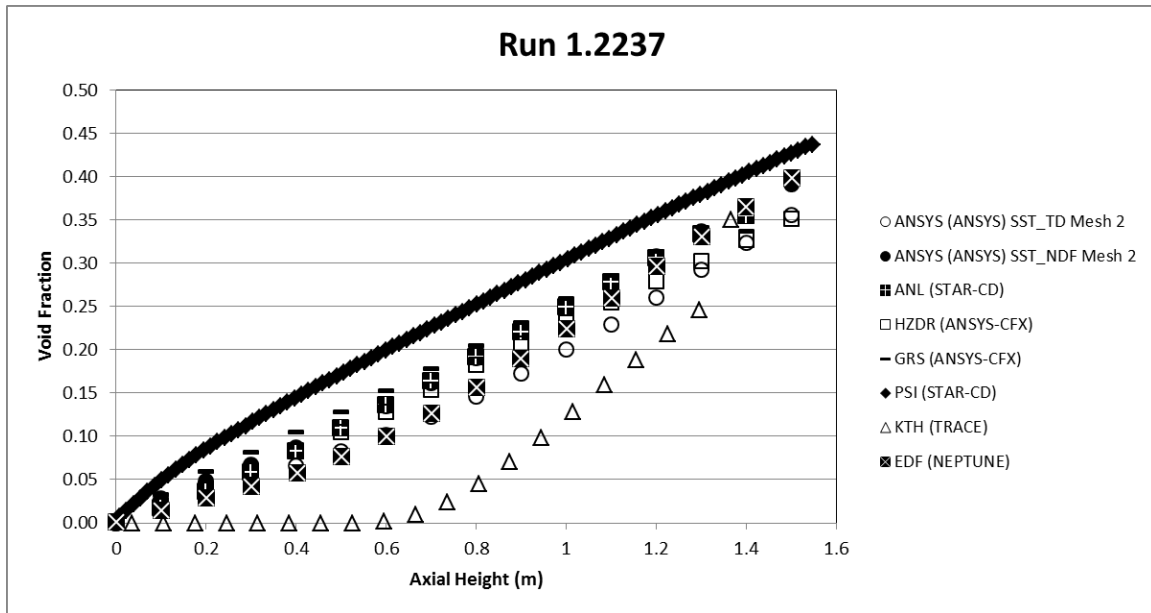


Figure AI.21 CFD Code Results of Run 1.2237

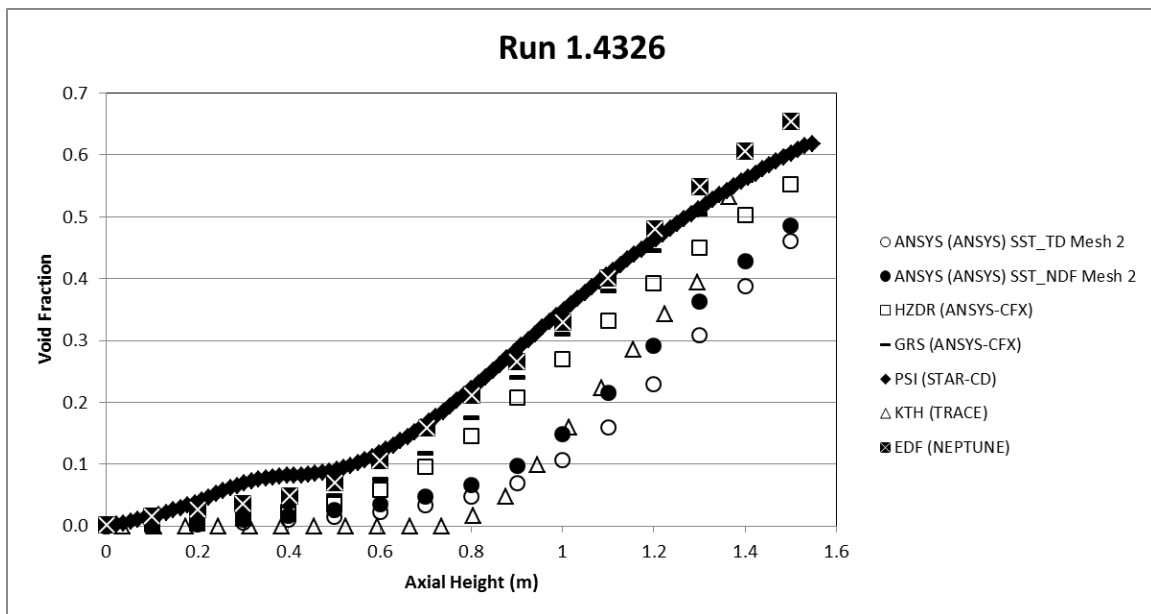
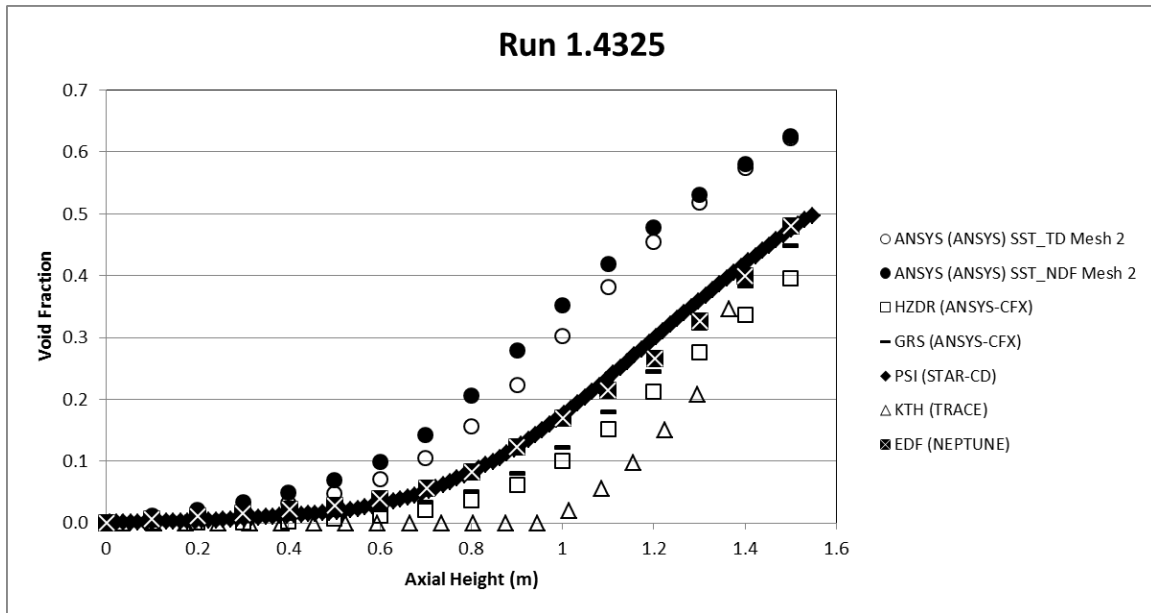


Figure AI.22 CFD Code Results of Run 1.4326



Appendix II Exercise I-2 Results

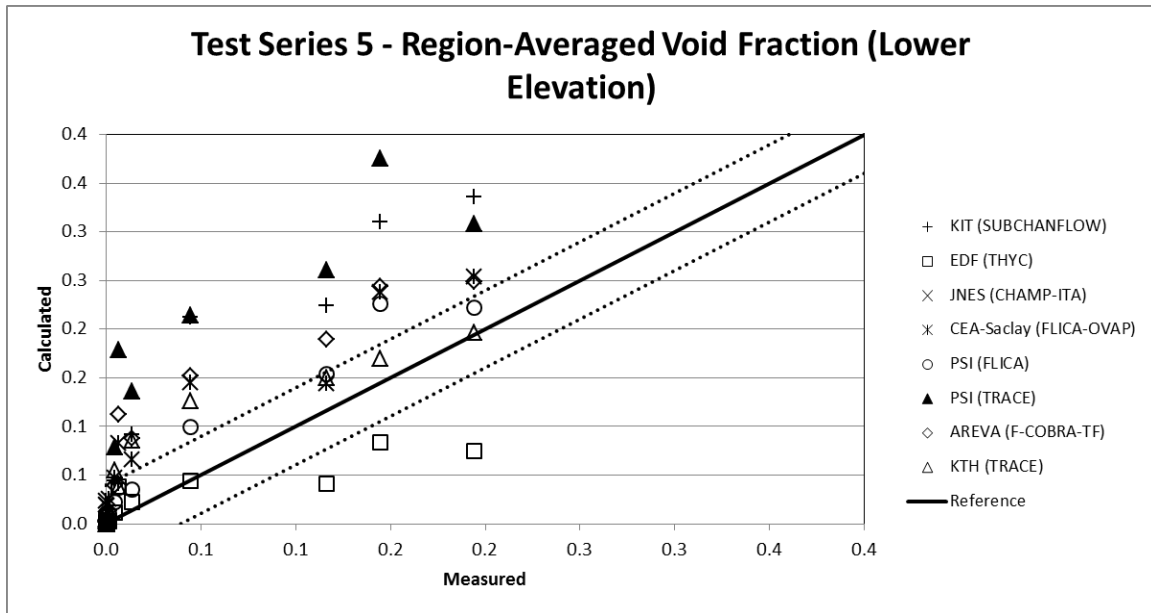


Figure AII.1 Test Series 5 Region-Averaged Void Fraction Results – Lower Elevation

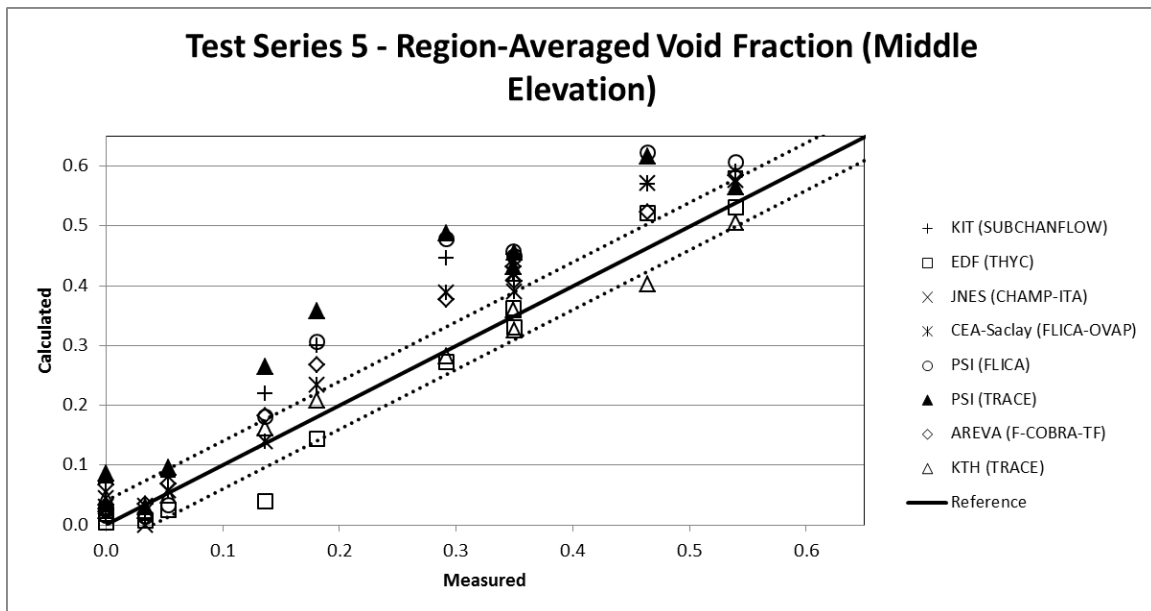


Figure AII.2 Test Series 5 Region-Averaged Void Fraction Results – Middle Elevation

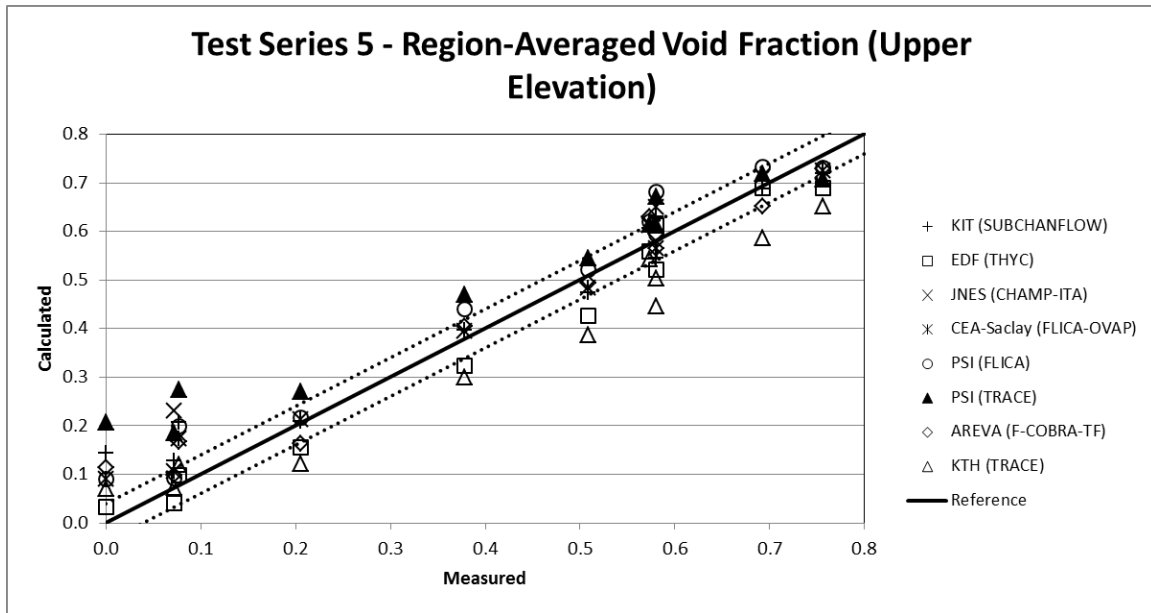


Figure AII.3 Test Series 5 Region-Averaged Void Fraction Results – Upper Elevation

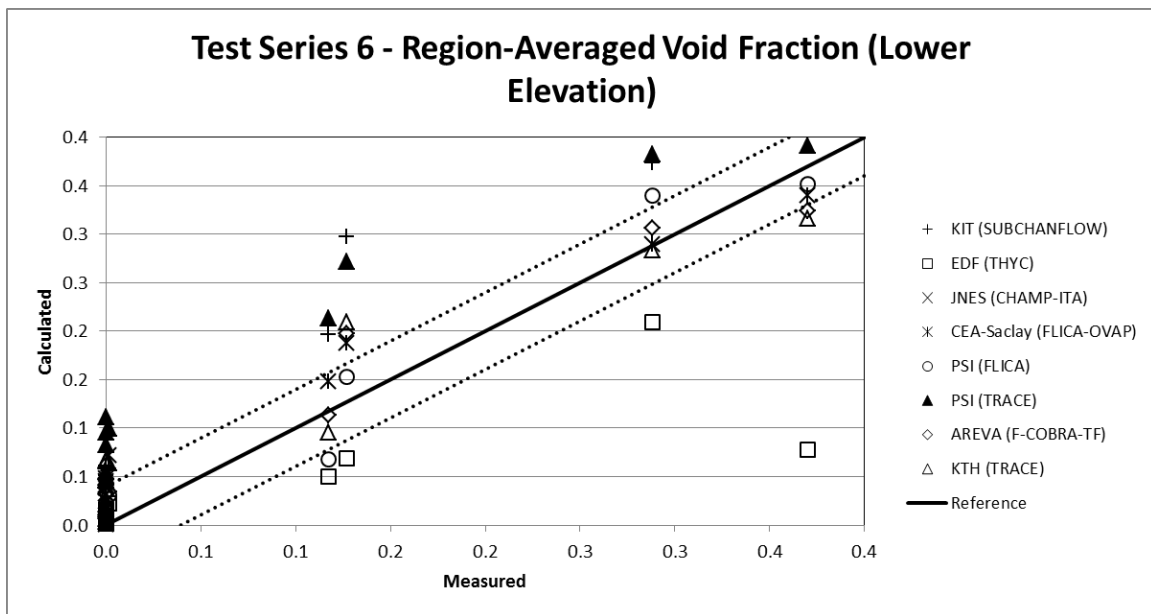


Figure AII.4 Test Series 6 Region-Averaged Void Fraction Results – Lower Elevation

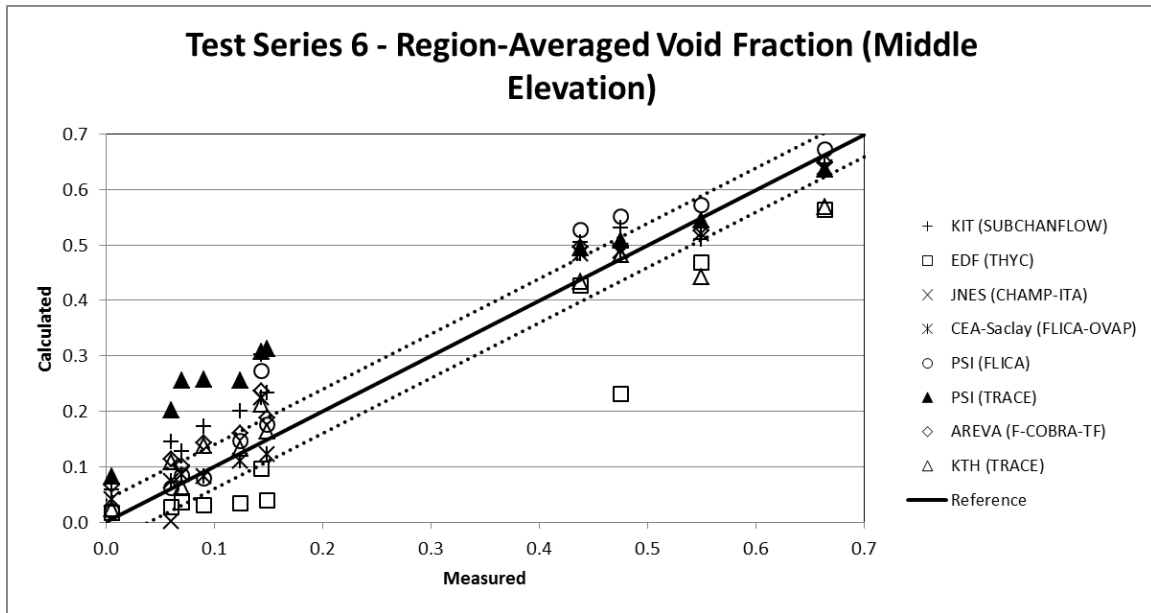


Figure AII.5 Test Series 6 Region-Averaged Void Fraction Results – Middle Elevation

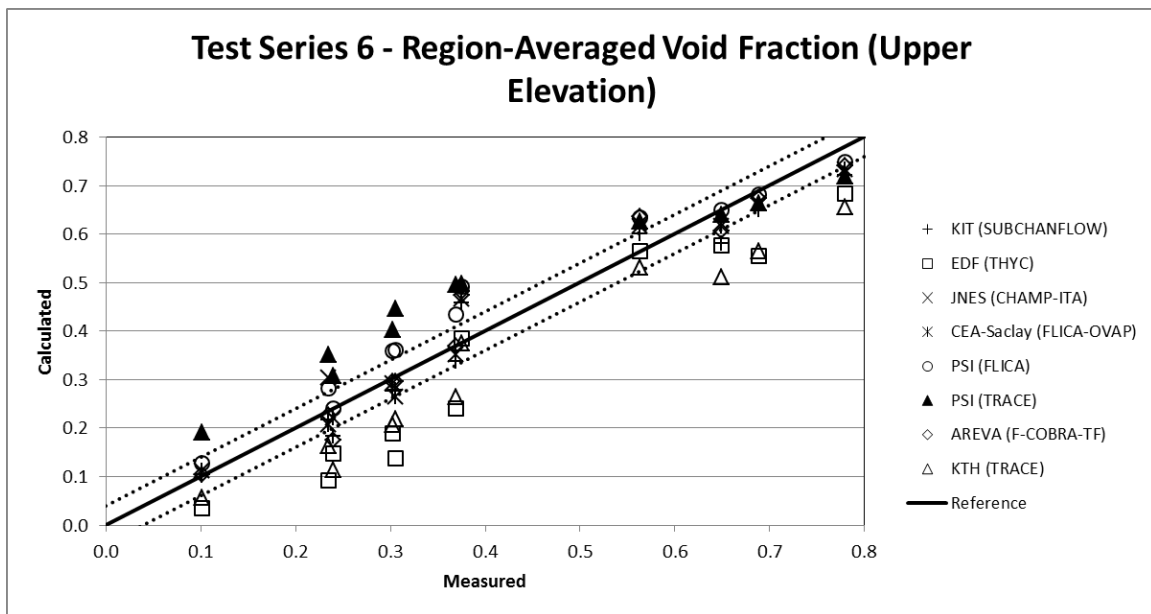


Figure AII.6 Test Series 6 Region-Averaged Void Fraction Results – Upper Elevation

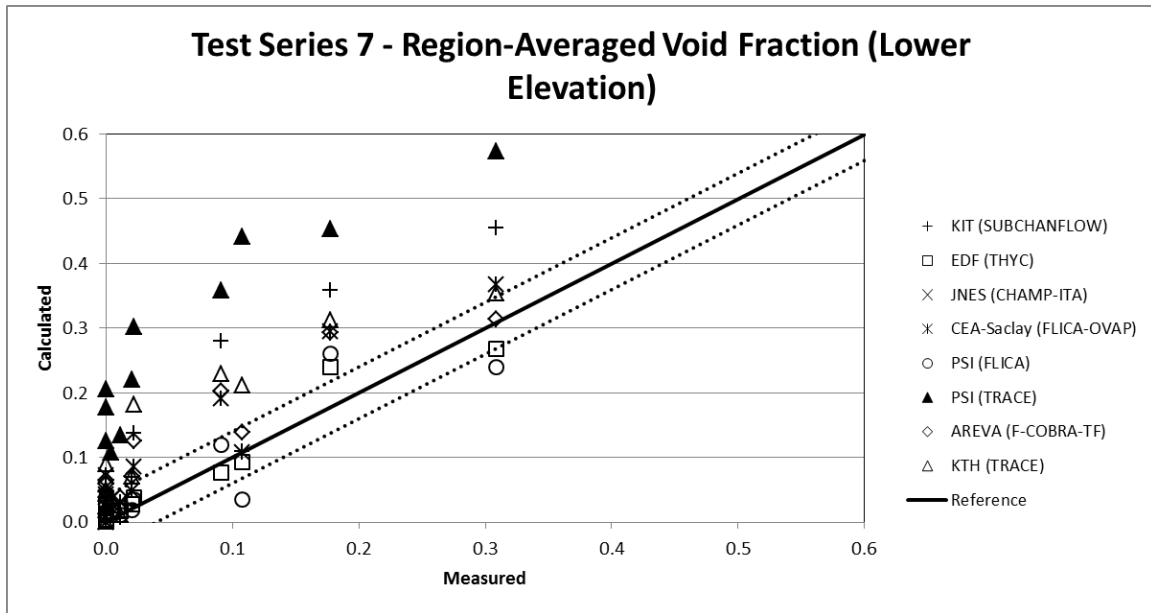


Figure AII.7 Test Series 7 Region-Averaged Void Fraction Results – Lower Elevation

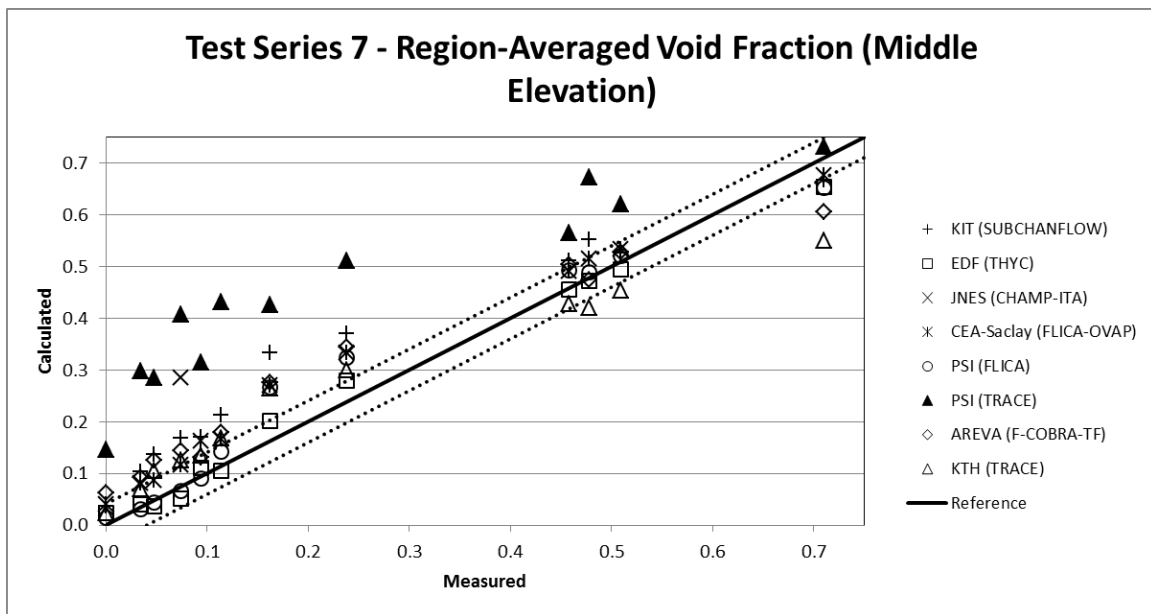


Figure AII.8 Test Series 7 Region-Averaged Void Fraction Results – Middle Elevation

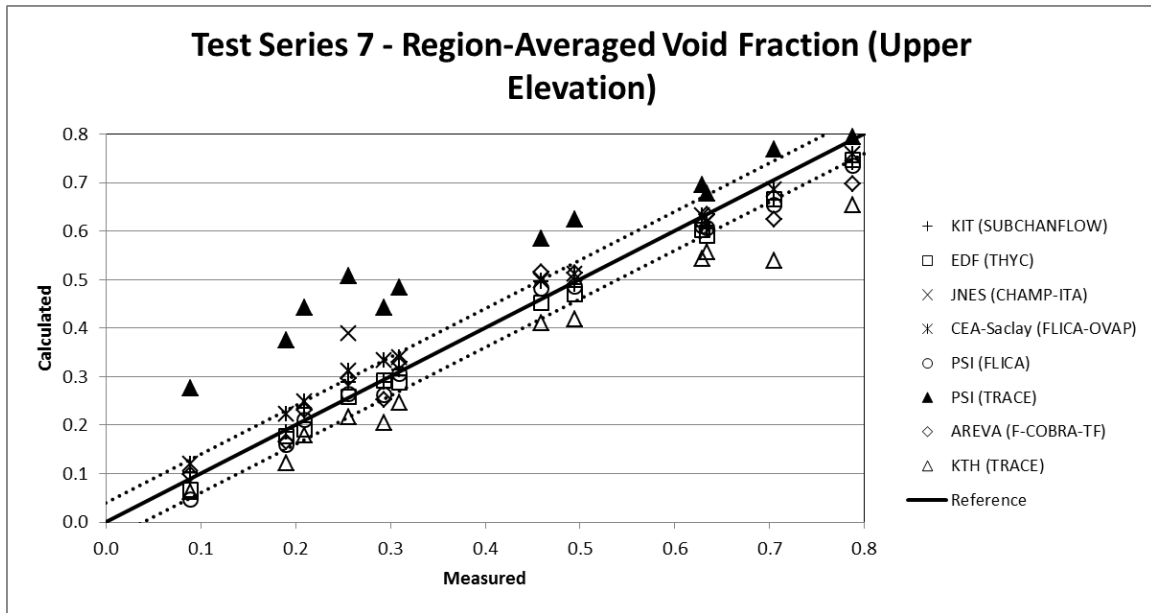


Figure AII.9 Test Series 7 Region-Averaged Void Fraction Results – Upper Elevation

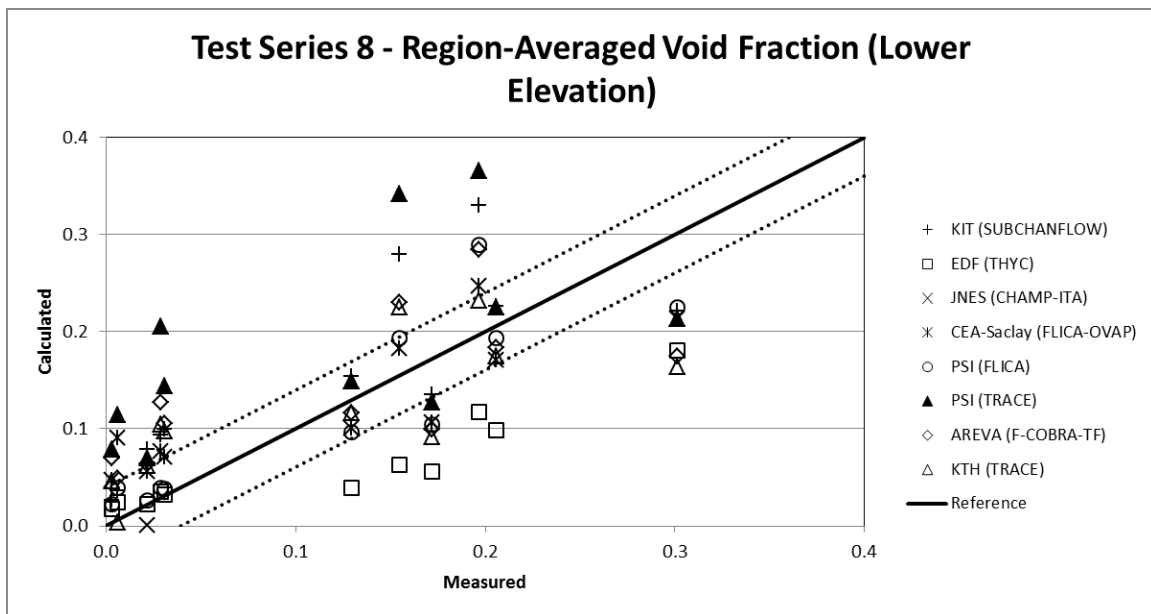


Figure AII.10 Test Series 8 Region-Averaged Void Fraction Results – Lower Elevation

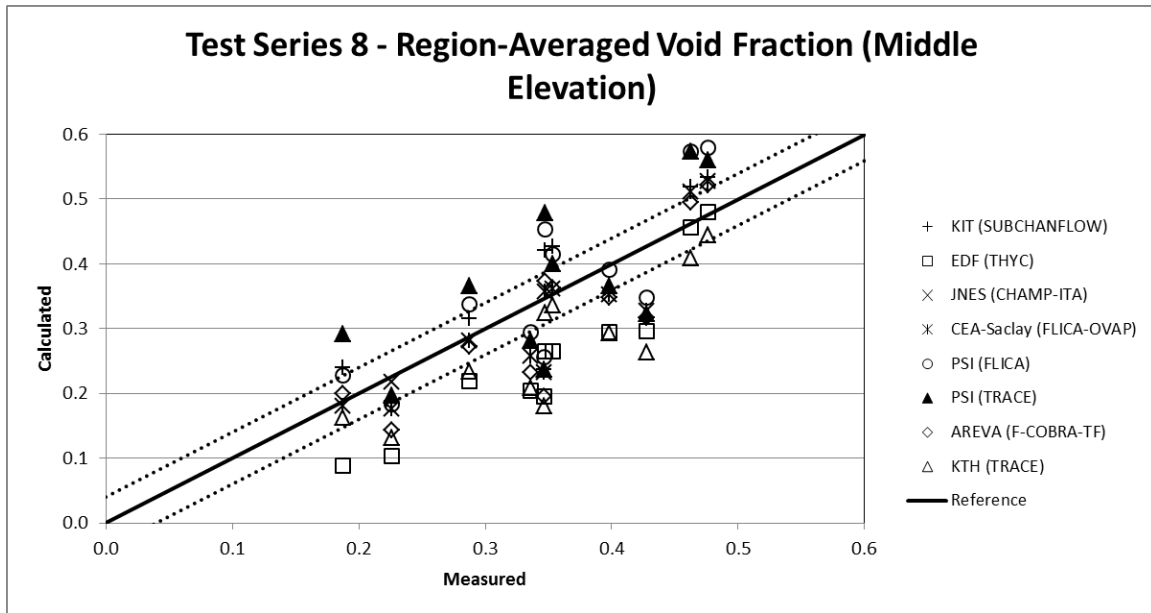


Figure AII.11 Test Series 8 Region-Averaged Void Fraction Results – Middle Elevation

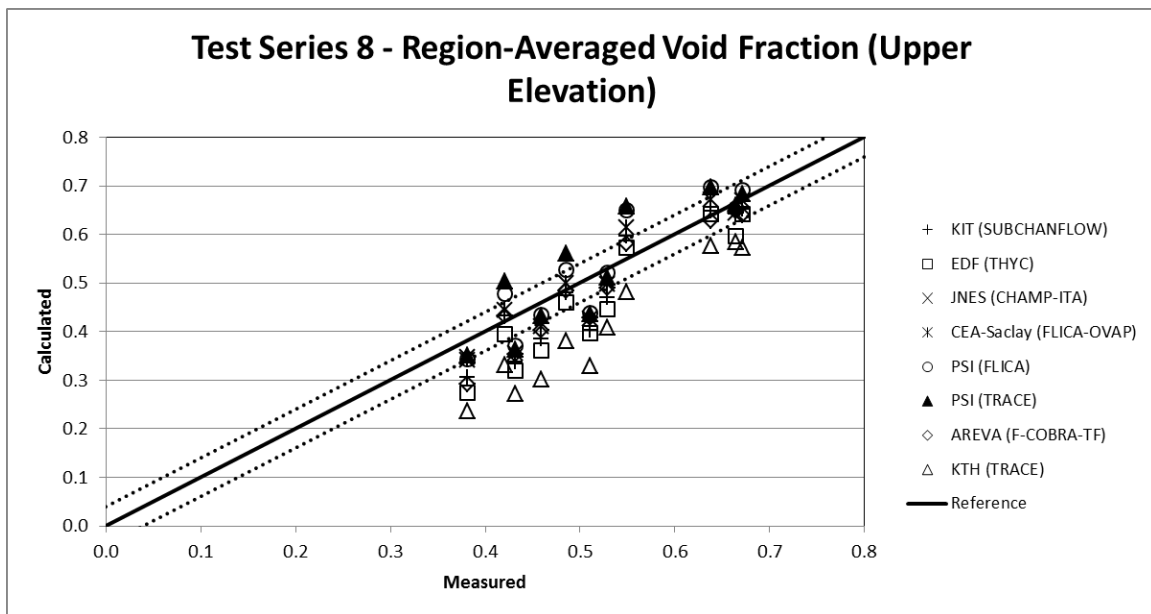


Figure AII.12 Test Series 8 Region-Averaged Void Fraction Results – Upper Elevation

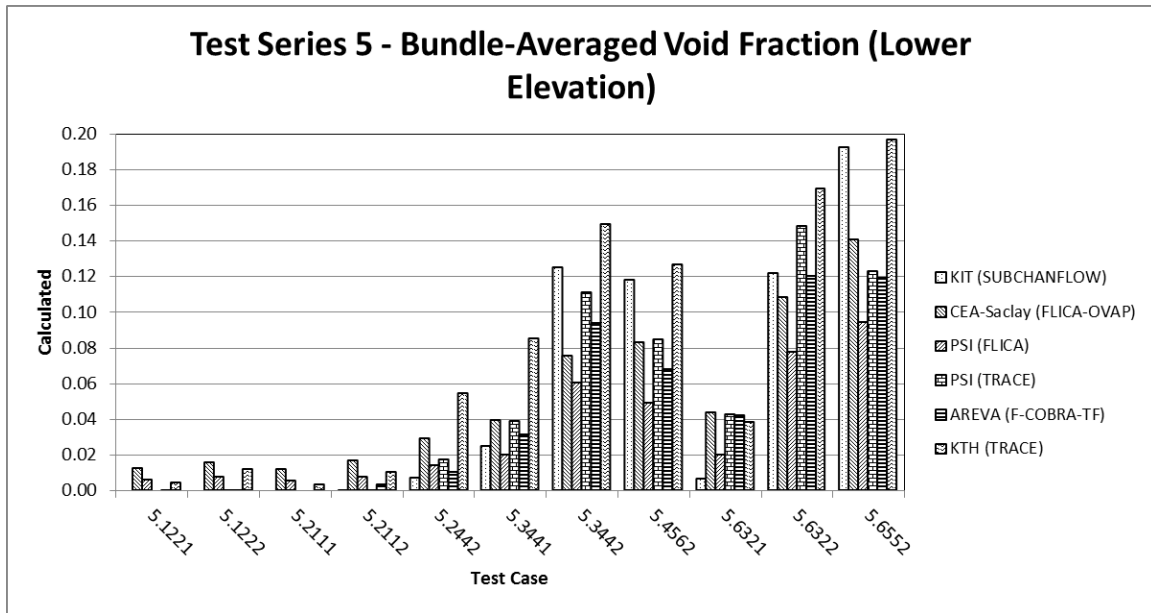


Figure AII.13 Test Series 5 Bundle-Averaged Void Fraction Results – Lower Elevation

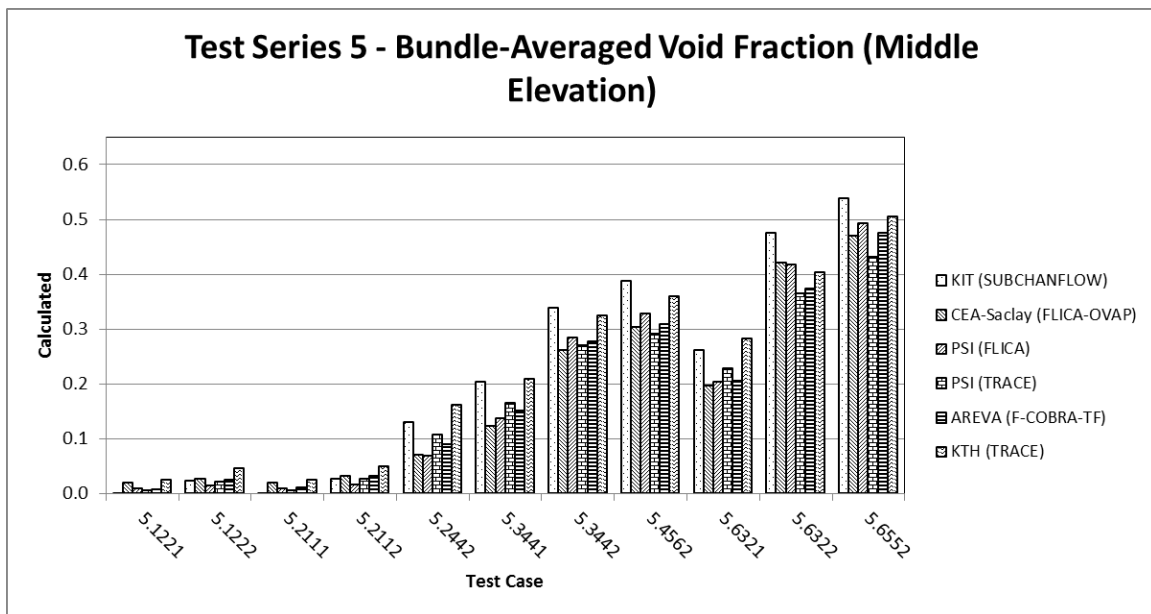


Figure AII.14 Test Series 5 Bundle-Averaged Void Fraction Results – Middle Elevation

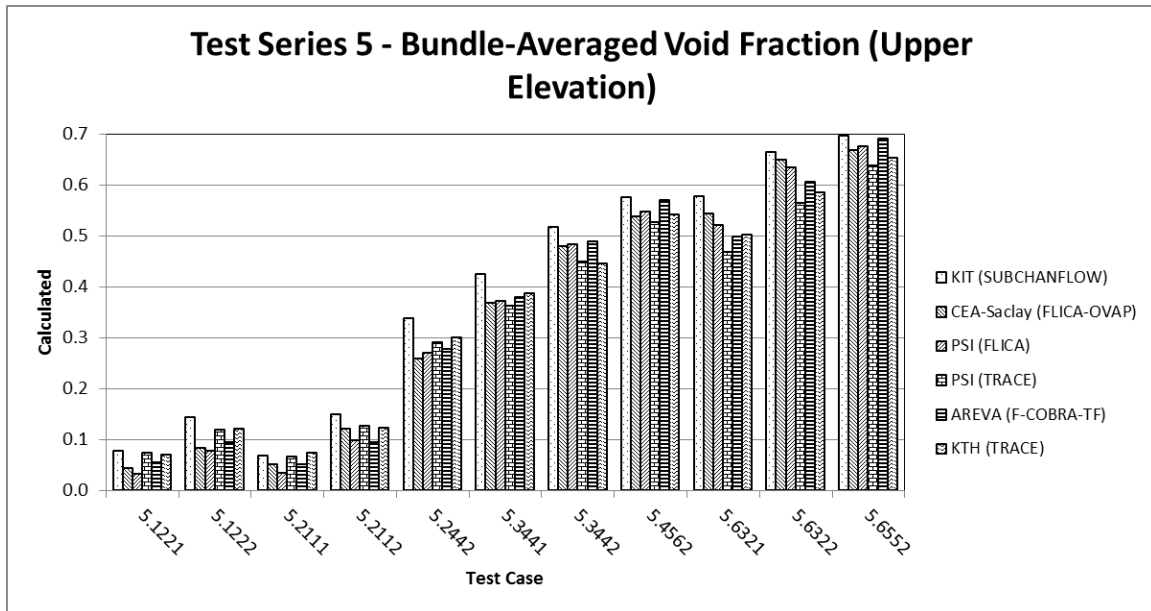


Figure AII.15 Test Series 5 Bundle-Averaged Void Fraction – Upper Elevation

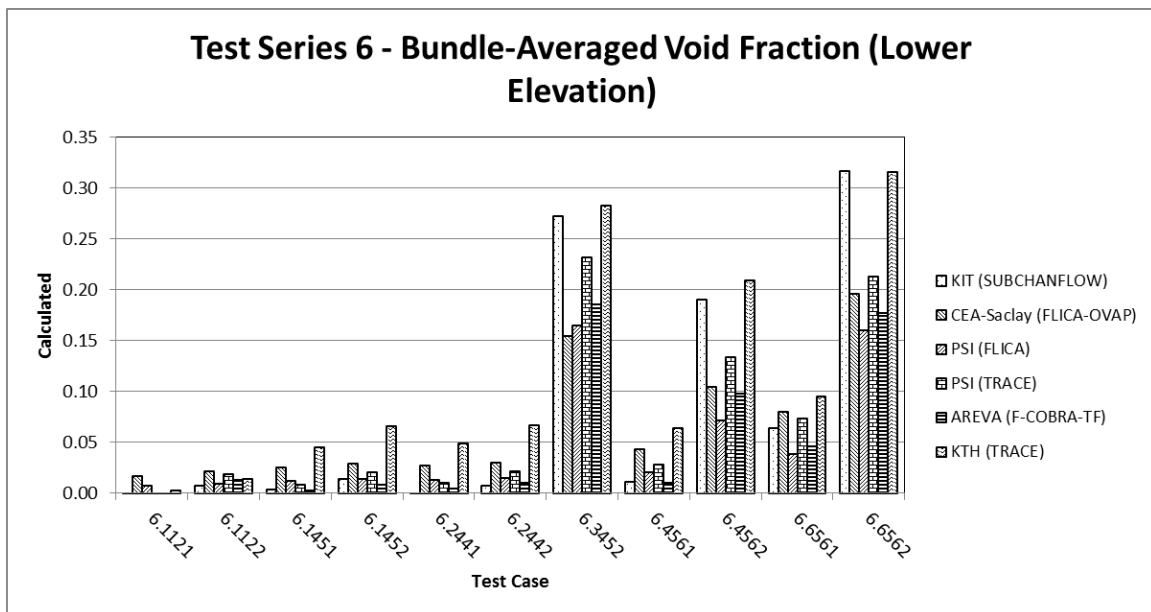


Figure AII.16 Test Series 6 Bundle-Averaged Void Fraction – Lower Elevation

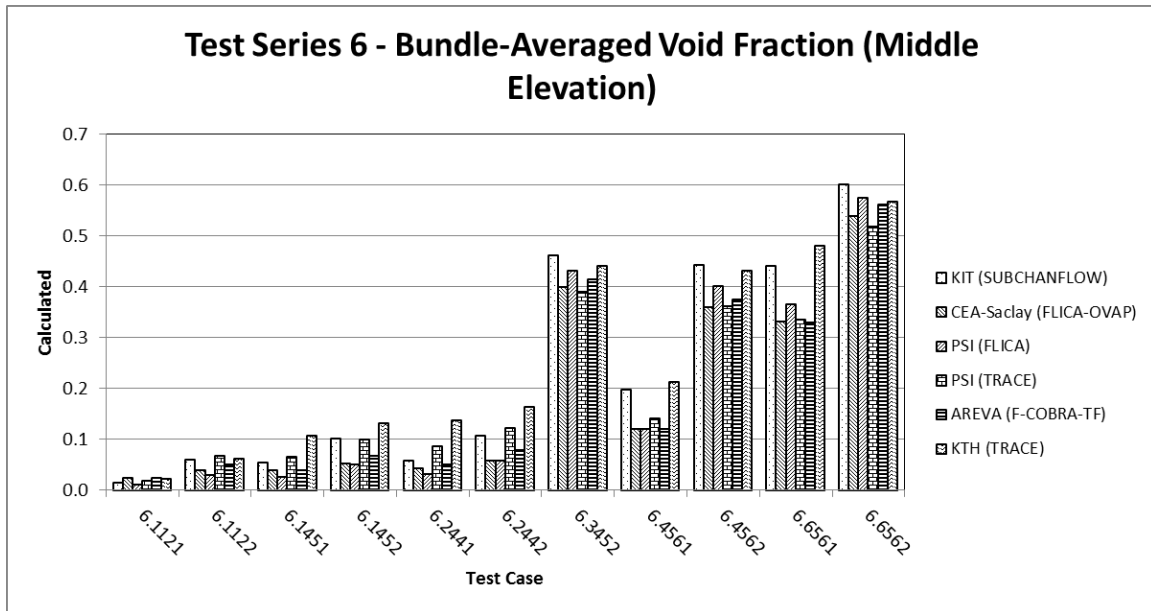


Figure AII.17 Test Series 6 Bundle-Averaged Void Fraction – Middle Elevation

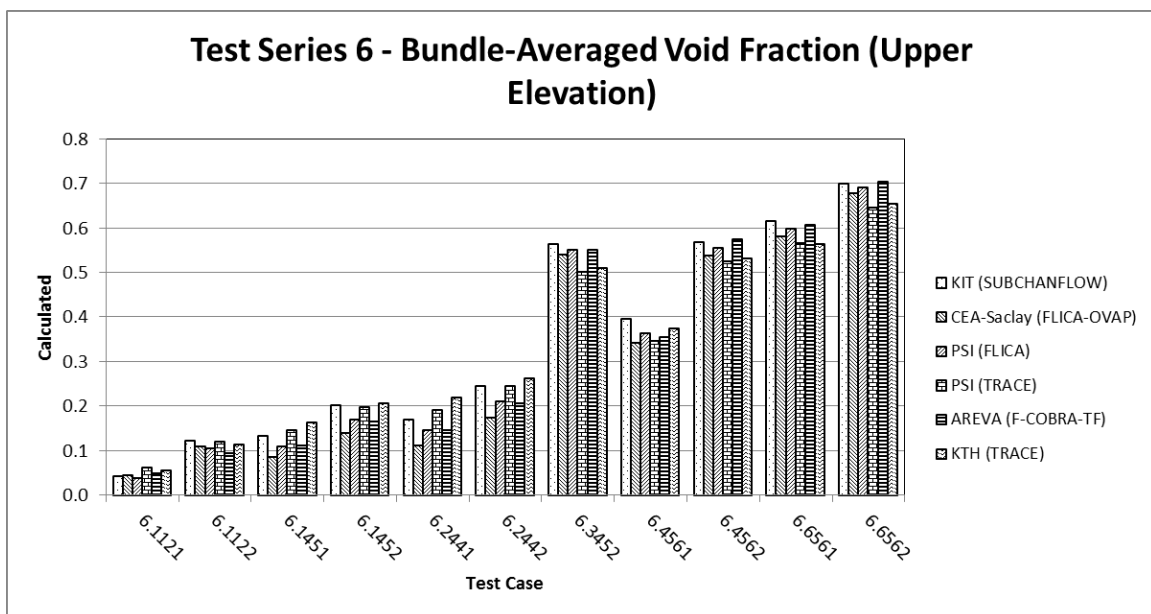


Figure AII.18 Test Series 6 Bundle-Averaged Void Fraction (Upper Elevation)

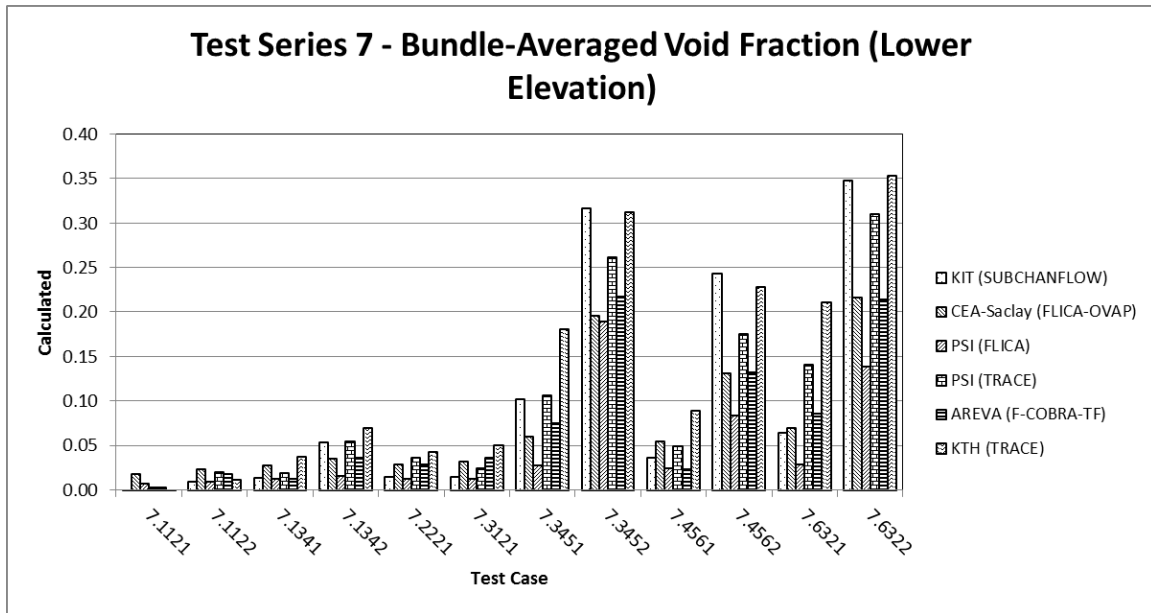


Figure AII.19 Test Series 7 Bundle-Averaged Void Fraction Results – Lower Elevation

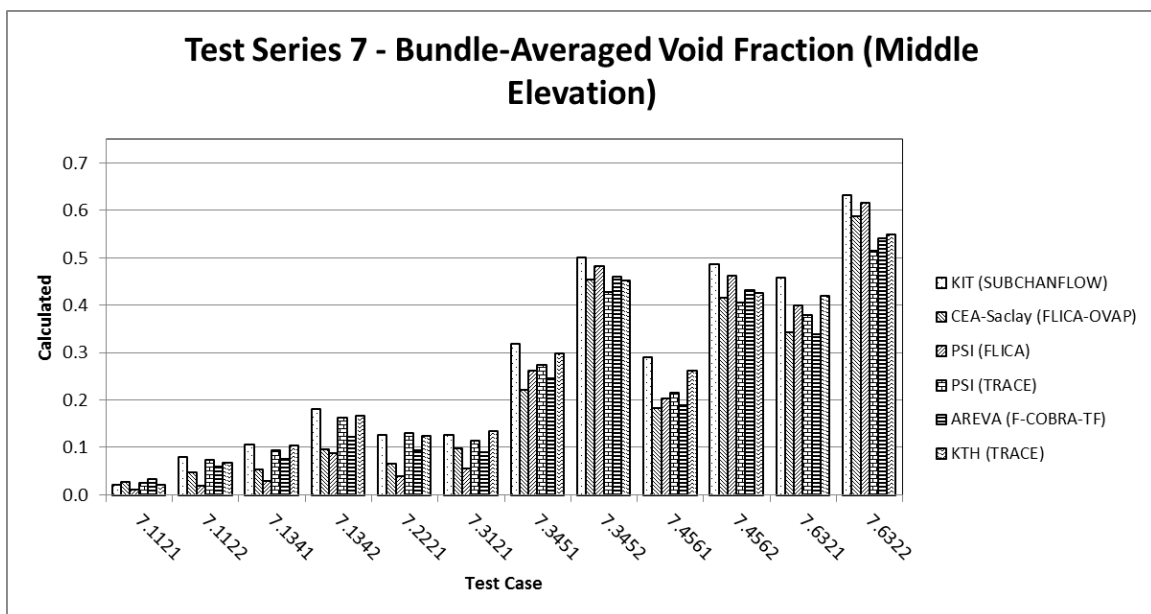


Figure AII.20 Test Series 7 Bundle-Averaged Void Fraction Results – Middle Elevation

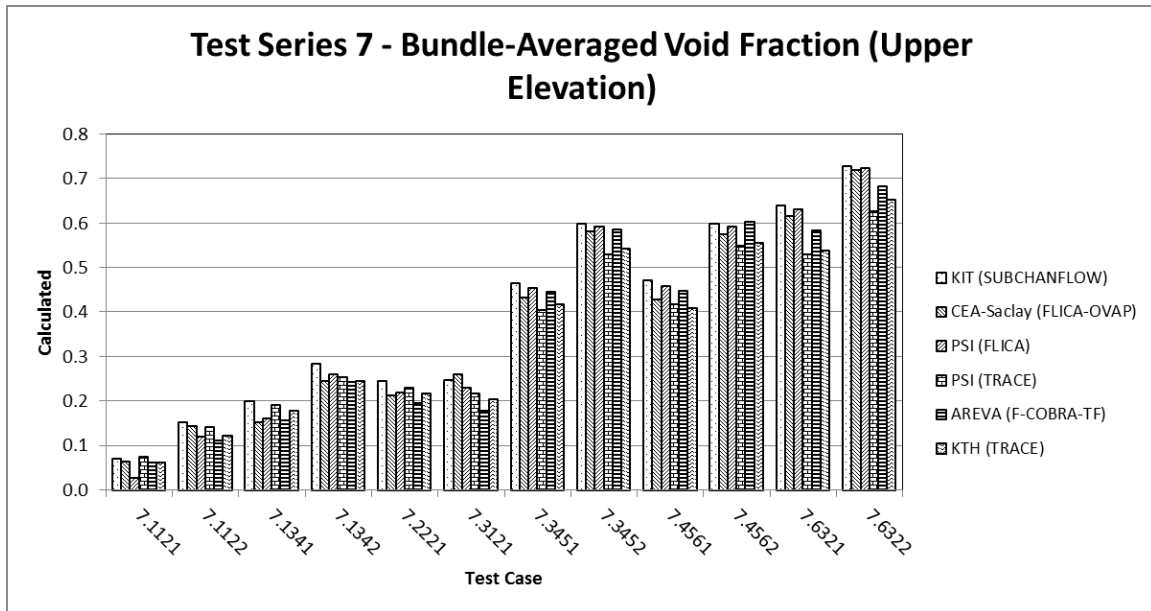


Figure AII.21 Test Series 7 Bundle-Averaged Void Fraction – Upper Elevation

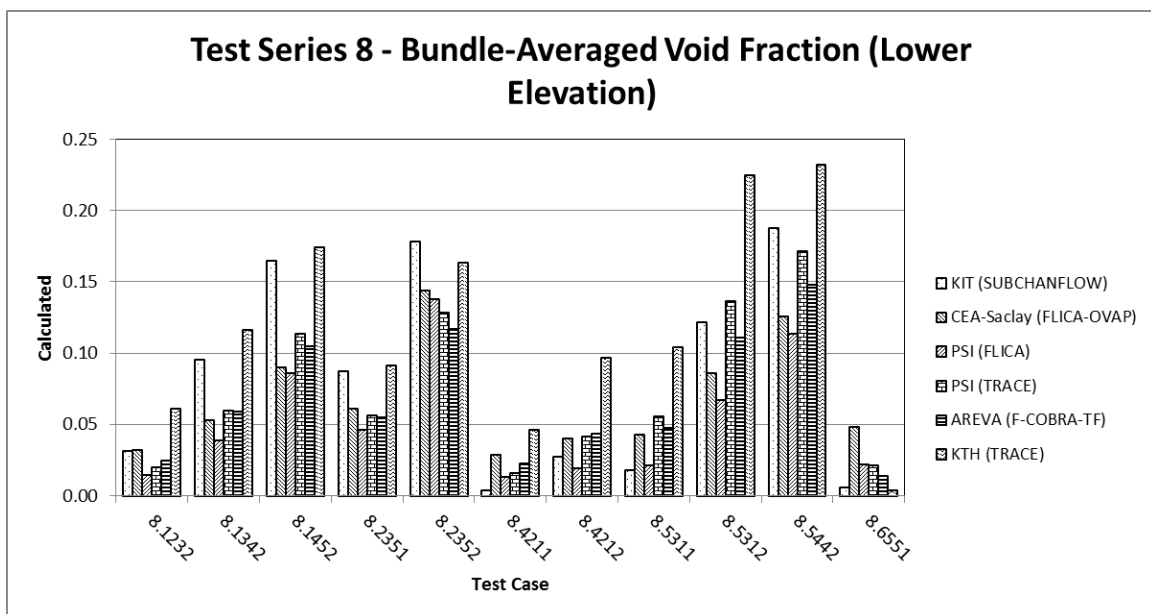


Figure AII.22 Test Series 8 Bundle-Averaged Void Fraction – Lower Elevation

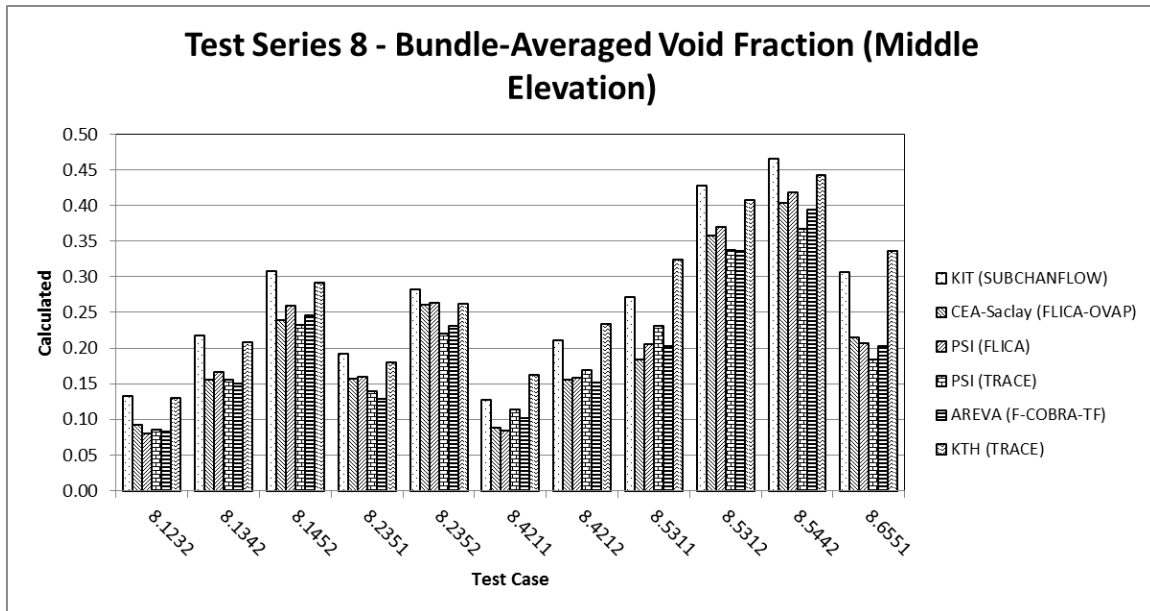


Figure AII.23 Test Series 8 Bundle-Averaged Void Fraction – Middle Elevation

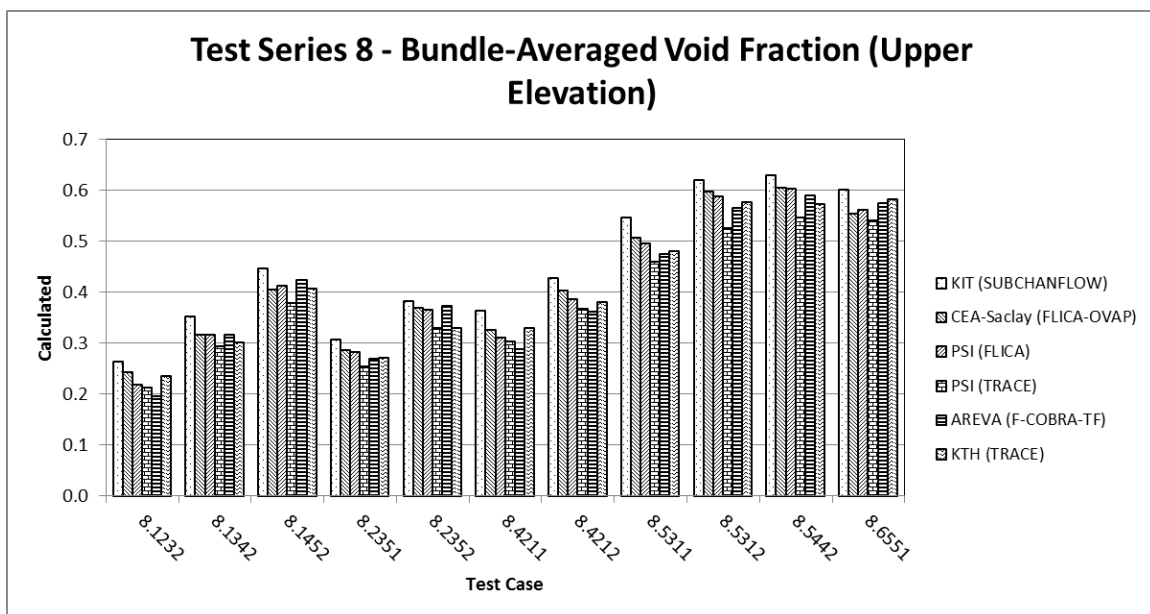


Figure AII.24 Test Series 8 Bundle-Averaged Void Fraction – Upper Elevation

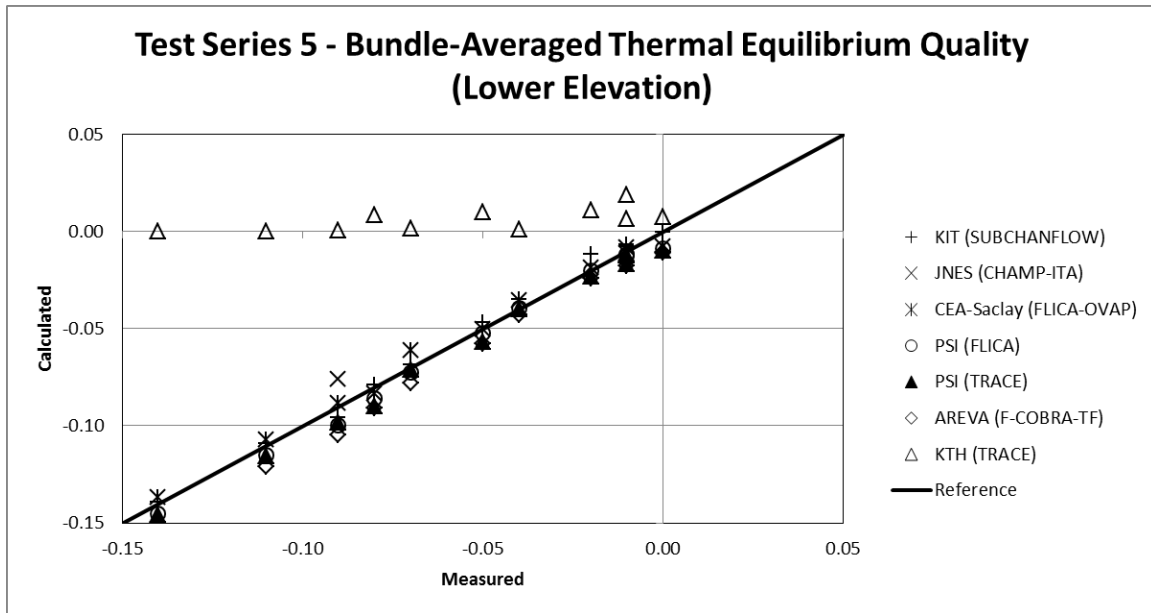


Figure AII.25 Test Series 5 Bundle-Averaged Thermal Equilibrium Quality – Lower Elevation

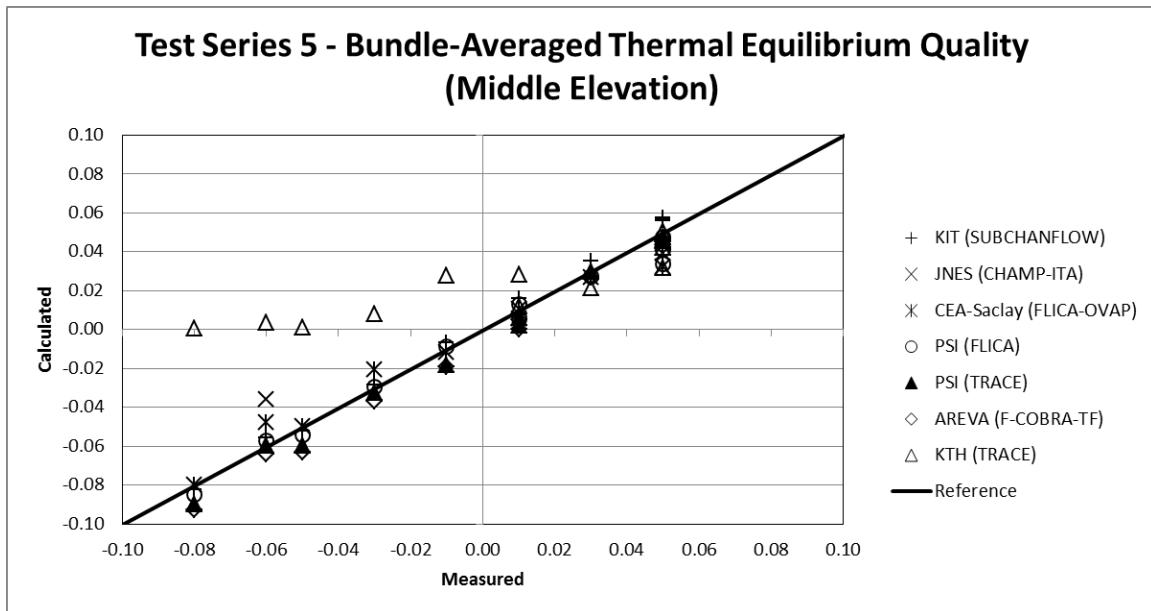


Figure AII.26 Test Series 5 Bundle-Averaged Thermal Equilibrium Quality – Middle Elevation

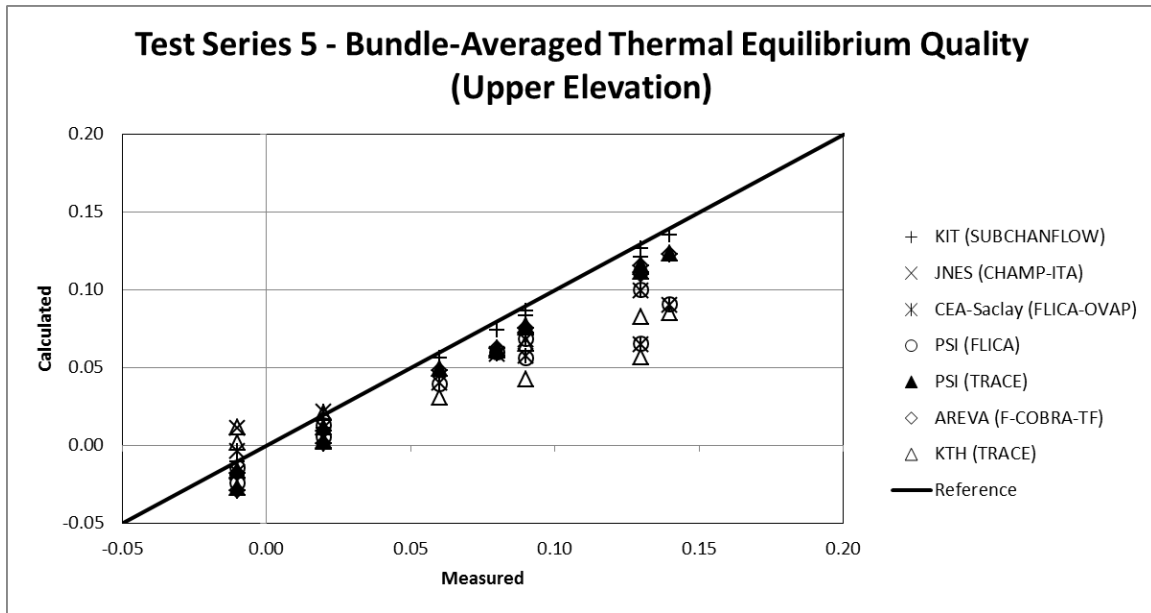


Figure AII.27 Test Series 5 Bundle-Averaged Thermal Equilibrium Quality – Upper Elevation

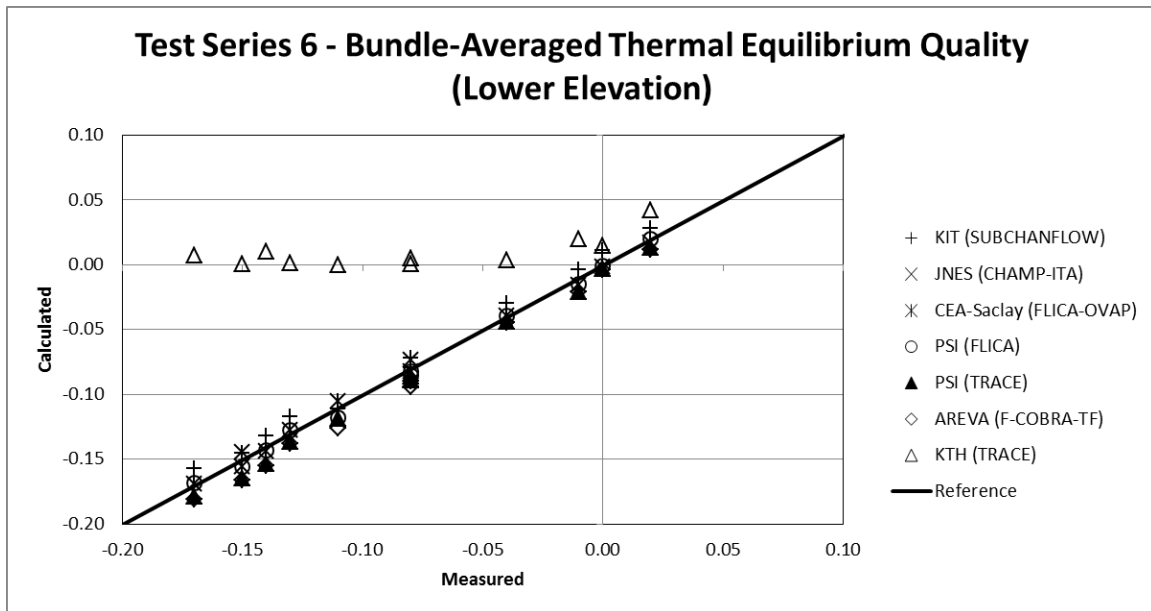


Figure AII.28 Test Series 6 Bundle-Averaged Thermal Equilibrium Quality – Lower Elevation

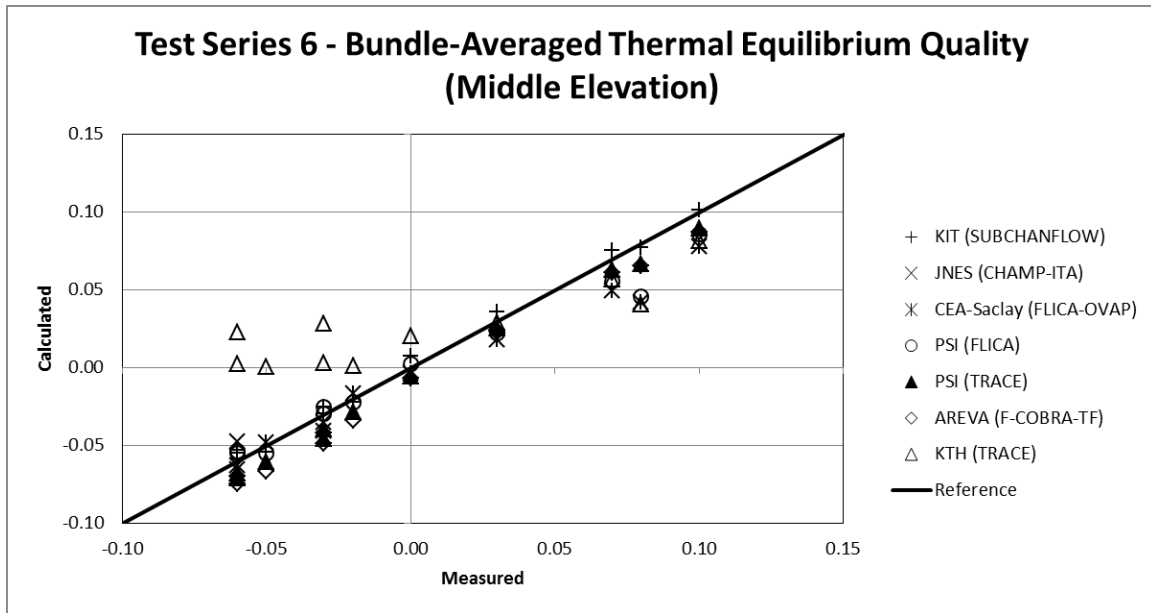


Figure AII.29 Test Series 6 Bundle-Averaged Thermal Equilibrium Quality – Middle Elevation

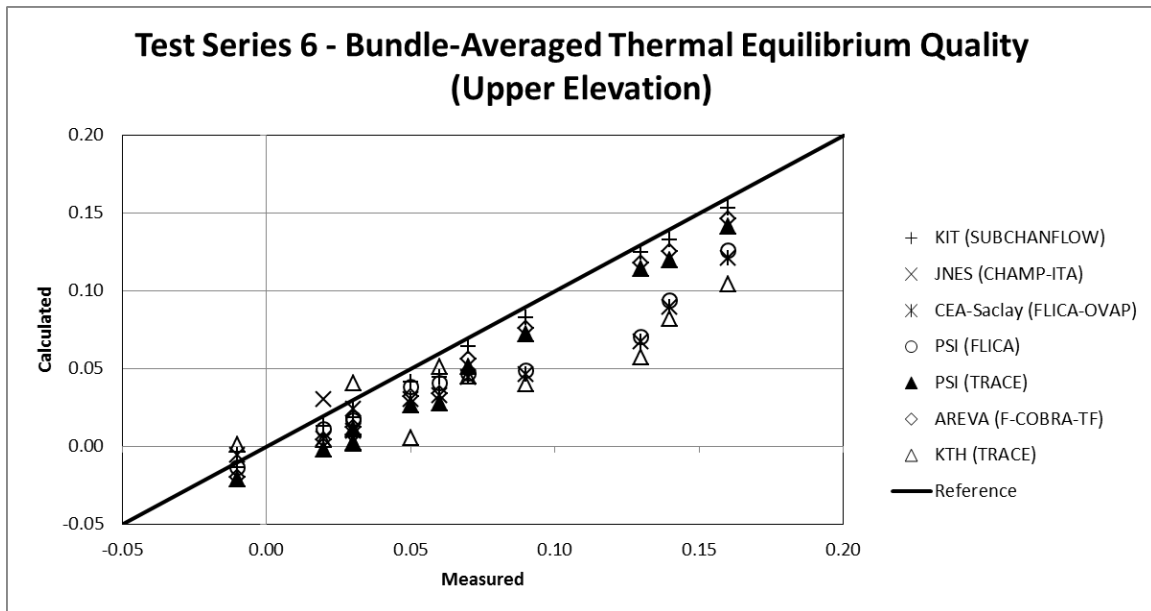


Figure AII.30 Test Series 6 Bundle-Averaged Thermal Equilibrium Quality – Upper Elevation

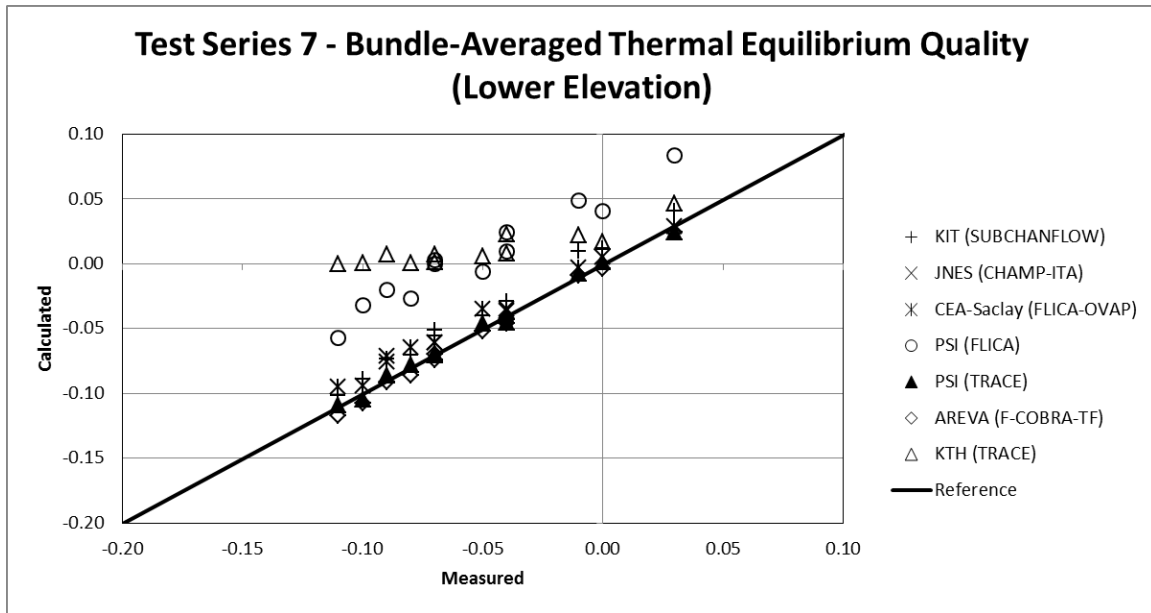


Figure AII.31 Test Series 7 Bundle-Averaged Thermal Equilibrium Quality – Lower Elevation

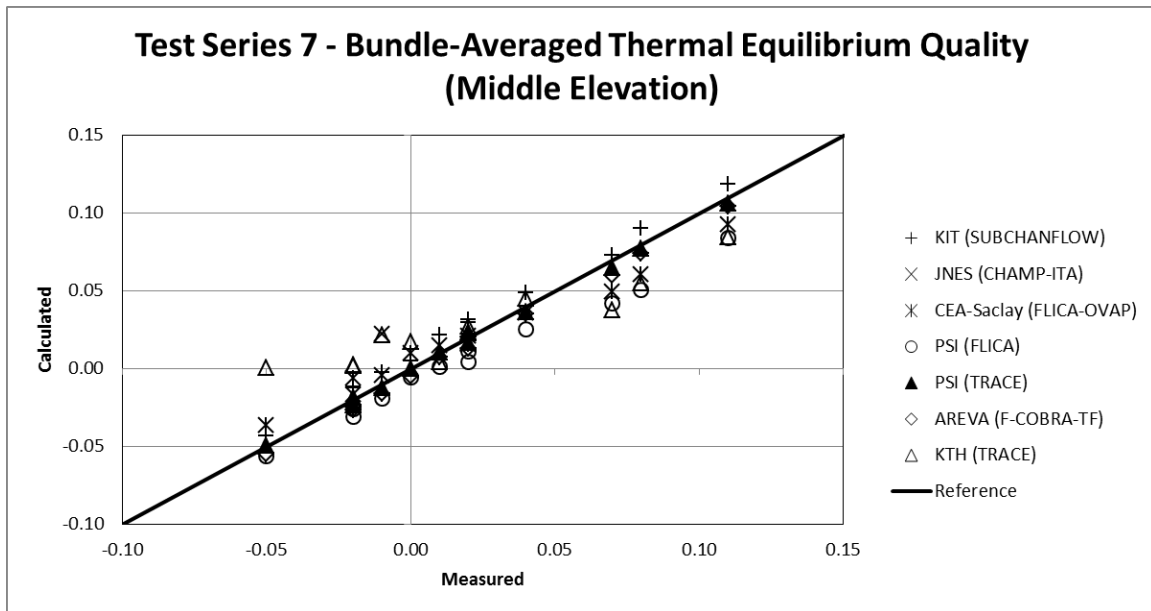


Figure AII.32 Test Series 7 Bundle-Averaged Thermal Equilibrium Quality – Middle Elevation

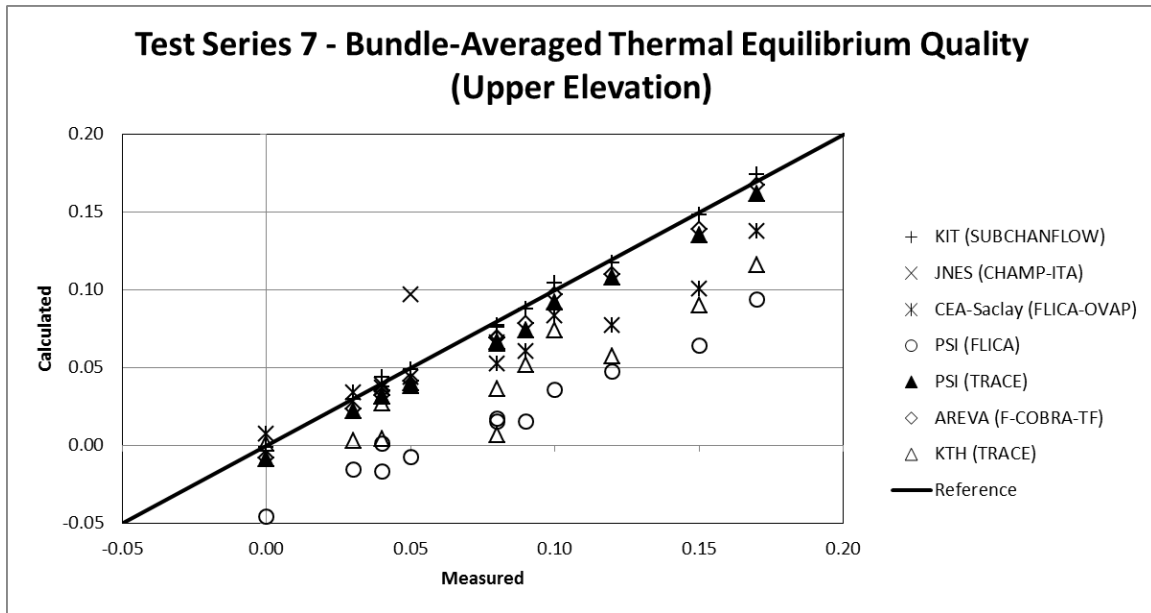


Figure AII.33 Test Series 7 Bundle-Averaged Thermal Equilibrium Quality – Upper Elevation

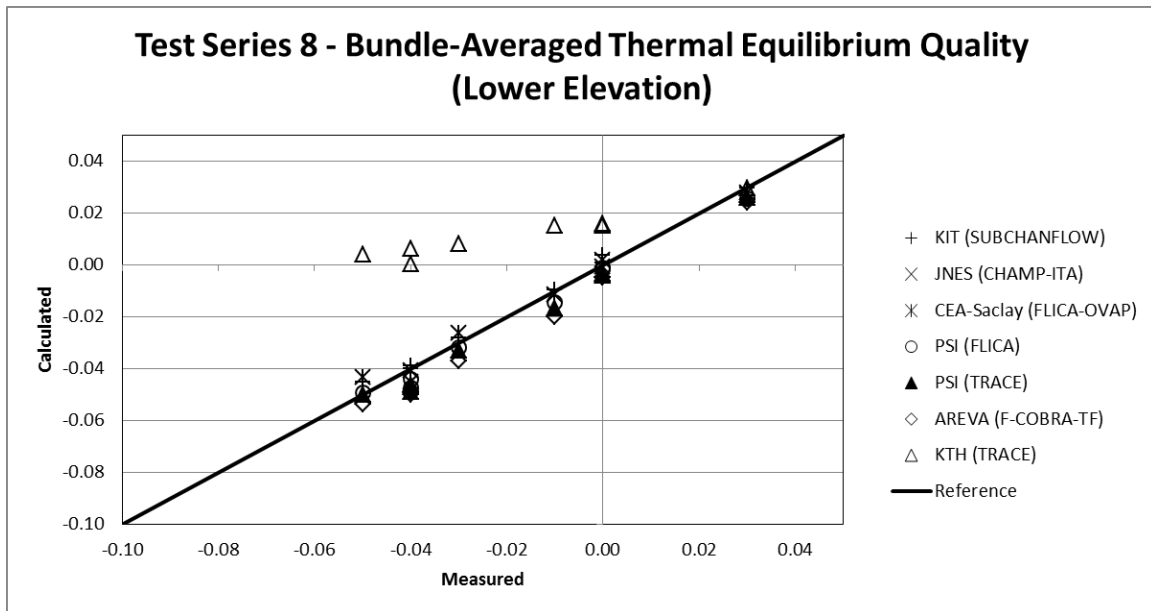


Figure AII.34 Test Series 8 Bundle-Averaged Thermal Equilibrium Quality – Lower Elevation

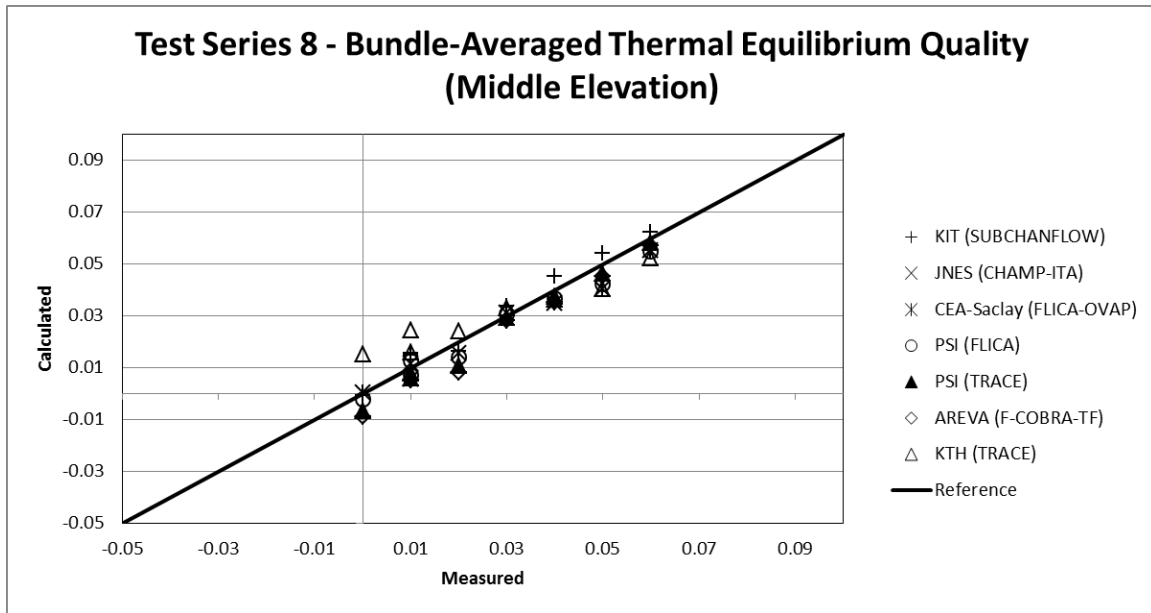


Figure AII.35 Test Series 8 Bundle-Averaged Thermal Equilibrium Quality – Middle Elevation

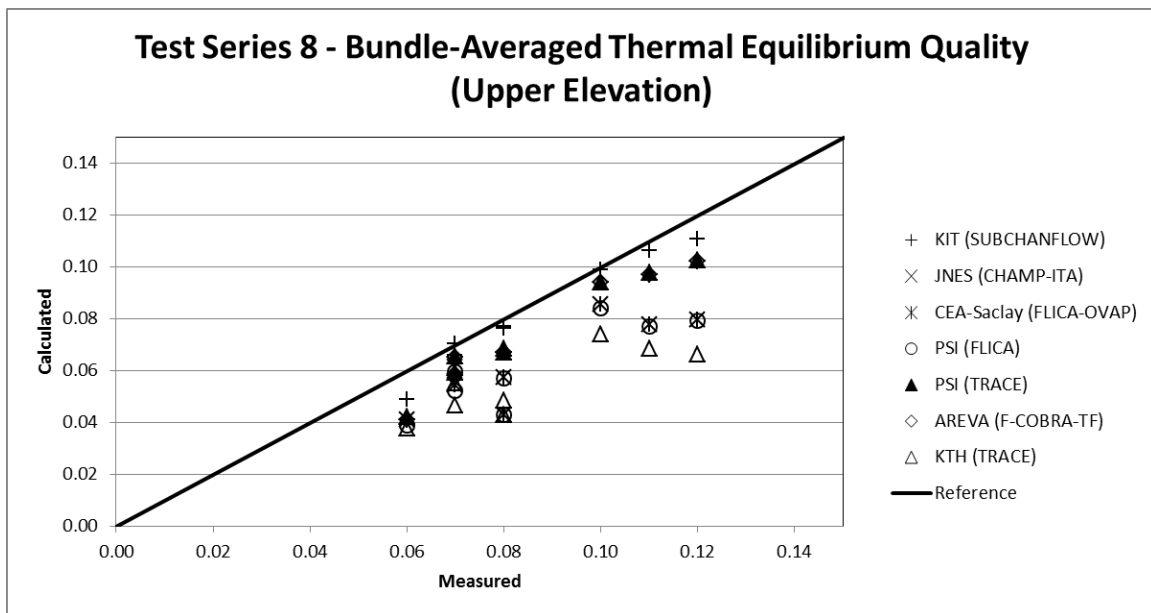


Figure AII.36 Test Series 8 Bundle-Averaged Thermal Equilibrium Quality – Upper Elevation

Table AII.1 Results of Recalculation of Bundle-Averaged Thermal Equilibrium Quality

Test Case	Bundle-Averaged Thermal Equilibrium Quality					
	Lower Elevation		Middle Elevation		Upper Elevation	
	Recalculated	Measured	Recalculated	Measured	Recalculated	Measured
5.1221	-0.151	-0.14	-0.095	-0.08	-0.032	-0.01
5.1222	-0.121	-0.11	-0.065	-0.05	-0.002	0.02
5.2111	-0.102	-0.09	-0.063	-0.06	-0.020	-0.01
5.2112	-0.075	-0.07	-0.036	-0.03	0.008	0.02
5.2442	-0.094	-0.08	-0.022	-0.01	0.059	0.08
5.3441	-0.059	-0.05	0.003	0.01	0.074	0.09
5.3442	-0.019	-0.01	0.043	0.05	0.114	0.13
5.4562	-0.026	-0.02	0.044	0.05	0.122	0.14
5.6321	-0.041	-0.04	0.001	0.01	0.048	0.06
5.6322	-0.014	-0.01	0.029	0.03	0.076	0.09
5.6552	-0.011	0	0.046	0.05	0.110	0.13
6.1121	-0.117	-0.11	-0.059	-0.05	-0.016	-0.01
6.1122	-0.085	-0.08	-0.027	-0.02	0.016	0.03
6.1451	-0.163	-0.15	-0.067	-0.06	0.005	0.02
6.1452	-0.134	-0.13	-0.038	-0.03	0.034	0.05
6.2441	-0.176	-0.17	-0.070	-0.06	0.010	0.03
6.2442	-0.152	-0.14	-0.044	-0.03	0.036	0.06
6.3452	0.015	0.02	0.091	0.1	0.147	0.16
6.4561	-0.088	-0.08	-0.005	0	0.058	0.07
6.4562	-0.020	-0.01	0.063	0.07	0.126	0.14
6.6561	-0.043	-0.04	0.026	0.03	0.077	0.09
6.6562	-0.002	0	0.067	0.08	0.119	0.13
7.1121	-0.107	-0.11	-0.048	-0.05	-0.004	0
7.1122	-0.077	-0.08	-0.018	-0.02	0.027	0.03
7.1341	-0.103	-0.1	-0.022	-0.02	0.038	0.04
7.1342	-0.069	-0.07	0.011	0.01	0.071	0.08
7.2221	-0.085	-0.09	-0.011	-0.01	0.044	0.05
7.3121	-0.045	-0.05	0.001	0	0.035	0.04
7.3451	-0.044	-0.04	0.037	0.04	0.098	0.1
7.3452	0.026	0.03	0.107	0.11	0.168	0.17
7.4561	-0.067	-0.07	0.017	0.02	0.081	0.09
7.4562	-0.006	-0.01	0.078	0.08	0.142	0.15
7.6321	-0.039	-0.04	0.024	0.02	0.071	0.08
7.6322	0.003	0	0.066	0.07	0.113	0.12
8.1232	-0.040		0.007		0.060	
8.1342	-0.014		0.038		0.097	
8.1452	0.008		0.071		0.142	
8.2351	-0.003	0	0.029	0.03	0.065	0.07
8.2352	0.026	0.03	0.058	0.06	0.094	0.1
8.4211	-0.050	-0.05	-0.007	0	0.042	0.06
8.4212	-0.033	-0.03	0.010	0.02	0.059	0.07
8.5311	-0.046	-0.04	0.008	0.01	0.068	0.08
8.5312	-0.017	-0.01	0.037	0.04	0.098	0.11
8.5442	-0.004	0	0.046	0.05	0.103	0.12
8.6551	-0.049	-0.04	0.006	0.01	0.067	0.08

Appendix III Exercise I-3 Results

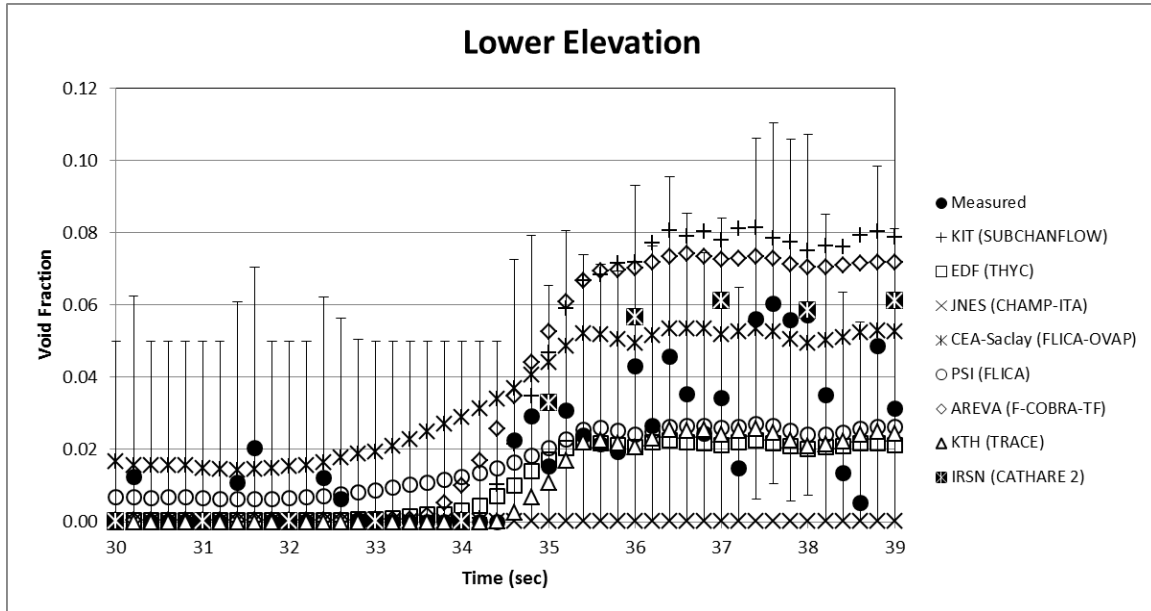


Figure AIII.1 Test Series 5T (Power Increase) – Lower Elevation Results

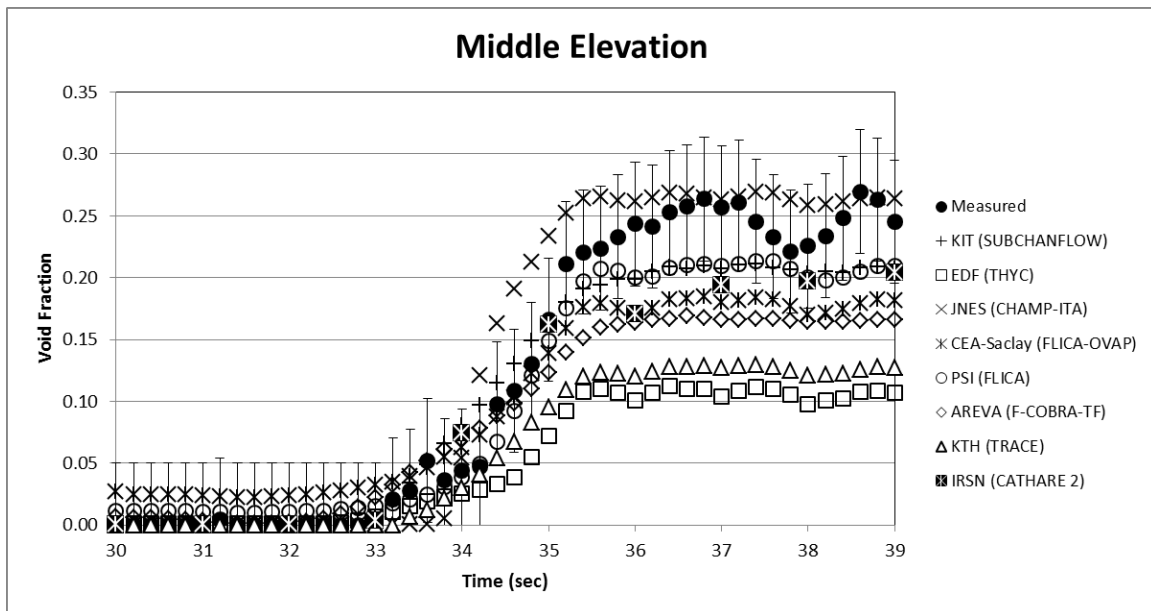


Figure AIII.2 Test Series 5T (Power Increase) – Middle Elevation Results

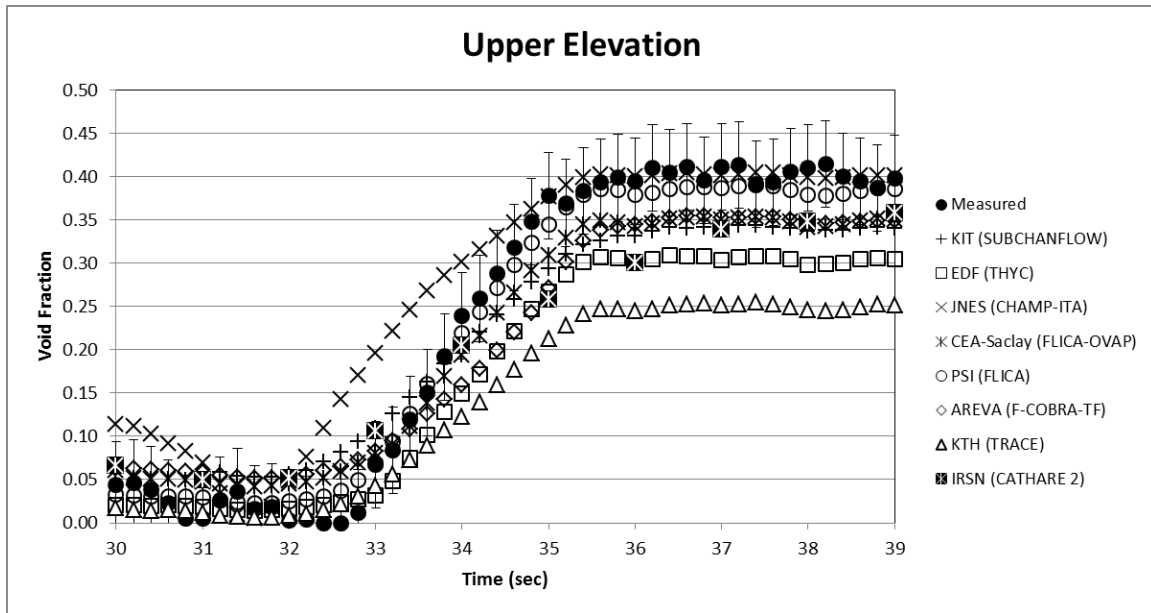


Figure AIII.3 Test Series 5T (Power Increase) – Upper Elevation Results

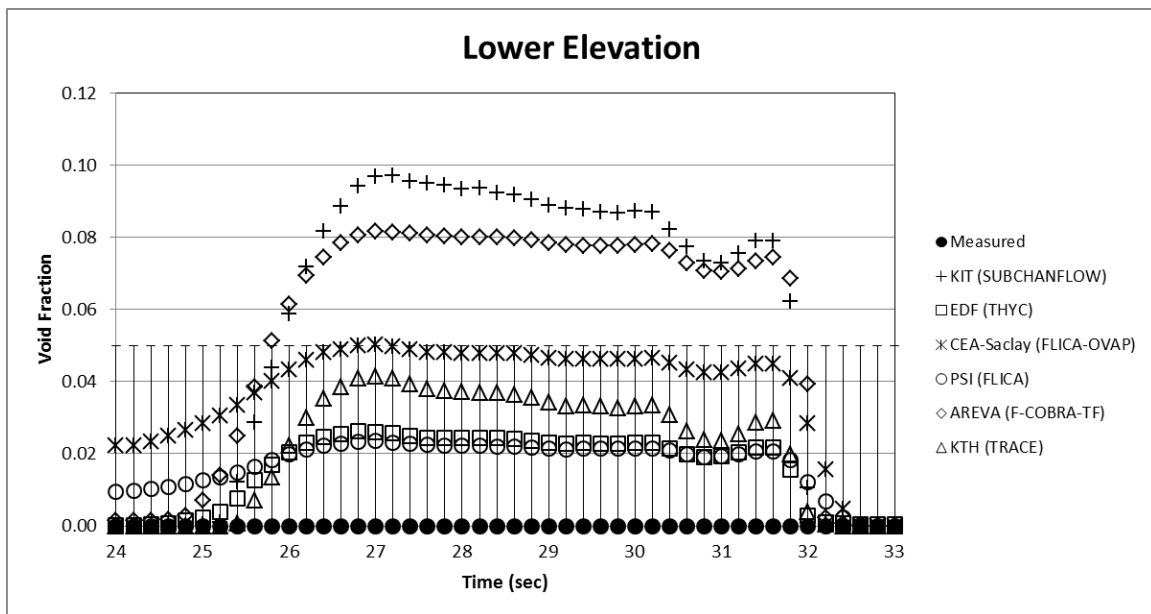


Figure AIII.4 Test Series 6T (Power Increase) – Lower Elevation Results

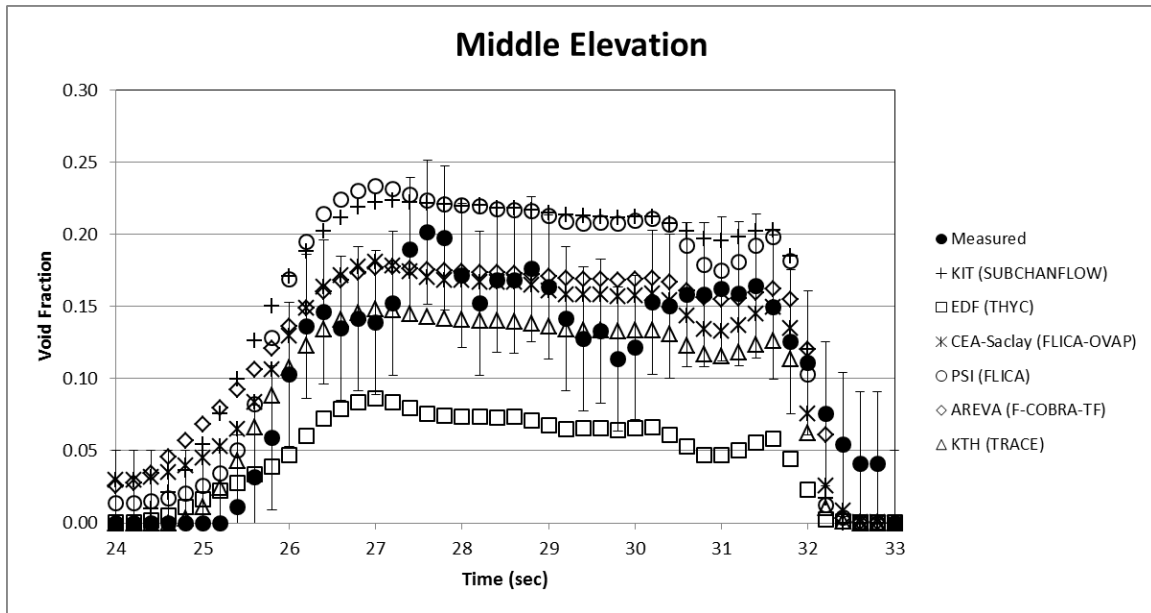


Figure AIII.5 Test Series 6T (Power Increase) – Middle Elevation Results

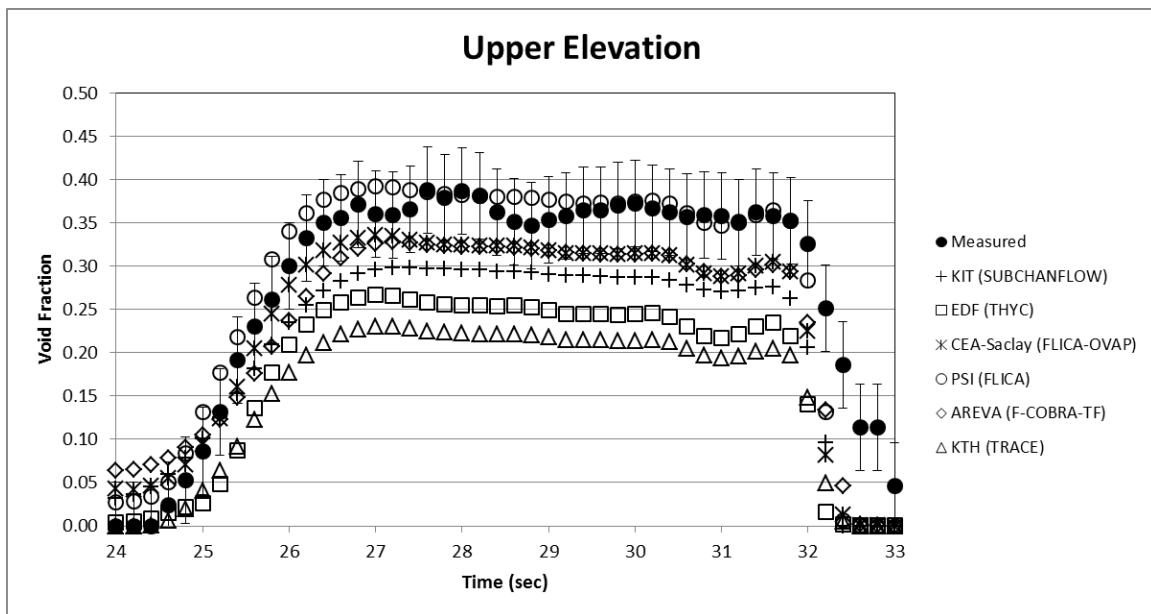


Figure AIII.6 Test Series 6T (Power Increase) – Upper Elevation Results

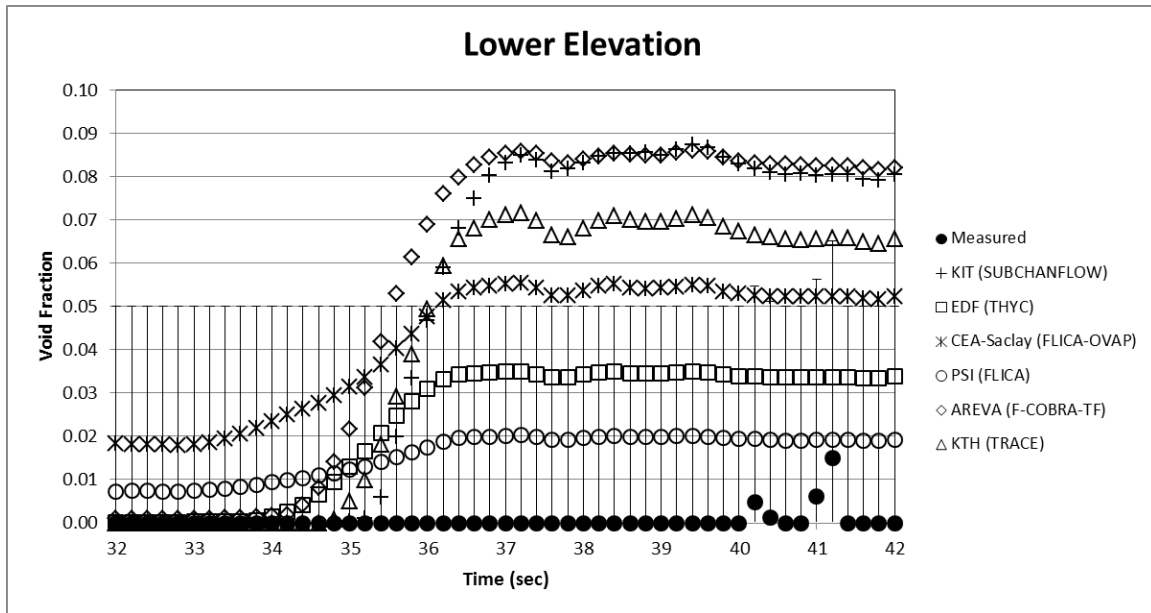


Figure AIII.7 Test Series 7T (Power Increase) – Lower Elevation Results

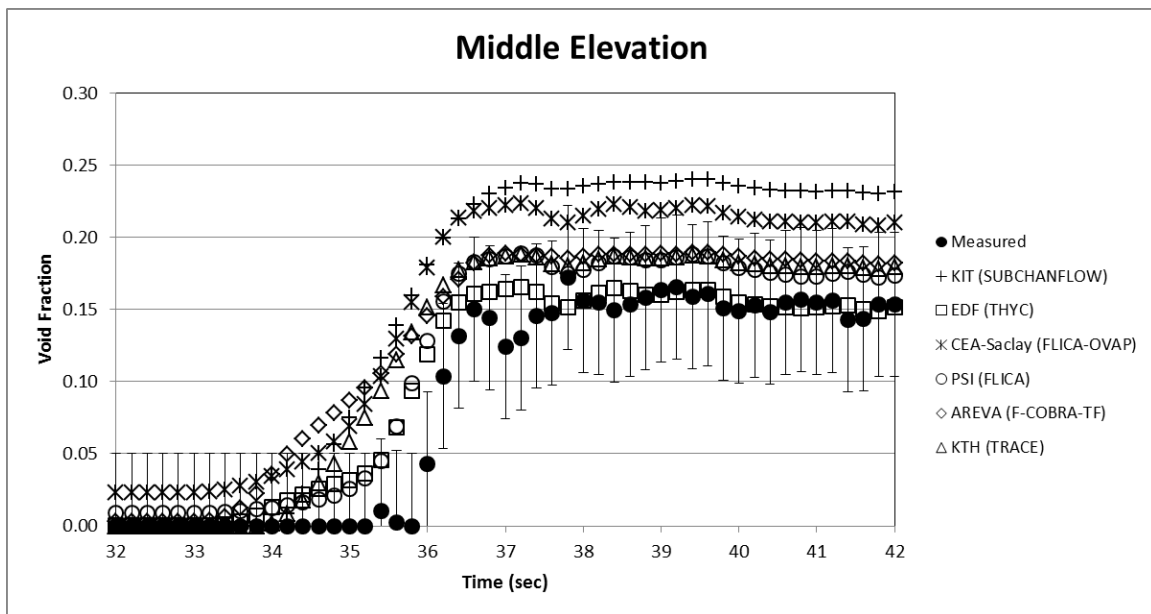


Figure AIII.8 Test Series 7T (Power Increase) – Middle Elevation Results

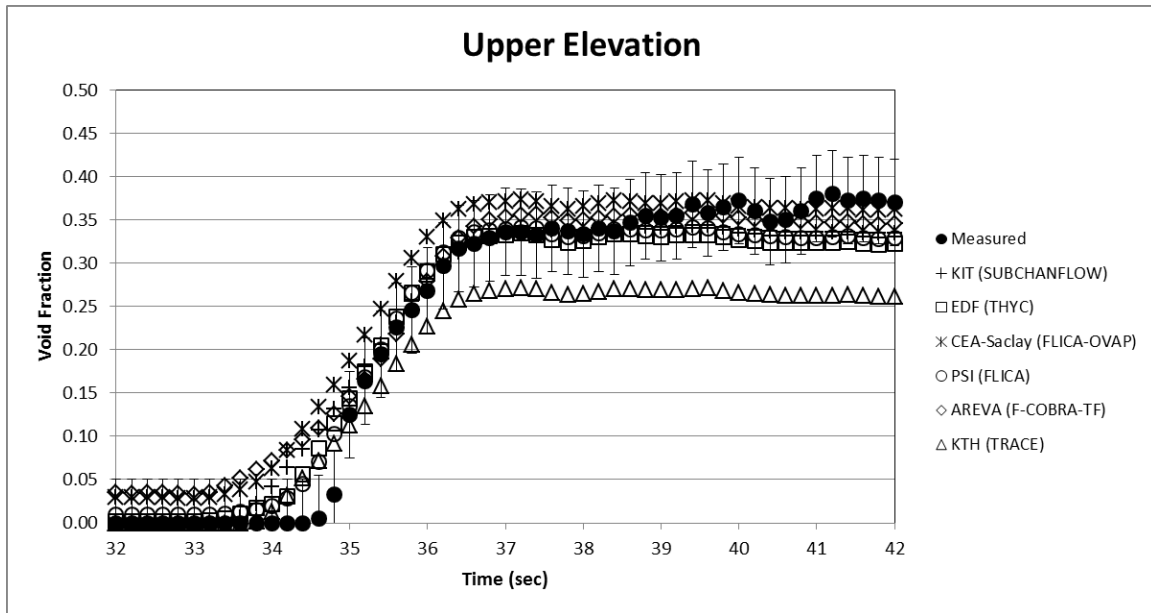


Figure AIII.9 Test Series 7T (Power Increase) – Upper Elevation Results

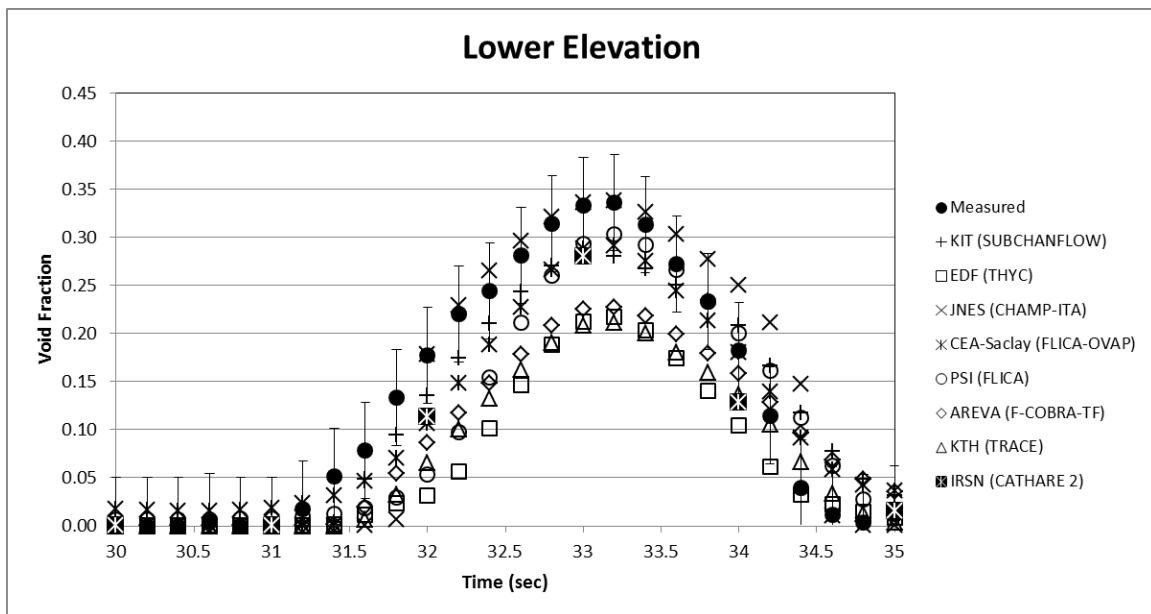


Figure AIII.10 Test Series 5T (Flow Reduction) – Lower Elevation Results

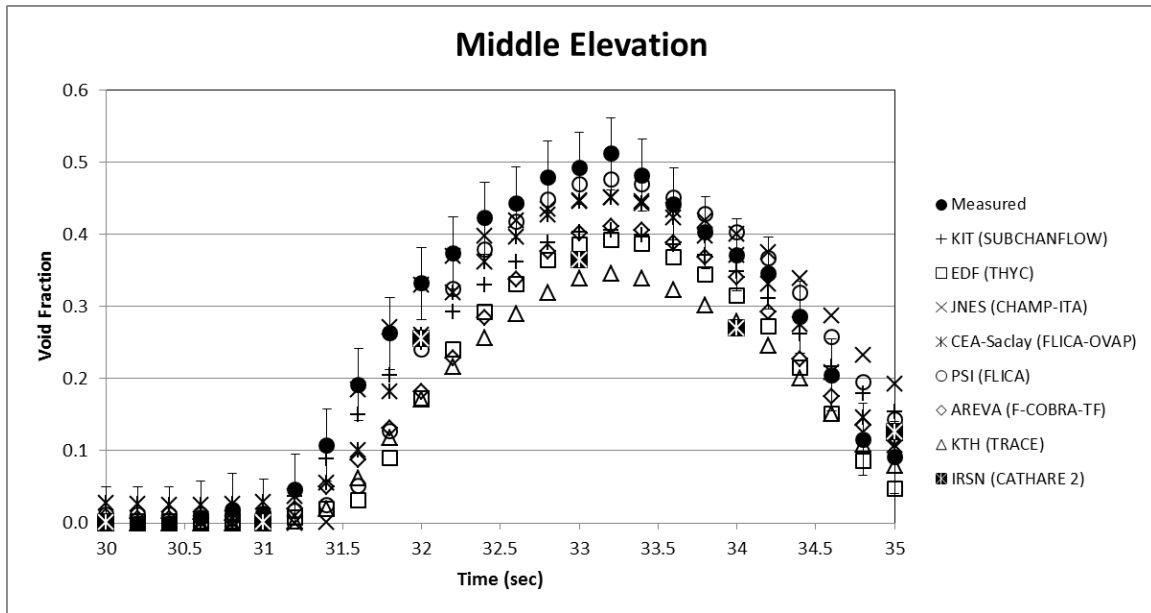


Figure AIII.11 Test Series 5T (Flow Reduction) – Middle Elevation Results

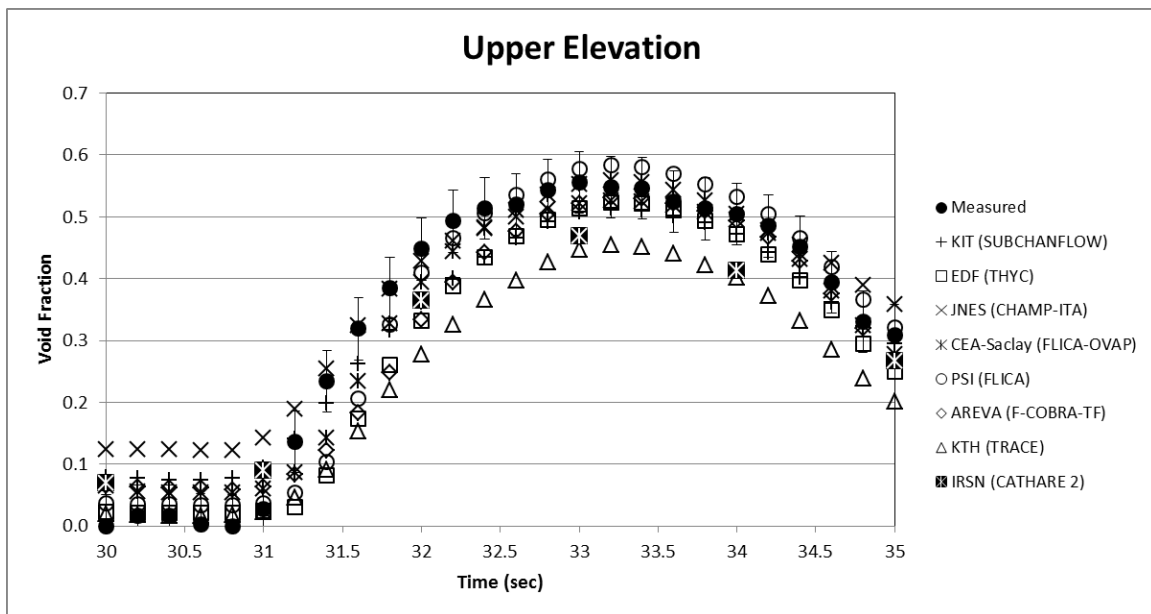


Figure AIII.12 Test Series 5T (Flow Reduction) – Upper Elevation Results

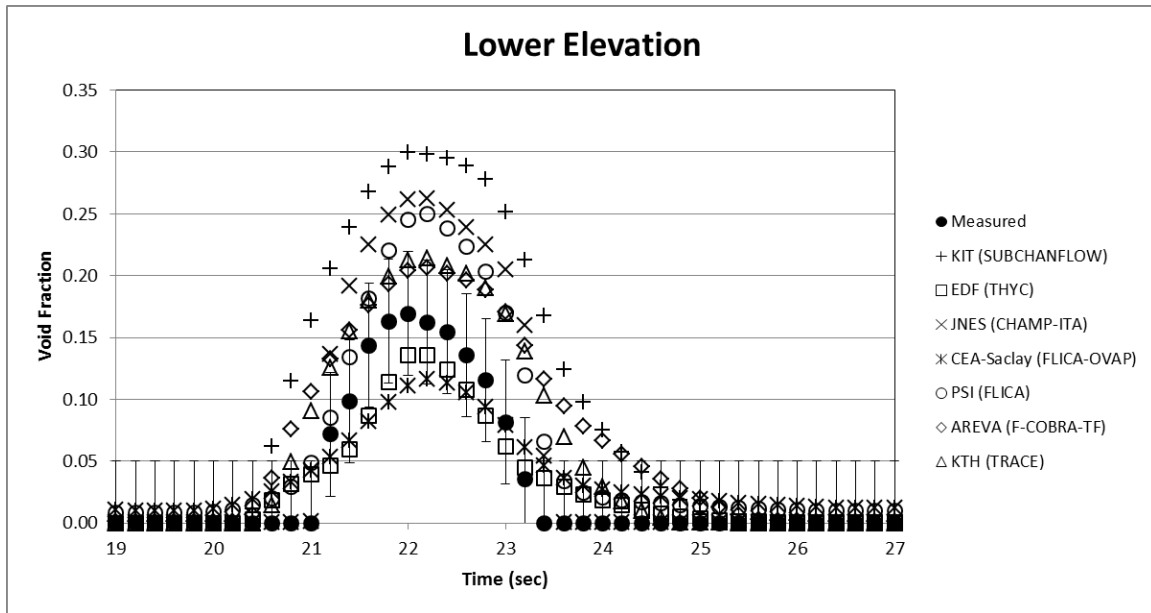


Figure AIII.13 Test Series 6T (Flow Reduction) – Lower Elevation Results

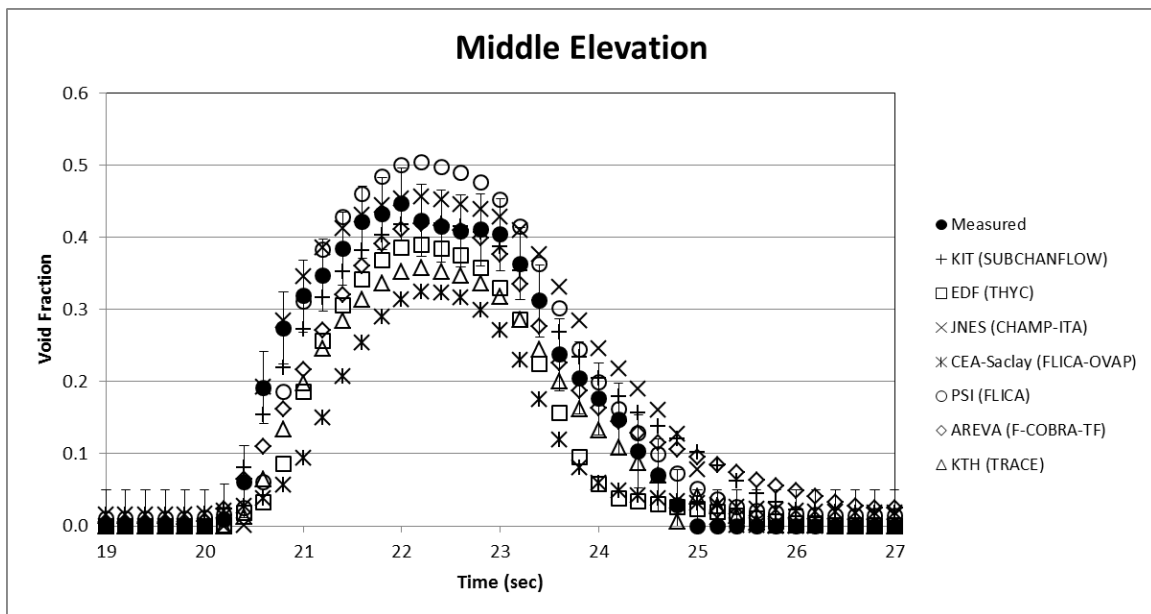


Figure AIII.14 Test Series 6T (Flow Reduction) – Middle Elevation Results

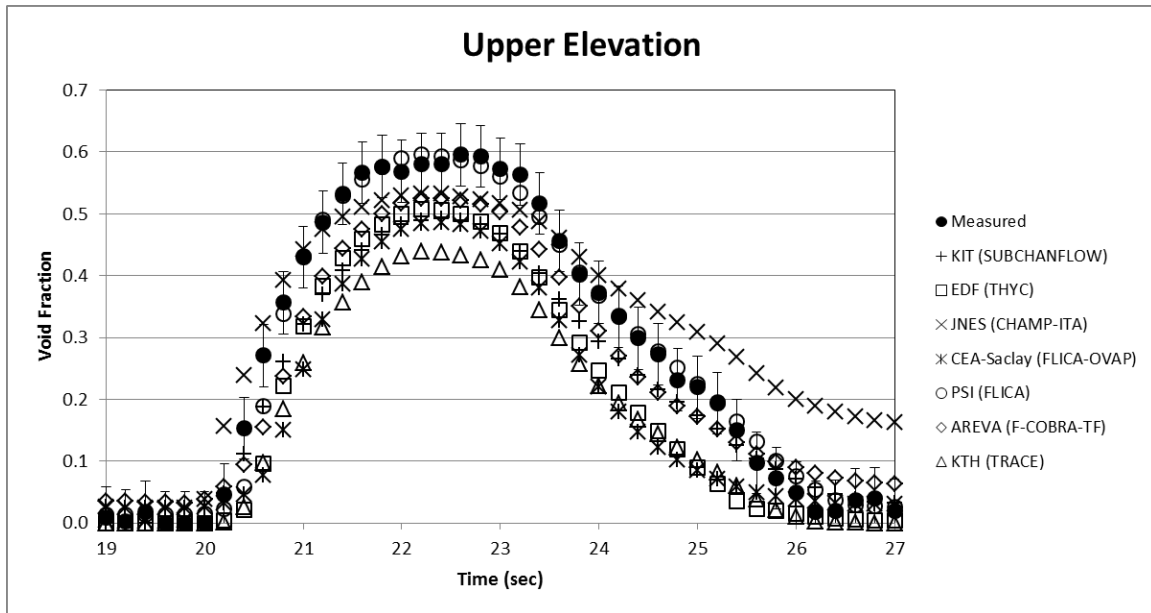


Figure AIII.15 Test Series 6T (Flow Reduction) – Upper Elevation Results

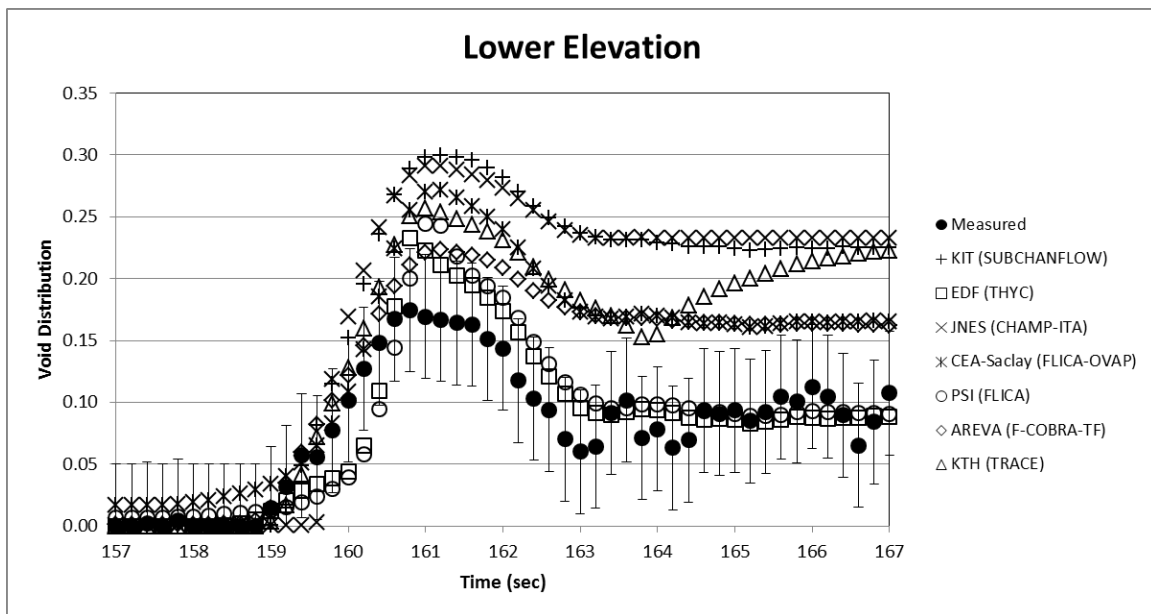


Figure AIII.16 Test Series 7T (Flow Reduction) – Lower Elevation Results

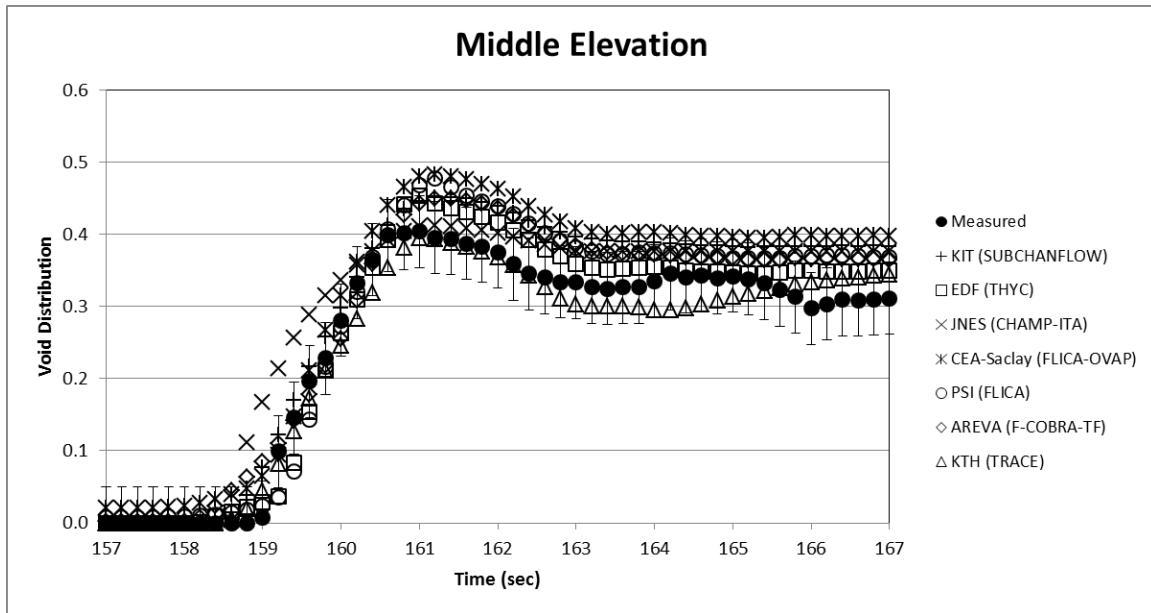


Figure AIII.17 Test Series 7T (Flow Reduction) – Middle Elevation Results

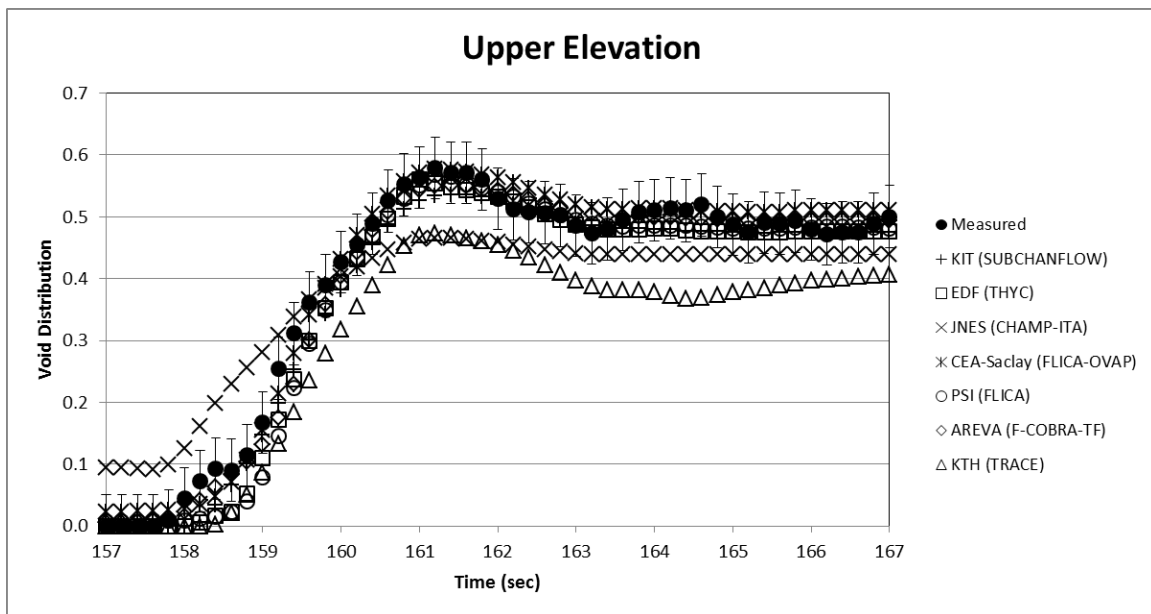


Figure AIII.18 Test Series 7T (Flow Reduction) – Upper Elevation Results

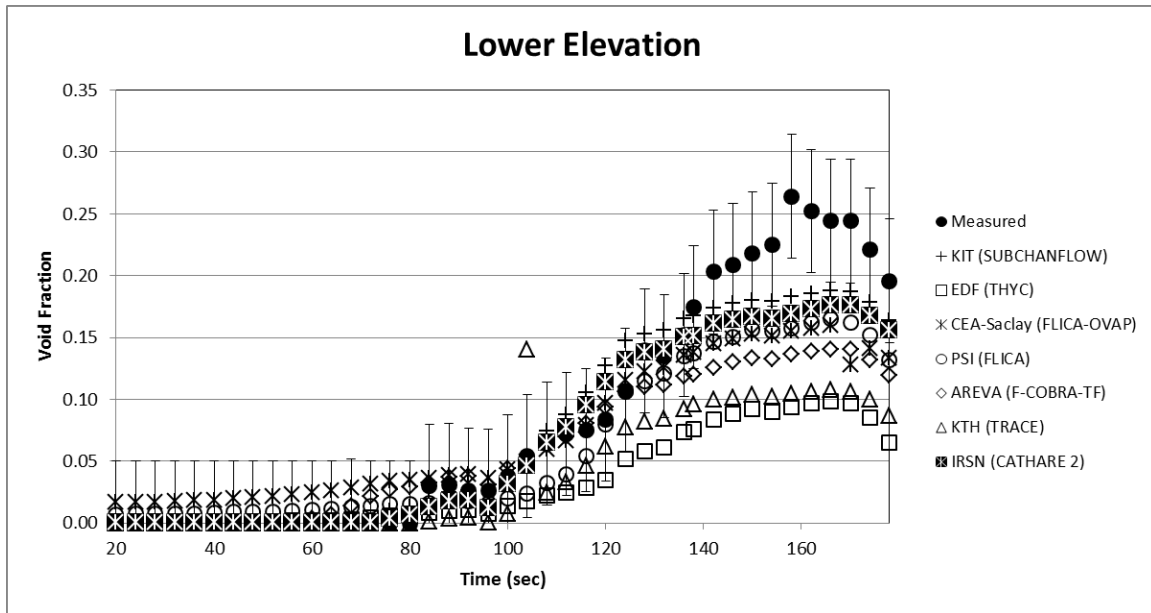


Figure AIII.19 Test Series 5T (Depressurization) – Lower Elevation Results

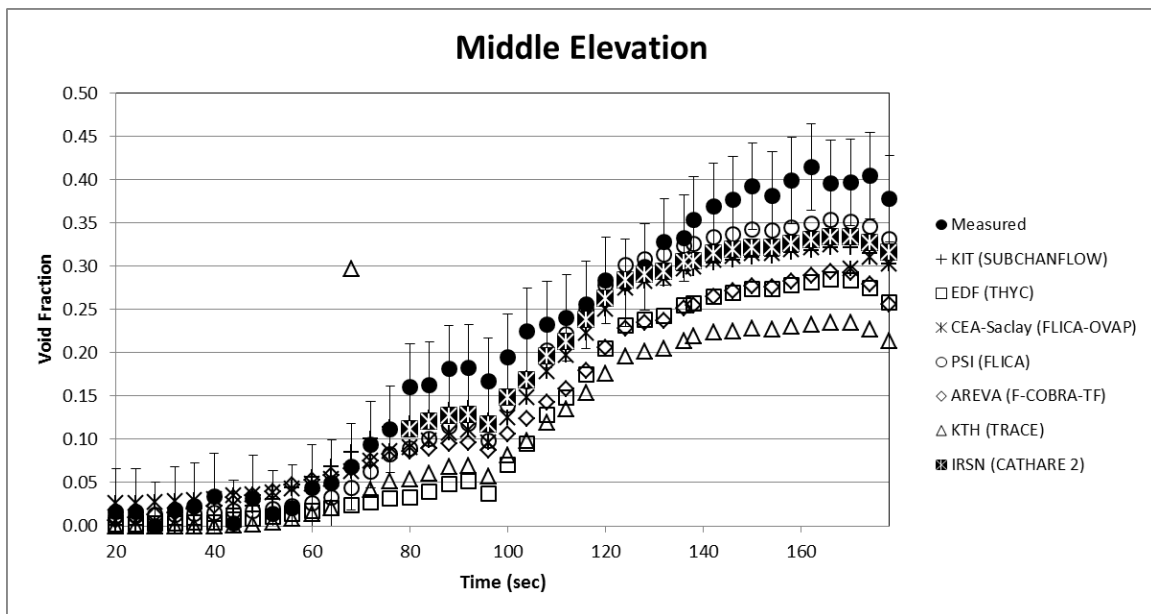


Figure AIII.20 Test Series 5T (Depressurization) – Middle Elevation Results

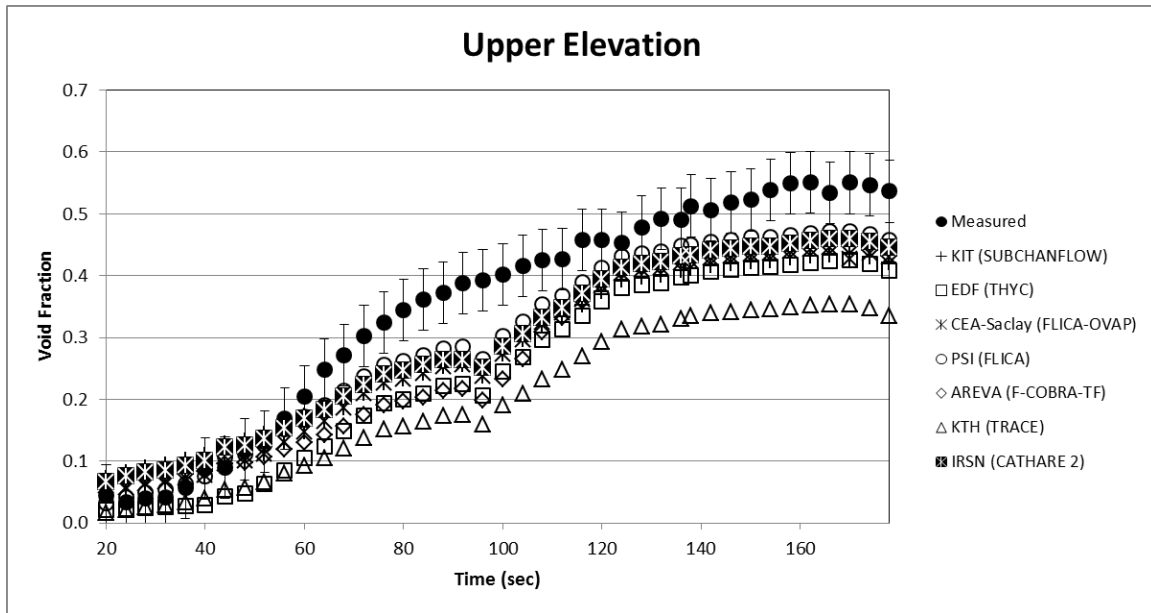


Figure AIII.21 Test Series 5T (Depressurization) – Upper Elevation Results

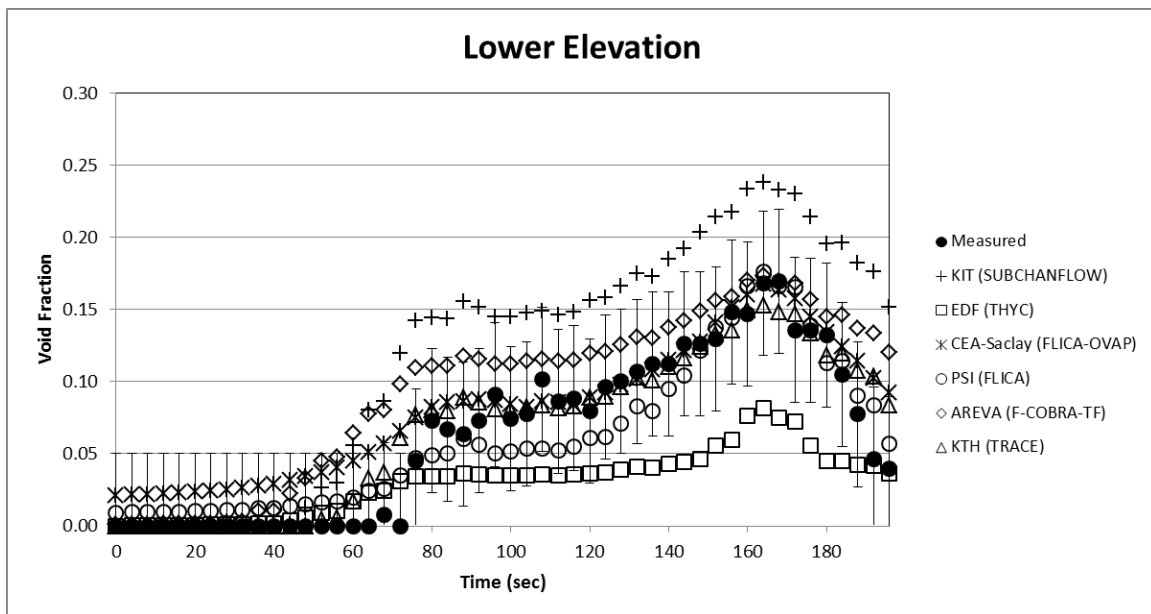


Figure AIII.22 Test Series 6T (Depressurization) – Lower Elevation Results

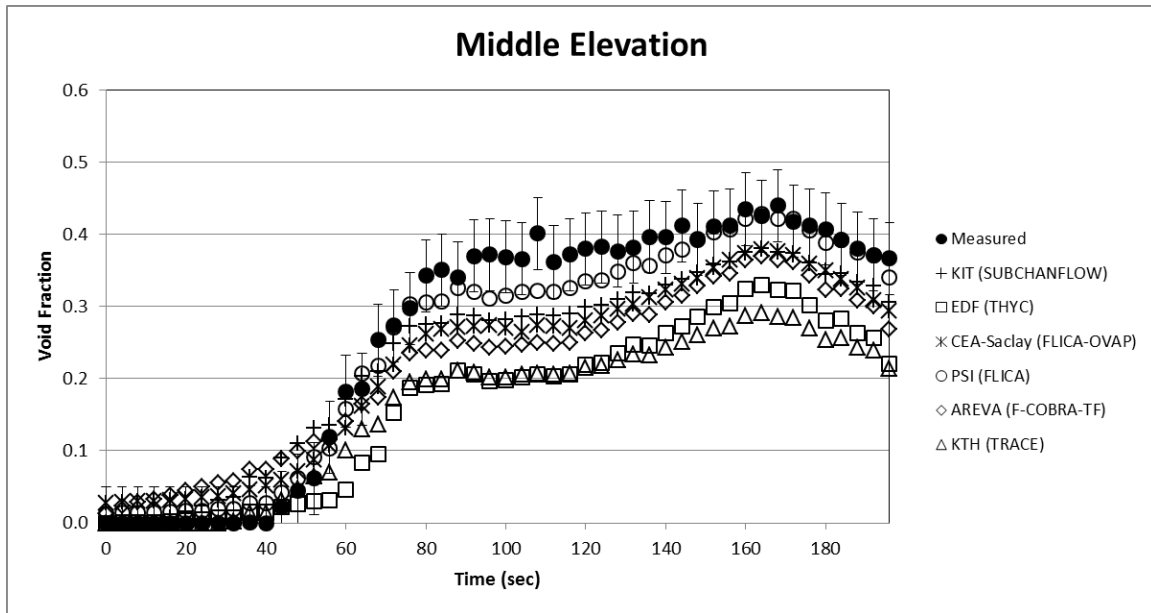


Figure AIII.23 Test Series 6T (Depressurization) – Middle Elevation Results

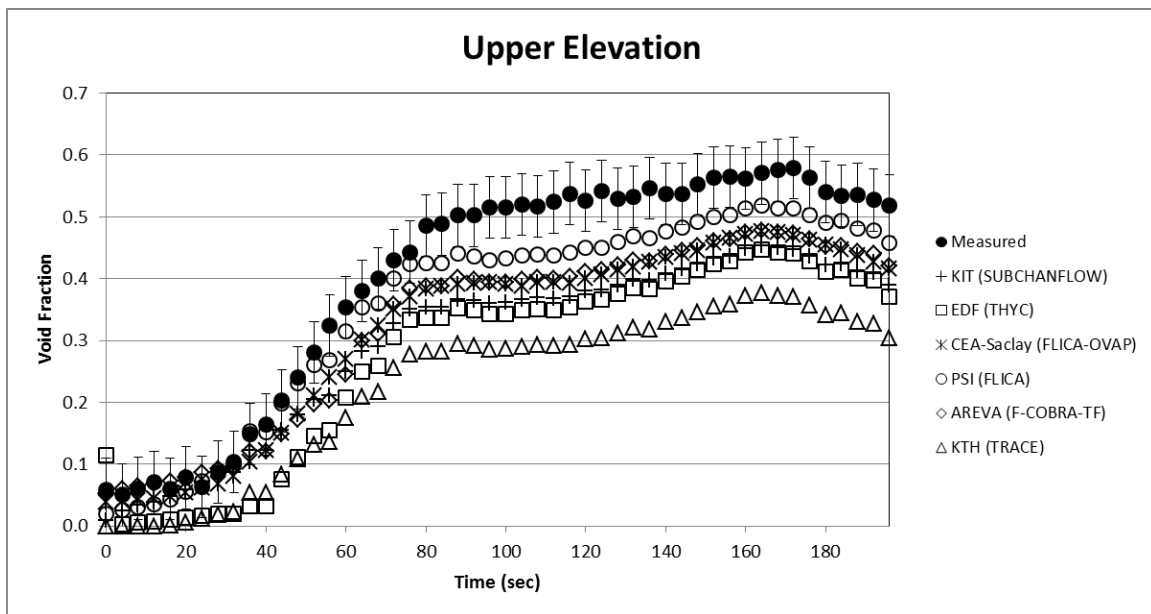


Figure AIII.24 Test Series 6T (Depressurization) – Upper Elevation Results

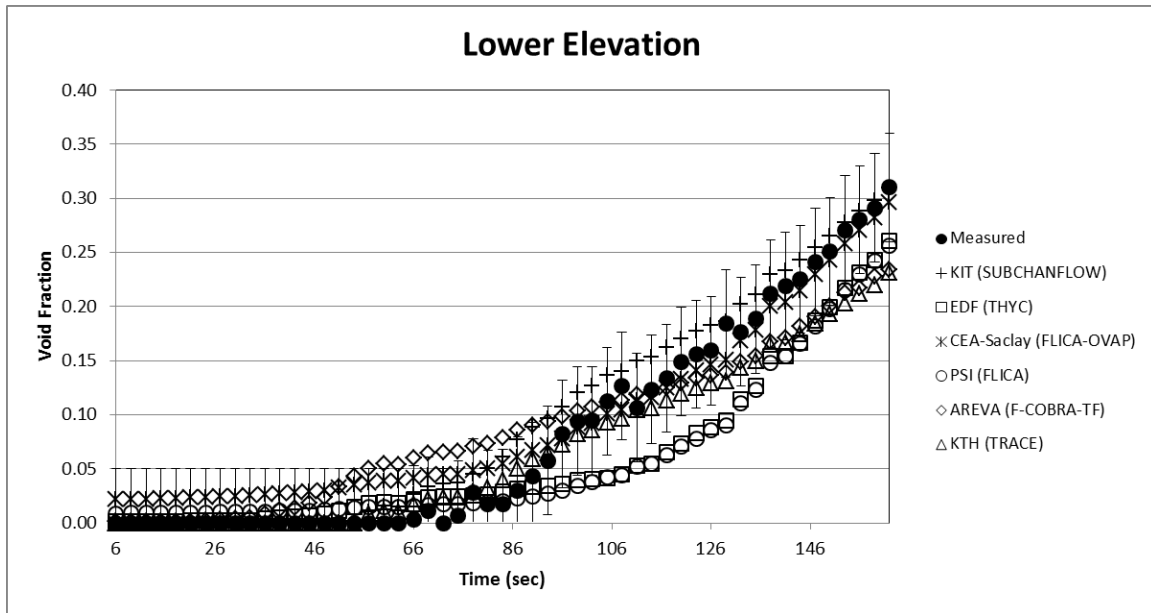


Figure AIII.25 Test Series 7T (Depressurization) – Lower Elevation Results

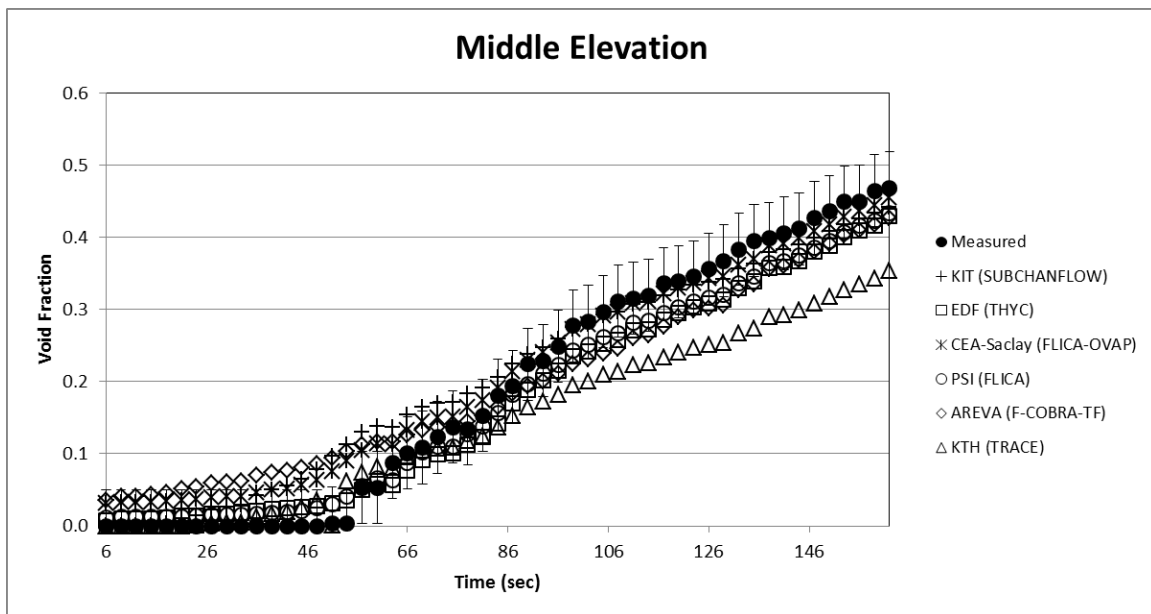


Figure AIII.26 Test Series 7T (Depressurization) – Middle Elevation Results

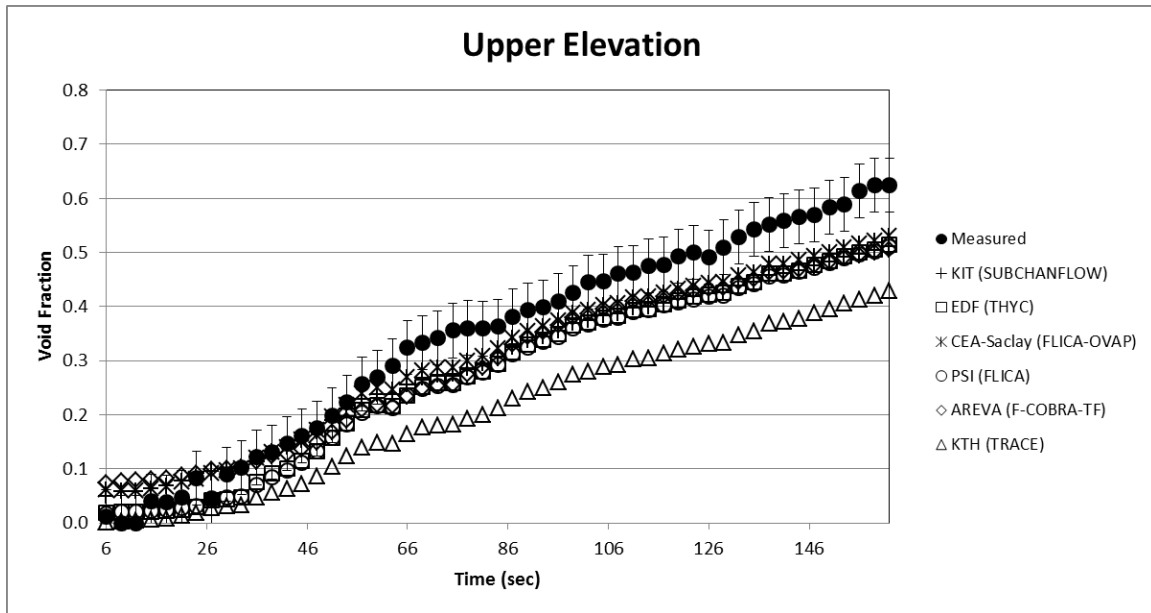


Figure AIII.27 Test Series 7T (Depressurization) – Upper Elevation Results

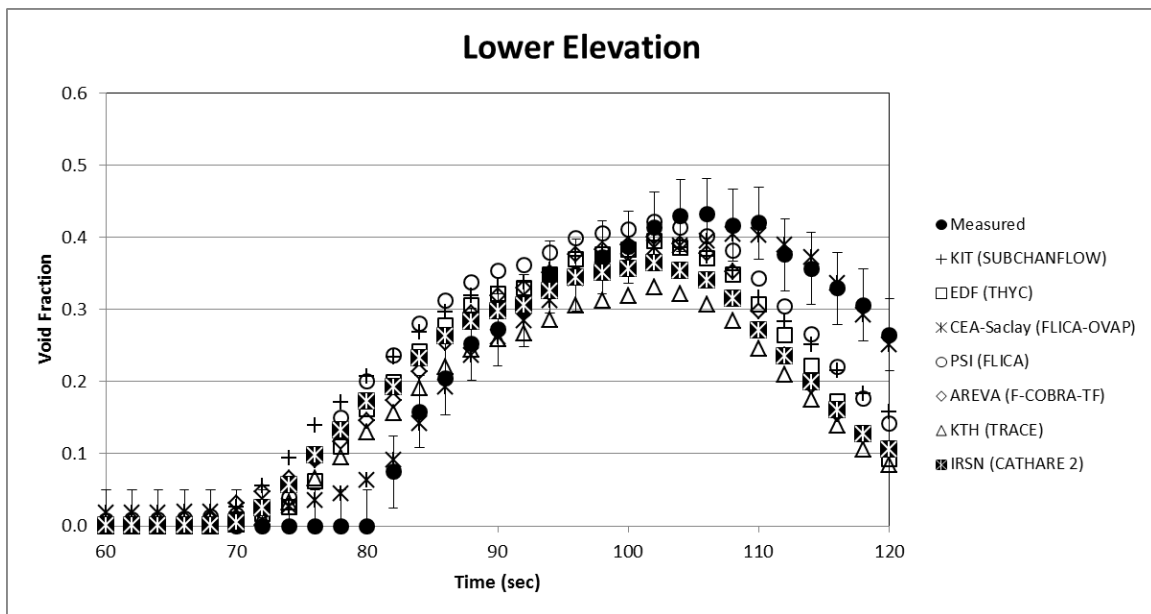


Figure AIII.28 Test Series 5T (Temperature Increase) – Lower Elevation Results

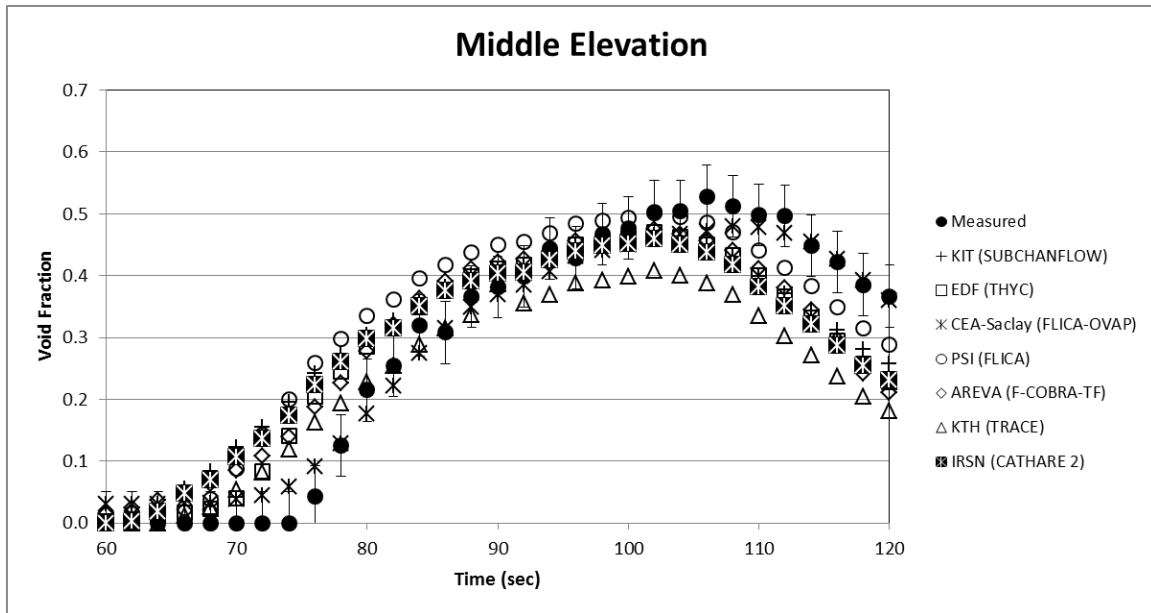


Figure AIII.29 Test Series 5T (Temperature Increase) – Middle Elevation Results

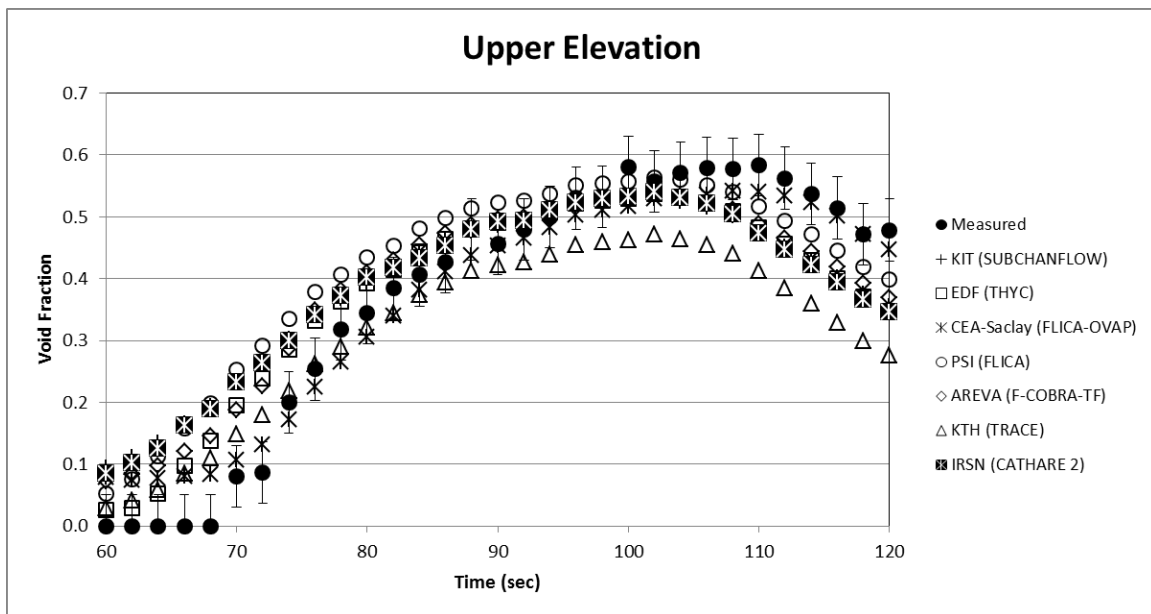


Figure AIII.30 Test Series 5T (Temperature Increase) – Upper Elevation Results

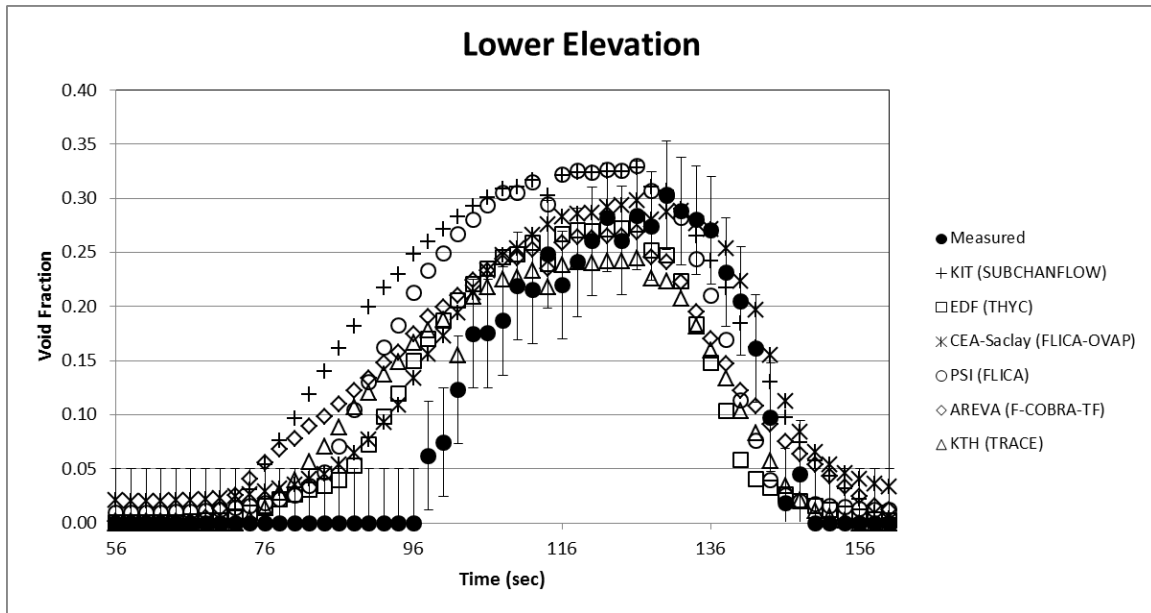


Figure AIII.31 Test Series 6T (Temperature Increase) – Lower Elevation Results

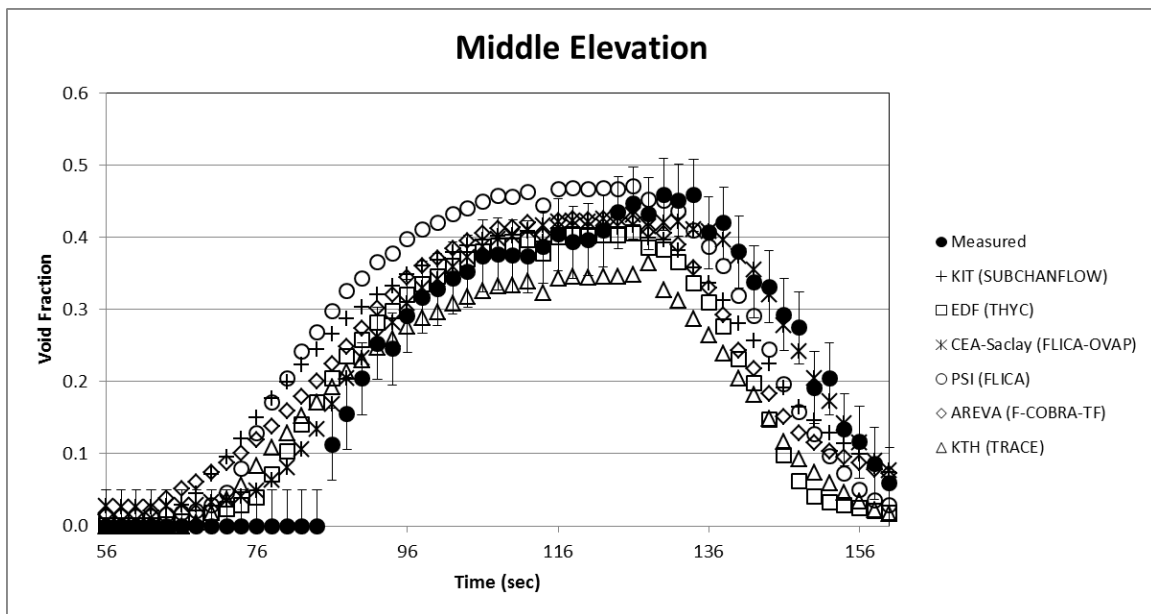


Figure AIII.32 Test Series 6T (Temperature Increase) – Middle Elevation Results

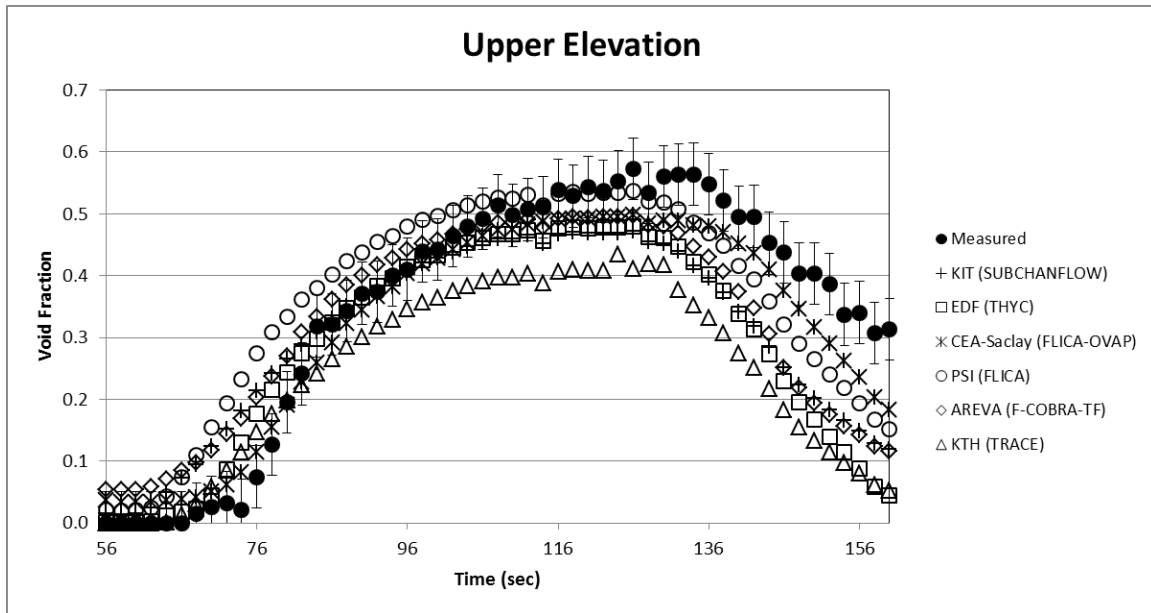


Figure AIII.33 Test Series 6T (Temperature Increase) – Upper Elevation Results

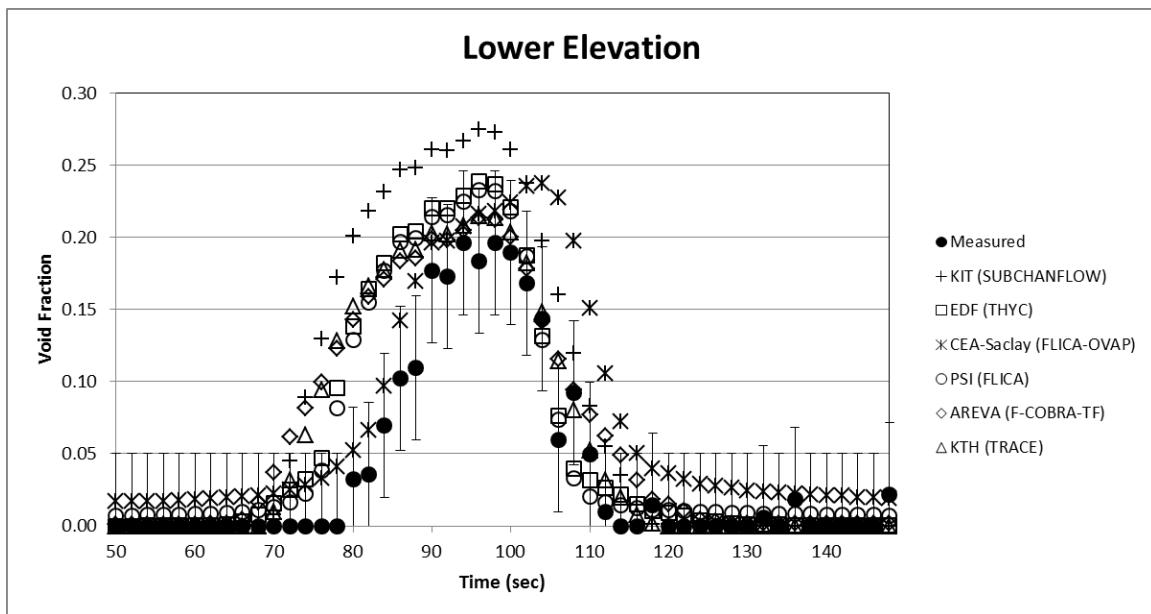


Figure AIII.34 Test Series 7T (Temperature Increase) – Lower Elevation Results

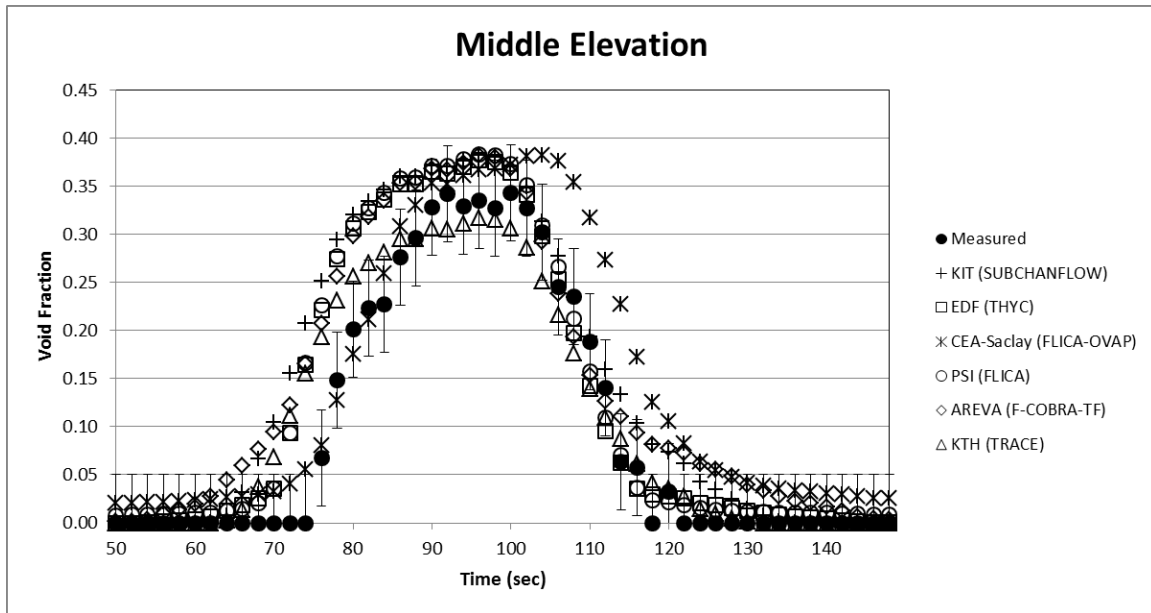


Figure AIII.35 Test Series 7T (Temperature Increase) – Middle Elevation Results

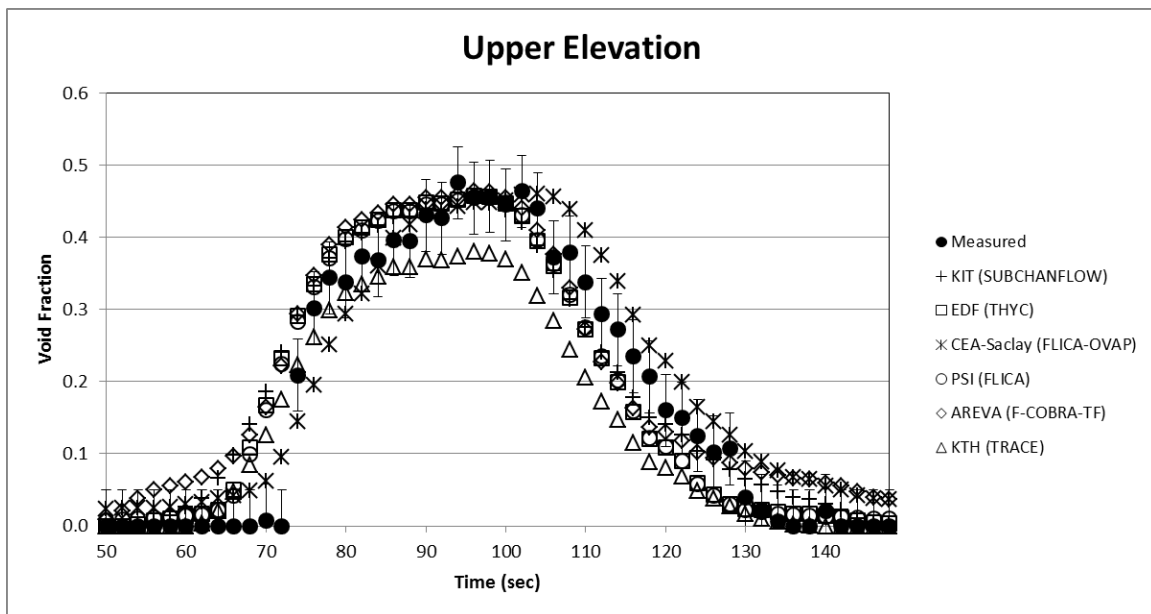


Figure AIII.36 Test Series 7T (Temperature Increase) – Upper Elevation Results

Appendix IV Exercise I-4 Results

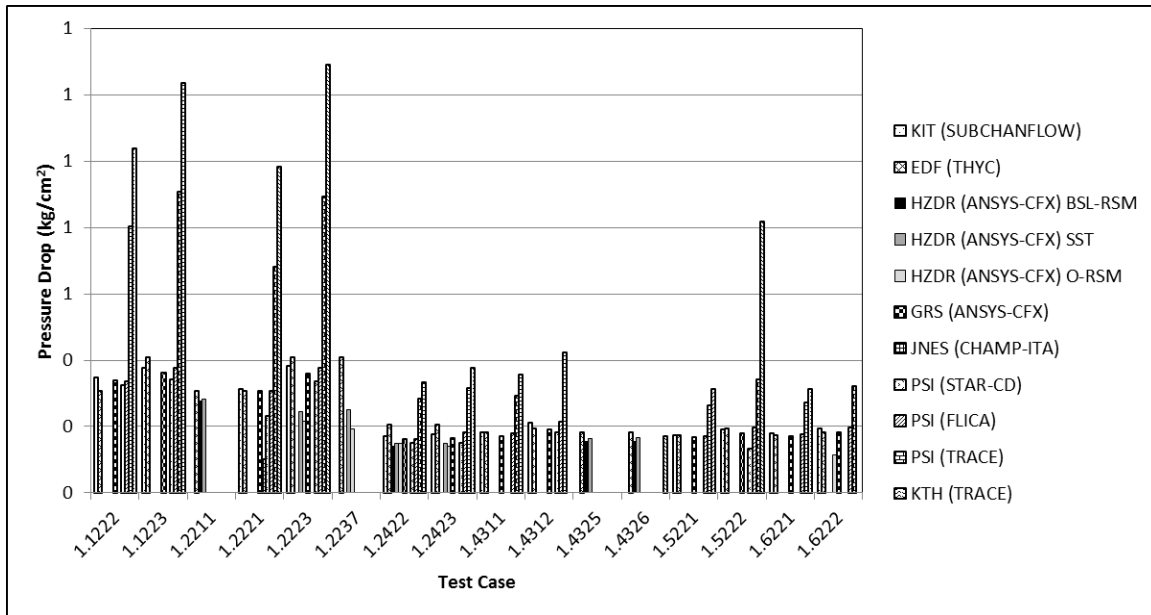


Figure AIV.1 Test Series 1 Pressure Drop Results

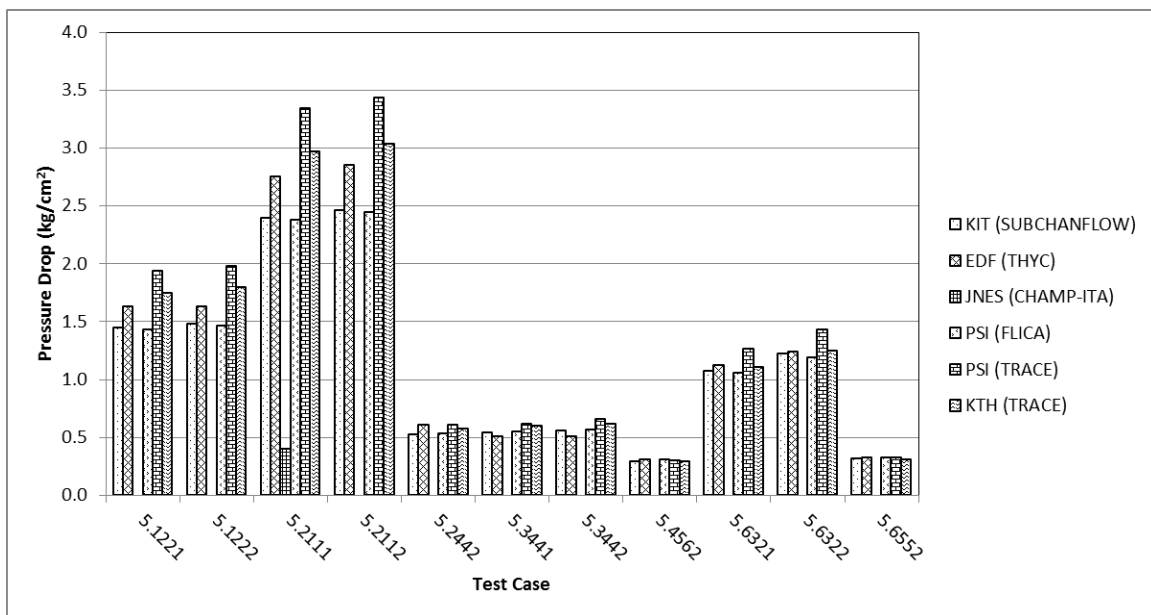


Figure AIV.2 Test Series 5 Pressure Drop Results

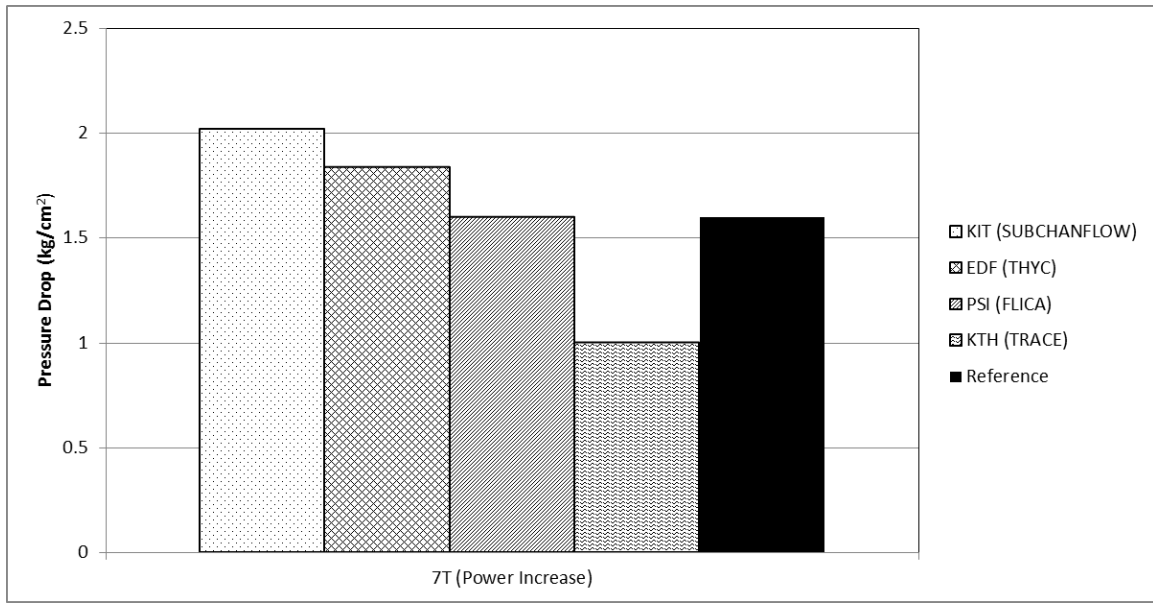


Figure AIV.3 Test Series 7T Pressure Drop Results

Appendix V Exercise II-1 Results

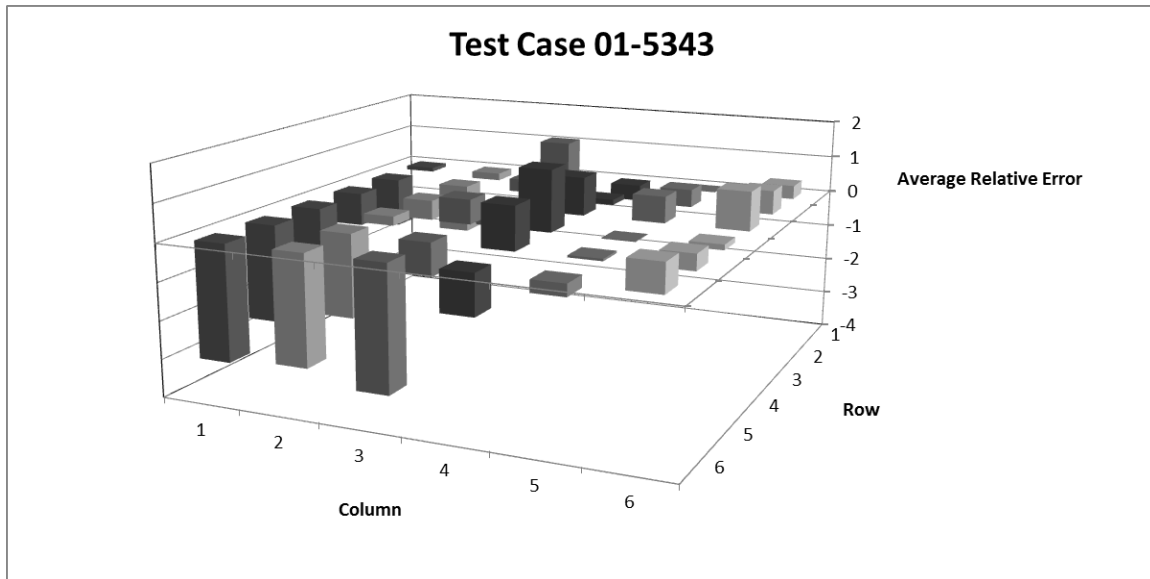


Figure AV.1 Test Case 01-5343 All Participants - Average Relative Error of Calculated Fluid Temperature

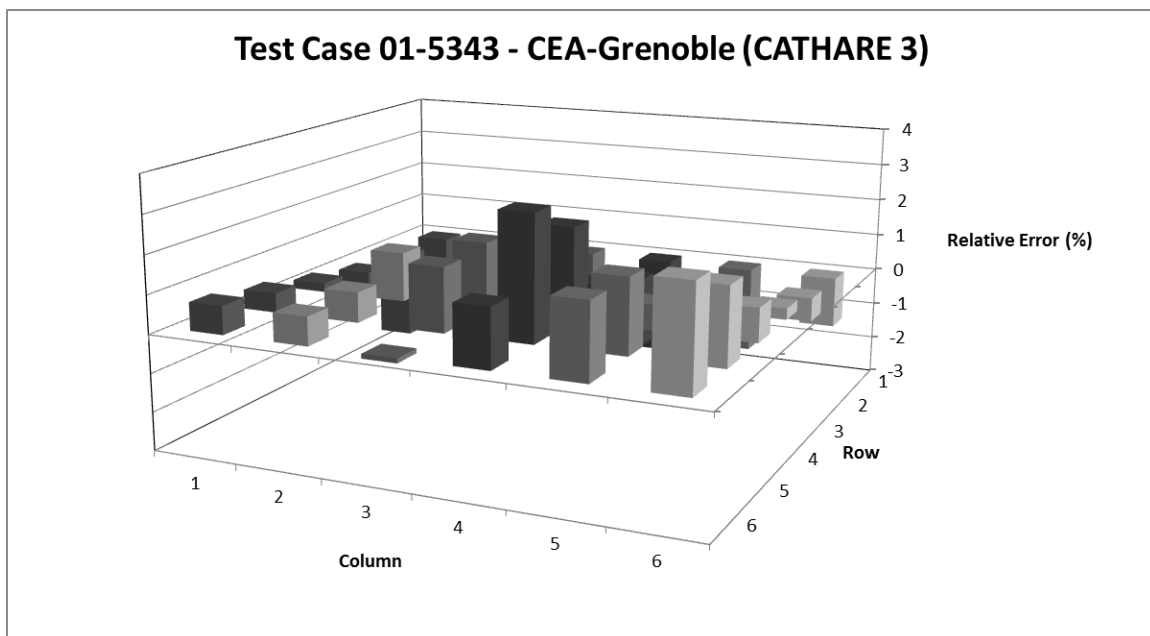


Figure AV.2 Test Case 01-5343 CATHARE 3 –Relative Error of Calculated Fluid Temperature

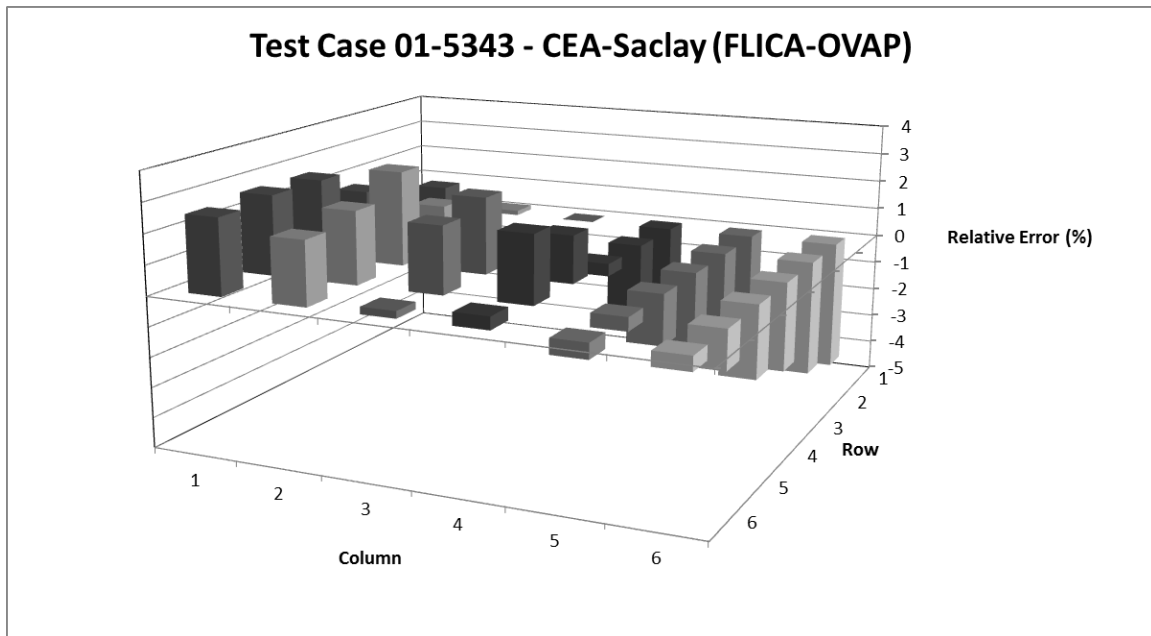


Figure AV.3 Test Case 01-5343 FLICA-OVAP – Relative Error of Calculated Fluid Temperature

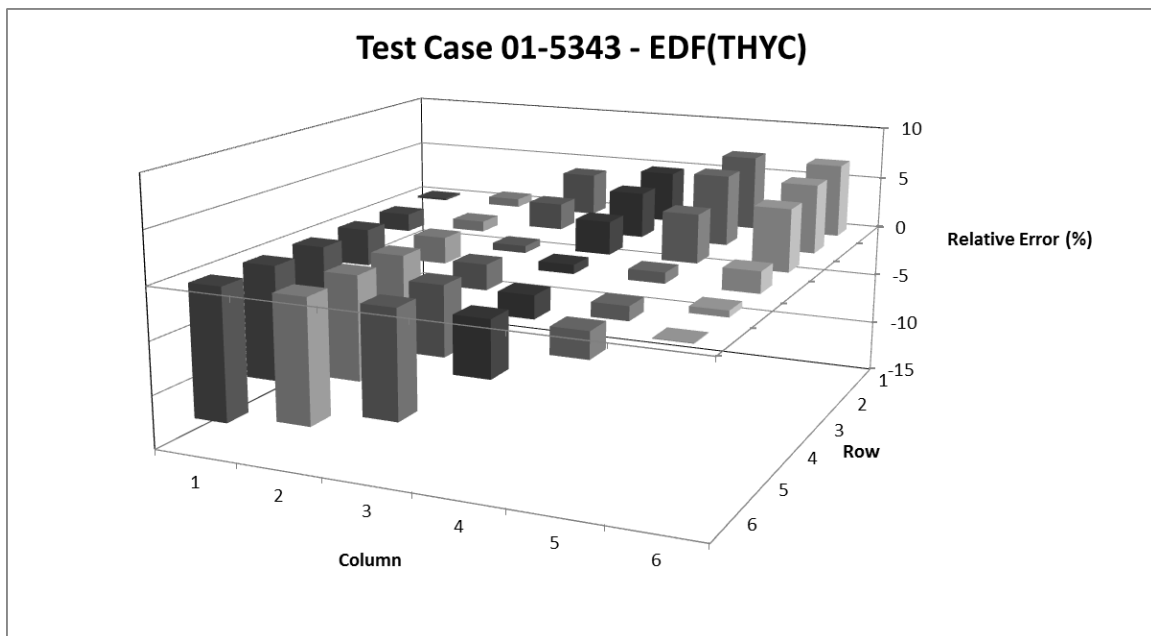


Figure AV.4 Test Case 01-5343 THYC – Relative Error of Calculated Fluid Temperature

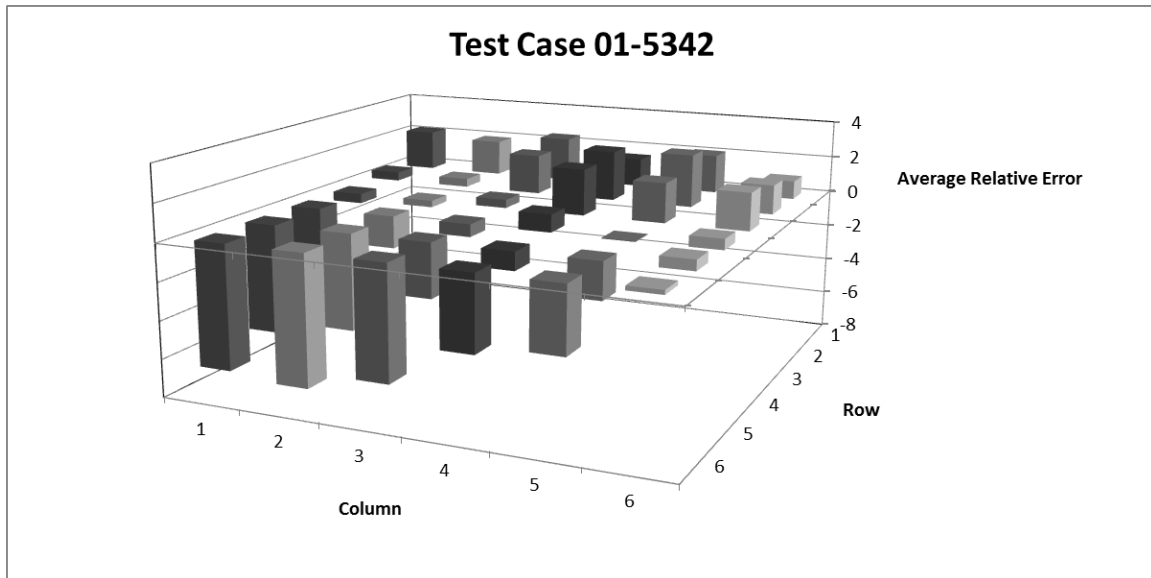


Figure AV.5 Test Case 01-5342 All Participants – Average Relative Error of Calculated Fluid Temperature

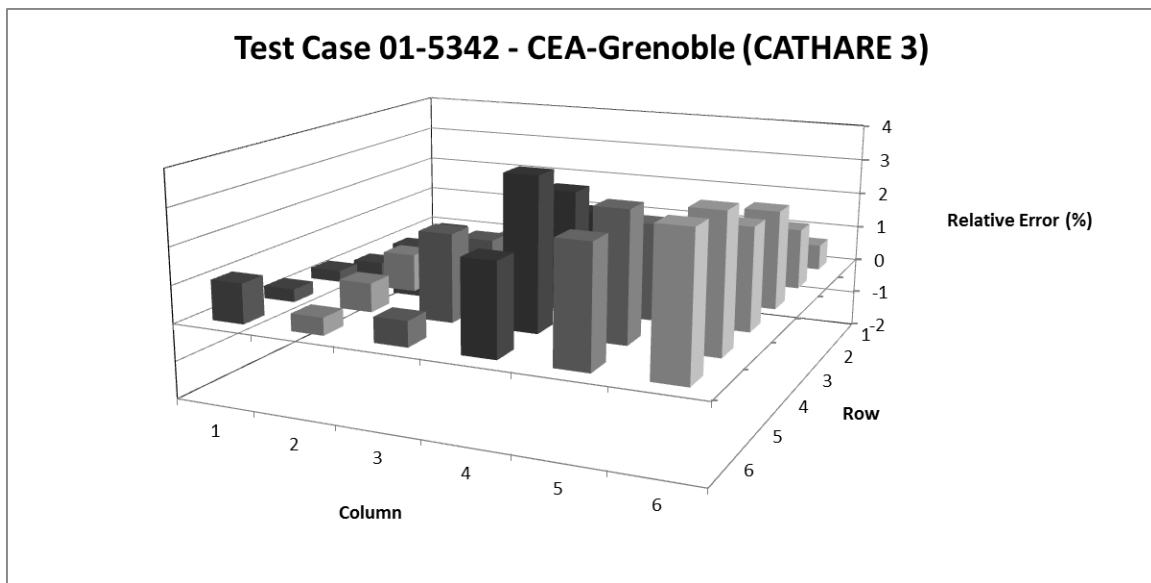


Figure AV.6 Test Case 01-5342 CATHARE 3 – Relative Error of Calculated Fluid Temperature

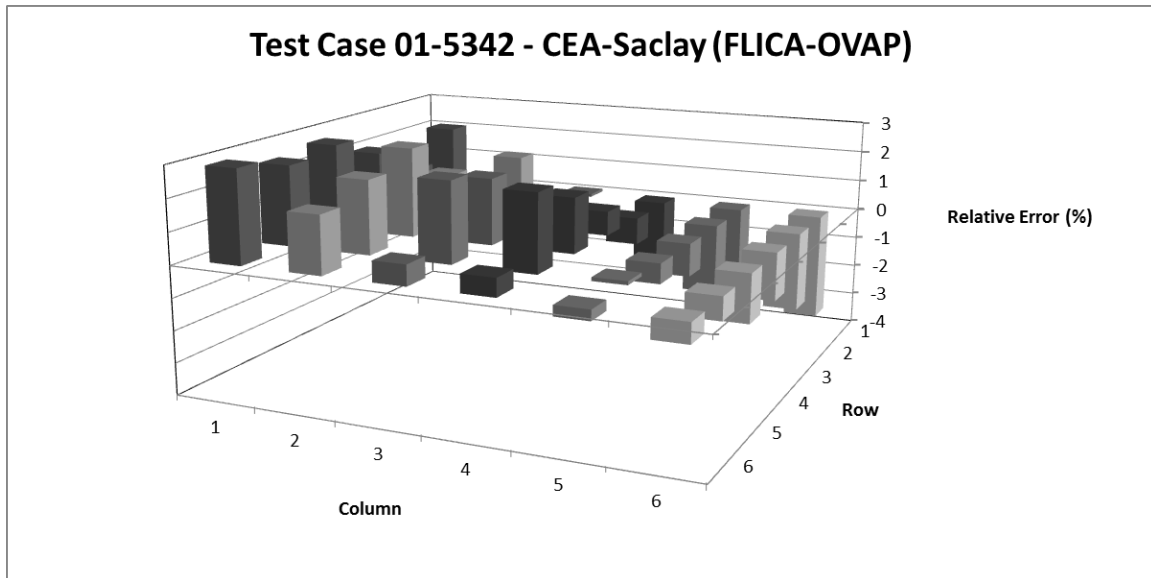


Figure AV.7 Test Case 01-5342 FLICA-OVAP – Relative Error of Calculated Fluid Temperature

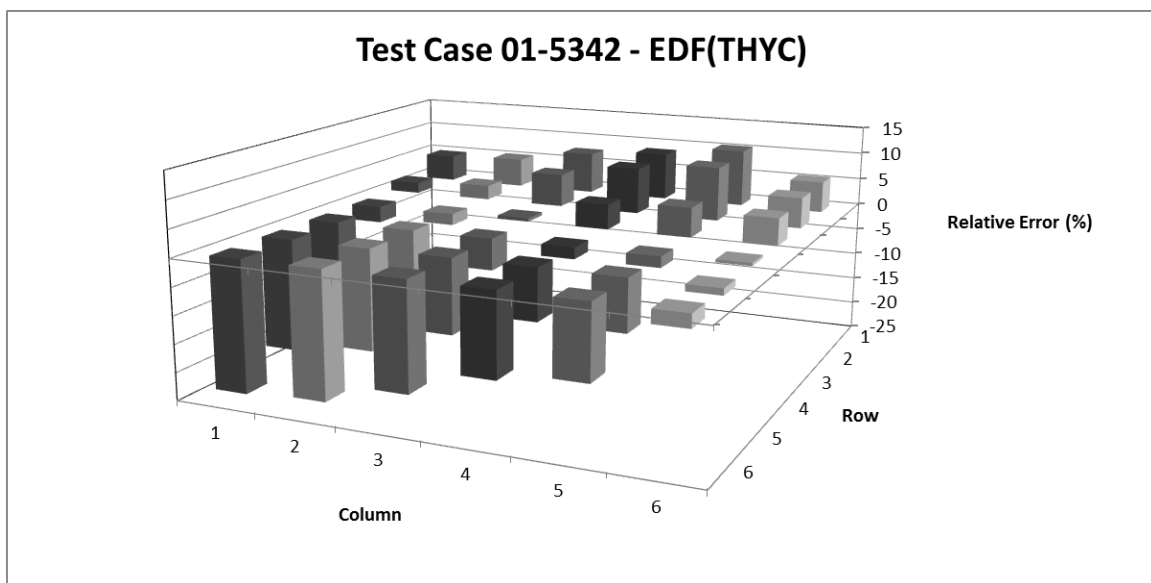


Figure AV.8 Test Case 01-5342 THYC – Relative Error of Calculated Fluid Temperature

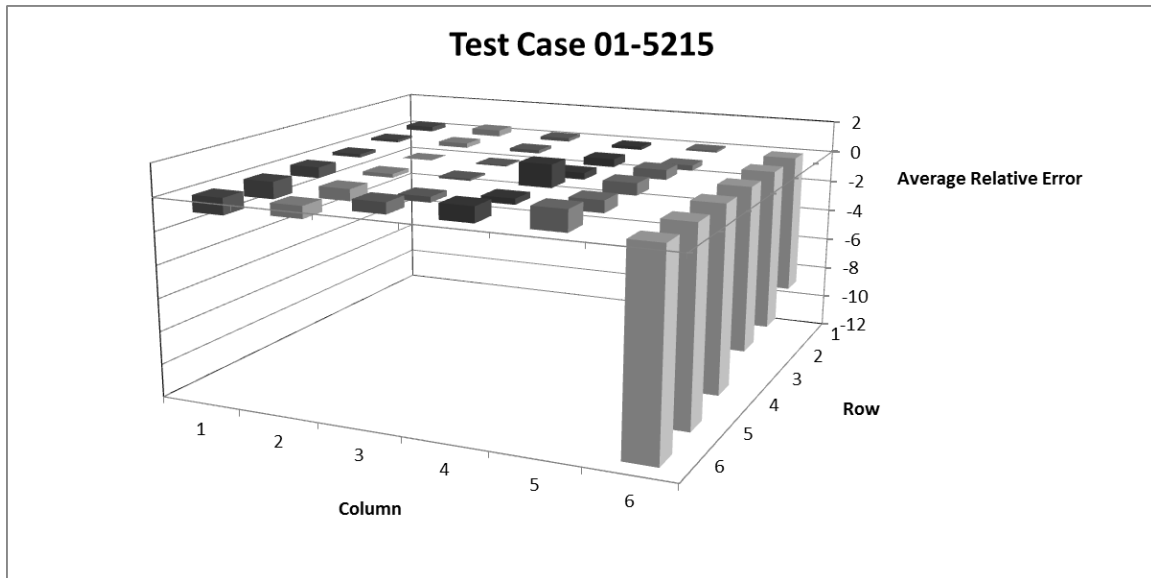


Figure AV.9 Test Case 01-5215 All Participants – Average Relative Error of Calculated Fluid Temperature

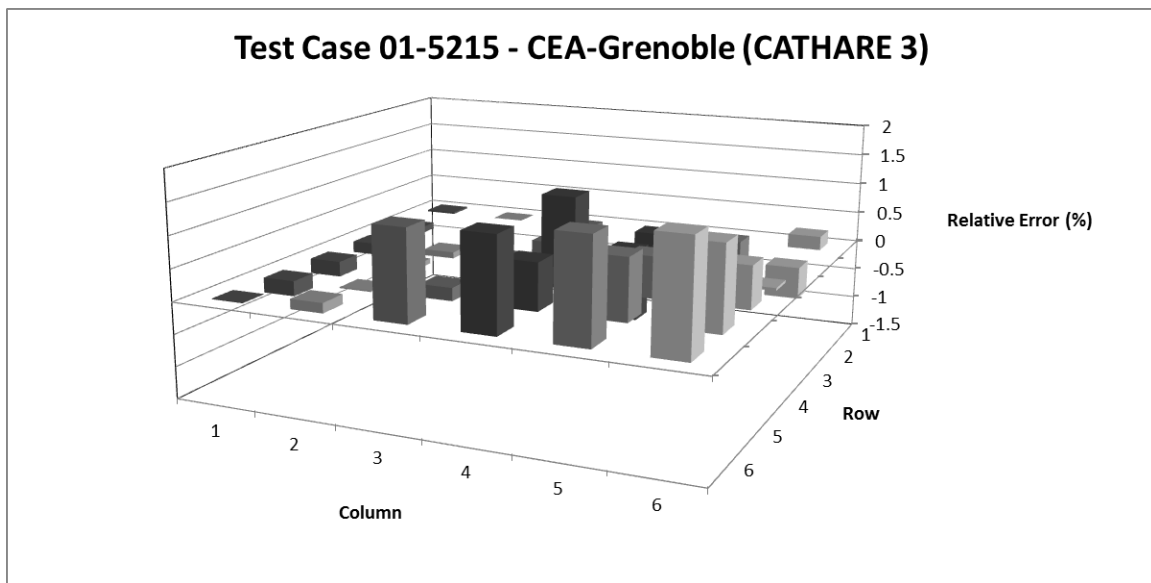


Figure AV.10 Test Case 01-5215 CATHARE 3 – Relative Error of Calculated Fluid Temperature

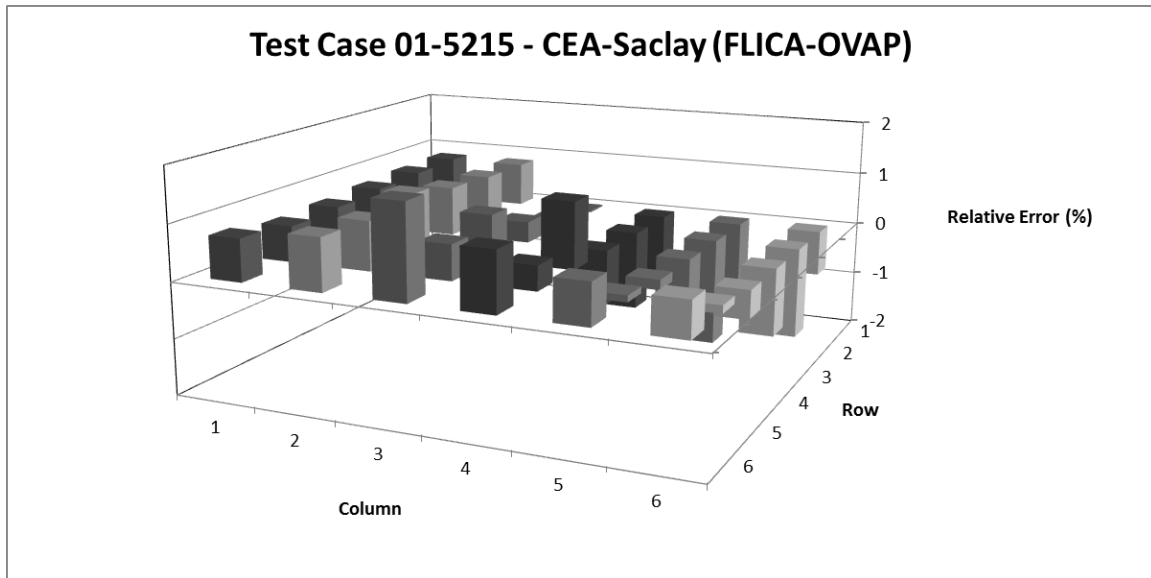


Figure AV.11 Test Case 01-5215 FLICA-OVAP – Relative Error of Calculated Fluid Temperature

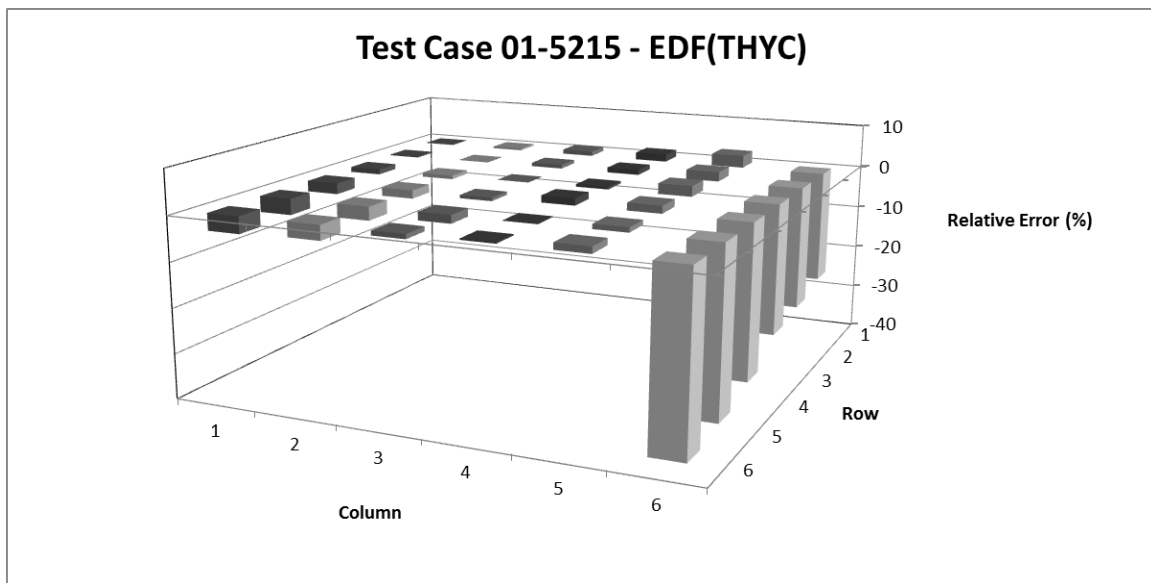


Figure AV.12 Test Case 01-5215 THYC – Relative Error of Calculated Fluid Temperature

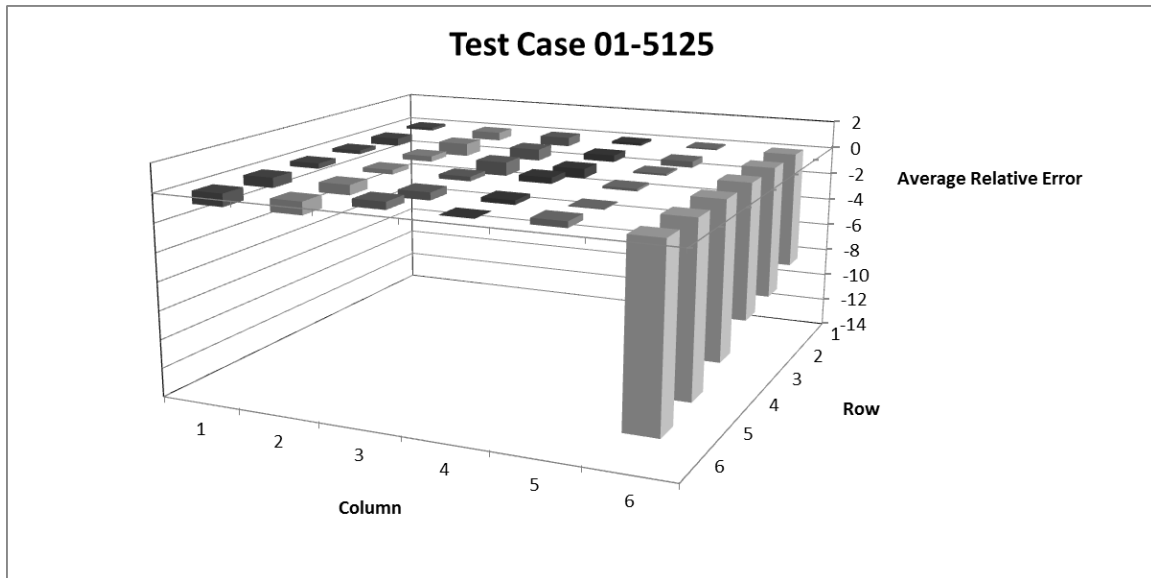


Figure AV.13 Test Case 01-5125 All Participants – Average Relative Error of Calculated Fluid Temperature

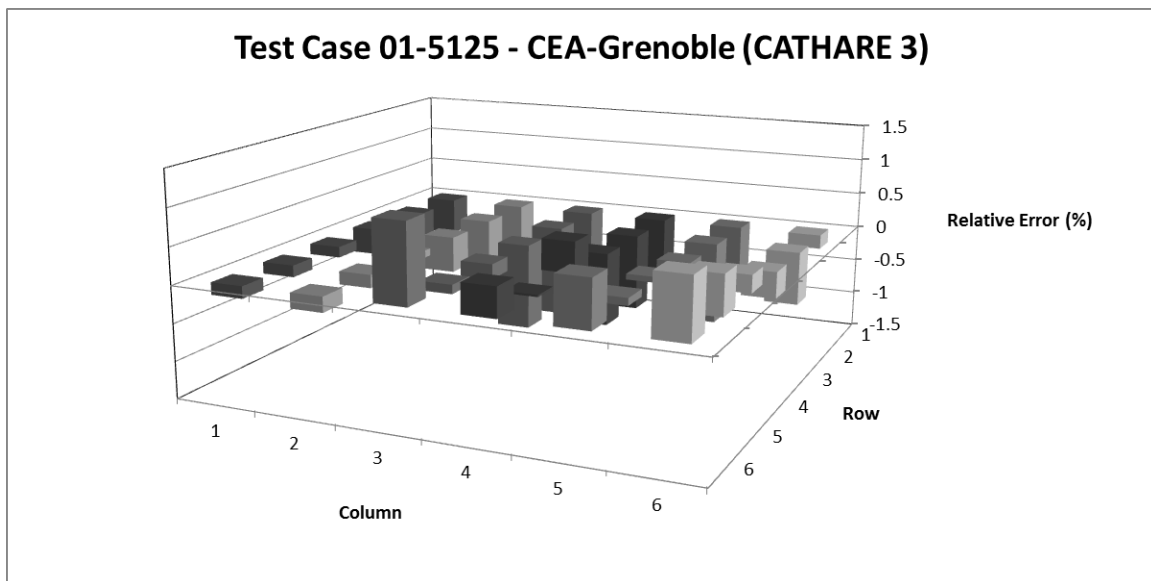


Figure AV.14 Test Case 01-5125 CATHARE 3 – Relative Error of Calculated Fluid Temperature

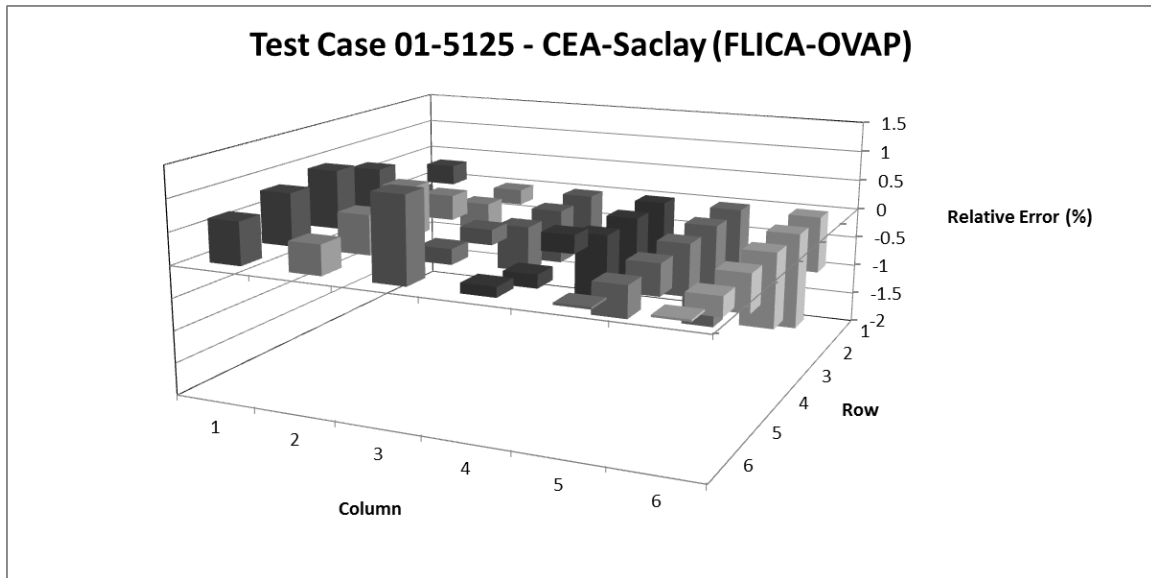


Figure AV.15 Test Case 01-5125 FLICA-OVAP – Relative Error of Calculated Fluid Temperature

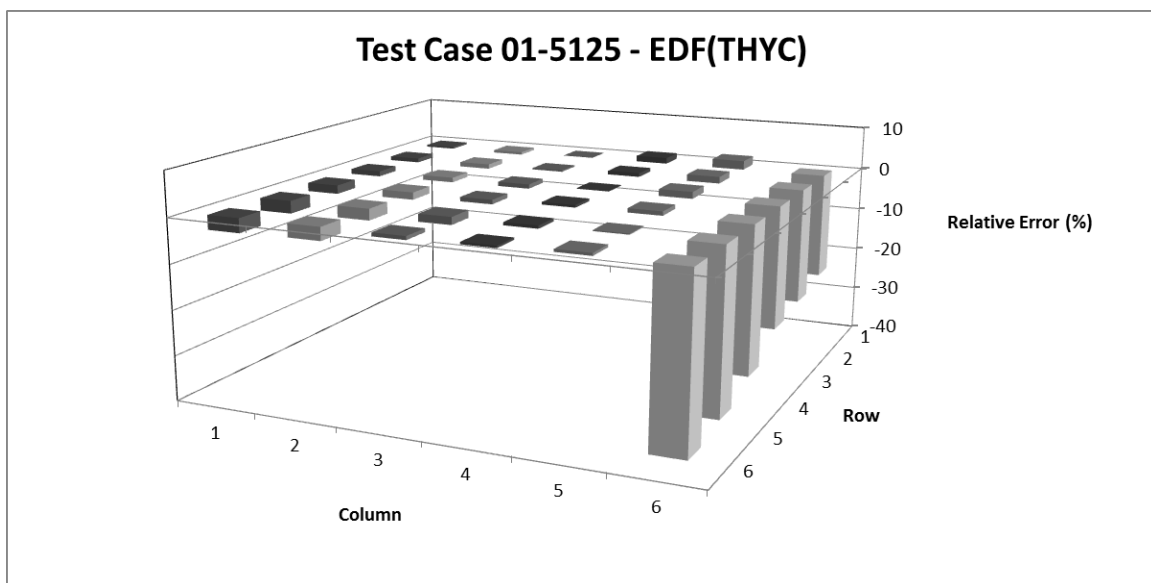


Figure AV.16 Test Case 01-5125 THYC – Relative Error of Calculated Fluid Temperature

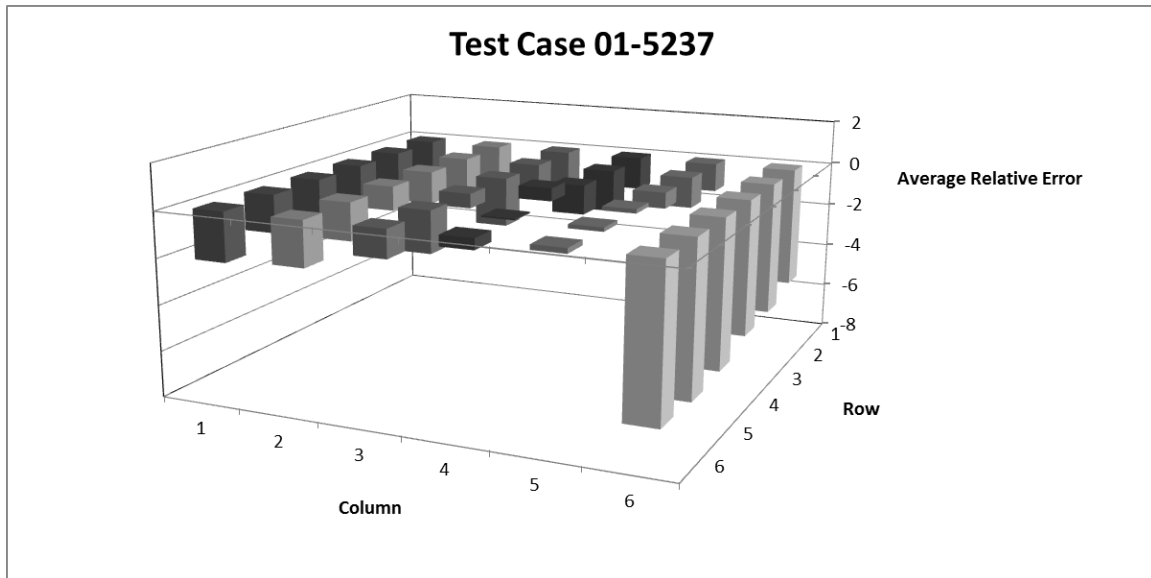


Figure AV.17 Test Case 01-5237 All Participants – Average Relative Error of Calculated Fluid Temperature

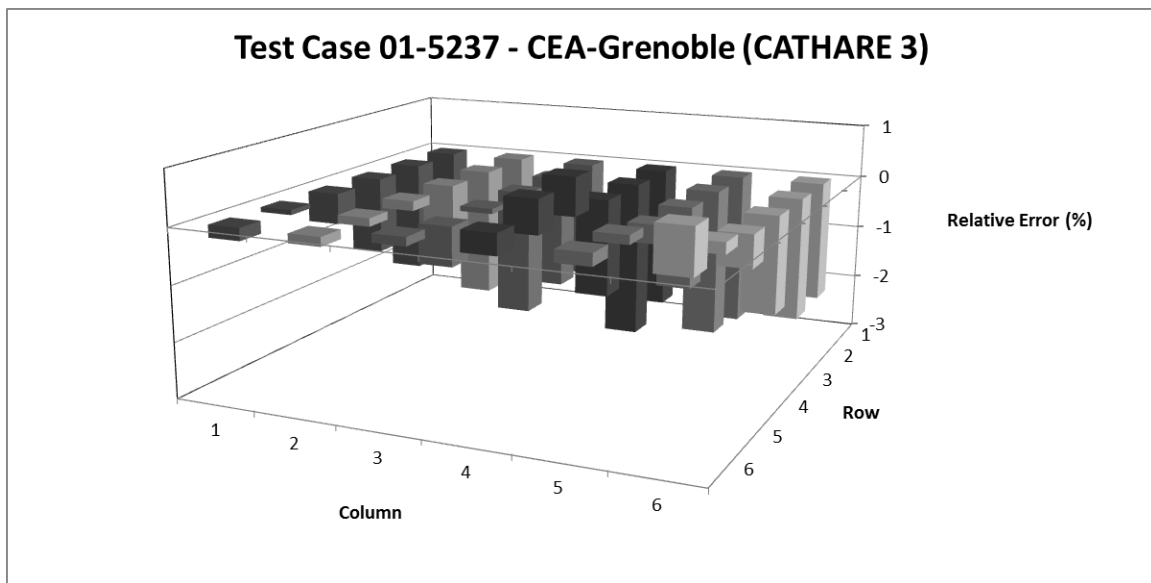


Figure AV.18 Test Case 01-5237 CATHARE 3 – Relative Error of Calculated Fluid Temperature

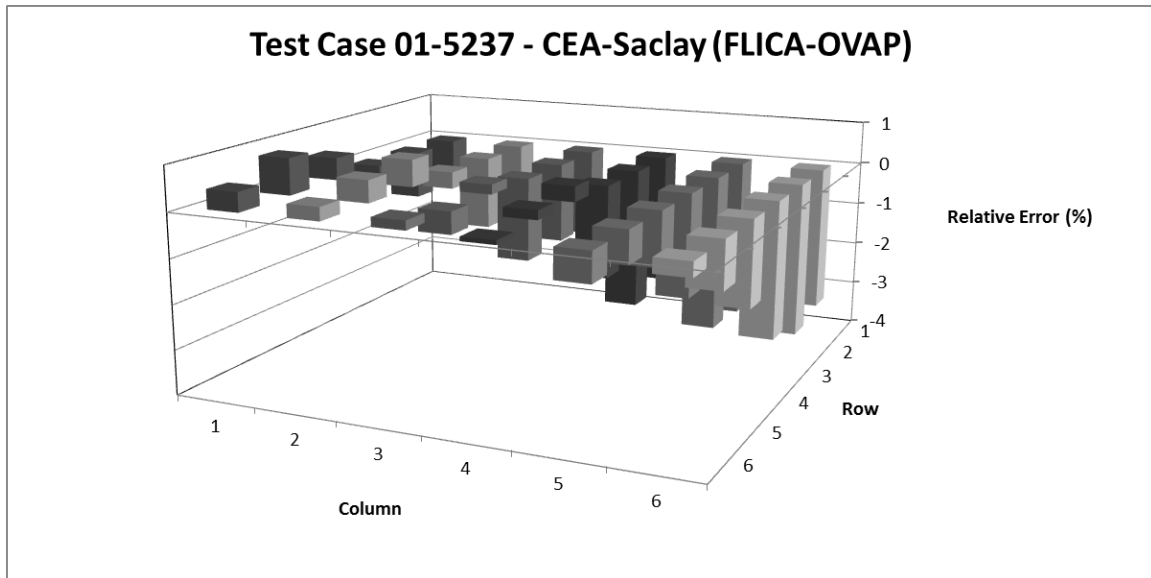


Figure AV.19 Test Case 01-5237 FLICA-OVAP – Relative Error of Calculated Fluid Temperature

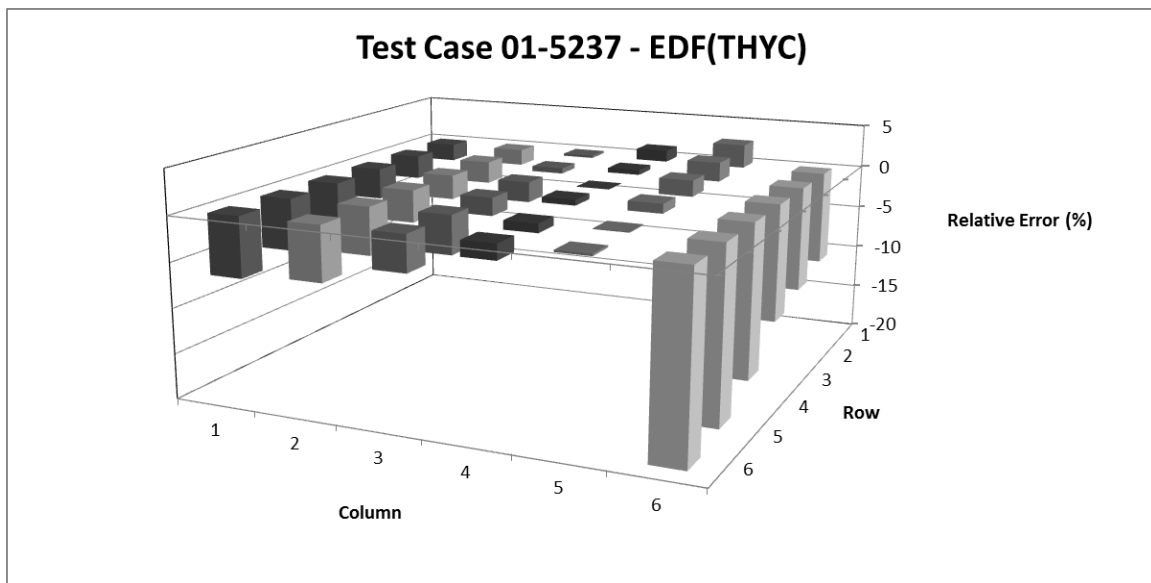


Figure AV.20 Test Case 01-5237 FLICA-OVAP – Relative Error of Calculated Fluid Temperature

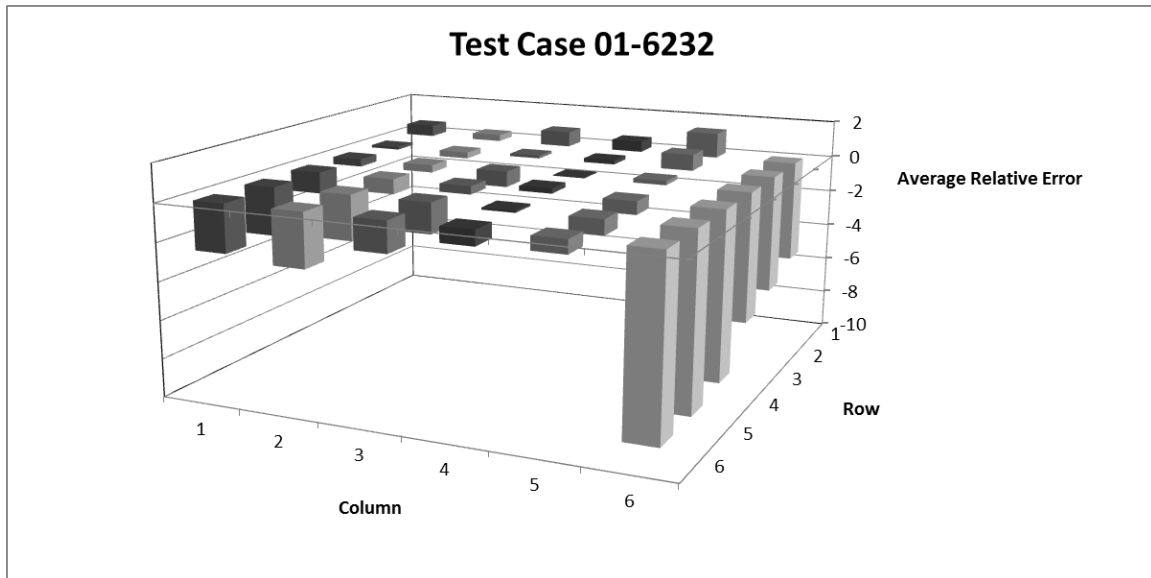


Figure AV.21 Test Case 01-6232 All Participants – Average Relative Error of Calculated Fluid Temperature

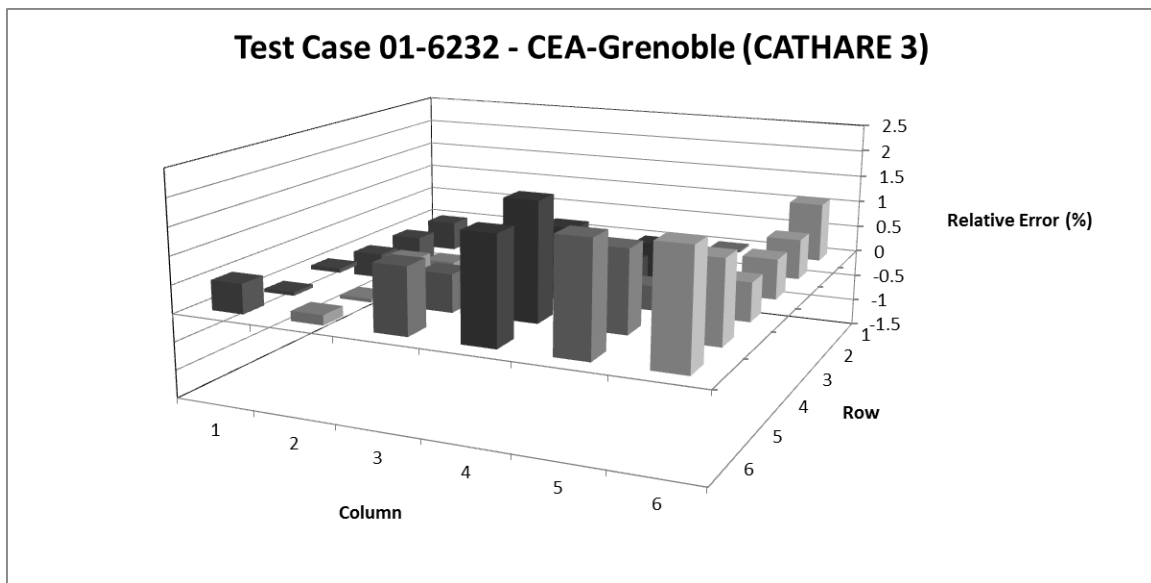


Figure AV.22 Test Case 01-6232 CATHARE 3 – Relative Error of Calculated Fluid Temperature

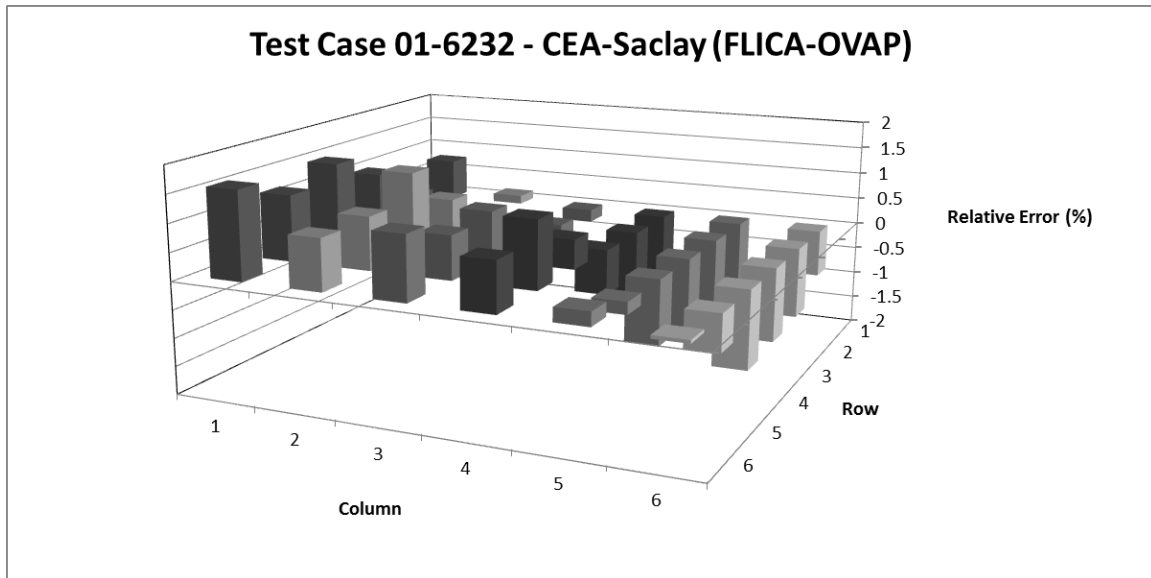


Figure AV.23 Test Case 01-6232 FLICA-OVAP – Relative Error of Calculated Fluid Temperature

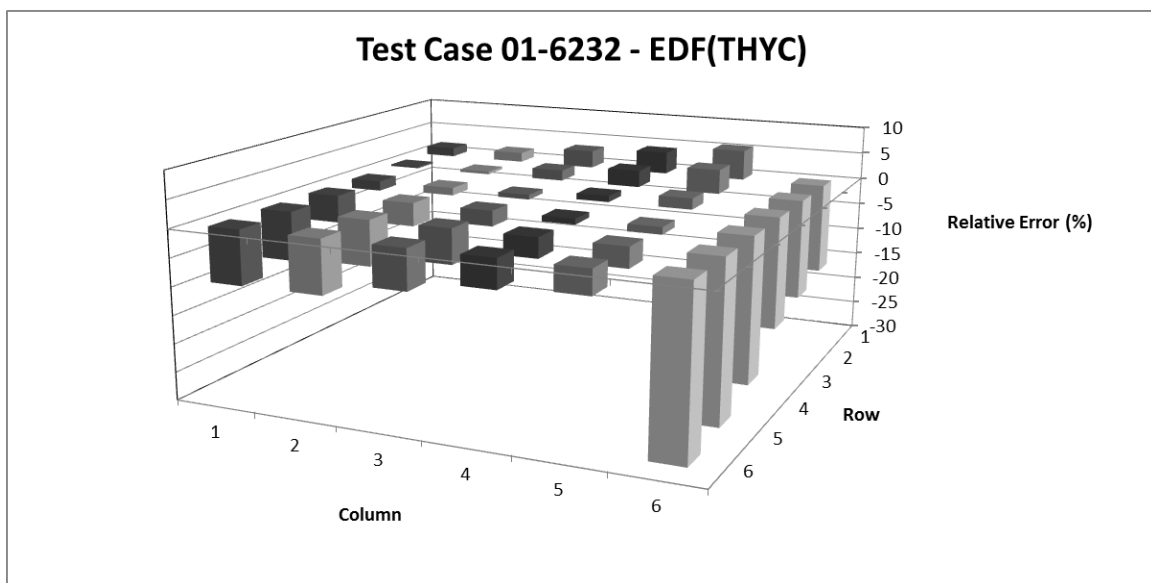


Figure AV.24 Test Case 01-6232 THYC – Relative Error of Calculated Fluid Temperature

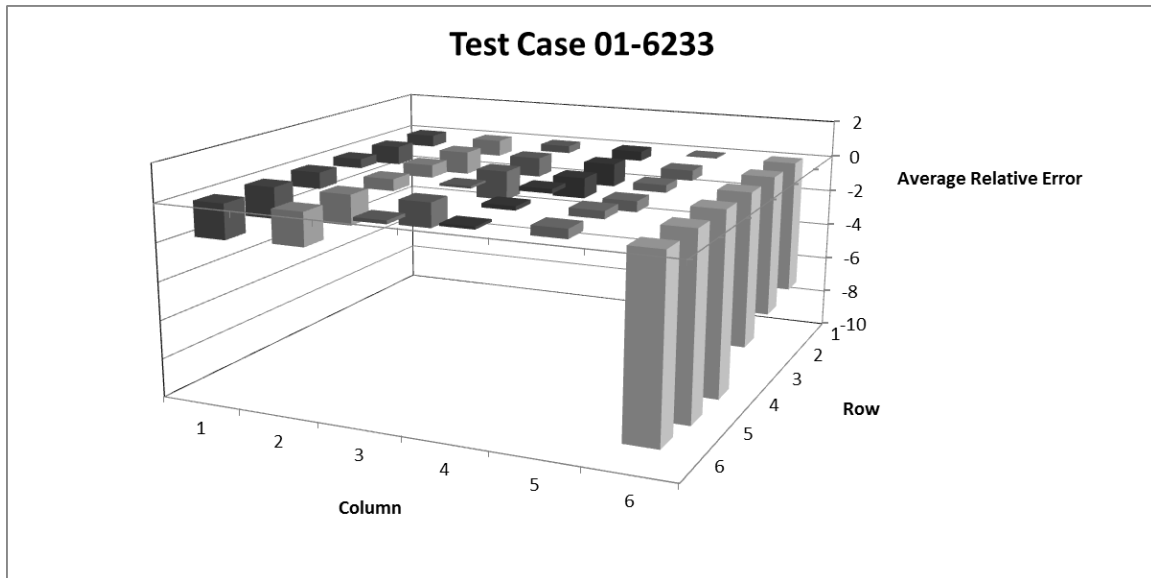


Figure AV.25 Test Case 01-6233 All Participants – Average Relative Error of Calculated Fluid Temperature

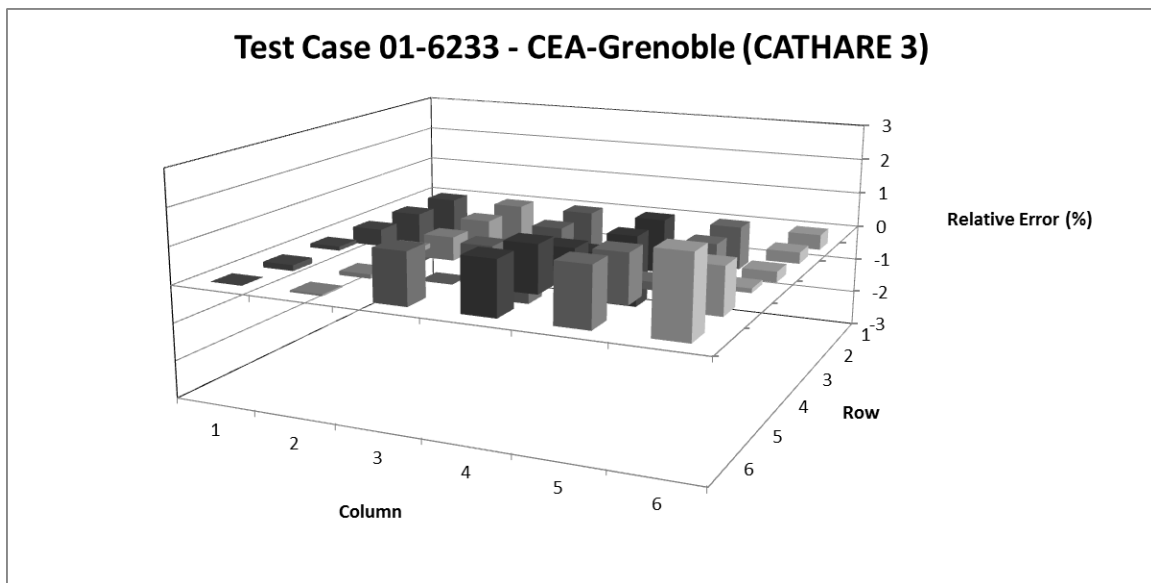


Figure AV.26 Test Case 01-6233 CATHARE 3 – Relative Error of Calculated Fluid Temperature

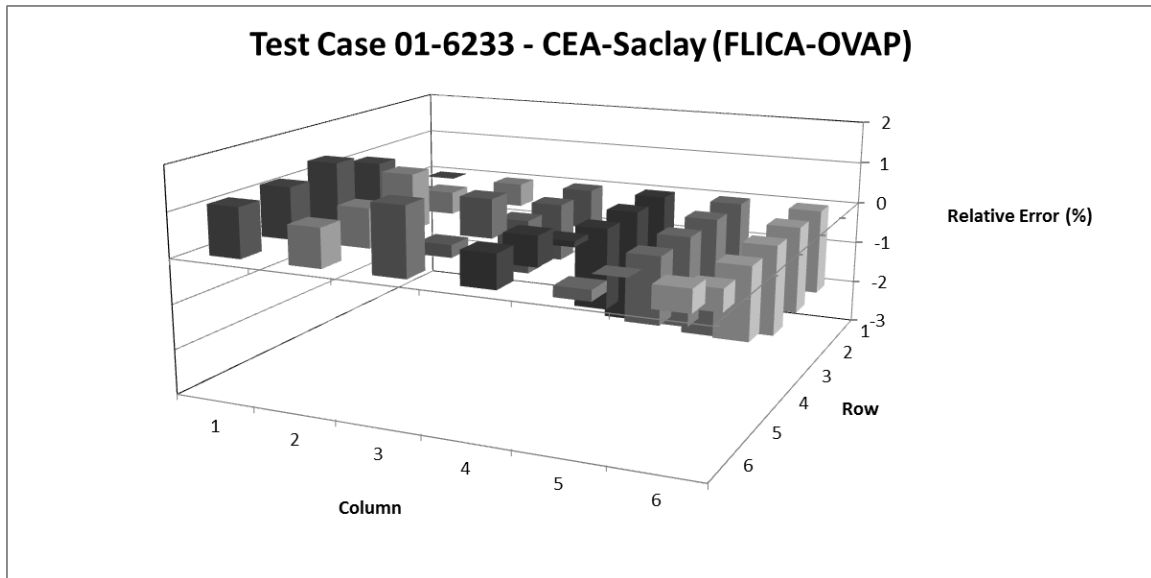


Figure AV.27 Test Case 01-6233 FLICA-OVAP – Relative Error of Calculated Fluid Temperature

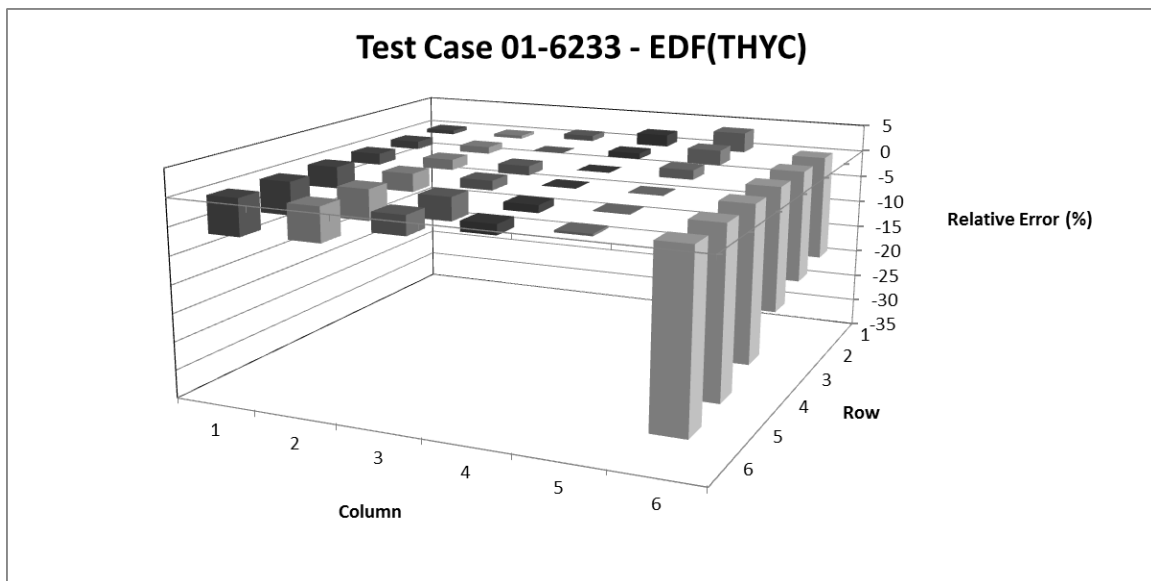


Figure AV.28 Test Case 01-6233 THYC – Relative Error of Calculated Fluid Temperature

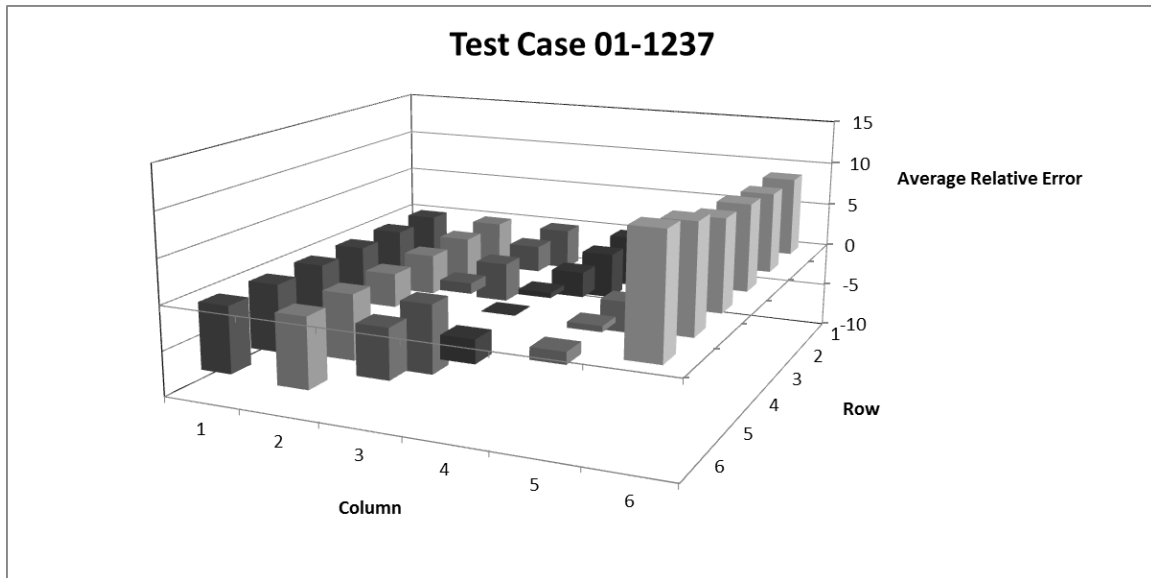


Figure AV.29 Test Case 01-1237 All Participants – Average Relative Error of Calculated Fluid Temperature

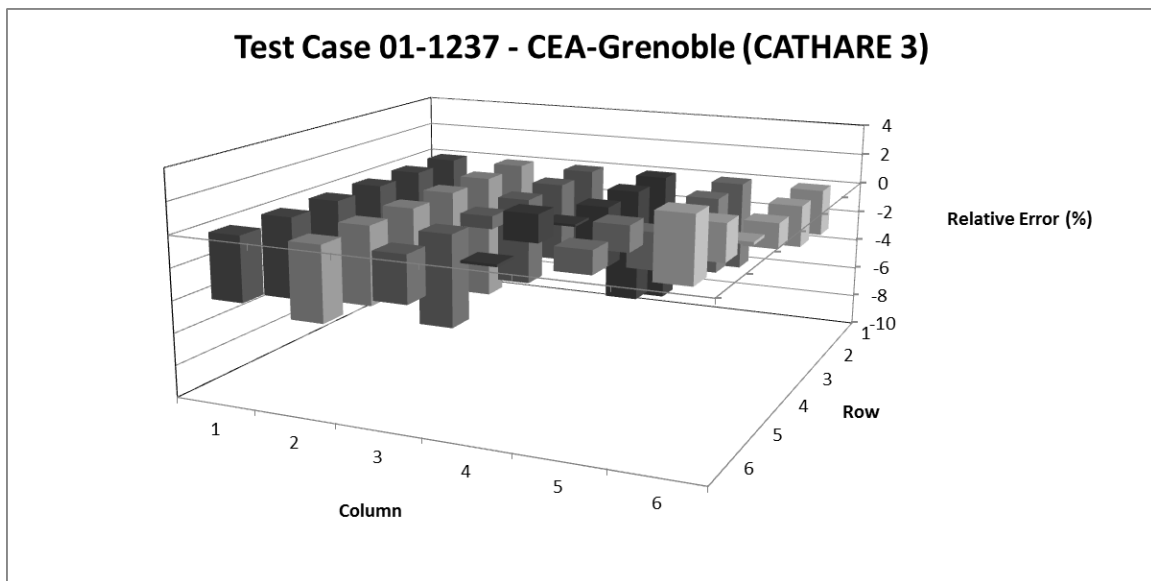


Figure AV.30 Test Case 01-1237 CATHARE 3 – Relative Error of Calculated Fluid Temperature

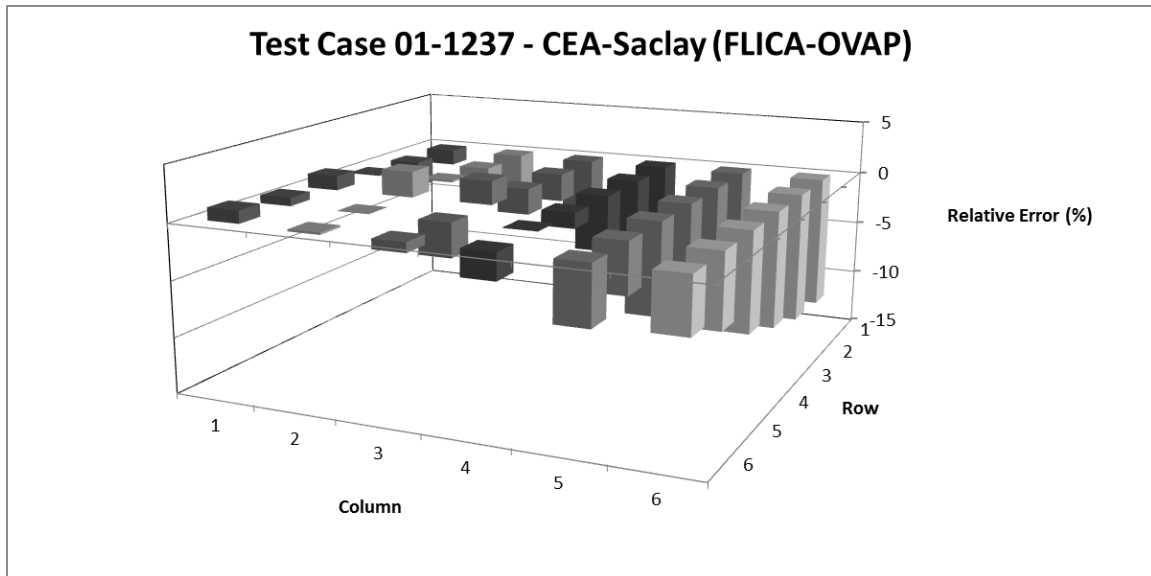


Figure AV.31 Test Case 01-1237 FLICA-OVAP – Relative Error of Calculated Fluid Temperature

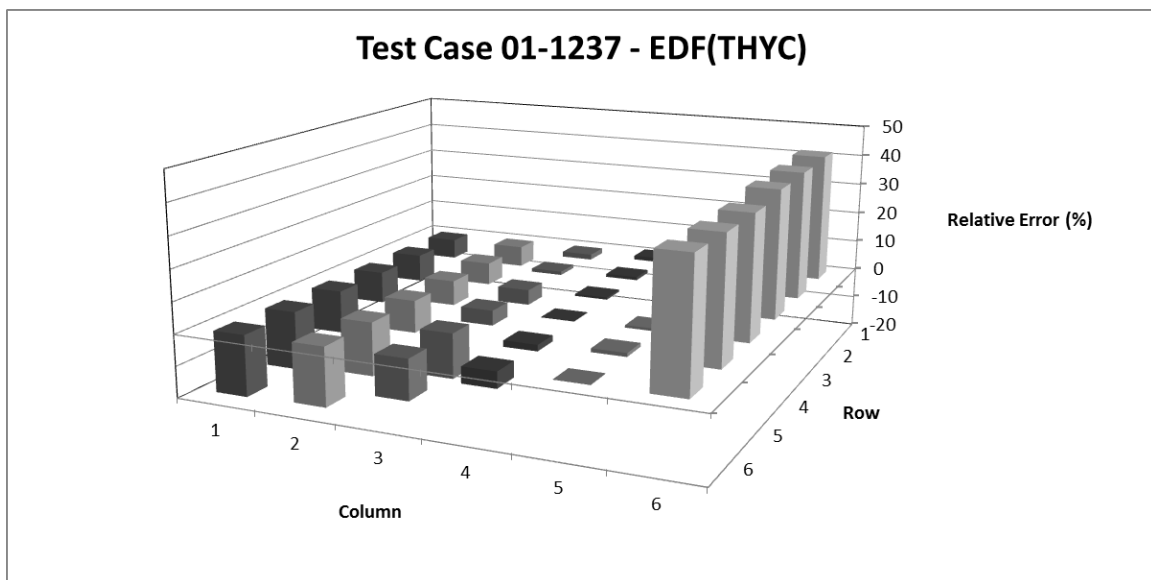


Figure AV.32 Test Case 01-1237 THYC – Relative Error of Calculated Fluid Temperature

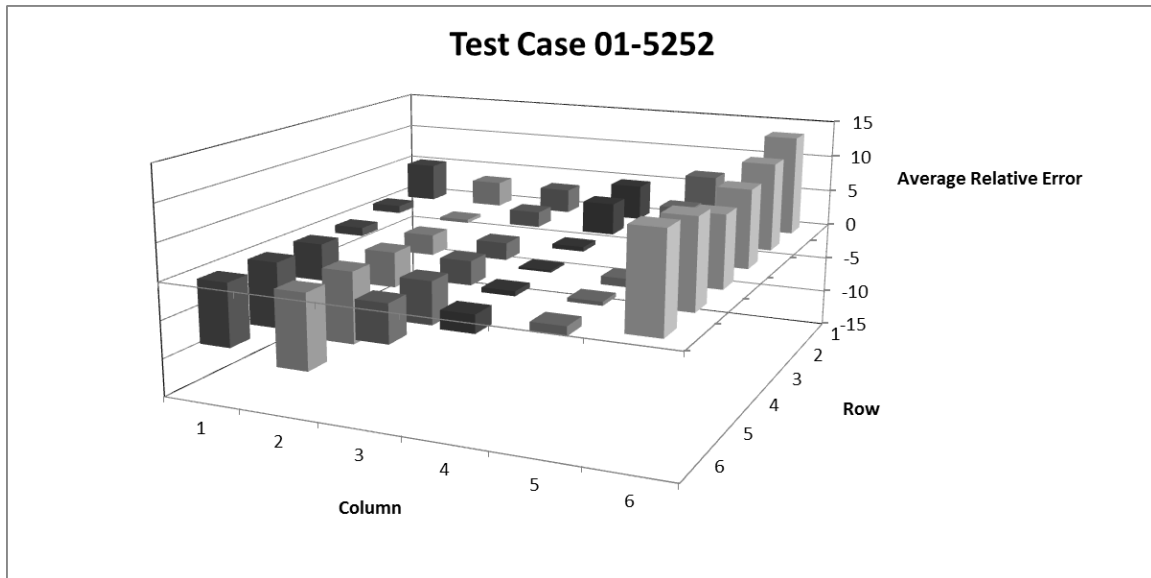


Figure AV.33 Test Case 01-5252 All Participants – Average Relative Error of Calculated Fluid Temperature

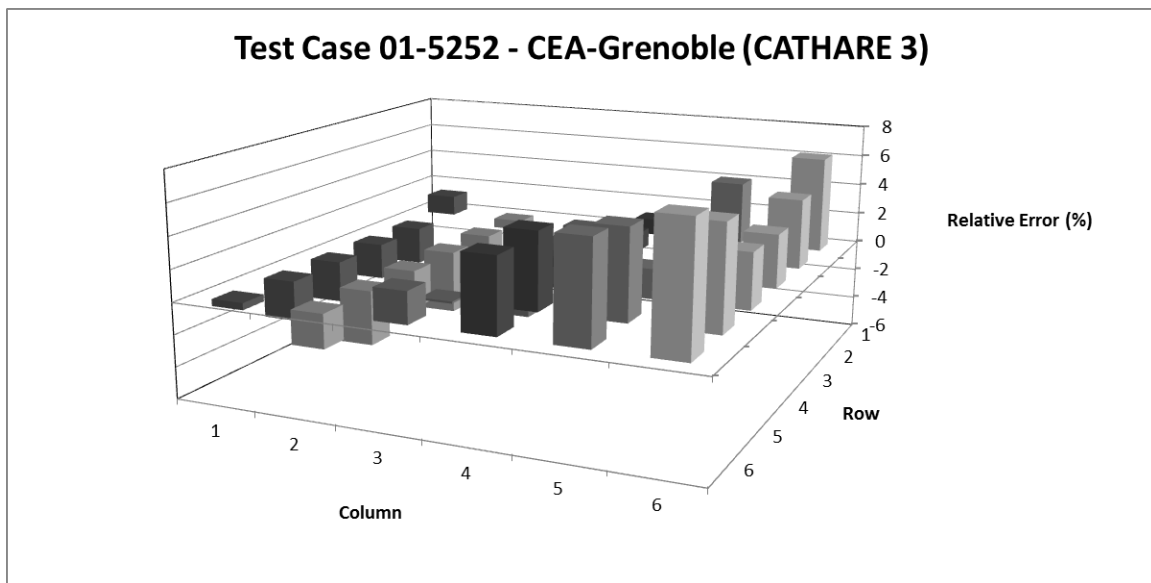


Figure AV.34 Test Case 01-5252 CATHARE 3 – Relative Error of Calculated Fluid Temperature

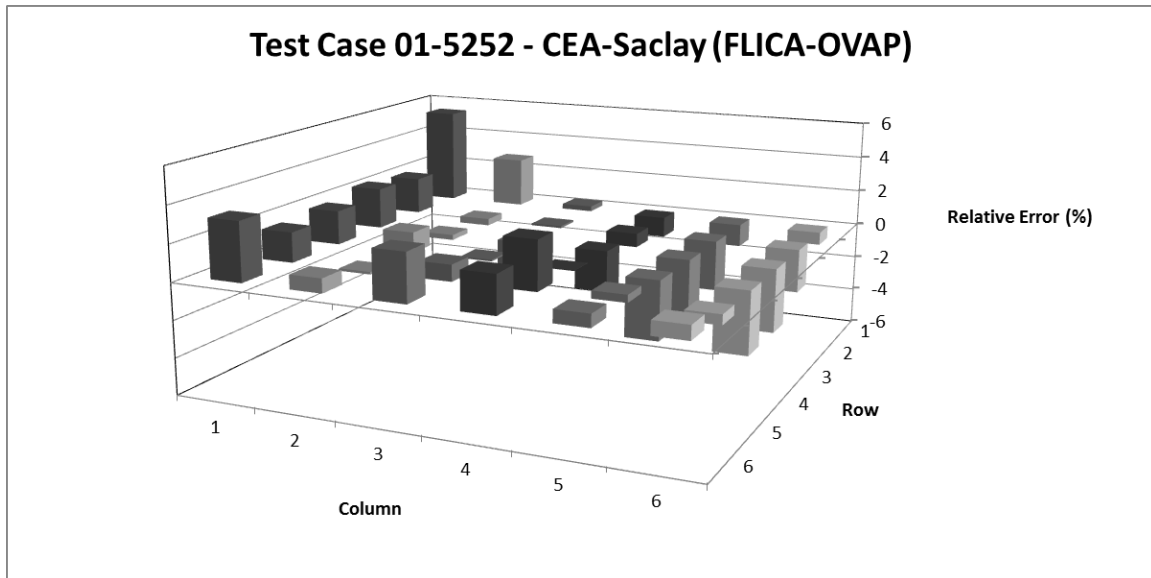


Figure AV.35 Test Case 01-5252 FLICA-OVAP – Relative Error of Calculated Fluid Temperature

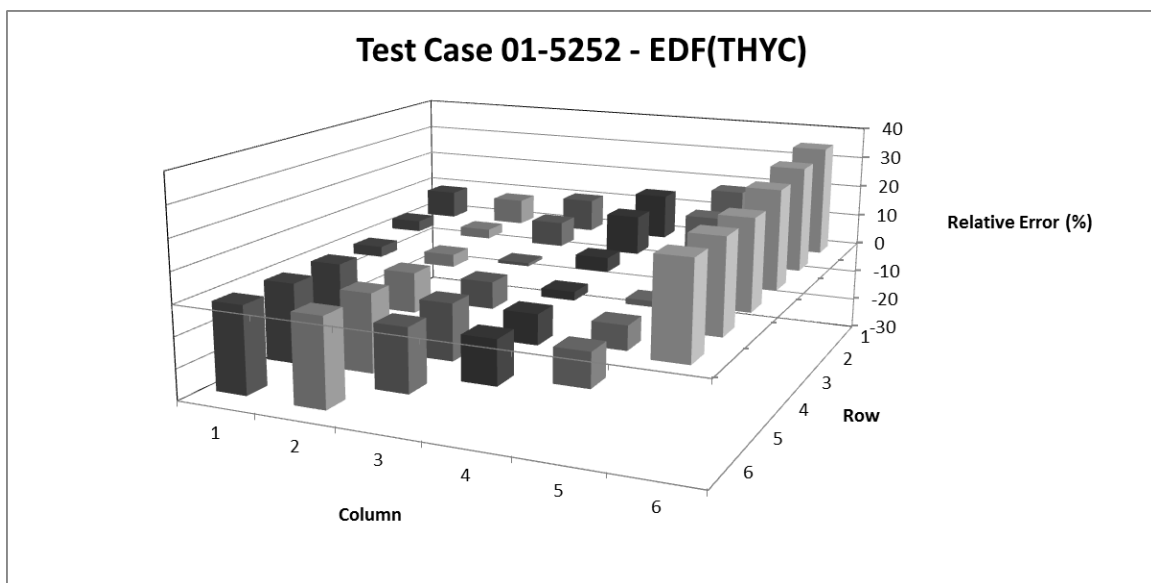


Figure AV.36 Test Case 01-5252 THYC – Relative Error of Calculated Fluid Temperature

Table AV.1 Relative Error (%) by Subchannel Type

		CEA-Grenoble (CATHARE 3)	CEA-Saclay (FLICA-OVAP)	EDF (THYC)
Test Case 01-5343	Corner	0.171	-0.397	-1.331
	Central	0.364	0.205	-0.552
	Side	-0.195	-0.584	-1.313
Test Case 01-5342	Corner	1.255	0.229	-3.856
	Central	1.379	0.808	-2.125
	Side	0.770	-0.033	-3.743
Test Case 01-5215	Corner	0.485	0.341	-16.946
	Central	0.036	0.130	0.197
	Side	0.188	0.112	-8.270
Test Case 01-5125	Corner	-0.021	0.023	-16.318
	Central	-0.483	-0.352	-0.328
	Side	-0.242	-0.171	-8.093
Test Case 01-5237	Corner	-0.845	-1.045	-9.837
	Central	-1.056	-1.123	-1.149
	Side	-1.123	-1.281	-5.491
Test Case 01-6232	Corner	0.762	0.358	-13.456
	Central	0.150	-0.125	-1.277
	Side	0.309	-0.040	-7.412
Test Case 01-6233	Corner	0.107	-0.106	-14.199
	Central	-0.511	-0.604	-0.975
	Side	-0.178	-0.349	-7.405
Test Case 01-1237	Corner	-2.598	-4.345	13.733
	Central	-3.675	-3.542	-3.602
	Side	-4.044	-4.919	4.388
Test Case 01-5252	Corner	3.711	2.165	11.100
	Central	-0.160	-0.705	-2.618
	Side	1.369	0.298	3.701

Appendix VI Exercise II-2 Results

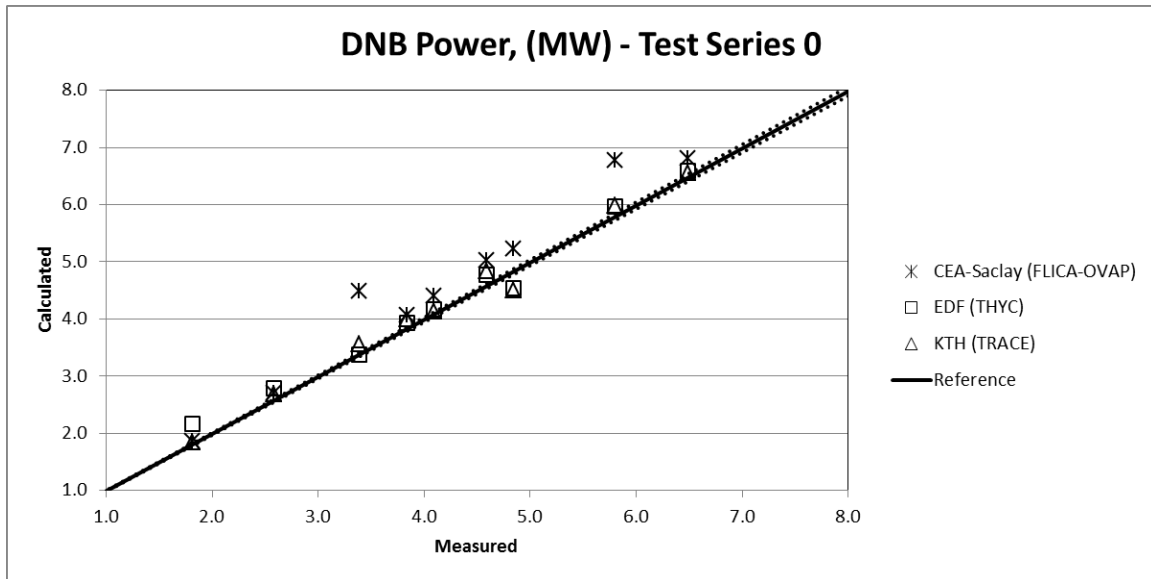


Figure AVI.1 Test Series 0 DNB Power Results

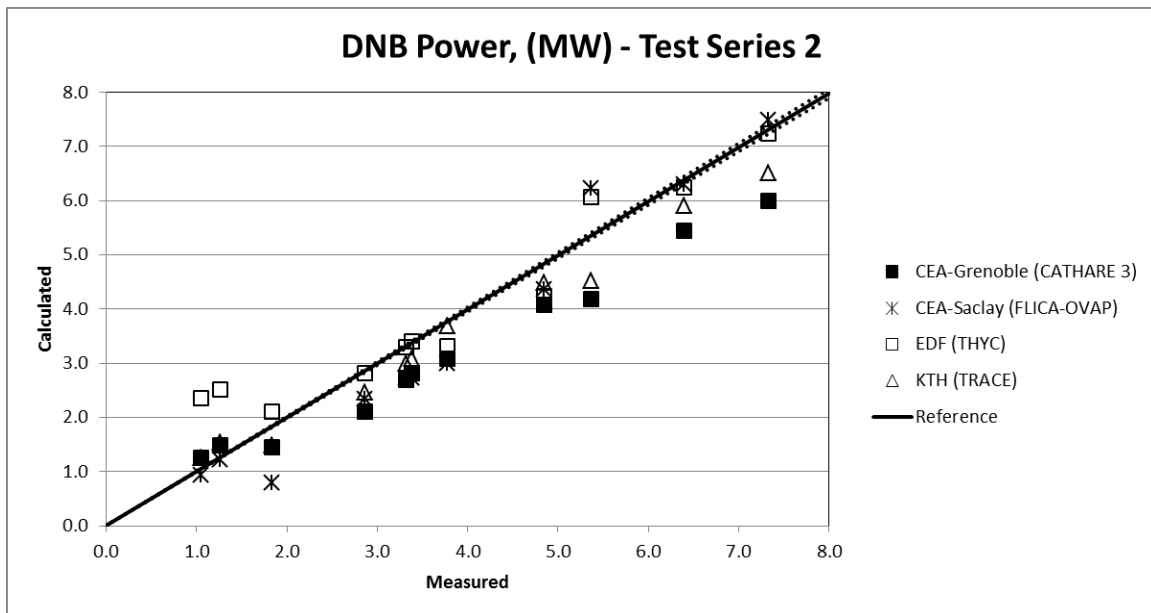


Figure AVI.2 Test Series 2 DNB Power Results

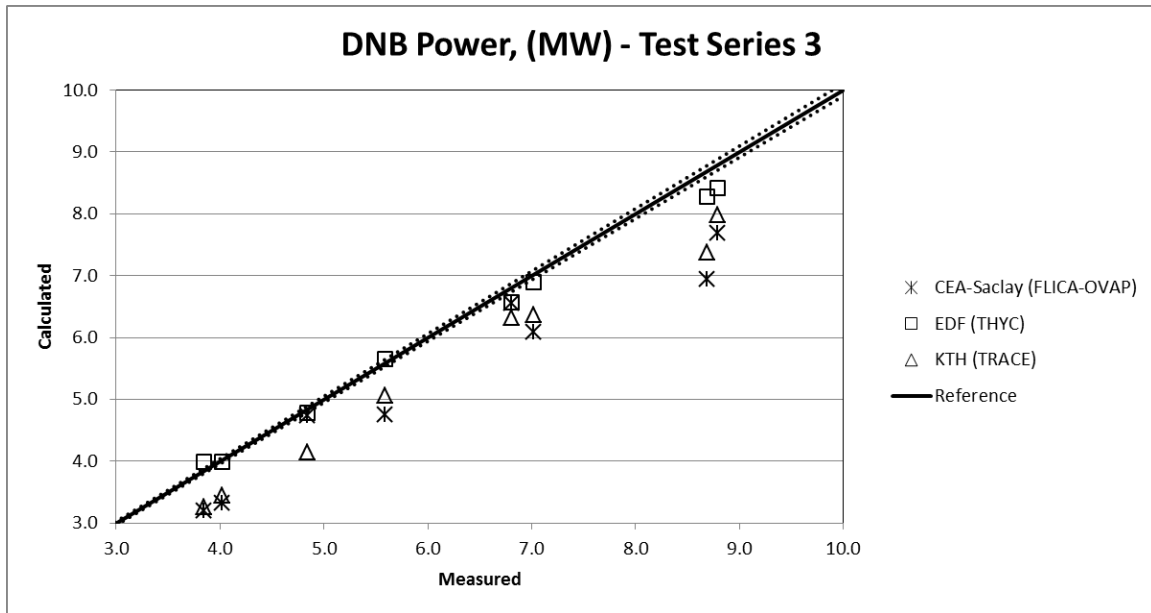


Figure AVI.3 Test Series 3 DNB Power Results

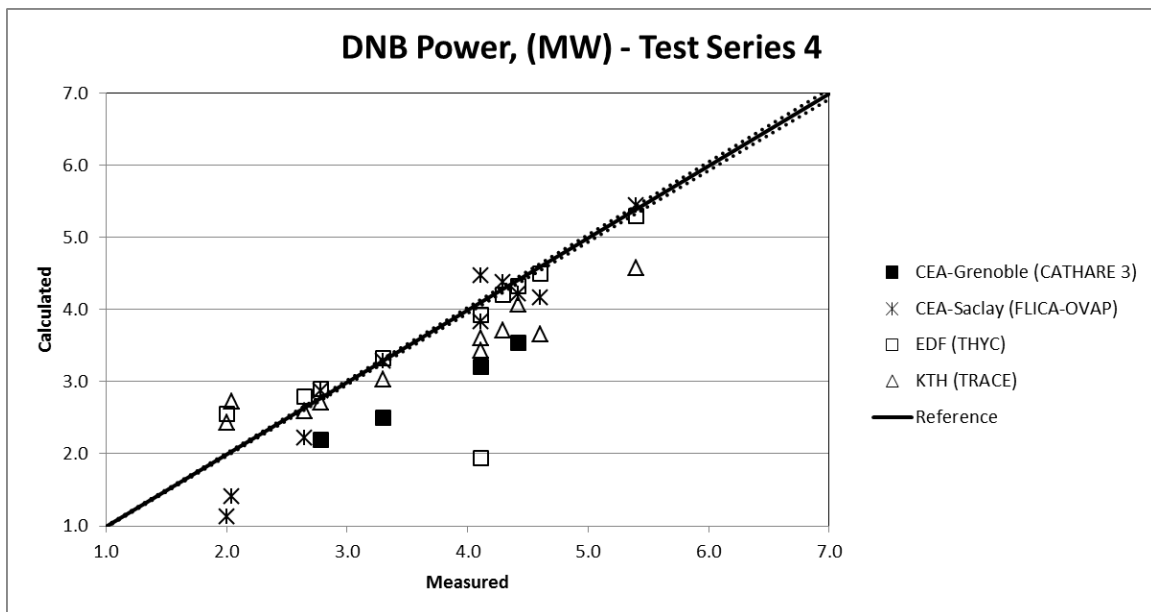


Figure AVI.4 Test Series 4 DNB Power Results

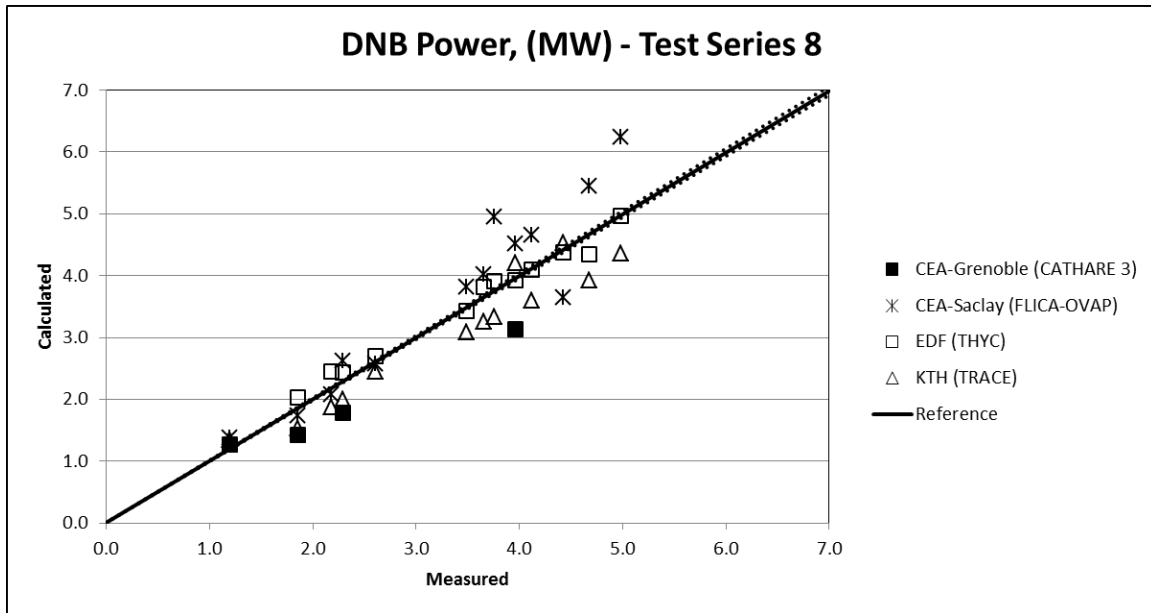


Figure AVI.5 Test Series 8 DNB Power Results

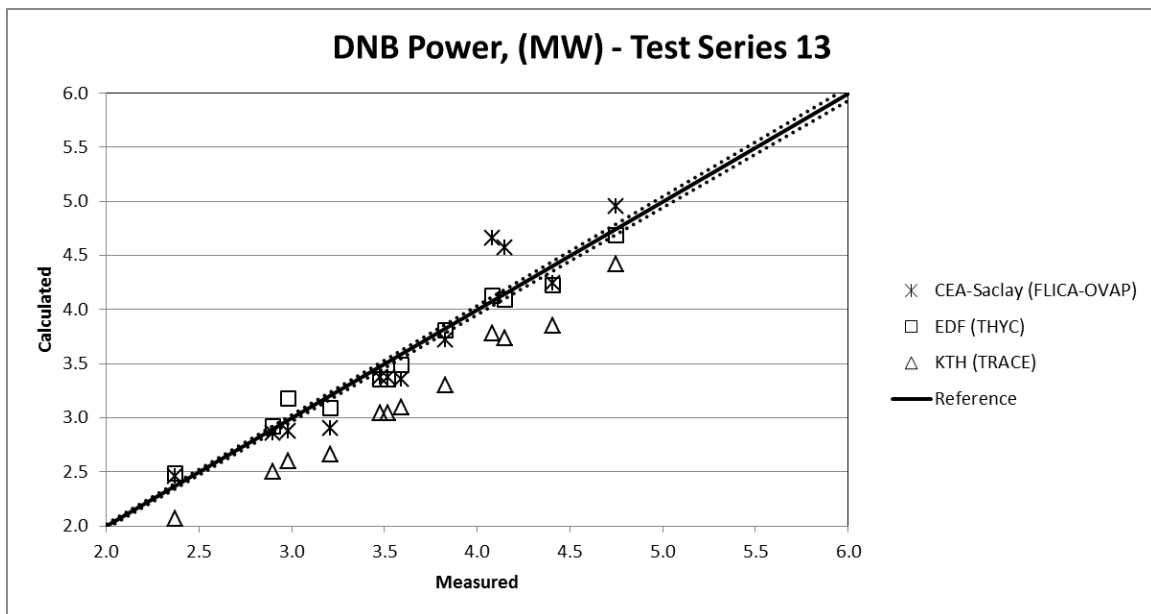


Figure AVI.6 Test Series 13 DNB Power Results

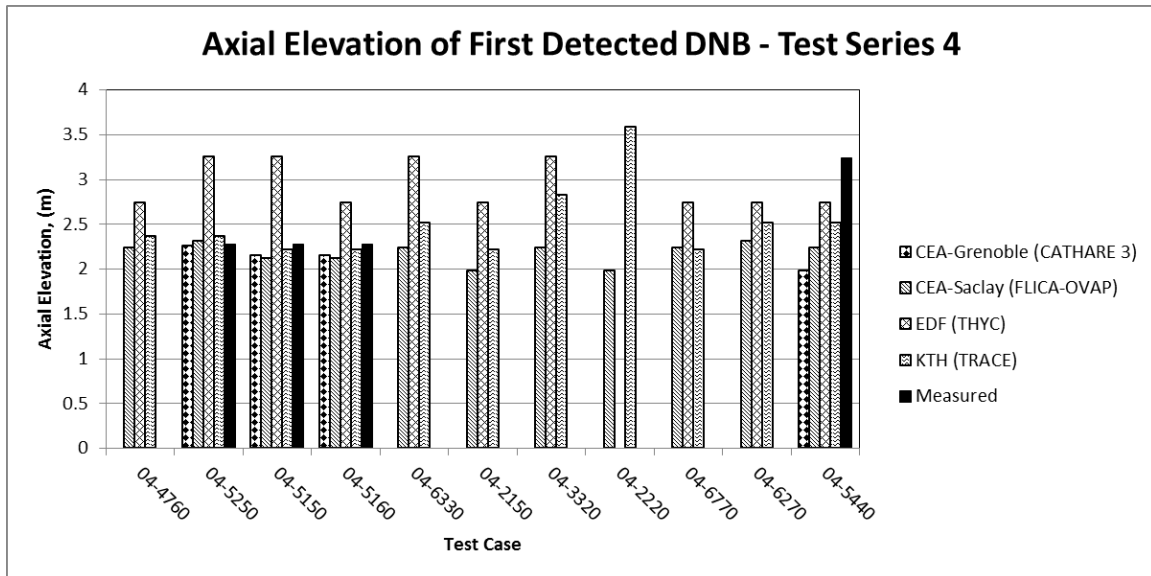


Figure AVI.7 Test Series 4 Elevation of First Detected DNB Results

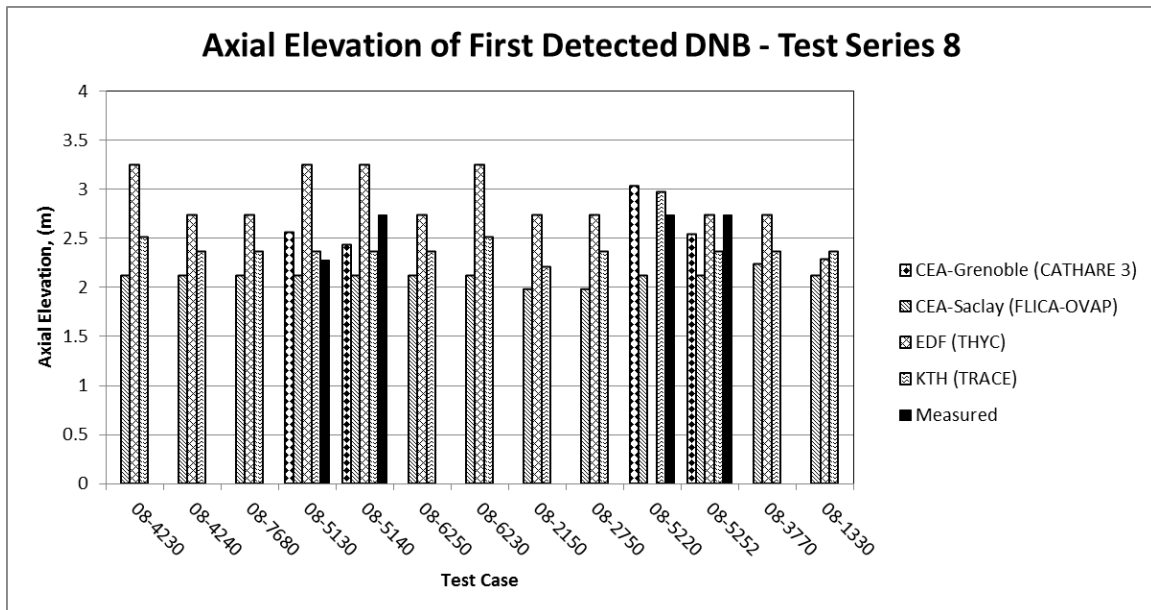


Figure AVI.8 Test Series 8 Elevation of First Detected DNB Results

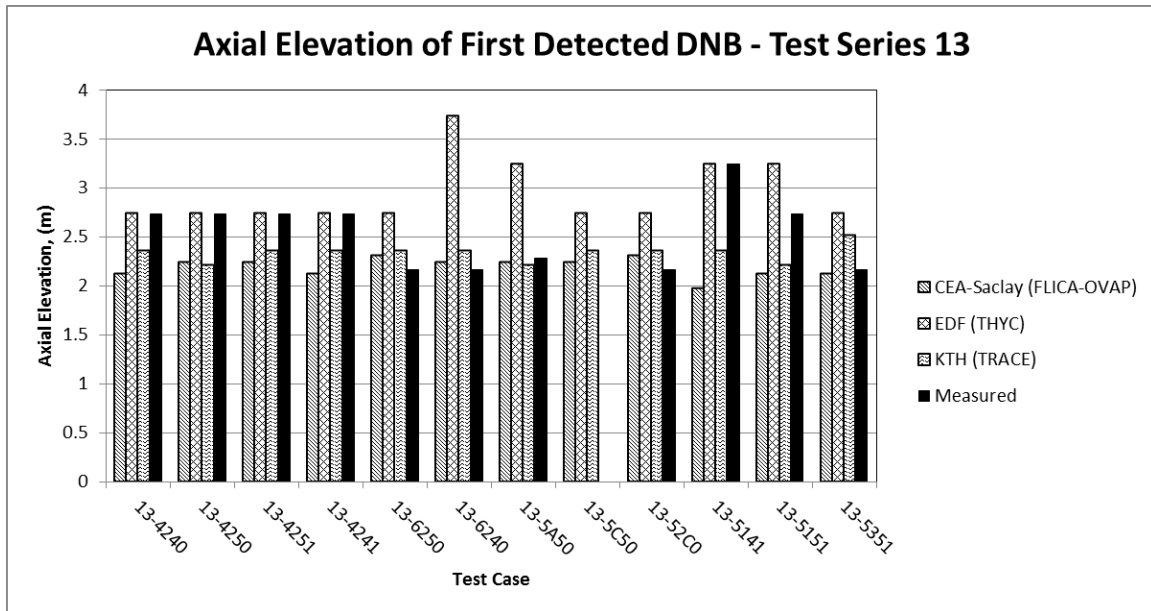


Figure AVL.9 Test Series 13 Elevation of First Detected DNB Results

Table AVL1 Radial Position of First Predicted DNB

Run No.	Radial Position of First Predicted DNB			
	CEA-Grenoble (CATHARE 3)	CEA-Saclay (FLICA-OVAP)	EDF (THYC)	Measured
04-4760		central	central	
04-5250	central	central	central	central
04-5150	central	central	central	central
04-5160	central	central	central	central
04-6330		central	central	
04-2150		central	central	
04-3320		central	central	
04-2220		central		
04-6770		central	central	
04-6270		central	central	
04-5440	central	central	central	central
08-4230		central	peripheral	central
08-4240		central	peripheral	central
08-7680		central	peripheral	central
08-5130	central	central	peripheral	central
08-5140	central	central	peripheral	central
08-6250		central	peripheral	central
08-6230		central	peripheral	central
08-2150		central	peripheral	central
08-2750		central	peripheral	central
08-5220	central	central		central
08-5252	central	central	peripheral	central
08-3770		central	peripheral	central
08-1330		central	peripheral	central
13-4240		central	central	central
13-4250		central	central	central
13-4251		central	central	central
13-4241		central	central	central
13-6250		central	central	central
13-6240		central	central	central
13-5A50		central	central	central
13-5C50		central	central	
13-52C0		central	central	central
13-5141		central	central	peripheral
13-5151		central	central	central
13-5351		central	central	central

Appendix VII Exercise II-3 Results

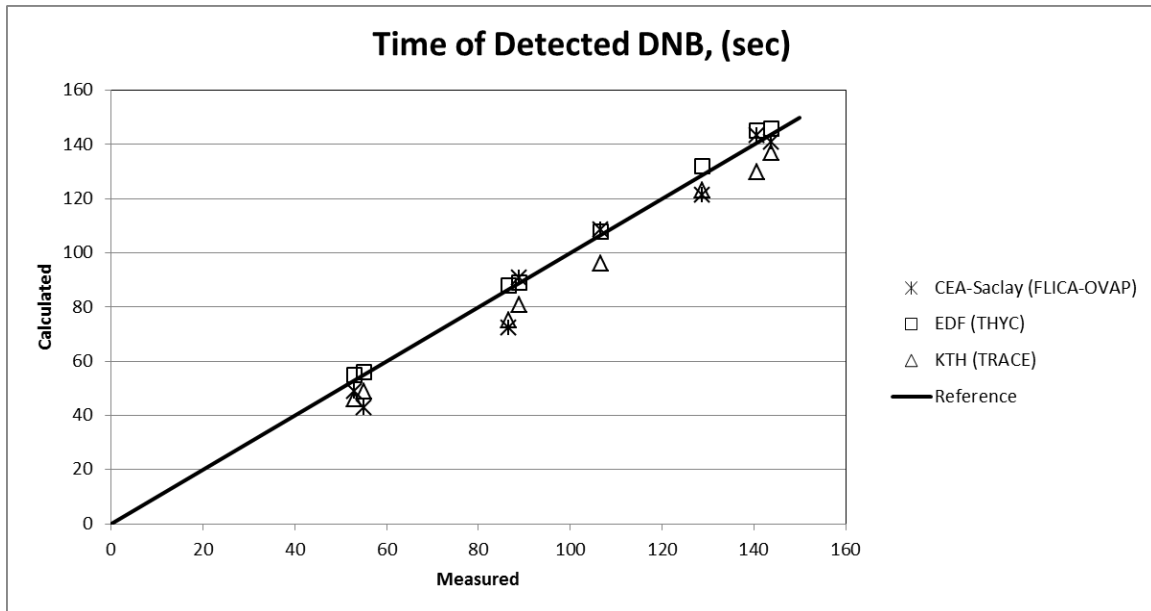


Figure AVII.1 Exercise 3 Time of Detected DNB Results

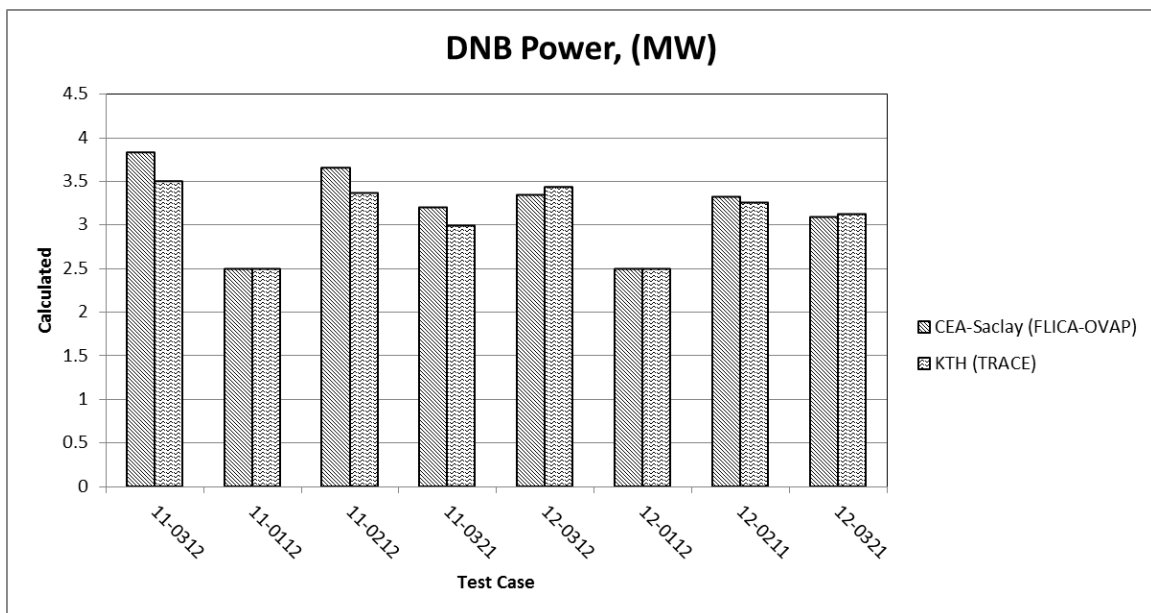


Figure AVII.2 Exercise 3 DNB Power Results